

Contents

Articles

Standards for Waveform Metrology Based on Digital Techniques	Barry A. Bell	377
The Diffusion of Charged Particles in Collisional Plasmas: Free and Ambipolar Diffusion at Low and Moderate Pressures	A. V. Phelps	407
Tables of the Inverse Laplace Transform of the Function e^{-s^β}	Menachem Dishon, John T. Bendler, and George H. Weiss	433

Conference Reports

International Conference on Narrow-Gap Semiconductors and Related Materials	D. G. Seiler and C. L. Littler	469
--	-----------------------------------	-----

News Briefs

GENERAL DEVELOPMENTS

483

- Electric-Field Meter Developed
- 1990 Annual Directory of NVLAP Labs Published
- Bioprocessing Research in Space
- Measuring Thermal Conductivity of Ceramics
- Commerce Report Tags 1990s "Emerging Technologies"
- ASTM Approves NIST Cone Calorimeter as Standard
- NIST Seeking Proposals for Courseware Standards
- New Phase Noise Measurement System Developed
- NIST Method Allows Quicker, Cheaper Analyses
- Quality Software to Be Focus of Upcoming Lectures
- First Labs Accredited for EMI Testing
- Standards for Low-Temperature Superconductors
- Computer Control to Assure Quality Welds
- Mechanical Properties and Performance Group Established
- Oxygen Compatibility of Aluminum-Lithium Alloys
- Oak Ridge National Laboratory and NIST Collaborate on Supermirrors
- NIST Installs New High-current 420 kV X-Radiography Facility
- Decomposition of Energetic Molecules from Metastable Vibrational States
- Revised POSIX Standard Approved
- Global Potential of Open Systems Interconnection (OSI) Technology
Demonstrated
- Hypertext Standardization Workshop Proceedings Published
- NIST Begins Structured Query Language (SQL) Validation Service
- High-Quality In-Situ $\text{YBa}_2\text{Cu}_3\text{O}_7$ Films Fabricated Using
A New State-of-the-Art Deposition System
- United States/Canada Renew SI Unit Agreements, Add Others
- Cooperative Program Tackles Automated Inspection
- Date Set for Uniform Gas Pump Pricing
- Design for a Radioscopic Image Quality Indicator
- Novel Process for Growing Crystals
- Security for "Open" Networks
- NIST Gatt Standards Code Activities Reported
- Computerized Welding Data Available
- Improved Testing for EM Susceptibility
- Near-Field Gain of Pyramidal Horns

CALIBRATION SERVICES	491
Noise Calibrations Extended	
 STANDARD REFERENCE MATERIALS	
Low-Alloy Steel Standards Available for Producers	491
Aqueous Solutions Valuable for Calibrating Instruments	
 STANDARD REFERENCE DATA	
PC Database Available for Biochemists	491
PC Database for Evaluating Refrigerants Announced	
New VEEL PC Program Offers Rapid Access to Data	
Major Expansion Announced for Mass Spectral Database	
New Mass Spectral Database of Common Compounds	
 <i>Calendar</i>	493

Standards for Waveform Metrology Based on Digital Techniques

Volume 95

Number 4

July–August 1990

Barry A. Bell

National Institute of Standards
and Technology,
Gaithersburg, MD 20899

Over the last decade the use of digital synthesis and sampling techniques for generating and measuring electrical waveforms has increased dramatically with the availability of improved digital-to-analog (D/A) and analog-to-digital (A/D) converters and related devices. With this evolution has come the need for physical laboratory standards and test methods to support the performance specifications of digital devices and the instruments in which they are used. This article describes the research and

development at NIST of several laboratory standards and test systems that utilize "digital technology" for characterizing data converters and for implementing various waveform synthesis and sampling instruments.

Key words: calibration; data conversion; digital synthesis; harmonic distortion; phase angle; waveform sampling.

Accepted: April 6, 1990

1. Introduction

In the early 1970s the NAS/NRC Evaluation Panel for the Electricity Division of the National Bureau of Standards (NBS) made recommendations that the Electrical Instruments Section begin to address the metrology problems associated with precision electrical/electronic instruments and test equipment where dynamic performance considerations were becoming paramount. In September 1974, a workshop was held at the NBS Gaithersburg facility to identify critical metrology needs associated with modern electronic instrumentation. The discussion topics, session notes, feedback reports, and conclusions of the workshop are well documented in an NBS Technical Note [1]. A general theme running through the summaries of the workshop discussions was the need for NBS to provide improved metrology support for the digital technology being incorporated in electrical/

electronic devices, test equipment, and systems, and to address dynamic as well as static test conditions.

A number of specific project activities recommended by the Panel and the 1974 Workshop were undertaken by what has since been renamed the Electronic Instrumentation and Metrology (EIM) Group [2]. This article is a synopsis of the description of some of the new physical laboratory standards, together with their operating principles and performance, that have come out of this research. The work to be described covers three general areas in the following order: data converter characterization, generating reference waveforms digitally, and measuring waveform parameters using digital sampling. These three areas are summarized briefly below.

1.1 Data Converter Characterization

Since a critical part of “digital” measurement technology involves the basic principles associated with converting analog signals to digital form and vice versa, an initial project was started for providing a basis by which to test precision data converters (both digital-to-analog (D/A) and analog-to-digital (A/D) converters, often designated as DACs and ADCs). A precision 20-bit D/A converter (DAC 20) was developed during the late 1970s to serve as the reference against which 12- to 18-bit converters could be compared [3]. A static test set was developed for providing these comparison measurements automatically [4]. A test set was also developed for measuring the dynamic performance of ADCs with up to 16 bits of resolution [5]. With the ability to quantify the linearity, offset, and gain errors of precision converters (both statically and dynamically), the limitations in the performance of these devices can be determined when used for synthesizing and sampling analog waveforms.

1.2 Generating Reference Waveforms Digitally

Concurrent with the development of DAC 20 was an effort to develop a precision audio-frequency phase angle standard that utilized 16-bit DACs to generate two output waveforms whose relative phase difference could be established digitally rather than with analog bridge methods [6,7]. By making use of 18-bit computations and 16-bit DACs, both the amplitude and phase of the two output waveforms from a dual-channel generator were digitally controlled in order to provide a low-frequency ac power source with amplitude and phase stability of 20 ppm and 1 μ rad, respectively, over a 100-s measurement period [8]. By using two DACs to prevent “glitches” in the stepped output waveform, a calculable rms ac voltage source has recently been developed. It can be used as a transportable ac reference standard with uncertainties at the 7-V rms level typically less than ± 10 ppm from 30 Hz to 15 kHz [9]¹. These physical standards are being used in several different automatic test systems at NIST to provide calibration services for phase angle meters, wattmeters and watthour meters (also var and varhour meters), and ac digital voltmeters.

1.3 Measuring Waveform Parameters Using Digital Sampling

The characterization of sample and hold (S/H) amplifiers and ADCs for sampling and digitizing waveforms was also part of the EIM Group’s development efforts during the 1970s [10,11]. An early application of precision synchronous waveform sampling was the development of a digital wattmeter that used 15 bit successive approximation ADCs, phase locked to the input signals, to provide power measurements good to an uncertainty of $\pm 0.02\%$ from dc to 2 kHz [12]. Using a 12-bit resolution data acquisition module (S/H, instrumentation amplifier, and ADC), together with an internal microcomputer, a low-frequency sampling voltmeter was developed that acquired ac voltage input signals below 10 Hz good to an uncertainty of $\pm 0.1\%$ with a total autoranging, settling, and measurement time of only two signal periods [13]. In the early 1980s the principles of asynchronous sampling of corresponding voltage and current signals were studied, and a wideband sampling wattmeter was developed, capable of measuring audio frequency power from 1 Hz to 10 kHz (with distortion harmonics up to 100 kHz) with an uncertainty of less than $\pm 0.1\%$ [14]. More recently, an equivalent-time sampling and digitizing system, based on a sampling voltage tracker (SVT) circuit, has been developed that has been shown to be capable of making state-of-the-art measurements of signals with frequencies up to 200 MHz [15]. These sampling instruments are also being used in both stand-alone and automatic test sets for calibrating wideband power meters, low-frequency voltmeters, and step/arbitrary waveform generators.

2. Data Converter Characterization

A number of special methods have been developed for testing various performance parameters of data converters, and commercial, general-purpose test sets for these devices are now available. However, these methods and systems typically are not capable of measuring the integral linearity, differential linearity, gain, and offset errors of 12- to 18-bit converters good to fractions of a least significant bit (LSB). (An LSB represents the resolution of a converter and is defined as (full scale range)/ 2^n where n is the number of bits of the converter.) For quantifying the accuracy errors of 12- to 18-bit data converters, test methods have been

¹Uncertainties quoted in this paper are taken from the references given and are not uniformly defined.

developed and test sets are available at NIST. A NIST calibration service for data converters is offered, as described in [16].

2.1 Measuring Static Transfer Characteristics

The primary property of concern when characterizing precision data converters is the relationship between the input and output variables under both static and dynamic conditions. The transfer characteristic for a DAC is shown in figure 1, where the straight dashed line indicates the ideal relationship between the digital input codes and the corresponding analog output levels. Due to offset voltages/currents, mismatches in the divider circuit (typically an R-2R ladder network), and other sources of nonlinearities, the actual characteristic deviates from the ideal. When an increase in the digital input code does not produce a corresponding increase in the analog output level, the behavior is described as nonmonotonic. Similarly, the transfer characteristic for an ADC is shown in figure 2, where the perfect "staircase" relationship between the analog input levels and the corresponding digital output codes represents the ideal. Due to noise from the logic circuits, speed limitations of the analog comparator, errors of the internal reference DAC, etc., the actual ADC

characteristic has the non-uniform steps and non-ideal edge transitions indicated in figure 2. Finding and quantifying these small deviations can be important in critical applications of precision data converters.

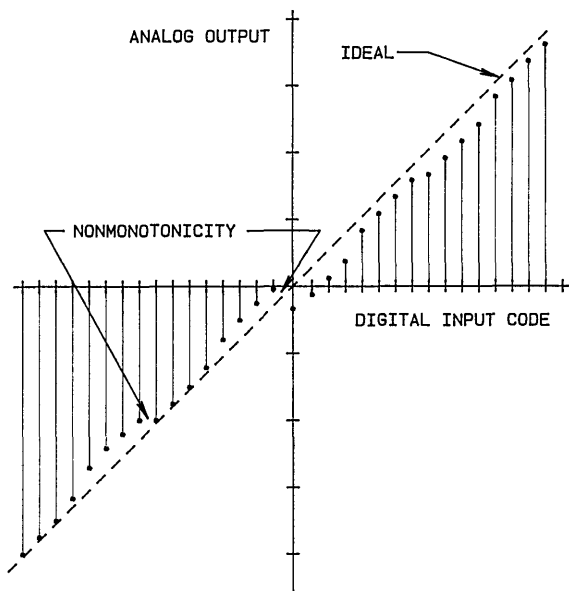


Figure 1. The transfer characteristics for an ideal and an actual DAC.

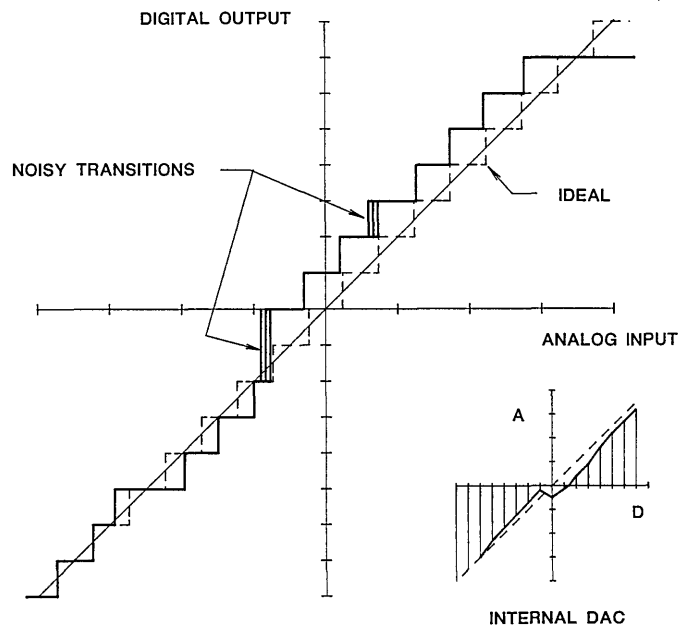


Figure 2. The transfer characteristics for an ideal and an actual ADC.

Figure 3 shows a simplified diagram of the NIST test set for measuring the essential parameters of the static transfer characteristic of precision data converters. The basic operation involves a comparison of outputs of the test DAC or ADC with the corresponding levels from the NIST DAC 20. This multirange, 20-bit+sign, programmable voltage source exhibits less than 1 ppm linearity error and incorporates a self calibration feature [3]. The design is based on an R-2R ladder network in the current steering mode, using miniature latching relays (to minimize thermal effects) with mercury-wetted contacts for the switches. Ten buffered, temperature-controlled, unsaturated standard cells (providing direct linkage to the legal volt) comprise the voltage reference.

For testing DACs, the DAC 20 standard and the test unit are given the same digital input code from the system controller via an IEEE-488 bus and coupler, with code conversion as needed. The difference in their analog output levels (error signal) is then amplified, digitized with a voltage to frequency (V/F) converter, and averaged over a 60-Hz period (to reduce power frequency noise). The error data (both binary and BCD coded) are displayed on front panel readouts and returned to the controller for logging and further analysis. By sequencing through all 2^n code states (or only 1024, corresponding to the ten most significant bits), the complete DAC static transfer characteristic can be determined with a full scale output resolution of 1 part in 2^{20} .

Testing an ADC is more complicated in that each digital output code from the test unit corresponds to a small *continuous range* of analog input values, as illustrated in figure 2. A complete determination of the ADC transfer characteristic requires locating and measuring each of the voltage levels corresponding to the transitions between digital codes. Transition level location in the NIST static data converter test set is accomplished by placing the test ADC in a feedback loop that controls the input voltage to the ADC, as shown in figure 3. The upper digital code of the transition level of interest is input over the IEEE-488 bus from the controller to a digital comparator whose other digital input comes from the ADC output (with code conversion, as needed). The digital comparator's "less than" output sets the polarity of a programmable voltage (+V, -V), which is switched to the input of an integrating amplifier. Thus, the output voltage from the integrator, switched to the input of the test ADC, ramps up (or down) until the upper transition level code is output from the ADC, whereupon the less than output from the digital comparator changes state, causing the slope of the integrator's output voltage to reverse. The ADC then outputs the lower transition level code so that the process continues at a preset clock rate (normally 10 kHz), generating a small ($\ll 1$ LSB) peak-to-peak triangle waveform at the ADC input with an average value very near the transition level. Once locked onto a transition level, that voltage is then measured by the same

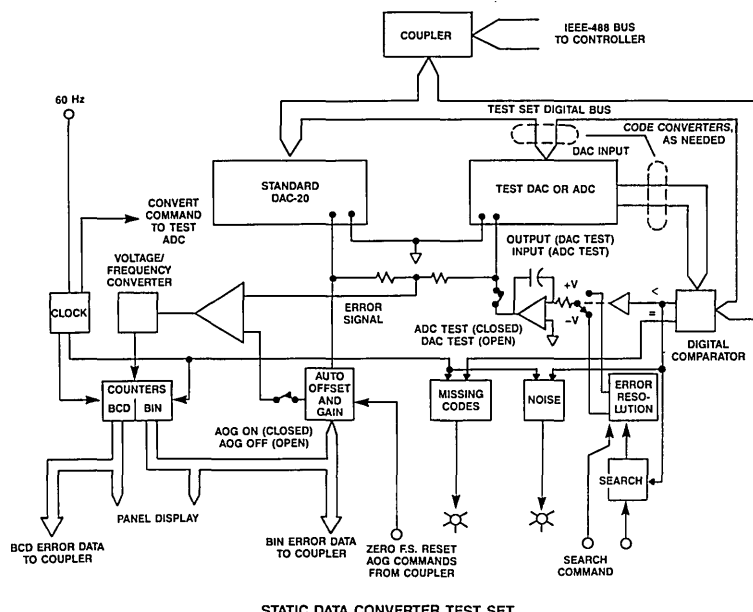


Figure 3. A simplified diagram of the NIST static data converter test set.

comparison circuitry described above for DAC testing. The error data are collected by sequencing through 1024 (or, all 2^n if desired) code states in order to determine the complete ADC static transfer characteristic. Since bits less significant than the 10th generally contribute insignificant errors, typically only $2^{10} = 1024$ codes are tested, corresponding to the 10 most significant bits.

2.1.1 Analyzing Static Linearity Errors At each of the 1024 codes the test set automatically measures the errors, defined as the difference between the output (input) of the DAC (ADC) under test and the output of reference DAC 20 (calibrated to have negligible linearity errors). These measured errors are then numerically corrected for offset and gain by the following calculations:

$$\epsilon'_i = \epsilon_i - \epsilon_0 - (\epsilon_{1023} - \epsilon_0)i/1023, \quad (1)$$

where ϵ'_i is the offset and gain corrected error at the i th code,
 ϵ_i is the measured error at the i th code,

i is the code index 0 to 1023,
 ϵ_0 is the measured error at the negative-most code, and
 ϵ_{1023} is the measured error at the positive-most code.

The values of ϵ' , obtained from testing over the full scale range of the converter are used to determine the maximum, minimum, and rms value. Shown in figure 4 are some representative linearity error vs codeword plots obtained from the NIST static data converter test set. Keep in mind that these error plots show the *deviations* from an ideal transfer characteristic. Since differential linearity error (DLE) is defined as the error in separation between adjacent code transition levels, these errors are associated with the discontinuities observed in the plots of figure 4 (assuming as before that the bits less significant than the 10th contribute insignificant errors). Major discontinuities almost always occur at major code transitions; consequently, an abbreviated test is used to provide actual measure-

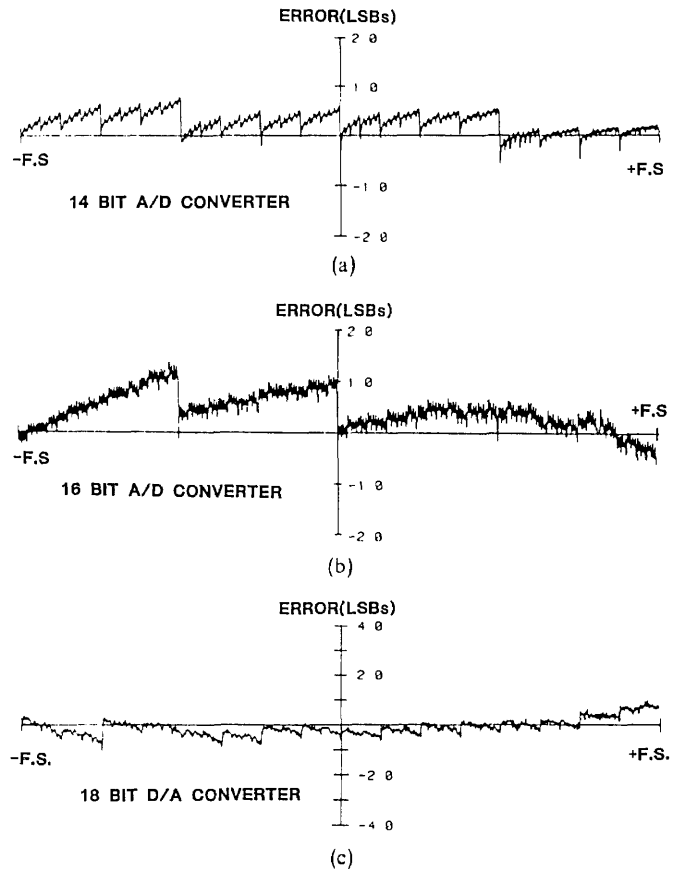


Figure 4. Typical linearity error plots. (a) 14-bit, 10- μ s ADC. (b) 16-bit, 32- μ s ADC. (c) 18-bit DAC, data average of five measurements.

ments of the DLEs at those $2(n-1)$ adjacent code pairs where the errors are likely to be the greatest. The DLE at each of these code pairs is simply computed as

$$\epsilon_{DL} = \epsilon_j - \epsilon_{j-1}, \quad (2)$$

where ϵ_j and ϵ_{j-1} are the measured linearity errors at the selected adjacent code pairs.

2.2 Measuring Dynamic Transfer Characteristics

For most applications of data converters, the relationship between the analog and digital input/output variables under dynamic conditions is a primary property of concern. For DACs, this represents a deviation of the static transfer characteristic due to the inherent settling time of the DAC. Given a change in the digital input code, there will be a characteristic time required for the analog output of the DAC to settle to a new static level within some tolerance. Generally, the maximum settling time can be observed by giving the DAC a full scale code change at its input. This large change in the input will exercise the switching circuitry associated with the most significant bits of the converter, which are the critical ones in terms of settling time.

Making an accurate measurement of the settling time of a precision DAC to within 1 LSB, however, is not a trivial matter since it requires a good measurement of both amplitude and time. Methods for accurately measuring the settling time of DACs (as well as amplifiers and step generators) have been developed at NIST. These can be used to determine settling times as short as 10 ns to within a settling error of $\pm 0.1\%$ [15] (or as short as 1 μs to within a settling error of ± 2 ppm [17]) for voltage output devices. Further improvements in the sampling voltage tracker system described in [15] are being pursued at the present time in order to improve the NIST capability to measure settling time accurately in the 1-10 ns region.

Dynamic errors in ADCs also are defined as any deviations from the static transfer characteristic that result from prior exercise, i.e., previous changes in input [5]. Since high-resolution (> 12 -bit) ADCs in most applications are preceded by an analog multiplexer or a S/H amplifier, exercising the ADC's input with a fast-settling voltage step gives a good representation of the dynamic input conditions during actual use. An accurate method for providing stepped input voltage changes to ADCs for dynamic testing purposes

was developed at NIST in the early 1980s [18]. Figure 5 shows a simplified diagram of the circuit used at NIST for dynamic ADC testing. It employs a programmable pulse level, V_p , which is converted to a programmable current that is then switched (with optical isolation) through a low-value (200 Ω) resistor (R_L) in series with the output of the feedback loop integrator. A programmable voltage step is thus superimposed on the transition level voltage established by the transition-locking feedback loop described above for static ADC testing.

Figure 6 gives some of the signal and timing diagrams associated with this test method, where the step changes to the programmed pulse level and back to the transition level are made between conversions, with time (Δt) allowed for the test ADC's specified settling time. Although the test ADC converts when the input voltage is at either level, the ADC output samples (fed back to the digital

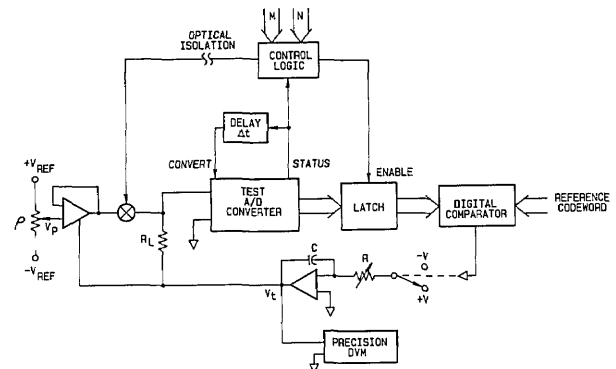


Figure 5. Simplified circuit diagram for the NIST dynamic ADC test set.

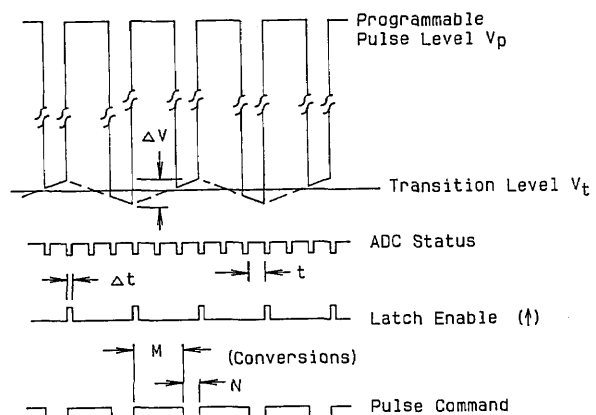


Figure 6. Timing diagrams, showing the relationships between the input voltage to the test converter (top) and three of the test set control signals.

comparator) are latched only for conversions made near the transition level. Any dynamic limitations of the test ADC (due to input buffer amplifier settling, internal DAC settling, delay in the internal analog comparator, etc.) will be manifest as a change in the static transition level that nominally would be maintained by the feedback loop. Therefore, the transition level maintained under the dynamic conditions just described is then measured by a precision digital voltmeter (DVM) and logged by the test set controller. Referring to the top waveform diagram in figure 6 (the input signal to the test converter), the portion of the signal about the transition level changes slowly, due to an adjustably long time constant of the integrator, with an amplitude given by

$$\Delta V = (V/RC)(M+N)(t + \Delta t), \quad (3)$$

where V is the input voltage to the integrator, M is the number of conversions made with the input at the programmable pulse level, N is the number of conversions made with the input at the transition level, t is the conversion time duration of the test ADC,

Δt is the time delay to allow for the pulse to return to the transition level and the test unit to respond, and RC is the time constant (τ) of the integrator.

Since the resolution of the transition level measurement is limited by ΔV , R (and, hence, τ) is adjusted to obtain an adequately small ΔV (nominally <0.1 LSB).

Figure 7 shows a 3-D plot of the dynamic linearity error data obtained from a 16-bit ADC on the NIST dynamic ADC test set. The codeword axis is the measured code transition level and the pulse level axis is the range of possible pulse level amplitudes applied to the test ADC, with the vertical axis being the corresponding error in LSBs. This "surface" of dynamic bit errors is typical of the multi-bit errors that can often be observed, as compared to the fractional static LSBs typical of most ADCs (e.g., fig. 4). By varying the test set parameters (M , N , and Δt) given in eq (3), one can investigate the cause of various features observed on the error surface [4].

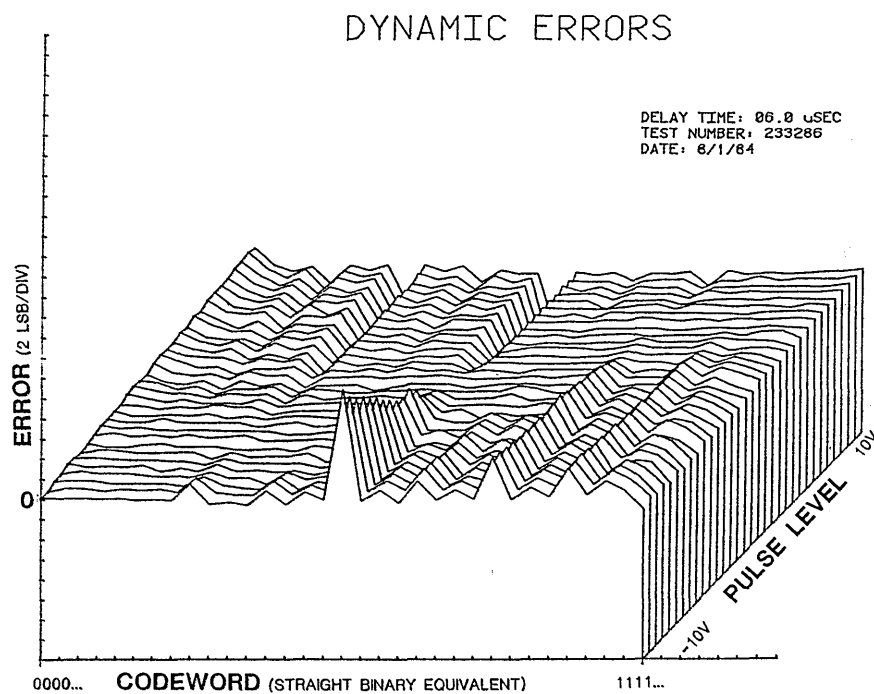


Figure 7. 3-D plot of typical dynamic linearity errors for a 16-bit ADC.

3. Generating Reference Waveforms Digitally

By making use of precision DACs that have small linearity errors (both statically and dynamically), reference waveforms can be generated by applying a time sequence of digital codes to the DAC and obtaining an analog output waveform consisting of steps corresponding to each of the input codes. Without further data processing on the input samples and the resultant output waveform, this stepped waveform is often referred to as a "zero order hold" reconstruction of the digital code sequence. Figure 8 (a) shows a representation of such an ideal stepped sinusoidal waveform in the time domain, with its corresponding line spectrum in the frequency domain given in figure 8 (b) (see the Appendix). Filtering out harmonics of the fundamental frequency located around multiples of the sampling frequency is relatively easy if the number of samples, N , is large enough so that the sampling harmonics are relatively small and fall outside the passband of the filter. The filtered output is then the original sine wave, only with its amplitude attenuated by the magnitude of the $\sin(\pi f/f_s)/(\pi f/f_s)$ function at the fundamental frequency. Of course, for imperfect filters and nonideal DACs, an actual line spectrum, such as the one shown in figure 8 (b), would have other small frequency components due to distortion and noise.

3.1 Audio Frequency Phase Angle Standard

As illustrated in figure 9, by changing the time sequence of digital codes that are input simultaneously to a second DAC, a pair of stepped sine waves can be generated having a relative phase angle difference that is established essentially by the calculated sets of sample points, independent of the fundamental frequency and any other timing considerations used in the digital synthesis process. This is the basis for a precision 2 Hz to 50 kHz Phase Angle Calibration Standard that was developed at NIST [20,21]. An earlier version of this design approach was used for generating reference phase angle signals up to 5 kHz [6,7].

A functional block diagram of the NIST Phase Angle Calibration Standard is shown in figure 10. A 20-bit, high-speed microprocessor (μ P) computes the data needed for generating the 0-100 V rms output waveforms (delivered to a test phase meter). A slower 8-bit μ P handles keyboard entries, correction data from the auto zero circuit, output scaling via the multiplying DACs (MDACs), and IEEE-488 interface and display functions (not shown). Eighteen-bit angle data (calculated by the 20-bit arithmetic logic unit (ALU) from phase and frequency keyboard entries) is fed sequentially to an angle-to-sine conversion module (sine table). Pairs of corresponding 16-bit amplitude data are then input simultaneously to the dual DACs through latches (not shown). The sample-

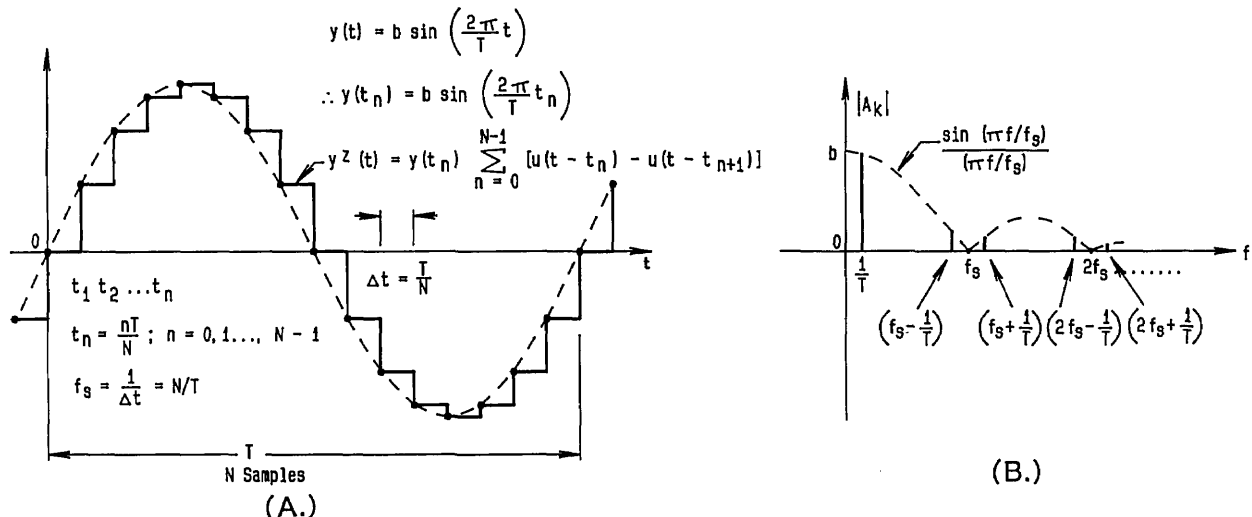


Figure 8. Time domain (a) and frequency domain (b) relationships of an ideal stepped (zero-order-hold) reconstruction of a sinusoidal waveform.

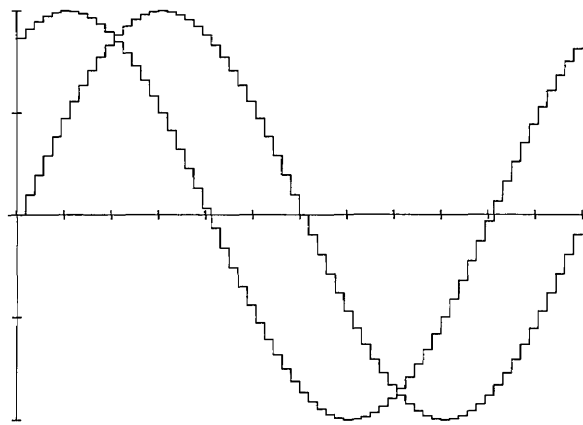


Figure 9. Stepped sine waves, phase difference 60° , 64 steps per cycle.

point strobe pulses to the latches are generated by a crystal-controlled time base (also not shown). Thus, the waveforms that are output from the two DACs look like those of figure 9. These waveforms are then filtered to remove the unwanted steps (sampling harmonics), as mentioned above in conjunction with figure 8. Since most phase meters have voltage ranges that can accept input signals both above and below the 7 V rms output from the lowpass (L.P.) filters, the two sine waves are then scaled either up or down (from keyboard-entered amplitude data) by the MDACs and amplifiers. These scaling circuits cause small phase differences between the two output waveforms. To minimize these differences, a quadrature phase detection circuit is used to measure and compensate for the residual differential phase at 90° , thus establishing a fixed point on the phase angle scale.

The angular resolution of the phase standard depends on the number of sample points per cycle

and on the amplitude resolution, corresponding to the number of bits of the DACs [20]. Each of the steps shown for the stepped sine waveform of figure 9 occur at a phase angle of

$$\phi_n = 2\pi n/N, \quad n = 1, 2, \dots, N \quad (4)$$

with an amplitude resolution of

$$\Delta V = 2V_p/2^M, \quad (5)$$

where N is the number of samples per cycle, M is the number of bits of the DAC, and V_p is the peak value of the sine wave.

That is, at each step the phase angle can be set precisely, but the amplitude is limited to a quantized value within the resolution of the DAC. For $N=64$ and $M=12$, $\phi_1=5.625^\circ$, and $\Delta V=V_p/2048$. Because the amplitude steps are quantized, the phase angle between the output waveforms will also be quantized, although not necessarily uniformly. Thus, small changes in the programmed phase angle will not necessarily cause the phase difference between the two output waveforms to change. By incrementing ϕ a small amount at the N sample points until at least one sample pair (180° apart) changes by ΔV , the theoretically attainable phase resolution can be determined. Simulations have shown that for $N=64$, $M=12$, 97 percent of the possible phase increments will be less than or equal to 0.005° [20]. Below a fundamental fre-

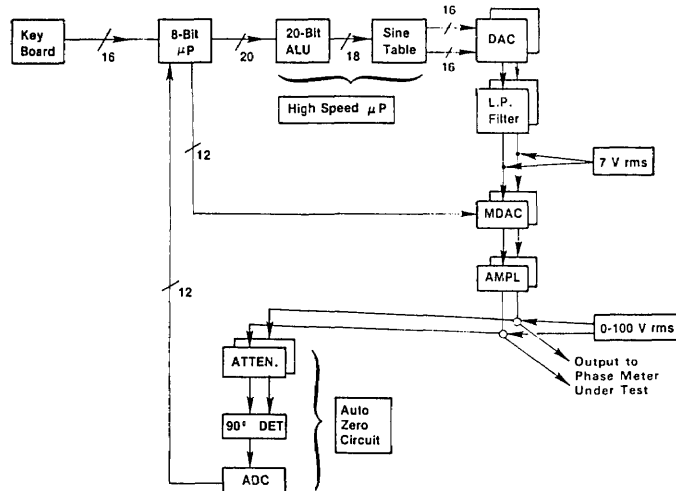


Figure 10. Block diagram of the NIST phase angle calibration standard.

quency of 5 kHz where the phase standard uses 16-bit DACs, the theoretical resolution is better than 0.001° .

Because actual DACs are not perfectly linear and noise limits the uncertainty of the auto-zero compensation circuit, the NIST phase standard departs somewhat from its theoretical performance. Figure 11 shows the experimentally determined linearity for the phase standard using a 180° bridge [7,20]. The upper plot (a) shows the departure from

the ideal 180° difference using 16-bit DACs at a frequency of 3125 Hz, generating the waveforms with both 64 and 128 samples per cycle. The lower plot (b) shows similar data obtained for the linearity using 12-bit DACs at a frequency of 31250 Hz. The range of the phase angle settings used for these plots is the basic 5.625° angle interval for $N=64$ and $M=12$. Using these and other experimental results, the maximum errors in the phase standard have been determined, as summarized in table 1.

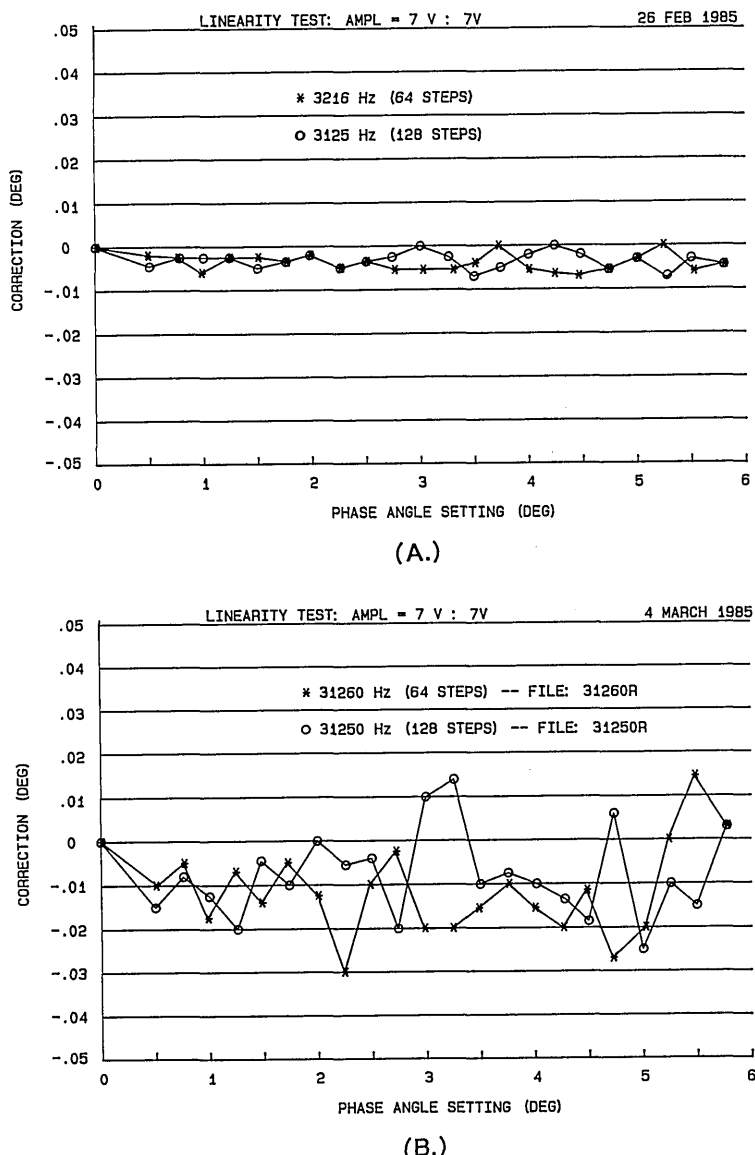


Figure 11. Measured phase linearity of the NIST phase angle calibration standard output (a) with 16-bit DACs at 3125 Hz, and (b) with 12-bit DACs at 31250 Hz (64 and 128 samples per cycle).

Table 1. Estimated maximum phase angle uncertainty (in millidegrees)

	60 Hz	400 Hz	5 kHz	15 kHz	30 kHz	50 kHz
Auto-zero corr. ^a	±1	±2	±5	±6	±12	±20
Linearity	±2	±2	±3	±10	±15	±20
7:1 voltage ratio	±1	±2	±3	b	b	±40

^a The uncertainty due to frequency adjustment is included.^b Data not available.

With the development of the above-described NIST Phase Angle Calibration Standard, an automated calibration service for precision phase meters is now available [22].

3.2 Power Calibration Source

The traditional method of calibrating precision wattmeters and watt-hour meters is to compare the readings of the meter-under-test (MUT) to a standard wattmeter or watt-hour meter connected in parallel. However, it is advantageous, particularly in an automatic test setup, to be able to supply a separate source of voltage and current ("phantom" power) to the MUT where the source of voltage, and current (and the relative phase angle) is known and stable. Such a digitally synthesized power calibration source was developed at NIST to provide known parameters in order to test and calibrate a new class of multifunction instruments capable of measuring voltage, current, power factor, and active and reactive power [23].

Figure 12 shows a block diagram of the NIST Power Calibration Source. The digital generator (shown in more detail in the lower part of fig. 12) is the heart of this source, and generates sine wave voltages V_1 and V_2 in a staircase approximation, as illustrated in figure 9. The waveforms in this case consist of 2048 steps per period at 60 Hz, which are then scaled by specially designed amplifiers A1 and A2 [24,25] to produce typical test voltages, V , ranging from 60 to 240 V rms, and typical test currents, I , ranging from 1 to 5 A rms. The relative phase angle between these voltages and currents applied to the MUT is determined essentially by the digital code sequences supplied to the MDACs from the random access memories (RAM1 and RAM2), similar to the technique used in the phase angle standard discussed above. In this generator, however, the codes to the MDACs are calculated by the controller (desktop computer), which uses sufficient numerical resolution to compute the sample points that roundoff or truncation errors in the

phase angle are negligible. Consequently, the angular resolution using 16-bit MDACs is approximately $1 \mu\text{rad}$ (0.000057°) [23]. The amplitudes of V_1 and V_2 are independently set between 0 and 10 V peak by controlling the dc reference voltages supplied to MDAC1 and MDAC2 with a pair of 18-bit DACS. Consequently, the amplitude resolution for the power calibration source is 1 part in 2^{18} (about 4 ppm).

The performance of the power calibration source (particularly at 60 Hz) has been measured using both a time-division-multiplier (TDM) wattmeter [26] as a transfer standard, and a current-comparator power bridge [27] as a ± 15 ppm laboratory standard. Once again the nonlinearities, gain error, etc. in the characteristics of the actual DACs and amplifiers used in synthesizing the voltage and current outputs of the power calibration source limit its performance. However, software gain corrections for any amplitude (based on a linear fit to a few data points) help to reduce voltage-dependent gain error by a factor of 5 to 10. Figure 13 shows the integral amplitude nonlinearity (after gain corrections) in the voltage and current over a 5-to-1 range, using the current-comparator power bridge, where 100 percent of full scale represents 240 V rms and 5 A rms, respectively. Thus, we see residual uncertainties of

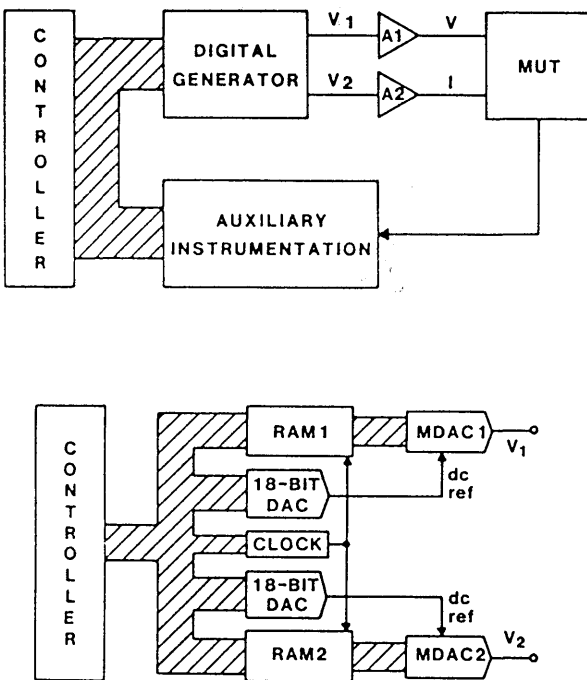


Figure 12. Block diagram of the NIST dual-channel power calibration source.

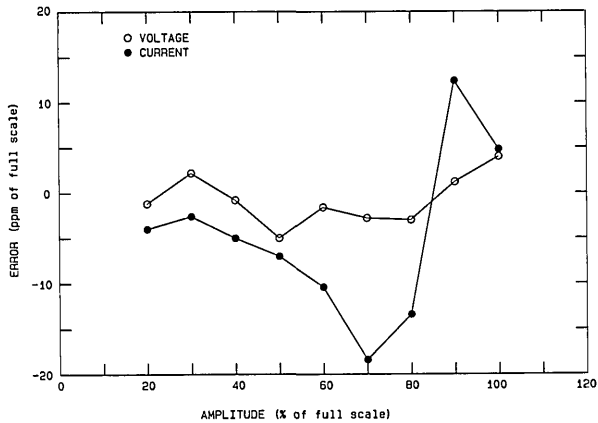


Figure 13. Integral amplitude nonlinearity in the power calibration source voltage and current outputs after gain corrections.

<±20 ppm for current and <±10 ppm for voltage. However, differential linearity errors (about small changes in the output voltage and current at full scale) are in the 5 ppm level, as seen from figure 14. Figure 15 shows the phase differential nonlinearity at zero power factor (90°), as measured by a TDM wattmeter. This plot demonstrates the 1 μrad resolution of both the digital generator and the TDM wattmeter. Finally, by comparing the power calibration source with the NIST current-comparator power bridge, figure 16 shows the agreement in active power to be within a ±30 ppm band at power factors from zero lead to zero lag. The two curves represent an envelope of data points where the pair of dots connected by a dashed line at a given phase angle are the extremes of the measured errors.

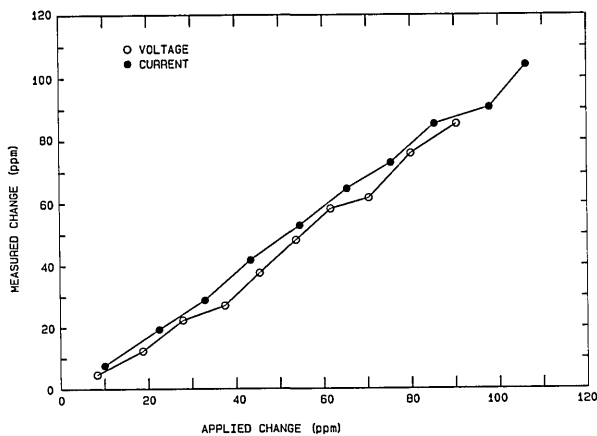


Figure 14. Differential nonlinearity of the voltage and current outputs around 120 V and 5 A rms.

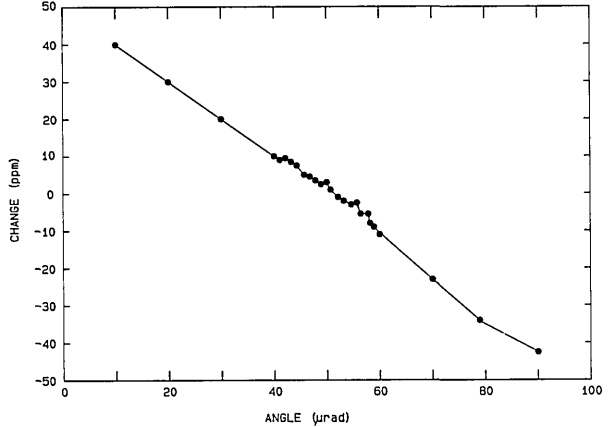


Figure 15. Phase differential nonlinearity: change in power indication of a TDM wattmeter (at zero power factor) versus change in phase angle from the NIST power calibration source.

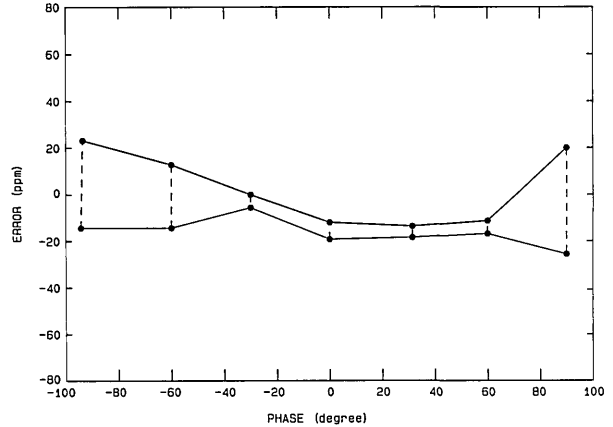


Figure 16. Maximum differences between the power calibration source and the NIST current-comparator power bridge, after correcting for current drift in the source.

3.3 Calculable RMS ac Voltage Source

For an ideal stepped sine wave, illustrated in figure 8(a), it can be shown that the rms value is identical to that of the corresponding pure sinusoidal waveform, i.e., $V_p/\sqrt{2}$ [28]. However, the stepped waveform contains harmonics in its frequency spectrum [see fig. 8(b)], so that the unfiltered reconstruction contains harmonic distortion relative to the fundamental frequency component. Consequently, there is a tradeoff between the exact rms accuracy of ideal stepped waveforms (with their inherent harmonic distortion) and the rms error inherent in filtered reconstructions (that can have no distortion for a perfect low pass filter).

Total harmonic distortion (or, distortion factor) is defined as [29]

$$\text{THD} = \frac{\text{rms value of all harmonics}}{\text{rms value of the fundamental}},$$

$$= (\sum_{i=2}^{\infty} A_i^2 / A_1^2)^{1/2}, \quad (6)$$

where A_i is the peak value of the i th harmonic, computed from

$$A_i = V_p [\sin(\pi f_i/f_s)/(\pi f_i/f_s)], \quad (7)$$

V_p is the peak value of the sine wave, f_i is the i th harmonic frequency, and f_s is the sampling frequency.

For comparison of the tradeoff between the rms error and THD between two sine wave reconstructions, table 2 shows these relationships for a stepped sine wave composed of 20 steps and another composed of 200 steps. It also shows a comparison with perfectly filtered (i.e., "brick wall") reconstruction.

Table 2. Comparison of rms error and THD for unfiltered and filtered stepped sine waves

No. of steps per period	Unfiltered Reconstruction		Filtered Reconstruction	
	rms error	THD	rms error	THD
20	0	8.9%	-0.4%	0
200	0	0.9%	-0.004%	0

An ac reference standard was developed at NIST in the early 1980s that used zero order hold digital waveform synthesis to produce both filtered and unfiltered sine wave reconstruction [30]. A built-in, rms-to-digital converter that used a thermal voltage converter (TVC) and voltage-to-frequency ADC was used to measure the rms value of the output waveform and provide error corrections.

Uncertainties of ± 50 ppm were achieved in the 0 to 7.07 V rms output voltage over a frequency range of 1 Hz to 50 kHz (with only 0.5% THD at 50 kHz using a lowpass, active filter). This ac reference is very useful for calibrating narrowband, rms-responding voltmeters having a $\pm 0.01\%$ accuracy specification.

However, new wideband voltmeters (and most thermal voltage converters) can respond to the harmonics in stepped waveforms, and still claim rms measurement accuracy below 0.01% (100 ppm). To provide a transportable ac source for these voltmeters at an accuracy of ± 10 ppm over a 30 Hz to 15 kHz range, a digitally synthesized source (DSS) using zero order hold reconstruction has been developed [31]. As indicated above (and shown in table 2), ideal stepped sine waves have no rms error and are, therefore, desirable rms reference waveforms.

Figure 17 shows a simplified circuit diagram of the dual-DAC synthesis approach used in the DSS. Its general design is similar to that of the generating circuits used for the phase angle standard and the power calibration source (see figs. 10 and 12). In addition, a "deglitching" technique (used to improve phase angle precision [32]) is employed in the DSS to enhance the quality of the generated steps. By toggling between the output currents of the two MDACs, which are updated with data from the latches at different phases of clock signals A and B, the output voltage steps from the amplifier are not subject to code-dependent transitions and settling-time errors from the MDACs. From t_1 to t_2 , MDAC2 supplies the output step (via switch S_3 and the output amplifier) while MDAC1 is settling to the level corresponding to the input code. At time t_2 new data from the ROM is latched into MDAC2, S_1 and S_4 are closed (S_2 and S_3 are opened), and MDAC1 now supplies current for the next output voltage step. Obviously, successive data are clocked from the ROM into the latches, alternately, at twice the rate of clocks A and B.

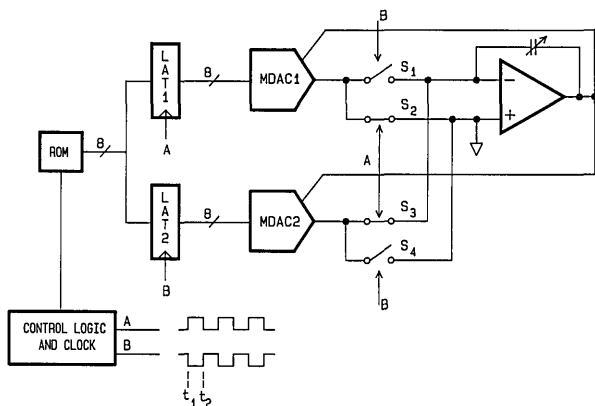
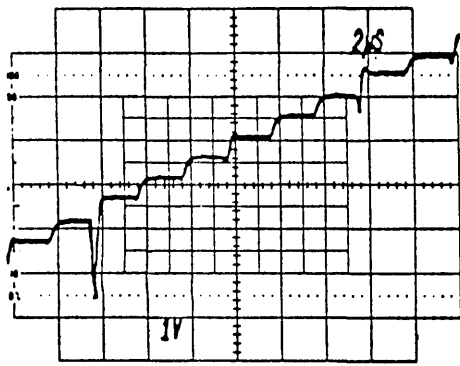


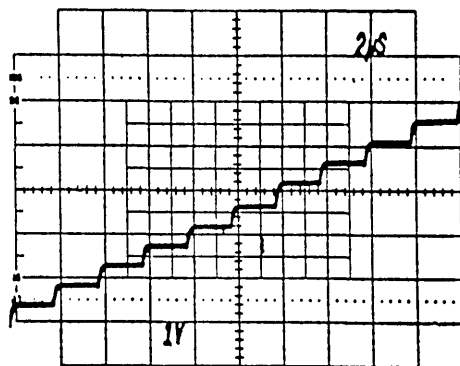
Figure 17. Simplified diagram of the circuit used in the dual-DAC, digitally synthesized source (DSS).

Of course, imperfect steps still remain due to small amounts of strobe feedthrough from the (fast CMOS) switches and finite bandwidth and slew rate limitations in the amplifier. However, as seen in figure 18, the improvement in the fidelity of the steps using this technique is significant. The major code transition glitch seen in figure 18 (a) and other structural differences between the steps are virtually eliminated in figure 18 (b).

The rms voltage of the waveforms generated by the DSS over its nominal frequency range is calculated by stepping through the sample points stored in the ROM at a low speed in order to measure the amplitude of each step with a high-accuracy DVM.



(A.)



(B.)

Figure 18. Oscilloscope traces of an unfiltered portion of a 28-step digitally synthesized sine wave (1-MHz clock rate). (a) Using a single DAC. (b) Using the dual-DAC deglitching technique.

The estimated rms value of the waveform using this "step calibration" is determined by computing the square root of the mean value of the squares of the measured step voltages, i.e.,

$$V_{\text{rms}} = \left[\sum_{i=1}^N [v_i(1+C)]^2 / N \right]^{1/2}, \quad (8)$$

where v_i is the voltage of the i th step

N is the number of steps in one period, and
 C is the DVM correction.

In order to assure that the estimate is good to a few ppm, the DVM nonlinearity must be only a few ppm of full scale and have similar short term stability during the test time. This computed rms value then will be valid for low-frequency waveforms, but will degrade at higher frequencies as imperfections due to transients become a larger portion of each of the steps.

The rms values of the outputs from two of the DSS prototypes have been measured at NIST with coaxial TVC standards at sine wave frequencies between 30 Hz and 15 kHz. The results of these step and thermal measurements are given in figure 19 for two different units (DSS1 and DSS2) using both internal and external clocks to synthesize 128-step sine wave approximations (A, B, and C). As a further demonstration, the results of measurements on a nonsinusoidal waveform (sine wave approximation with 30% third harmonic) are shown in D. The plots show the average difference between three sets of measurements consisting of two step calibrations (represented by the dashed line) and five thermal measurements (plotted points with one standard deviation error bars) at each frequency. Agreement between the two measurements is better than ± 5 ppm from 30 Hz to about 2 kHz. A small capacitor on the output amplifier (see fig. 17) is initially adjusted to obtain flatness of the rms value to within ± 10 ppm from 2 to 15 kHz. Recent designs have now extended this performance up to 50 kHz.

4. Measuring Waveform Parameters Using Digital Sampling

To make accurate measurements of signal waveforms that can be stored and processed further with a computer requires the use of precision ADCs having small linearity errors (both statically and dynamically), as described above. In order to

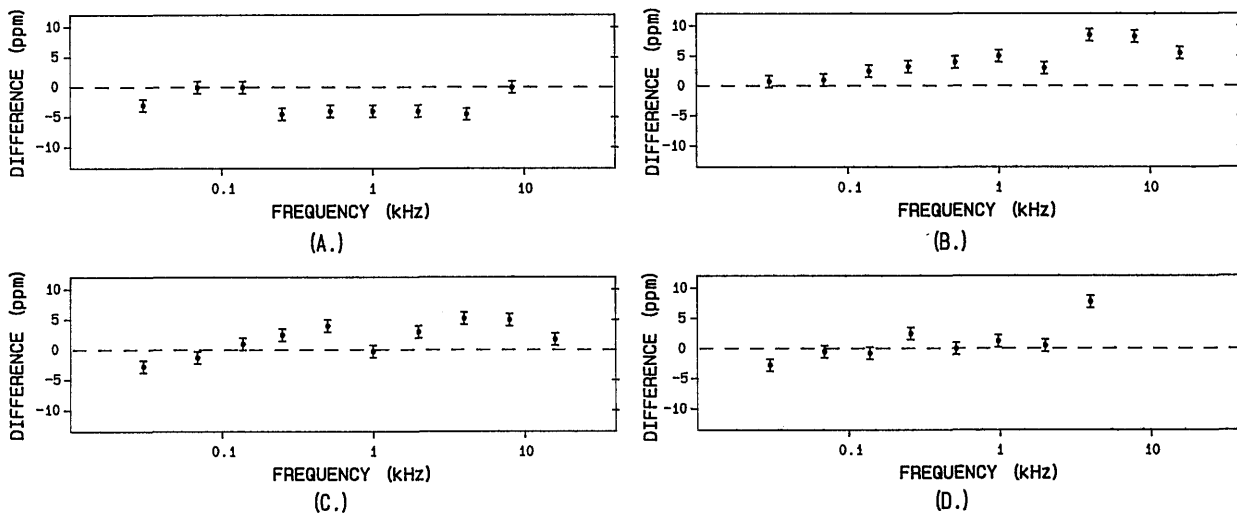


Figure 19. The difference in ppm between the rms value computed by the step calibration (dashed line) and the rms value measured using thermal techniques: (a) DSS1 using the internal clock to generate a sine wave. (b) DSS2 using the internal clock to generate a sine wave. (c) DSS2 using an external clock to generate a sine wave. (d) DSS2 using an external clock to generate a (nonsinusoidal) waveform.

convert fast signals that change during the conversion time of the ADC, a sample-and-hold (S/H) or track-and-hold (T/H) circuit is inserted between the signal source and the ADC to capture samples of the waveform and hold the ADC input signal at a steady level while the ADC completes a conversion cycle. Often there are also signal conditioning amplifiers and filters, as well as multiplexing switches, employed in a complete data acquisition channel. Figure 20 shows a block diagram of a typical multichannel measurement system. Analogous to the reconstruction of analog waveforms using a time sequence of digital input codes to a DAC (described earlier), the process of digital waveform sampling generates a time sequence of digital output codes from an ADC, corresponding to the amplitude levels of the analog input waveform at the sampling instants.

In order to understand the limitations imposed by using digital sampling methods to measure the parameters of signal waveforms, a short discussion on the basics of sampling theory is provided in the Appendix.

4.2 Low-Frequency ac Sampling Voltmeter

The speed and versatility that is possible with digital waveform sampling of low-frequency ac

waveforms was demonstrated with the development of the NIST Low-Frequency ac Sampling Voltmeter [35]. An rms low-frequency (0.1 to 50 Hz) voltmeter/calibrator had been developed at NIST about the same time, and employed a multi-junction thermal converter device for making accurate rms-to-dc conversions. This instrument is capable of making ac transfer measurements (comparing ac input voltages against its internal calibrator), good to $\pm 0.02\%$ accuracy [36]. The thermal converter-based instrument serves as the standard in a NIST calibration service for ac voltmeters and calibrators from 0.1 to 10 Hz [37]. With the sampling-based voltmeter, rms measurements good to $\pm 0.1\%$ accuracy at 10 mV to 10 V levels from 0.1 Hz to 120 Hz are available, as are measurements of the input signal frequency, total harmonic distortion (THD), and the rms value of the ac component (only). Also, the sampling instrument uses “window crossing” and error function algorithms in the software of its internal microcomputer to permit measurements within two signal periods at frequencies below 10 Hz [38]. Thus, measurements of a 0.1 Hz signal can be made in 20 s (2 s for a 1 Hz signal), which is 2–10 times faster than the thermal converter-based instrument.

Figure 21 shows a simplified block diagram of the low-frequency sampling voltmeter. Function-

ally similar to the measurement system shown in figure 20, this instrument employs a low-noise, differential-input preamplifier with programmable gain-setting resistors, so that four decades of gain can be programmed from the microcomputer via the memory, timing, and control section. A data acquisition module consisting of an S/H amplifier, an instrumentation amplifier, and a 12-bit ADC (11

bits plus sign bit) provides the sampling, signal conditioning, and digitizing of the preamplifier output signals. With the three programmable input voltage ranges of the data acquisition module, a total of 12 gain settings are available using combinations of preamplifier gain and data acquisition range settings. The memory, timing, and control block contains the instruction program (2048 16-bit words)

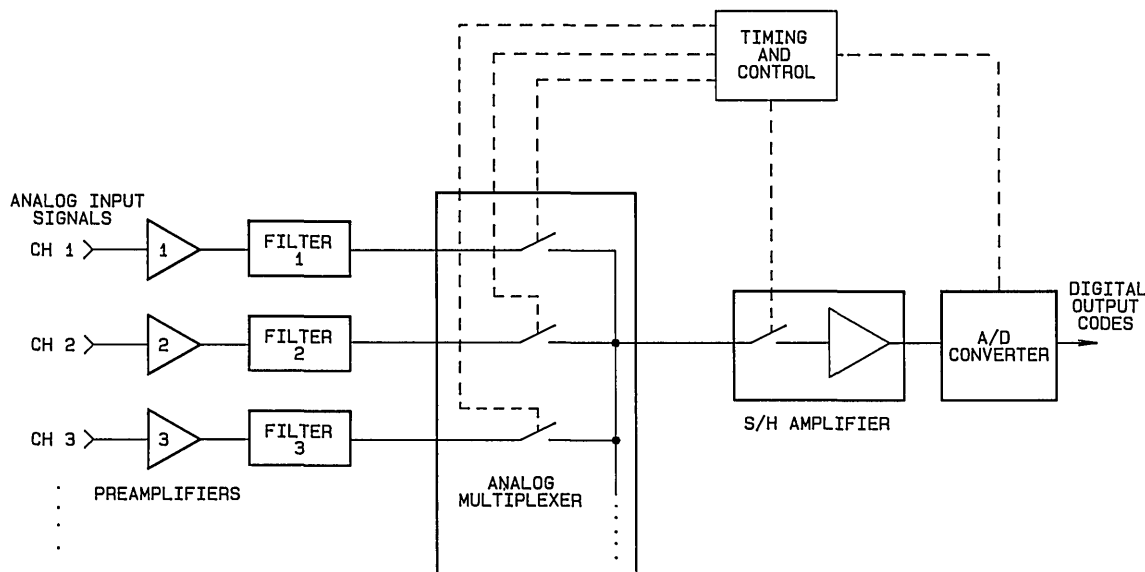


Figure 20. Block diagram of a typical multichannel sampling measurement system.

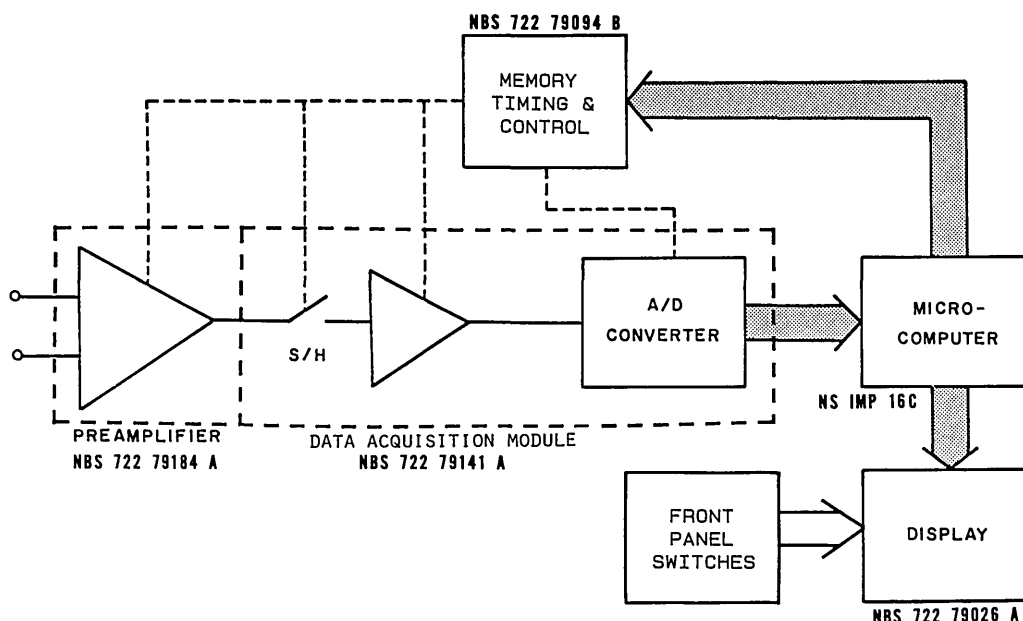


Figure 21. Simplified block diagram of the NIST low-frequency sampling voltmeter.

stored in read-only-memories (ROM), as well as a small amount of random-access-memory (RAM) for temporary storage of input values and program variables. The 16-bit microcomputer used for this application was chosen for its powerful microprogrammable instruction set that allowed straightforward implementation of the multiplications used in computing the fast Fourier transform needed for calculating THD.

Because the algorithm for calculating rms value requires an accurate value for the period of the sinusoidal input signal, the initial sampling sequence is used to obtain an approximate value for the period (see fig. 22). During the first cycle (T_1), sampling is begun at any arbitrary point on the waveform, after possible adjustment of the preamplifier gain. Since the frequency may be as low as 0.1 Hz or as high as 120 Hz, a decision is made, based on the slope of the signal, whether a fast (8 kHz) or slow (500 Hz) sampling rate will be used to find the approximate period. With the sampling rate set at 500 Hz, an initial reading is taken; a higher and lower threshold value is then calculated with respect to this initial reading. Thus, an “initial window” of sample values is established, as shown in figure 23. Depending on the number of samples it takes to cross the upper or lower threshold, the sampling rate continues to be 500 Hz, or else the sampling rate clock is reset to 8 kHz, and the measurement sequence is restarted. After the waveform is sampled further, and a “2nd window crossing” is found, approximately one signal period has elapsed. The sampling rate clock is then set for 128 times the approximate frequency (f_0), the reciprocal of the approximate period, and sampling continues for slightly more than one period (cycle T_2).

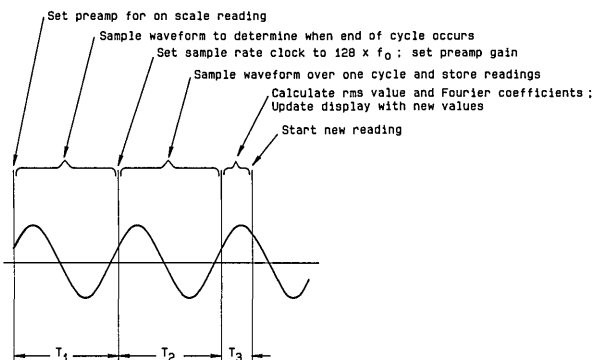


Figure 22. The time sequence of the measurement cycle in the voltmeter, relative to a typical sinusoidal input.

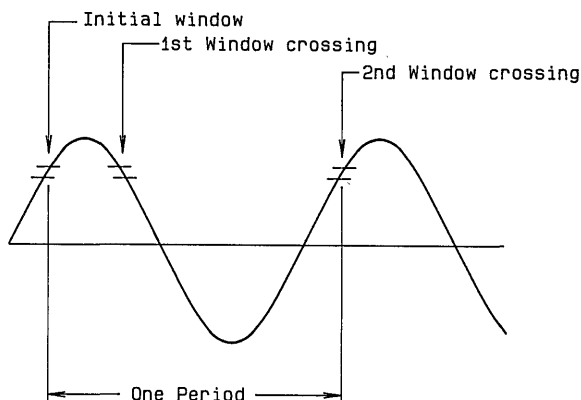


Figure 23. Approximate period detection using window crossing.

To determine the signal period more exactly, an autocorrelation technique is performed using sample points taken during T_2 . To take possible effects of noise and frequency modulation (FM) into account, 147 samples are taken during T_2 . The correlation is then accomplished by evaluating an error function, E_f , that consists of summing the difference in the values of samples taken at approximately corresponding times in the cycle:

$$E_f = \sum_{i=1}^n |E_i - E_{i+N}| \quad (9)$$

where N is the variable number of samples in period (125, 126, 127, 128, 129, 130, and 131),

E_i are sample values at the beginning of the cycle,

E_{i+N} are corresponding values at the beginning of the next cycle, and

n is the number of difference values summed; 16 points chosen, based on empirical testing.

If the period was exactly an integral number of samples and the input signal was free of noise or FM, this sum would go to zero for $N=128$. Since this is rarely the case, N is varied from 125 to 131 until a minimum value for the error function is found. However, because this error function can exhibit an undesired second minimum that can be difficult to distinguish from the true minimum, the two smallest sums of the seven error functions of (9) are used to linearly interpolate to the minimum point between them [38].

The rms value of the input is then calculated in a straightforward manner from the appropriate set of stored samples. The sample values are squared and summed using 32-bit precision arithmetic. For the “ac only” feature of this instrument, the mean squared value is calculated as usual, and then the square of the average of the input samples (the dc component) is subtracted before taking the square root for the net ac rms value.

To obtain the dc, fundamental, and first 30 harmonic components of the input signal, the data samples from the second cycle (T_2) are used to calculate the coefficients of the discrete Fourier transform (DFT) of the signal. This calculation is accomplished by using a 64-point radix 2 fast Fourier transform (FFT) algorithm. The magnitudes of these coefficients are then used to calculate the THD as a figure of merit of the signal as a pure sine wave. However, this instrument is designed mainly for measuring low-distortion sinusoidal signals, with the highest computed harmonic being

$$f_{\max} = 30f_0, \quad (10)$$

so that

$$f_s = 128f_0 > 2f_{\max}, \quad (11)$$

thus more than satisfying eq (15A) (see the Appendix) for the Nyquist frequency criterion to prevent aliasing.

4.3 Wideband Sampling Wattmeter

With the widespread use of solid-state thyristor switching devices for controlling the delivery of electrical power, the need has grown for making accurate measurements of highly distorted power signals. To meet this need a wideband sampling wattmeter was developed. This wattmeter uses asynchronous sampling of its input waveforms to realize a measurement uncertainty of less than $\pm 0.1\%$ of the full scale range for fundamental frequencies from 1 Hz to 10 kHz (and harmonics up to 100 kHz) [14]. A prototype instrument, constructed in the mid 1980s, is programmable from the front panel and has the necessary hardware and software to optimize the sampling frequency and to make corrections for truncation errors [39]. In the early 1970s the feasibility was demonstrated for making precision ac power measurements ($\pm 0.02\%$ accuracy up to 2 kHz) using a sampling technique, and

computing the power with a suitable algorithm [40].

In contrast with the synchronous (phase-locked) sampling method used in the earlier sampling wattmeter (and the correlation approach used in the low-frequency ac sampling voltmeter described above), asynchronous sampling of the two input (voltage and current) waveforms is used in the wideband sampling wattmeter. That is, the average power for the periodic input signals is calculated by using the approximation given by

$$W = 1/n \sum_{k=0}^{n-1} V(t_k) I(t_k), \quad (12)$$

where $V(t_k)$ and $I(t_k)$ are the uniformly spaced samples,

n is the total number of samples in the record, and

W is the indicated average power.

The sampling times, t_k , are not synchronized with the period (i.e., frequency) of the input signals. Consequently, the interval over which the summation is taken does not coincide with an integral number of cycles of the input signals. Figure 24 shows the relationship between the sample times and the associated voltage and current signals. To calculate the power in such signals, the sample values from a finite interval (the summation interval) of the waveforms are used, as indicated by the circled sample values. With the sample interval, γ , expressed in radians, the voltage and current samples are given by

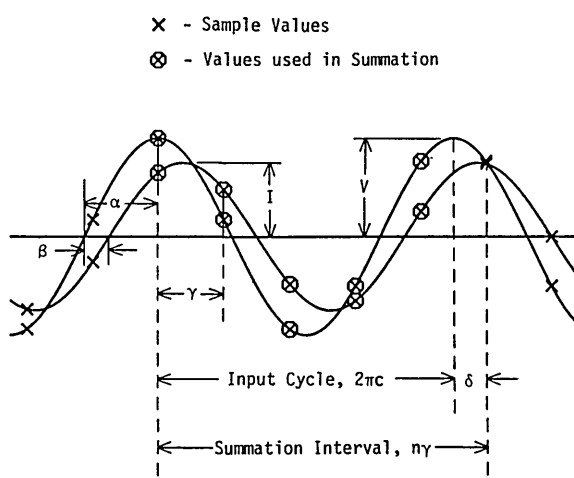


Figure 24. Asynchronous sampling of voltage and current sine waves showing the relationship of various sampling parameters. In this example, $c = 1$, $n = 5$, $\alpha = 90^\circ$, $\beta = -30^\circ$, $\tau = 80^\circ$, and $\delta = -40^\circ$.

$$V(t_k) = V_k = V \sin(k\gamma + \alpha) \quad (13)$$

and

$$I(t_k) = I_k = I \sin(k\gamma + \alpha + \beta), \quad k=0 \text{ to } n-1 \quad (14)$$

where k is the sample number,

α is the starting voltage phase angle,

β is the relative phase angle between the voltage and current, and

V and I are the peak values.

For a signal of period T seconds and a sampling rate of r samples per second,

$$\gamma = 2\pi/rT. \quad (15)$$

Using eq (13), the approximate average power is then,

$$W = \frac{VI}{2} [\cos\beta - 1/n \sum_{k=0}^{n-1} \cos(2k\gamma + 2\alpha + \beta)]. \quad (16)$$

The true power, P , is just the first term in this expression, so that the second term is the error due to the nonintegral number of samples in the period (i.e., truncation error, E). The difference between the summation interval, given by $n\gamma$, and the nearest integral number of cycles, c , of the input signal is defined as the truncation angle, δ ; that is,

$$\delta \equiv 2\pi c - n\gamma. \quad (17)$$

The truncation error then can be shown to be expressed as [14]

$$E = \frac{VI}{2n} \frac{\sin \delta}{\sin \tau} \cos(2\alpha + \beta - \delta - \gamma). \quad (18)$$

This expression shows that if the truncation angle, δ , is zero, then E is zero, which is the reason why many sampling wattmeters use synchronous sampling. Although the wideband sampling wattmeter described here has asynchronous sampling, it uses trigger and cycle counting hardware, as shown in the block diagram of figure 25, to control the summation interval. By starting and stopping the summation interval with a trigger pulse synchronized with the signal being measured, the truncation angle, δ , is kept to less than the sample interval, γ . For $\gamma \leq 90^\circ$, eq (18) shows that the maximum error occurs when $\sin \delta = \sin \gamma$ and the cosine term is ± 1 . Then, the maximum error is given by

$$E_{\max} = \pm \frac{VI}{2n}, \quad (19)$$

showing that the maximum truncation error can be made small by taking a large number of samples, n , independent of the input signal frequency. With the NIST wideband sampling wattmeter, power measurements are typically made with an n of greater than 150,000 samples so that the truncation error is negligible. With a sampling rate of 300 kHz, this number of samples requires a summation interval of about one-half second.

With the truncation error due to asynchronous sampling minimized, the remaining measurement errors are a combination of the errors in the scaling amplifiers, the track and hold (T/H) amplifiers, and the 12-bit A/D converters shown in figure 25. The

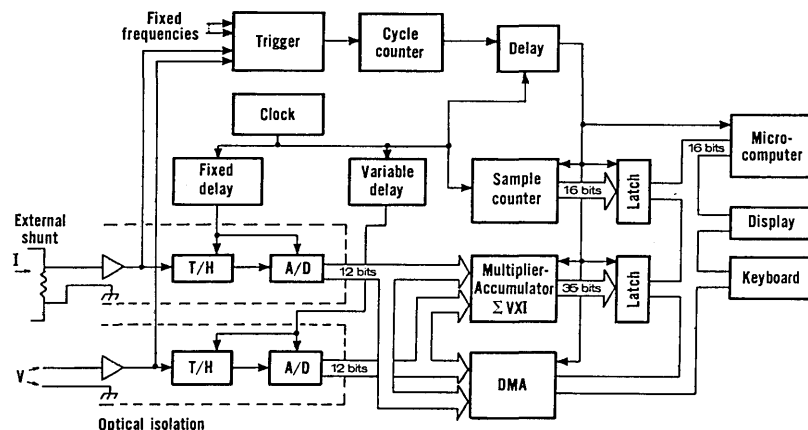


Figure 25. Block diagram of the NIST wideband sampling wattmeter.

T/H and ADC modules were tested with the NIST static data converter test set described previously and found to have rms linearity errors $<\pm 0.5$ LSB, or $<\pm 0.012\%$ of full scale. Differential time delays between the two input amplifiers (as much as 46 ns) are compensated to within 1 ns by the programmable fixed and variable delay units that control the time when the convert command signals are applied to the T/H and ADC modules. The need to correct for this error can be illustrated by considering that if the wattmeter is measuring a 10 kHz power signal at half-power-factor, i.e., a phase angle of 60°, then a differential time delay of only 18 ns could cause an error of $\pm 0.2\%$ of the true power value.

Figure 26 shows the percent rms error of the NIST wideband sampling wattmeter as a function of frequency (on the 1 V range), determined by comparing its measurements results with those from an ac voltmeter whose frequency response up to 100 kHz had been established using NIST-calibrated thermal voltage converter standards. The error in both the rms value of each channel and the product (simulated power) function is well within the desired goal ($\pm 0.1\%$), even out through 50 kHz. The results for the 0.1-, 0.2-, and 0.5-V ranges are better than these, and those for the 10- and 500-V ranges using a specially-designed 100-to-1 attenuator are poorer by a factor of about two. Comparison tests made with a standard thermal wattmeter [41] showed agreement to within $\pm 0.03\%$ of full scale over the frequency range from 40 Hz to 2 kHz [14]. Since distorted waveforms can be decomposed by Fourier analysis into harmonically-related sine waves, and assuming that linearity (and, hence, superposition) holds, the performance of the wideband sampling wattmeter for measuring distorted waveforms can be predicted by using the errors shown in figure 26.

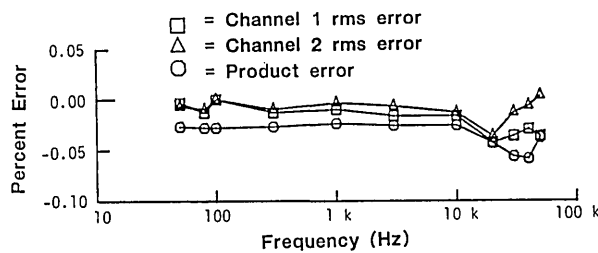


Figure 26. RMS error (in percent) versus frequency for each channel and for the product (simulating a unity power factor input signal).

4.4 Sampling Voltage Tracker

A third method of accurately sampling and digitizing repetitive waveforms has been employed at NIST in the development of a sampling voltage tracker (SVT) system. This system is capable of making state-of-the-art equivalent-time measurements for signals with frequency components up to 200 MHz [15]. The rf rms voltage measurement accuracy of this system has been shown to be comparable to that of thermal voltage converter standards [42].

The equivalent-time sampling process implemented by the SVT is somewhat different from that illustrated in figure 38 (see the Appendix). The SVT is constrained by its design to sample each point on the waveform numerous times (over as many waveform periods), and the data processed to estimate the value at that point on the waveform. Then, the time base is incremented one sampling interval to acquire and process samples for the next point, and so on, until the entire sequence of estimated sample values is obtained. It should be noted that no large amount of memory is required by this method in order to perform the averaging process.

As with any sampling system, timing jitter affects the measurement accuracy of the SVT. However, unlike many sampling systems, the SVT is insensitive to timing jitter over all locally monotonic regions of the input waveform. This property results from the statistical estimator that is used by the SVT to deduce the "true" sample values from many time-jittered observations—the so-called Markov estimator. It has been investigated [43] and found to be equivalent to the median estimator, which is known to be unbiased for monotonic functions. On the other hand, the sample mean, which is typically used in most sampling systems, is generally biased for any function that has second or higher order derivatives.

Figure 27 illustrates the basic components of an integrating feedback amplifier SVT circuit, of the type used in the NIST SVT system. The analog comparator is triggered by strobe pulses to make successive comparisons of the input waveform amplitude with that of the feedback signal from the integrator, at a given instant on the input waveform. The feedback signal, obtained by integrating the emitter-coupled logic (ECL) level waveform from the output of the comparator, is an estimate of the amplitude at a given point on the input waveform. When the average (dc) level of the feedback signal amplitude matches that of the input, the

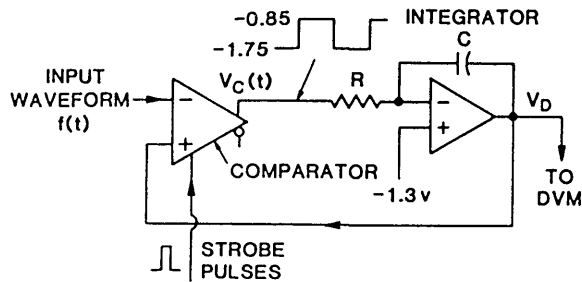


Figure 27. Basic circuit of the NIST sampling voltage tracker.

comparator output is a square wave. Consequently, the output of the integrator is a triangle wave whose peak-to-peak amplitude is made relatively small by adjusting the RC time constant of the integrator. As shown in figure 28, a precision DVM is used to measure the average value of the integrator output waveform. The process is repeated at successive points, determined by a precision time-delay generator, until the entire input waveform has been sampled and the computer/controller has reconstructed the waveform in equivalent-time.

In order to use the NIST SVT as an accurate waveform measurement tool, its performance as a precision sampling system has been characterized in terms of static and dynamic linearity errors, time base errors, and step and frequency response errors [15].

4.4.1 Linearity Errors Figure 29 shows a typical plot of the static linearity error obtained by supplying known, programmable dc voltages to the SVT input terminals, recording the readings, and performing a linear regression of the form

$$Y = ax + b \quad (20)$$

on the results. The residuals of the fit are the static linearity errors. Dynamic linearity errors (or har-

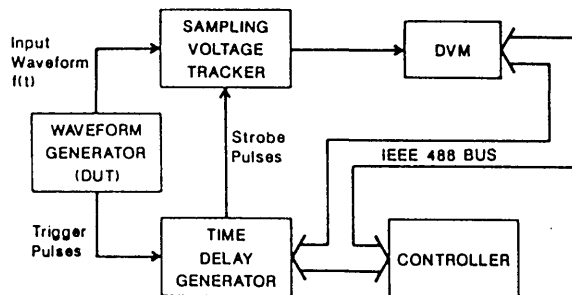


Figure 28. Block diagrams of a complete SVT system.

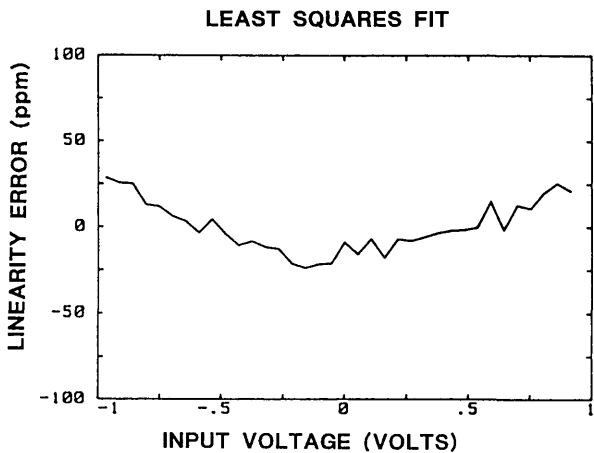


Figure 29. Typical plot of the SVT linearity errors.

monic distortion) are measured by inputting high purity sine waves, and fitting an ideal sine wave to the recorded samples. The residuals of the fit in this case include not only the amplitude linearity errors, but also errors due to nonlinearities in the time base (which are minimized by using an averaging technique explained in the next paragraph). Figure 30 shows typical plots of the dynamic linearity errors for 1 V and 50 mV sine wave input signal amplitudes, at a frequency of 50 MHz; similar data were obtained for other frequencies. The rms linearity error versus frequency, expressed as a percentage of the rms value of the fitted sine wave, can be

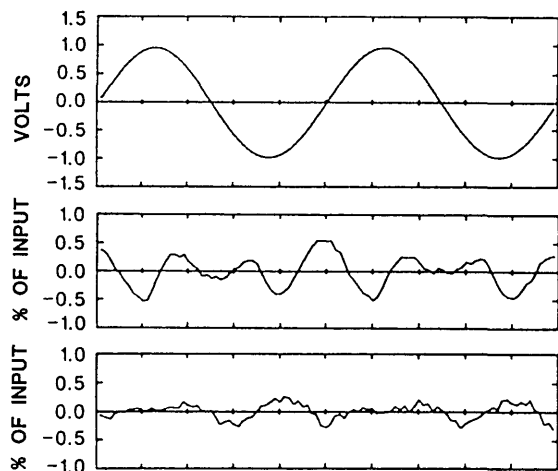


Figure 30. Typical plot of a digitized 50 MHz sine wave (top) and dynamic linearity errors derived from curve fitting for 1-V peak input (middle), and 50-mV peak input (bottom). The horizontal scale is 4 ns per division.

found in table 3 (together with other characteristics that summarize the performance of the NIST SVT system). Note that the linearity errors (given as a percentage of the applied signal) generally decrease at lower signal levels.

4.4.2 Time-Base Errors Nonlinearities in the time base cause displacements of the sampling instants, which in turn cause apparent amplitude errors proportional to the derivative of the signal being measured. By incrementally shifting the phase of the input sine-wave signal relative to the trigger pulse, a record is obtained in which the time-base errors are shifted with respect to the phase of the sine wave. This process is repeated m times. The records are then realigned in phase and averaged point-by-point, which requires two periods of the signal. The time-base errors can be estimated by subtracting the averaged data, in which the time-base errors have been filtered out, from the nonaveraged records, and dividing by the derivative of the signal at each sample point (regions near the cusps of the sine wave where the derivative approaches zero, of course, must be avoided). The results of such measurements are given in figure 31 for two different time bases. In both cases the period of each record was 100 ns (two cycles of the 20-MHz test sine wave), the equivalent-time sampling interval was 1 ns, and the $m=9$ shifted records provide up to 10 estimates

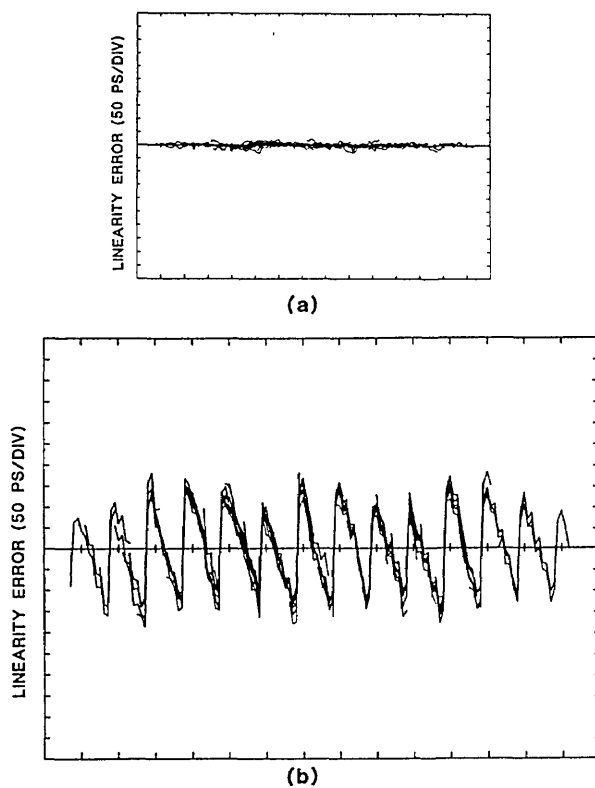


Figure 31. Time-base linearity errors for (a) and (b): two different time bases. The errors shown in (a) result from ten different data sets overlaid for each plot. In (a) the linearity errors are buried in noise. The horizontal scale is 10 ns per division.

Table 3. Performance summary of the SVT

	dc	1	10	20	50	100	200	300	MHz
Linearity Error									
1 V (peak)	0.002	0.03	0.06	0.08	0.39	1.4	4.2	9	%
50 mV (peak)			0.06	0.12	0.20	0.2	0.7	1.3	%
Gain Error	0		0.004	0.02	0.30	0.7	-0.3	-4.5	%
Bandwidth (3 dB)				600					MHz
Step Response									
• Transition Duration (10–90 %)				600					ps
• Settling Time (–1 to +1 V step)					4				ns
0.1 %									ns
0.02 %					20				ns
• Long Term Settling Error (0–1 μ s)									
–1 to +1 V step					± 0.4				mV
Time Base Linearity Error									
100 ns epoch					<2				ps rms
Time Base Phase Noise, >1 Hz						<10			ps peak

per sample point. The time base used for figure 31(a) has small random errors of only 7 ps over the ~140 ns time epoch; figure 31(b) is an example of a time base where the linearity errors are much more evident. The periodicity of these errors is due to the interaction of the separate coarse and fine adjustment circuitry used in this time base.

Another significant source of time-base errors is the result of timing jitter (phase noise) between the strobe pulses and the input signal. Phase-noise components in the measured signal, the trigger signal, and the time-delay generator all contribute to the overall phase-noise error. The low-frequency components of this noise cause relatively slow variations in the integrator feedback signal; these can be observed by monitoring the feedback signal on an oscilloscope. With the delay set to sample the input waveform at a point where the rate of change is high, amplitude fluctuations in the feedback signal resulting from phase noise are easily observed with the scope set for high sensitivity and ac coupling. The observed peak amplitude is the product of the peak phase displacement (expressed in units of time) and the time rate of change of the input signal at the nominal sampling instant. For low phase-noise signals, the equivalent timing uncertainty measured in this way on the NIST SVT was less than 10 ps (peak).

4.4.3 Step and Frequency Response Errors
The transition duration (rise time) and settling-time performance of the NIST SVT is shown in figures 32, 33, and 34. The measurement of fast step-response performance at high accuracy is difficult be-

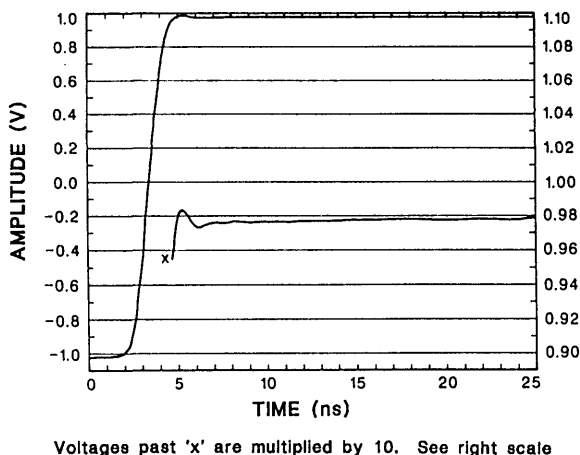


Figure 32. Response of the NIST SVT to a 2-V step from the NIST programmable step generator, showing settling to within $\pm 0.1\%$ of full scale range (FSR) in 4 ns. Note that the lower curve is a magnified version of the final settling, with the scale given on the right hand side of the plot.

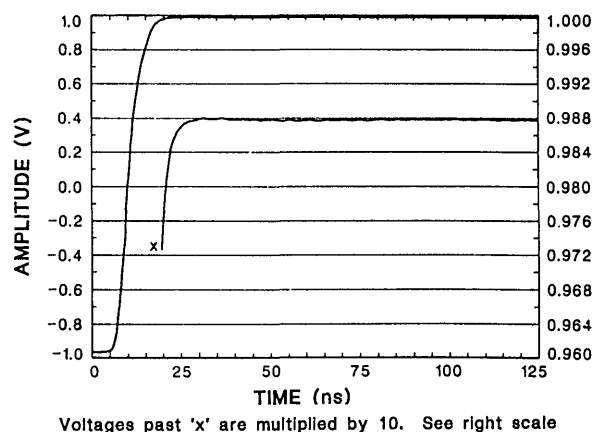


Figure 33. Response of the NIST SVT to a 2-V step from a slower, more accurate version of the NIST programmable step generator, showing settling to within $\pm 0.02\%$ of FSR in 20 ns.

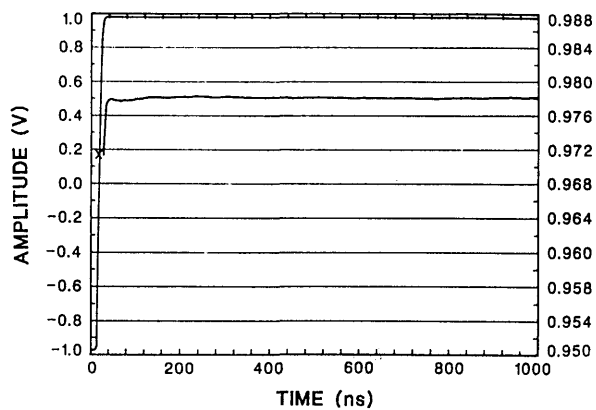


Figure 34. Longer term response of the NIST SVT to a step from the slower NIST programmable generator, showing aberrations less than 0.4 mV (0.02% of FSR) out to 1 μ s.

cause of the lack of reference waveform generators having the requisite characteristics. Some of the best reference waveform sources available for this work have been those developed by NIST [44,45,46]. The NIST programmable voltage step generator was used to obtain the short and long term settling response of the SVT shown in figures 32, 33, and 34. The step response data given in table 3 are derived from these plots.

Accurate measurement of the frequency response of the NIST SVT is also difficult, since the direct measurement requires using sine-wave sources having high spectral purity and known amplitude uncertainty in the 1 to 1000 MHz range. Alternatively, indirect measurements based on time-domain data require fast risetime, fast settling

step generators, preferably with transition durations of 300 ps or less [47]. The step generator used for these measurements is an improved, commercial version of the NIST Reference Flat Pulse Generator [44] with the manufacturer-specified rise time of ~ 400 ps. The step is sampled with an equivalent-time sampling rate sufficient to give negligible aliasing errors over the frequency range of interest. The discrete impulse response is then computed from the step-response data, and the frequency-magnitude spectrum is obtained by a Fourier transform of the impulse response. For one type of comparator that was used in the NIST SVT, figure 35 (a–c) shows: (a) the last 4% of the sampled input step, (b) the frequency response computed from this data, and (c) the gain error relative to the first spectral line at 1.2 MHz. The lower trace of figure 35 (b) is the frequency response of the composite step generator-SVT system. The upper trace is an estimate of the actual frequency response of the NIST SVT itself, obtained by deconvolving the equivalent response of the (nonideal) input step, estimated from rise time measurements of the input step and an assumed single pole model.

5. Conclusion

By the mid 1970s it was apparent that digital techniques would have significant advantages over analog methods for reducing the problems of offset, drift, and noise in making precise electrical measurements. Also, the proliferation of digital computers into laboratories and offices in the 1980s spurred the need to convert analog signals into digital form and vice versa. Consequently, there has been a corresponding requirement for better means to support the performance specifications of digital devices and associated instrumentation.

The NBS/NIST program in the research and development of new test methods and physical standards for this purpose has provided the improved capabilities described in this article. These digital-based standards and associated test methods also have been described in numerous journal and conference papers and talks. The work now provides the basis for new, improved NIST calibration services and special tests.

Future efforts will likely concentrate on similar approaches for supporting the devices and instru-

ments used in automatic test systems, such as high-speed digitizers and arbitrary waveform generators. Characterizing the performance of electronic stimulus and measurement devices continues to be a challenge as the testing technology changes.

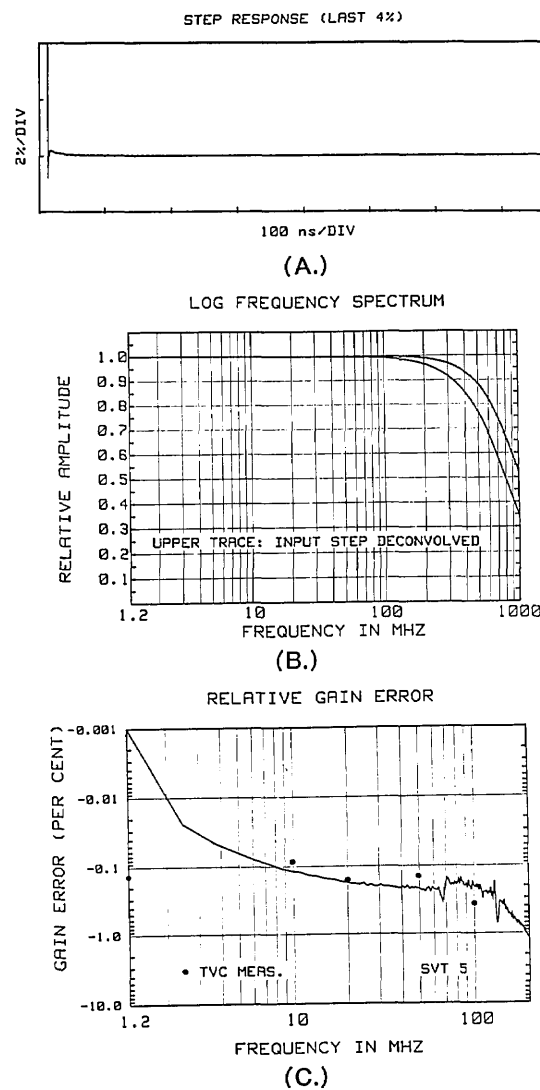


Figure 35. Gain corrections derived from measurements of the NIST SVT response to the output from a fast (~ 400 ps transition duration) step generator: (a) the last 4% of the step response, (b) the corresponding frequency response computed from the step response data, and (c) the gain error relative to the first spectral line at 1.2 MHz.

6. Appendix

6.1 Relationship Between $y_z(t)$ and Its Fourier Series Line Spectrum

In the notation of figure 8(a), $f_s = N/T$ is the sampling frequency, and the sampling times are $t_n = nT/N = n/f_s$, $n = 0, 1, \dots, N-1$. Then, over the time interval $0 \leq t \leq T$, the stepped waveform $y_z(t)$ can be written as

$$y_{zN}(t) = \sum_{n=0}^{N-1} y(t_n)[u(t-t_n) - u(t-t_{n+1})], \quad (1A)$$

where $u(t)$ is the usual unit step function, conveniently defined as a discontinuous step that occurs when its argument is zero, i.e.,

$$\begin{aligned} u(t) &= 0, \quad t < 0 \\ &= 1, \quad t \geq 0. \end{aligned}$$

Hence, a rectangular pulse between t_n and t_{n+1} is readily described by the time difference of two such step functions, and the stepped waveform is created by indexing n over the N sample points on the waveform. Extending $y_{zN}(t)$ periodically for all t , one obtains the periodic function $y_z(t)$, which can be written as a Fourier series of exponential terms,

$$y_z(t) = \sum_{k=-\infty}^{+\infty} C_k \cdot e^{j2\pi kt/T}, \quad (2A)$$

or, as indicated in the line spectrum of figure 8(b), as a trigonometric Fourier series,

$$y_z(t) = A_0/2 + \sum_{k=1}^{+\infty} A_k \cdot \cos(2\pi f_k t + \Theta_k),$$

where

$$\Theta_k = -\tan^{-1}[Im(C_k)/Re(C_k)], \quad f_k = k/T,$$

and $A_k(f)$ vs. frequency is the plot of the line spectrum.

Given the C_k coefficients of eq (2A), A_k can be found from

$$A_k = 2(C_k \cdot C_{-k})^{1/2}. \quad (3A)$$

It is known that the Fourier transform of a continuous periodic function such as $y_z(t)$,

$$F(y_z(t)) = \int_{-\infty}^{+\infty} y_z(t) \cdot e^{-j2\pi ft} dt, \quad (4A)$$

is a sum of equally spaced impulses in the frequency domain, i.e.,

$$F(y_z(t)) = F(f) = 2\pi \sum_{k=-\infty}^{+\infty} C_k \cdot \delta(f - k/T),$$

where the C_k (coefficients of the exponential Fourier series) are related to the truncated function $y_{zN}(t)$ through the formula

$$C_k = 1/T \int_0^T y_{zN}(t) \cdot e^{-j2\pi kt/T} dt, \quad (5A)$$

and $\delta(f)$ is the usual Dirac unit impulse function, conveniently defined as an infinite amplitude spike (with an area of one) that occurs when its argument is zero, i.e.,

$$\begin{aligned} \delta(f) &= \infty, \quad f = 0 \\ &= 0 \quad \text{elsewhere,} \end{aligned}$$

and

$$\int_{-\infty}^{+\infty} W \delta(f) df = W,$$

where W is the area under (or “weight” of) the impulse.

[See reference [19] (Papoulis, Ch. 3); in particular, the integral in eq (4A) has to be interpreted in the sense of distributions (Papoulis, Appendix I).]

Since

$$\begin{aligned} 1/T \int_0^T [u(t-t_n) - u(t-t_{n+1})] e^{-j2\pi kt/T} dt \\ = e^{-j2\pi kn/N} \cdot \frac{1 - e^{-j2\pi k/N}}{j2\pi k/T}, \end{aligned}$$

then eq (5A) can be evaluated as

$$C_k = b/T \sum_{n=0}^{N-1} \sin(2\pi n/N) \cdot e^{-j2\pi kn/N} \cdot \frac{1 - e^{-j2\pi k/N}}{j2\pi k/T}. \quad (6A)$$

The summation over N terms of the $\sin(2\pi n/N) \cdot e^{-j2\pi kn/N}$ combination can be computed by means of the formula for finite geometric sums since

$$\begin{aligned} \sin(2\pi n/N) \cdot e^{-j2\pi kn/N} \\ = \frac{\{e^{j2\pi(1-k)/N}\}^n - \{e^{-j2\pi(1+k)/N}\}^n}{2j}. \end{aligned} \quad (7A)$$

If the factor $1-k$ or $1+k$ in the exponents is not a multiple of N , the corresponding summation is zero; hence, $C_k=0$ if neither $1-k$ nor $1+k$ is a multiple of N . If $1-k$ is a multiple of N and, hence, $1+k$ is not, then the exponentials involving $1-k$ are equal to 1 (and sum up to N), and those involving $1+k$ sum up to zero. Thus, in this case

$$C_k = b(N/2j) \cdot \frac{1-e^{-j2\pi k/N}}{j2\pi k}. \quad (8A)$$

Similarly, if $1+k$ is a multiple of N ,

$$C_k = -b(N/2j) \cdot \frac{1-e^{j2\pi k/N}}{j2\pi k}. \quad (9A)$$

Equations (8A) and (9A) are valid for both positive and negative k values. To compute A_k from eq (3A), either C_k or C_{-k} must be expressed by eq (8A) and the other coefficient by eq (9A). Thus,

$$\begin{aligned} A_k &= 2 \left\{ b^2 N^2 / (16\pi^2 k^2) \cdot (1 - e^{j2\pi k/N}) (1 - e^{-j2\pi k/N}) \right\}^{1/2}, \\ &= bN/2\pi k \cdot [2 - 2\cos(2\pi k/N)]^{1/2}, \\ &= bN/\pi k \cdot \sin(\pi k/N). \end{aligned} \quad (10A)$$

Since $f_s=N/T$ and $f_k=k/T$,

$$k/N = \frac{k/T}{N/T} = f_k/f_s. \quad (11A)$$

Therefore,

$$|A_k| = b \left| \frac{\sin(\pi f_k/f_s)}{\pi f_k/f_s} \right|, \quad (12A)$$

which is shown plotted in figure 8(b). QED.

6.2 Some Basics on Sampling Theory

Figure 36 (a) shows a periodic waveform of arbitrary shape in the time domain that can be described by a Fourier series (shown expressed as a series of exponential terms rather than the trigonometric series). Each term is one of a pair of complex conjugates whose coefficient, C_k , is the amplitude of the corresponding frequency in the line spectrum of figure 36 (b). If this were a single arbitrary pulse, its frequency domain representation would be found by taking the Fourier transform:

$$\begin{aligned} F[y_t(t)] &= \int_{-\infty}^{+\infty} y_t(t) e^{-j2\pi ft} dt \\ &= F(f), \end{aligned} \quad (13A)$$

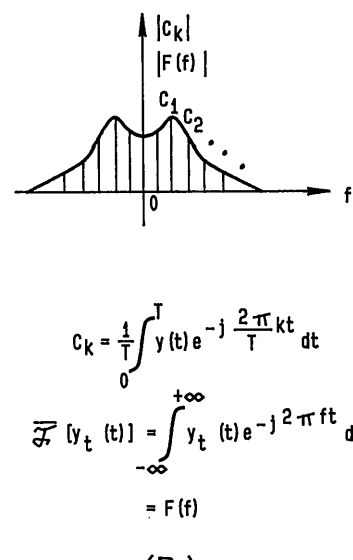
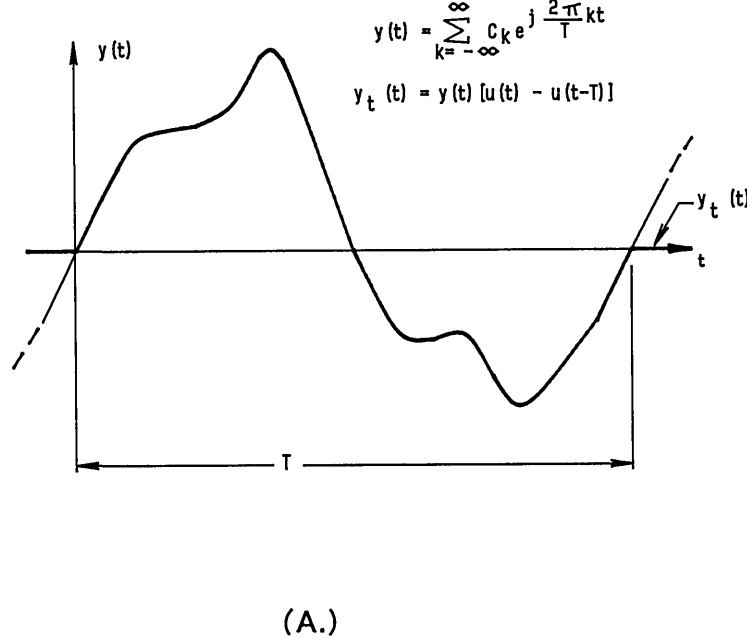


Figure 36. Time domain (a) and frequency domain (b) relationships for both a periodic and single occurrence arbitrary waveform.

where $y_i(t)$ is the transient arbitrary pulse, and $F[\cdot]$ is the frequency dependent Fourier transform.

In this case, the frequency representation is a continuous function of frequency rather than a discrete line spectrum.

When synchronously sampling this waveform, as shown in figure 37 (a), the sample set mathematically can be given a discrete time domain representation $y^*(t_n)$ that is a series of impulses at the times t_n , whose areas (or "weights") are equal to $y(t_n)$:

$$y^*(t_n) = \sum_{n=0}^{N-1} y(t_n) \delta(t - n\Delta t), \quad (14A)$$

where $\Delta t = T/N$ is the sampling time interval,
 T is the period or record length of
the sample set,
 N is the total (integral) number of
samples, and
 $\delta(t - n\Delta t)$ is a unit impulse at $t = n\Delta t$.

The sampled time function has a corresponding discrete Fourier transform (DFT), which can be shown to be the regular Fourier transform shifted along the frequency scale at infinite multiples of the sampling frequency [33], where $f_s = 1/\Delta t = N/T$ [see fig. 37 (b)]. Obviously, to prevent overlapping spectra (or aliasing) requires that

$$f_s \geq 2f_{\max}. \quad (15A)$$

For periodic waveforms, nonoverlapping requires that

$$N > 2k + 1. \quad (16A)$$

These are the usual forms for the well-known Nyquist frequency criterion that comes from communication theory [34].

In order to satisfy the Nyquist frequency criterion when the highest frequency in a periodic signal becomes comparable to the available maximum sampling frequency, waveform sampling is done in "equivalent-time" rather than in real time. Figure 38 is an illustration of equivalent-time sampling where N samples of the waveform are taken over equivalent time NT , rather than taking N samples in real time T . Each sample is obtained by incrementing one additional sampling interval (relative to the sync pulse) in each successive period of the signal. Multiple sets of N samples may be obtained, and averaging performed on corresponding sample points, in order to reduce the effects of noise and jitter. This method works even for signals with frequency components above the sampling frequency, as long as the effective sampling frequency (reciprocal of the equivalent-time sampling interval) satisfies the Nyquist criterion. Equivalent-time sampling requires periodic signals that are cycle-to-cycle repeatable (except for noise and jitter limitations). Also, as with real time sampling, the time base must be linear over the time interval T , and stable over the record length, as well as accurate.

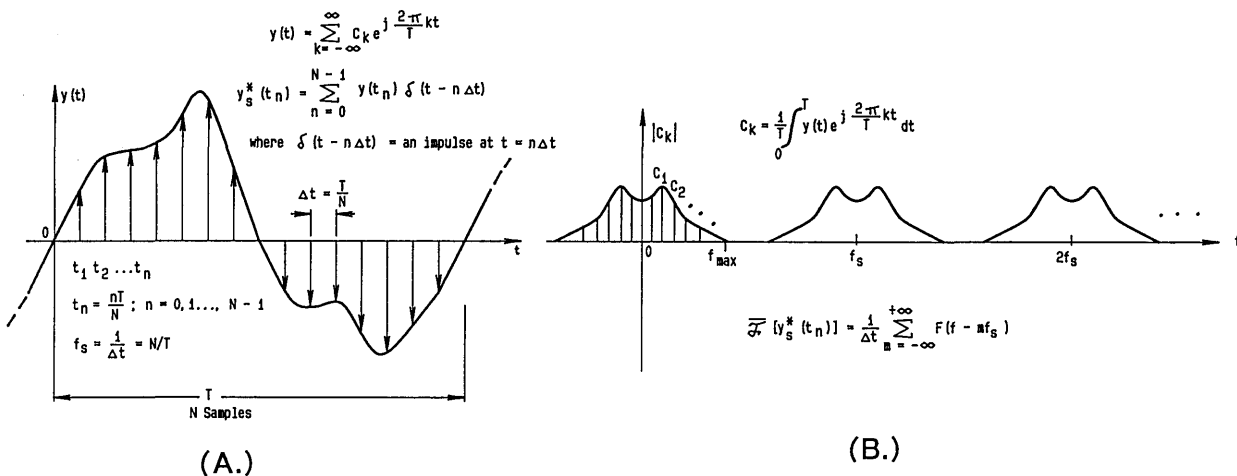


Figure 37. Time domain (a) and frequency domain (b) relationships for a sampled arbitrary waveform.

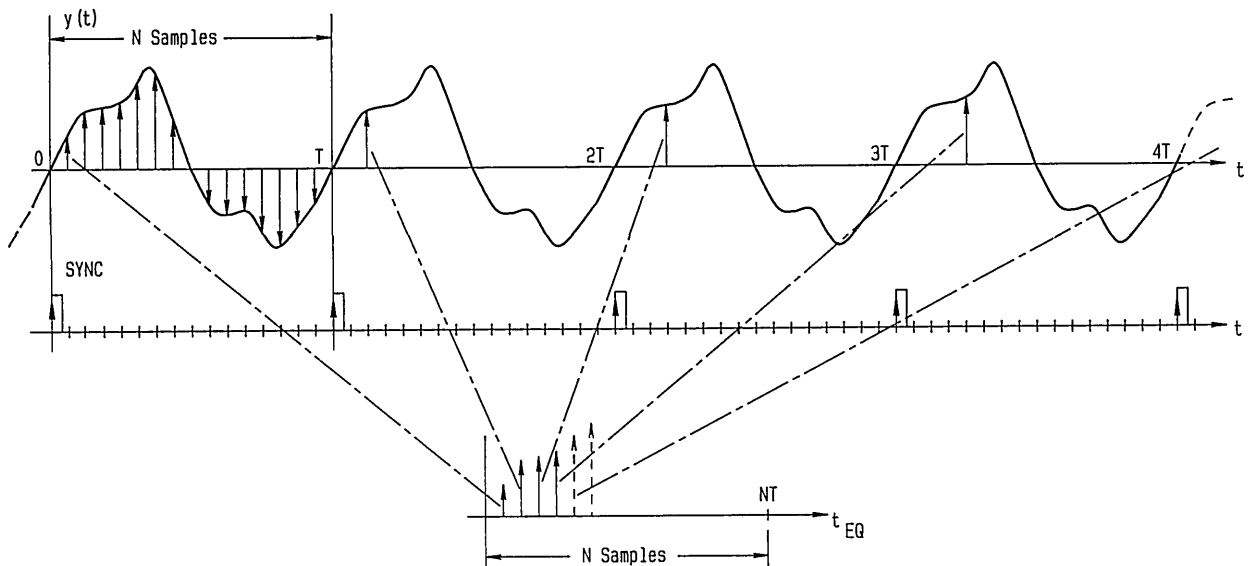


Figure 38. Illustration of a typical equivalent-time sampling process. Waveform samples are obtained at a rate N times slower than in real time sampling.

7. Acknowledgments

This article is a synopsis of the work done by the staff of the Electronic Instrumentation and Metrology Group whose accomplishments made it possible. The assistance of Dr. H. Engler of Georgetown University in preparing the analysis on the relationship between a stepped waveform and its Fourier series line spectrum (given in the Appendix) is gratefully acknowledged. I would also like to thank Dr. B. N. Taylor for his encouragement to prepare this overview paper, and for providing the initial impetus for the program of the EIM Group.

About the Author: Barry A. Bell is a Group Leader in the Electricity Division of the NIST Center for Electronics and Electrical Engineering.

8. References

- [1] Richman, P., Editor, Critical Electrical Measurement Needs and Standards for Modern Electronic Instrumentation, NBS Tech Note 865, May 1975.
- [2] Bell, B. A., Editor, Proceedings of a Seminar on Digital Methods in Waveform Metrology, Natl. Bur. Stand. (U.S.), Spec. Publ. 707, 177 pages (Oct. 1985).
- [3] Souders, T. M., and Flach, D. R., A 20 Bit + Sign, Relay Switched D/A Converter, Natl. Bur. Stand. (U.S.), Tech. Note 1105, 21 pages (Oct. 1979).
- [4] Souders, T. M., and Flach, D. R., IEEE Trans. Instrum. Meas. IM-28, 239 (1979).
- [5] Souders, T. M., Flach, D. R., and Wong, T. C., IEEE Trans. Instrum. Meas. IM-32, 180 (1983).
- [6] Turgel, R. S., and Oldham, N. M., IEEE Trans. Instrum. Meas. IM-27, 460 (1978).
- [7] Turgel, R. S., Oldham, N. M., Stenbakken, G. N., and Kibalo, T. H., NBS Phase Angle Calibration Standard, Natl. Bur. Stand. (U.S.), Tech. Note 1144, 143 pages, July 1981.
- [8] Oldham, N. M., IEEE Trans. Power Appar. PAS-104, 3117 (1985).
- [9] Oldham, N. M., Hetrick, P. S., and Xiangren, Z., IEEE Trans. Instrum. Meas. IM-38, 368 (1989).
- [10] Tewksbury, S. K., Meyer, F. C., Rollenhagen, D. C., Schoenwetter, H. K., and Souders, T. M., IEEE Trans. Circuits Syst. CAS-25, 419 (1978).
- [11] Souders, T. M., IEEE Trans. Instrum. Meas. IM-27, 409 (1978).
- [12] Turgel, R. S., IEEE Trans. Instrum. Meas. IM-23, 337 (1974).
- [13] Field, B. F., IEEE Trans. Instrum. Meas. IM-27, 369 (1978).
- [14] Stenbakken, G. N., IEEE Trans. Power Appar. Syst. PAS-103, 2919 (1984).
- [15] Souders, T. M., Schoenwetter, H. K., and Hetrick, P. S., IEEE Trans. Instrum. Meas. IM-36, 956 (1987).
- [16] Simmons, J. D., Editor, NIST Calibration Services User's Guide 1989, Natl. Inst. Stand. Tech. (U.S.), Spec. Publ. 250, 186 pages, Jan. 1989.
- [17] Schoenwetter, H. K., IEEE Trans. Instrum. Meas. IM-32, 22 (1983).
- [18] Souders, T. M., IEEE Trans. Instrum. Meas. IM-31, 3 (1982).
- [19] Papoulis, A., The Fourier Integral and Its Applications, McGraw-Hill Book Company, Inc., New York (1962).

- [20] Turgel, R. S., IEEE Trans. Instrum. Meas. **IM-34**, 509 (1985).
- [21] Turgel, R. S., NBS 50 kHz Phase Angle Calibration Standard, Natl. Bur. Stand. (U.S.), Tech. Note. 1220, 73 pages, April 1986.
- [22] Turgel, R. S., J. Res. Natl. Bur. Stand. (U.S.) **93**, 53 (1988).
- [23] Oldham, N. M., Laug, O. B., and Waltrip, B. C., IEEE Trans. Instrum. Meas. **IM-36**, 341 (1987).
- [24] Laug, O. B., IEEE Trans. Instrum. Meas. **IM-34**, 639 (1985).
- [25] Laug, O. B., IEEE Trans. Instrum. Meas. **IM-36**, 994 (1987).
- [26] Miljanic, P., Stojanovic, B., and Bosnjakovic, P., The Development of a High Precision Time-Division Power Meter, Conference on Precision Electromagnetic Measurements (CPMEM) '84 Digest, Delft, the Netherlands, pp. 67–68.
- [27] Oldham, N. M., and Petersons, O., IEEE Trans. Instrum. Meas. **IM-34**, 521 (1985).
- [28] Oldham, N. M., Digital Waveform Synthesis Techniques, Natl. Bur. Stand. (U.S.), Spec. Publ. 707, (Oct. 1985), pp. 1–13.
- [29] IEEE Standard Dictionary of Electrical and Electronics Terms, IEEE, New York, NY, 1988.
- [30] Oldham, N. M., IEEE Trans. Instrum. Meas. **IM-32**, 176 (1983).
- [31] Oldham, N. M., Hetrick, P. S., and Zeng, X., IEEE Trans. Instrum. Meas. **IM-38**, 368 (1989).
- [32] Hess, D. T., and Clarke, K. K., IEEE Trans. Instrum. Meas. **IM-36**, 394 (1987).
- [33] Stearns, S. D., Digital Signal Analysis, Hayden Book Company, Inc., New Jersey (1975).
- [34] Shannon, C. E., and Weaver, W., The Mathematical Theory of Communication, University of Illinois Press, seventh paperback printing, (1978).
- [35] Bell, B. A., Field, B. F., and Kibalo, T. H., A Fast Response, Low-Frequency Sampling Voltmeter, Natl. Bur. Stand. (U.S.), Tech. Note 1159, 113 pages, August 1982.
- [36] Schoenwetter, H. K., IEEE Trans. Instrum. Meas. **IM-27**, 259 (1978).
- [37] Schoenwetter, H. K., AC Voltage Calibrations for the 0.1 Hz to 10 Hz Frequency Range, Natl. Bur. Stand. (U.S.), Tech. Note 1182, 58 pages, Sept. 1983.
- [38] Field, B. F., A Sampling Approach to the Measurement of Low Frequency Voltage Waveforms, Ph.D. Thesis, Univ. of Md., Dept. of EE, Dec. 8, 1978.
- [39] Stenbakken, G. N., Laug, O. B., Kibalo, T. H., Bell, B. A., and Perrey, A. G., NBS Wideband Sampling Wattmeter, Natl. Bur. Stand. (U.S.), Tech. Note 1221, 103 pages, May 1987.
- [40] Turgel, R. S., Sampling Techniques for Electric Power Measurement, Natl. Bur. Stand. (U.S.), Tech Note 870, 35 pages, June 1975.
- [41] Schuster, G., IEEE Trans. Instrum. Meas. **IM-25**, 529 (1976).
- [42] Souders, T. M., and Hetrick, P. S., IEEE Trans. Instrum. Meas. **IM-38**, 451 (1989).
- [43] Souders, T. M., Flach, D. R., Hagwood, C., and Yang, G., The Effects of Timing Jitter in Sampling Systems, Conference Record of the 1989 IEEE Instrumentation and Measurements Technology Conference (IMTC/89), April 27–29, Washington, DC (April, 1989) pp. 199–203.
- [44] Andrews, J. R., Bell, B. A., Nahman, N. S., and Baldwin, E. E., IEEE Trans. Instrum. Meas. **IM-32**, 27 (1983).
- [45] Schoenwetter, H. K., IEEE Trans. Instrum. Meas. **IM-33**, 196 (1984).
- [46] Schoenwetter, H. K., IEEE Trans. Instrum. Meas. **IM-36**, 428 (1987).
- [47] Souders, T. M., and Flach, D. R., IEEE Trans. Instrum. Meas. **IM-36**, 433 (1987).

The Diffusion of Charged Particles in Collisional Plasmas: Free and Ambipolar Diffusion at Low and Moderate Pressures

Volume 95

Number 4

July–August 1990

A. V. Phelps

Joint Institute for Laboratory Astrophysics,
National Institute of Standards and Technology and
University of Colorado,
Boulder, CO 80309

The interpretation of measurements of the properties of weakly ionized plasmas in terms of diffusion of electrons and ions is reviewed both critically and tutorially. A particular effort is made to tie together various aspects of charged particle diffusion phenomena in quiescent, partially ionized plasmas. The concepts of diffusion length and effective diffusion coefficient and the treatment of partially reflecting boundaries are developed in the limit of the space-charge-free motion of the electrons or ions. A simplified derivation of the screening length for space charge electric fields is followed by a review of the conventional derivation of diffusion in the ambipolar limit. A discussion of the scaling parameters of the ratio of the diffusion length to the screening length and the ratio of the diffusion length to the ion mean-free-path leads to a map used to

correlate published models covering the complete range of these parameters. The models of measurements of the diffusion of electrons, several types of positive ions, and negative ions are reviewed. The role of diffusion in the decay of charged particle densities and wall currents during the afterglow of a discharge is then considered. The effects of collapse of the space charge field and of diffusion cooling are reviewed. Finally, the application of the diffusion models to a number of different discharges is discussed.

Key words: ambipolar diffusion; boundaries; diffusion cooling; discharge maintenance; electrons; free diffusion; negative ions; positive ions; screening length; space charge.

Accepted: May 21, 1990

1. Introduction

The interpretation and planning of measurements of the properties of partially ionized, quiescent plasmas at low and moderate pressures usually requires an understanding of the loss of charged particles by diffusion to the walls. This paper is a review of models and associated experiments on the effects of space charge on the diffusion of charged particles to the walls of a discharge vessel for a wide range of discharge conditions. Previous reviews of this subject are those of Oskam [1] and of Cherrington [2]. For the most part, we will be concerned with transport perpendicular to applied electric and magnetic fields, e.g., we will not con-

sider space charge and transport in the cathode fall or the large amplitude oscillations of electrons and ions driven by a high frequency field [3]. Phenomena which can be described by the models discussed range from nearly unperturbed or free-fall motion of electrons and ions at the low gas and charged-particle densities, through low-pressure fluorescent lamps and lasers, to the near equilibrium transport of electrons and ions in high pressure, high-temperature arcs.

This paper is both critical and tutorial in nature. It is assumed that the reader has at least a general familiarity with gas discharges and associated colli-

sion phenomena. This author still finds the review by Druyvesteyn and Penning [4] to be the most useful general discussion of gas discharges and related phenomena. Important reviews of specialized aspects include: collision phenomena, McDaniel [5]; electron energy distribution functions, Holstein [6], Allis [7] and Kumar, Skulanderud, and Robson [8]; microwave discharges, Brown [3] and McDonald [9]; ion drift and diffusion in uniform electric fields, McDaniel and Mason [10]; electron transport, Huxley and Crompton [11] and Hunter and Christopoulou [12]; electrical breakdown, Raether [13] and Dutton [14]; glow discharges, Francis [15]; spark channel formation, Craggs [16] and Gallimberti [17]; and gas lasers, Cherrington [2].

This discussion is divided into three major sections. In section 2 we consider the diffusion of charged particles in the absence of space charge fields. Under that topic we discuss the concept of the diffusion length, the treatment of boundary conditions, and the use of the boundary condition to calculate effective diffusion coefficients for a single type of charged particle for a wide range of gas densities. We do not discuss the very extensive work on the effects of diffusion on the electron or ion energy distributions in space-charge free and spatially uniform, applied electric fields [7,8,18–20]. The second part of the paper, section 3, is concerned with the calculation of the effects of space charge electric fields. We begin with a derivation of the Debye screening length. We then calculate the electric field strength and the ambipolar diffusion coefficient appropriate to electrical discharges with high electron densities and high gas densities. This is followed by a consideration of the range of mean-free paths, screening lengths, and diffusion lengths appropriate to various experimental conditions. The presently available theory ranges from models appropriate to the free-fall of charged particles in the absence of space charge fields to models for high gas densities and charge densities. We consider the theory of the transition from ambipolar diffusion of the charged particles at high gas densities and then at low gas densities. Next the theory is reviewed for high electron and ion densities but a range of gas densities from very low values to very large values. Finally, we discuss theoretical results which cover the whole range of gas and charge densities. In the last major section, section 4, applications of the models to specific experimental discharges are reviewed. Except in section 4.1.2 we assume that the electron energy distribution is independent of position and is determined by an applied

dc or high frequency electric field or by the gas temperature.

2. Space-Charge-Free Diffusion

2.1 Diffusion Length

In this section we review models for the diffusion of charged particles in the absence of space charge fields and at high enough gas densities such that the boundary conditions are simple. Equations describing the electron and ion behavior under these conditions are [7]

$$\frac{\partial n_q}{\partial t} = -\nabla \cdot \Gamma_q + k_i n n_e, \quad (1)$$

$$\Gamma_q = -D_q \nabla n_q \pm \mu_q n_q E, \quad (2)$$

where q is e for electrons or $+$ is for positive ions and the $+$ and $-$ signs are for ions and electrons, respectively. Equation (1) is the continuity equation for the electron density n_e or for the density n_+ , where Γ_q is the flux density for the electrons or ions. According to eq (1) the time derivative of the electron density is equal to the outflow of electron particle flux plus the production by electron impact ionization. This latter term contains the rate coefficient for ionization k_i , the neutral atom density n , and the electron density n_e . Equation (2) expresses the electron and ion flux densities in terms of the density gradients and the contributions from charged particle drift in any field that may be present. Here D_q is the diffusion coefficient and μ_q is the mobility for the electrons or ions. In this section we will assume that only a single type of charged particle is present and that electric fields are negligible.

If we combine the continuity equation and the flux equation we obtain the relation between the production term and the loss of charged particles by diffusion [7], i.e.,

$$\frac{\partial n_q}{\partial t} = D_q \left[\frac{1}{r} \frac{\partial}{\partial r} \left(r \frac{\partial n_q}{\partial r} \right) + \frac{\partial^2 n_q}{\partial z^2} \right] - k_i n n_q. \quad (3)$$

Equation (3) is written in a form appropriate to cylindrical geometry and includes diffusion in both the radial direction and the axial direction. As shown in the next section, the electron/ion density is approximately zero at absorbing boundaries. The lowest mode solution [2,7] to eq (3) is then

$$n_q(r, z, t) = n_{q0} \exp(\nu t) \cos\left(\frac{\pi z}{L}\right) J_0\left(\frac{2.4 r}{R}\right). \quad (4)$$

Substitution of eq (4) into eq (3) gives

$$\nu = k_i n - \frac{(nD_a)}{n\Lambda^2} = \nu_i - \nu_w, \quad (5)$$

where

$$\frac{1}{\Lambda^2} = \left(\frac{\pi}{L}\right)^2 + \left(\frac{2.405}{R}\right)^2, \quad (6)$$

ν_i is the ionization frequency, and ν_w is the frequency of particle loss to the walls. Here L and R are the length and radius of the container, respectively. We will use the concept of the diffusion length Λ [5,7], defined for cylindrical geometry by eq (6), to characterize the size of the container throughout this report. For parallel plane geometry $R = \infty$ in eq (6) and $\Lambda = L/\pi$, where L is now the electrode separation. The approximations made in assumption of zero density at the boundary are discussed in section 2.2.

2.2 The Effect of Boundaries

In this subsection we are concerned with a mathematical treatment of the effects of boundaries on the solution to the diffusion equation. Our approach is to solve for the transport of charged particles using the techniques of astrophysics in order to take into account the effects of charged particle reflection at the boundaries [21]. We begin with equations for the intensity $I(\Theta, z)$, flux $\Gamma(z)$, and density $n_q(z)$ of charged particles, taken from the theory of radiation transport [22].

$$\cos \Theta \frac{dI(\Theta, z)}{dz} = -QnI(\Theta, z) + \frac{Qn}{4\pi} \int d\Omega' I(\Theta', z) + \frac{S(z)}{4\pi}, \quad (7)$$

$$\Gamma(z) = \int d\Omega I(\Theta, z) \cos \Theta, \quad (8)$$

and

$$n_q(z) = \frac{1}{v} \int d\Theta I(\Theta, z). \quad (9)$$

Here v is the speed of the particles, which are assumed to be monoenergetic. Equation (7) describes the attenuation of the beam of charged particles of intensity I . This intensity is assumed to be a function of the single dimension z and the angle Θ with

respect to the direction of positive z . The left-hand side of eq (7) gives the rate of change of the intensity with respect to position. The $\cos \Theta$ factor represents the projection of the intensity in the direction z . The first term on the right-hand side of this equation gives the loss of intensity as the result of isotropic elastic collisions with a cross section Q . The second term represents the effects of collisions which scatter the charged particles into the solid angle $d\Omega$ about the direction of the intensity. The 4π factor is the result of the assumption of isotropic scattering. The last term in this equation represents production of charged particles, which is also assumed to be isotropic. Equations (8) and (9) are expressions for the current density in the z direction and for the density of charged particles in terms of integrals over the intensity.

Equations (7)-(9) are solved using what is known as the two-stream approximation. In the formulation from Chandrasekhar [22], the two streams are assumed to lie on the surface of a cone making an angle Θ_i with the positive z direction. With this approximation one obtains equations for I_+ , representing the intensity in the $+z$ direction, and I_- , representing the intensity in the $-z$ direction which are

$$\cos \Theta_i \frac{dI_{\pm}}{dz} = -\frac{QnI_{\pm}}{2} + \frac{QnI_{\mp}}{2} + \frac{S(z)}{4\pi}, \quad (10)$$

and

$$-\cos \Theta_i \frac{dI_{\mp}}{dz} = -\frac{QnI_{\mp}}{2} + \frac{QnI_{\pm}}{2} + \frac{S(z)}{4\pi}. \quad (11)$$

In this section only the subscripts $+$ and $-$ refer to direction relative to the z axis and not to the sign of charge. The flux or particle current density and the particle density are then given by

$$\Gamma(z) = 2\pi \cos \Theta_i (I_+ - I_-), \quad (12)$$

and

$$n_q(z) = \frac{2\pi}{v} (I_+ + I_-). \quad (13)$$

On the right-hand side of eq (10) we first have the loss of the I_+ component of intensity due to collisions. The second term is the gain due to collisions of the other component of the intensity. Finally one has the source term. Equation (11) is a similar equation giving the continuation of the negatively-directed component. Equations (12) and (13) give

expressions for the current density and the particle density in terms of the positive and negative components of the intensity. It should be noted that with the choice of $\cos\Theta_i = 1/\sqrt{3}$, the equations for the flux and density in the two stream approximation to the angular distribution are identical to those obtained with the first two terms of the spherical harmonic expansion [21].

Our next step [21] is to rewrite eqs (10)–(13) in forms similar to those of eqs (1) and (2). Adding eqs (10) and (11) for I_+ and I_- gives

$$\cos\Theta_i \frac{d(I_+ - I_-)}{dz} = \frac{S(z)}{2\pi}, \quad (14)$$

while subtracting the equations yields

$$\cos\Theta_i \frac{d(I_+ + I_-)}{dz} = -Qn(I_+ - I_-). \quad (15)$$

Term by term comparison of eqs (14) and (15) with eqs (1) and (2) in the limits of $E=0$ and $dn_q/dt=0$ leads one to define a diffusion coefficient for this approximation by

$$D_q = \cos^2\Theta_i \frac{v}{Qn} = \frac{v}{3Qn} = \frac{\lambda_q v}{3}, \quad (16)$$

where λ_q is the mean-free-path for the particle of charge type q . If one adopts a Gaussian weight factor of $\cos\Theta_i = 1/\sqrt{3}$ as discussed by Chandrasekar [22], then one obtains the familiar form for the diffusion coefficient [21] given in the second and third equalities of eq (16).

We now come to the part of the derivation directly concerned with boundary conditions and follow the treatment of Chantry, Phelps, and Schulz [21]. We express the boundary condition at $z=0$ by writing the intensity leaving the boundary I_+ as equal to a reflection coefficient times the intensity I_- arriving at the boundary, i.e., $I_+ = \rho I_-$. Substitution of this relationship into eqs (13) and (15) yields the magnitude of the normalized slope of the density of charged particles at the boundaries, i.e.,

$$\left| \frac{1}{n_q} \frac{dn_q}{dz} \right| = \frac{Qn}{\cos\Theta_i (1+\rho)} \frac{(1-\rho)}{(1+\rho)} = \frac{\sqrt{3}(1-\rho)}{\lambda_q(1+\rho)} = \frac{1}{\ell_q}. \quad (17)$$

Equation (17) is often called the Milne boundary condition [23].

The meaning of the various terms in the boundary condition represented by eq (17) are illustrated in figure 1. The dashed line shows the

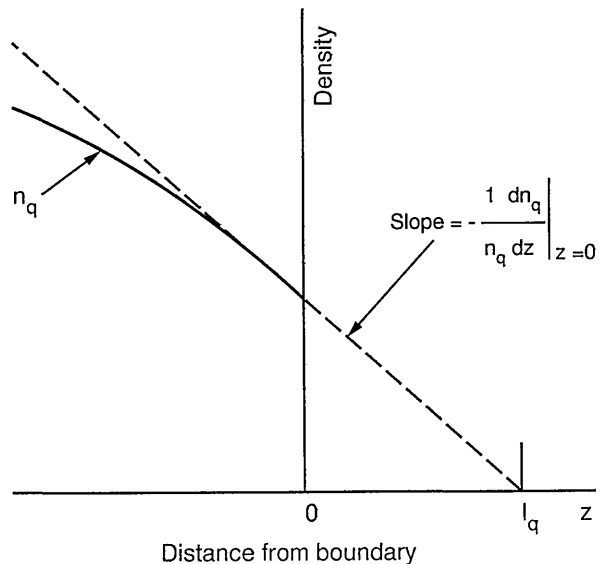


Figure 1. Boundary condition for electron and ion densities.

value of $(1/n)(dn/dz)$ at $z=0$. The intercept of this line with the abscissa occurs at a distance beyond the boundary equal to $\ell_q = (1+\rho)\lambda_q/\sqrt{3}(1-\rho)$. In the limit of zero reflection $\ell_q = \lambda_q/\sqrt{3}$. A more detailed calculation [23,24] leads to the conclusion that for planar geometry the $\sqrt{3}$ in eq (17) should sometimes be replaced by a number between 1.41 and 1.5 depending on the reflection coefficient.

2.3 Effective Diffusion Coefficient

We now consider the boundary condition appropriate to the problem of diffusion in an infinite cylinder and in the limit of a steady-state solution. We follow the treatment of McCoubrey [25]. The fundamental mode solution to eq (3) is the well-known zero-order Bessel function, i.e., $n(r) = J_0(jr/R)$. Substitution of this solution into the boundary condition, eq (17), yields the relation between the quantity j , the radius of the cylinder R , the mean-free path λ_q , and the reflection coefficient ρ

$$\frac{j J_1(j)}{R J_0(j)} = \frac{\sqrt{3}(1-\rho)}{\lambda_q(1+\rho)}. \quad (18)$$

Note that j is smaller than the value of 2.4 which is the first root of $J_0(j)$. For parallel plane geometry the left hand side of eq (18) becomes $j \tan(j)/L$. Substitution of eq (18) into eq (3) yields the condition for a steady-state discharge, i.e., the discharge “maintenance” condition,

$$k_i n = \frac{D_q j^2}{R^2} = \frac{D_{sq}(\Lambda/\lambda_q, \rho)}{\Lambda^2}, \quad (19)$$

or for cylindrical geometry

$$n D_{sq}(\Lambda/\lambda_q, \rho) = \left(\frac{j(\Lambda/\lambda_q, \rho)}{2.405} \right)^2 n D_q. \quad (20)$$

In the second equality of eq (19), we have chosen to express the results in terms of an effective diffusion coefficient D_{sq} .

Chantry [24] has recently proposed a simple empirical approximation to eq (20) which is

$$\frac{D_{sq}}{D_q} = \frac{1}{\left(1 + \frac{\xi \ell_q}{\Lambda^2} \right)} \quad (21)$$

where ξ is the volume of the discharge chamber divided by its surface area and the “extrapolation length” ℓ_q is defined by eq (17). This relation is useful for arbitrary geometry, e.g., ξ/Λ is $2.405/2$ for infinite cylindrical geometry and $\pi/2$ for parallel plane geometry. The curve and points of figure 2 show plots of the ratio D_{sq}/D_q as a function of the ratio $\Lambda^2/\xi \ell_q$ for $\rho=0$. The solid curve is eq (21) while the circles are calculated from eq (20) for cylindrical geometry [25]. The squares are calculated from the corresponding equation for parallel-plane geometry. The agreement among the values shown by the points and the curve is evidence of the success of Chantry’s approximation. Figure 2 shows that the effective diffusion coefficient D_{sq} used to describe the loss of charge particles in eq (19) approaches D_q as the container size increases and the extrapolated length ℓ_q and mean-free-path λ_q decrease. At low values of $\Lambda^2/\xi \ell_q$ the value of D_{sq} decreases below the high pressure limit.

Since a cursory glance at figure 2 makes it appear that charged particle losses to the wall become much less important as the mean-free path becomes longer, we show in figure 3 a plot of the wall loss frequency ν_w , defined in eq (5) and normalized to its value at low densities ν_{w0} , as a function of the gas density. The horizontal scale for figure 3 is actually $\Lambda^2/\xi \ell_q$, which is proportional to gas density through $1/\ell_q$. At low gas densities the loss frequency $\nu_w = \nu_{w0}$ is independent of density, i.e., collisions are negligible and the charged particles move freely to the wall. At large gas densities the wall loss frequency varies inversely with gas density and is given by the $\nu_w = D_q/\Lambda^2 = \lambda_q v / 3\Lambda^2$, where D_q and λ_q vary inversely with density. Figure 3 shows that the transition between the two regions occurs when $\Lambda^2/\xi \ell_q$ is equal to 1. Note that the transition seen here between the two limiting forms of loss to the boundary is often observed for neutral free radicals in chemical reactors [26].

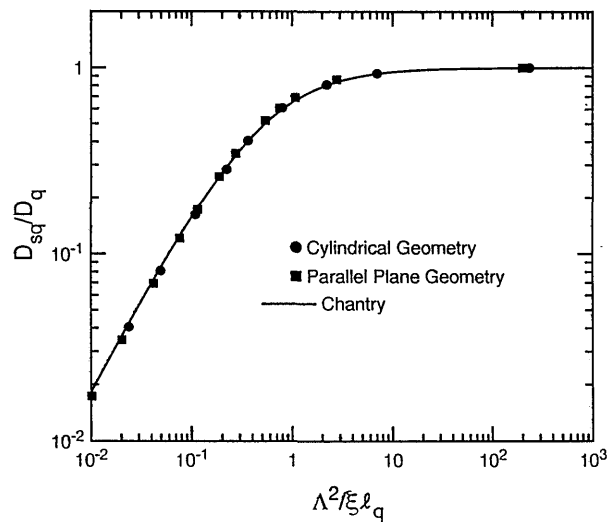


Figure 2. Normalized diffusion coefficient for a single type of particle.

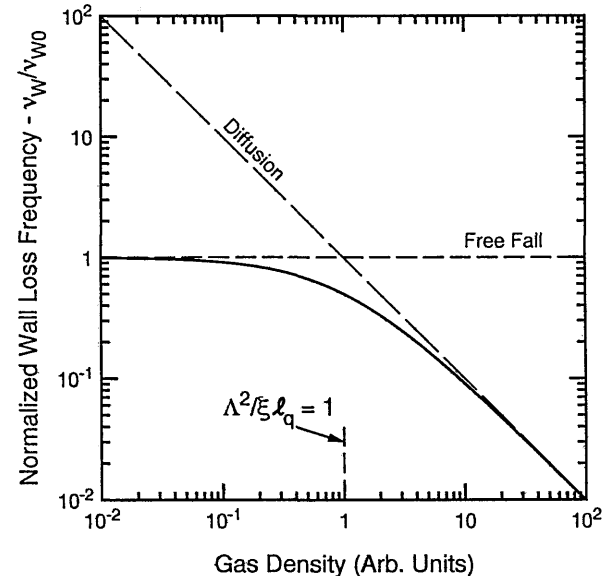


Figure 3. Apparent diffusion coefficient vs gas density.

3. Effects of Space Charge on Diffusion of Electrons and Ions

We begin this section with a simple formulation of the length which characterizes space charge phenomena in steady-state plasmas, i.e., the screening length. We then consider limiting forms of the theory of effects of the self-consistent electric field or space charge field on the steady-state diffusion problem. Finally, we review the general solutions and compare empirical approximations to the results of numerical models.

3.1 Screening Length

The screening or shielding length [27] characterizes the distance over which an electric potential change influences the charge distribution. The spatial variation of the potential $V(r,z)$ is related to the positive ion and electron densities by Poisson's equation, i.e.,

$$\nabla^2 V(r,z) = -\frac{e}{\epsilon_0} \left(n_+ - n_- - n_e \right). \quad (22)$$

Note that here and in the rest of this paper, the subscripts + and – refer to positive and negative ions. Plasmas with several types of ions, including negative ions, will be considered in section 3.4. For the purposes of this discussion, we assume one dimensional geometry and that either positive ions or electrons are dominant and of nearly uniform density. The solution to eq (22) is then

$$\Delta V = \frac{n_q e}{2\epsilon_0} \Delta z^2, \quad (23)$$

where n_q is the density of charged particles. We then characterize this change by the distance required for the potential energy to change by an energy equal to half that of the particle temperature, i.e., by $e\Delta V = kT_q/2$. This distance is called the screening or Debye length λ_{Dq} and is given by

$$\lambda_{Dq}^2 = \frac{\epsilon_0 k T_q}{e^2 n_q} = \frac{k T_q}{8\pi Ry a_0 n_q}, \quad (24)$$

where in the second equality λ_{Dq} is in m, kT_q is the charged particle temperature in eV, n_q is in m^{-3} , $Ry = 13.6$ eV, and $a_0 = 5.29 \times 10^{-10}$ m. Note that the screening length for electrons and ions differ because of differing temperature and densities. We will be primarily concerned with the electron screening length λ_{De} .

The screening length relation is used for scaling the results of space charge controlled motion and can also be derived from the detailed theories, such as that of Allis and Rose [28], to be discussed in section 3.3.2.

3.2 Ambipolar Diffusion Theory for High Electron, Ion, and Gas Densities: ($\Lambda/\lambda_{De} >> 1$ and $\Lambda/\lambda_+ >> 1$)

We now consider the effects of space charge in the limits for which the screening length and the mean-free path for positive ions λ_+ are much

smaller than the diffusion length Λ , i.e., in the region of high electron, ion, and gas densities but negligible electron-ion recombination, etc.. This problem was solved many years ago by Schottky [29] and the resultant diffusion is termed ambipolar diffusion. One begins with expressions for the flux of electrons and ions:

$$\Gamma_e(z) = -D_e \nabla n_e - \mu_e n_e E_s, \quad (25)$$

and

$$\Gamma_+(z) = -D_+ \nabla n_+ + \mu_+ n_+ E_s. \quad (26)$$

Equation (25) shows that in the limits considered here the electron flux is equal to the negative of a diffusion term minus a term representing the drift of electrons in response to the electric field E_s generated by the difference in the electron and ion densities, i.e., the space-charge field. A similar expression is given in eq (26) for the positive ions. Note that the sign of this mobility or drift term has been changed as is appropriate to the change in sign of the charge. For the steady-state problems of interest to us the electron flux is equal to the positive ion flux so that there is no build-up of charge difference, i.e., Γ_e is equal to Γ_+ . Next it is assumed that $n_e - n_+ < < n_e$ or n_+ , i.e., the quasi-neutrality assumption. With these assumptions eqs (25) and (26) yield an expression for the space charge electric field:

$$E_s = - \frac{\left(D_e - D_+ \right)}{\left(\mu_e + \mu_+ \right)} \frac{\nabla n_{e,i}}{n_{e,i}} \approx - \frac{D_e \nabla n}{\mu_e n}. \quad (27)$$

In the second equality we assumed that $D_e > D_+$ and $\mu_+ > > \mu_e$, as is usually the case. In this limit the electric field is determined entirely by the electrons.

Substitution of eq (27) for the electric field into eq (25) shows that the two terms on the right-hand side essentially cancel each other. Physically this means that the electron diffusion current is balanced rather closely by the electron drift current and that the electrons essentially sit in a potential well. The potential well appropriate to parallel plane geometry is drawn in figure 4. It is based on the approximate solution for an absorbing boundary, i.e., that $n(z) = n_0 \cos(\pi z/L)$ so that $V(z) = (D_e/\mu_e) \ln[\cos(\pi z/L)]$. Note that this potential becomes infinite at the boundary so that the electrons cannot escape. The resolution of this

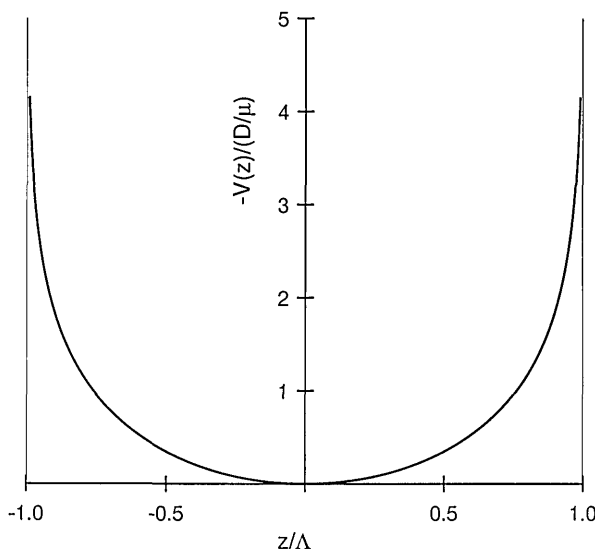


Figure 4. Ambipolar space charge potential as seen by electrons.

difficulty through departures from the ambipolar limit, i.e., the presence of a space charge sheath, near the boundary is treated in the models of section 3.3.

The final expression for the positive ion flux is

$$\Gamma_+ = -\frac{(\mu_e D_+ + \mu_+ D_e)}{(\mu_e + \mu_+)} \nabla n_+ = -D_a \nabla n_+, \quad (28)$$

where for $\mu_e > > \mu_+$

$$D_a \approx \left(1 + \frac{D_e / \mu_e}{D_+ / \mu_+}\right) D_+ \approx \left(1 + \frac{T_e}{T_+}\right) D_+. \quad (29)$$

The effective diffusion coefficient D_a is known as the ambipolar diffusion coefficient. Equation (29) shows that when the electron D_e / μ_e ratio is much greater than the positive ion D_+ / μ_+ ratio, as in an active discharge, then the ambipolar diffusion coefficient is much greater than the positive ion diffusion coefficient. The motion of the positive ions in the potential shown in figure 4 is that of a continually accelerating drift. We will see later how this model fails as one approaches the boundaries of the discharge tube.

The electron and ion mobilities and diffusion coefficients have been assumed constant in eqs (25)–(29). The effects of an E/n dependent ion mobility have been considered by Frost [30] and by Zakharyova, Kagan, and Perel' [31]. Other geometries,

such as coaxial cylinders, have been considered [32–34]. The second equality in eq (29) assumes that the electron and ion energy distributions are Maxwellian at temperatures of T_e and T_i , respectively. When the electron energy distribution is not Maxwellian the concept of a temperature is only approximately correct and it is better to retain eD_e / μ_e from the first equality of eq (29) rather than use kT_e [35]. The effects of a non-Maxwellian ion energy distribution apparently have not been discussed in this context.

Two useful limits of eq (29) are the thermal equilibrium limit, i.e., $T_e = T_+$, and the active discharge limit, i.e., $T_e >> T_+$. The thermal equilibrium limit is often applicable in the afterglow of pulsed discharges [1,5] and results in

$$D_a = 2 D_+. \quad (30)$$

This subject will be considered further in section 3.5.1. The active discharge limit often applies in the positive column, etc., [4] and results in

$$D_a = \frac{D_e}{\mu_e} \mu_+ \approx \frac{T_e}{T_+} D_+. \quad (31)$$

This limit will be considered in more detail in section 4.1.1.

3.3 Transitional Ambipolar Diffusion

3.3.1 Map of Λ/Λ_{De} and Λ/Λ_+ Space In order to correlate various experimental and theoretical investigations of ambipolar diffusion, we have shown in figure 5 a schematic of the range of diffusion lengths, positive ion mean-free-paths, and screening lengths considered in the theories we will discuss, i.e., $0 < \Lambda/\Lambda_{De} < \infty$ and $0 < \Lambda/\Lambda_+ < \infty$. The space-charge free limit resulting in independent particle transport which we considered in section 2 corresponds to moving downward along the left-hand side of this square. At the upper left corner we have the independent diffusion of the electrons and the positive ions. At the lower left corner we have the collision-free and field-free, i.e., “free fall,” motion of the ions and electrons to the boundary. The ambipolar diffusion limit considered in section 3.2 occurs in the upper right-hand corner of the square, where both the mean-free-path and the screening length are short compared to the diffusion length. The transition from free diffusion to ambipolar diffusion at high gas densities which occurs along the top side of the square is discussed in section 3.3.2. This is followed in section 3.3.3 by a

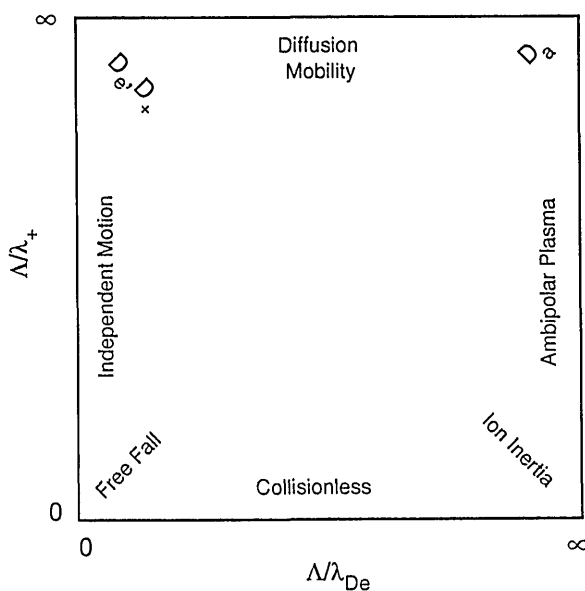


Figure 5. Map of transitional ambipolar diffusion parameters and solutions.

summary of theory of the collisionless transition along the bottom of the square from space charge free to space charge dominated or ambipolar motion. This theory includes inertial effects which describe the acceleration of ions in the absence of collisions. The theory including both collision and inertia terms is summarized in section 3.3.4 for the limit of $\lambda_{De} \ll \Lambda$, i.e., along the right-hand side of the square. Section 3.3.5 summarizes theoretical results applicable to all of figure 5. Positive ion diffusion for $\Lambda/\lambda_+ > 1$ is discussed in section 3.3.6.

3.3.2 The Transition from Free to Ambipolar Diffusion at High Gas Densities: $\Lambda/\lambda_+ \gg 1$ and $0 < \Lambda/\lambda_{De} < \infty$ We now consider the transitional ambipolar diffusion problem for electrons and positive ions corresponding to experiments in which the mean-free-path is much smaller than the diffusion length, and in which the electron screening length may vary from much smaller than the diffusion length to much larger than the diffusion length. This problem was first solved by Allis and Rose [28] and we will summarize their results. The applicable equations are

$$\Gamma_e(z) = -D_e \nabla n_e - \mu_e n_e E_s, \quad (25)$$

$$\Gamma_+(z) = -D_+ \nabla n_+ + \mu_+ n_+ E_s, \quad (26)$$

$$\nabla \cdot \Gamma_{e,+} = k_i n n_e, \quad (32)$$

and, since $n_- = 0$, eq (22) becomes

$$\nabla^2 \cdot V(r,z) = -\nabla \cdot E_s(r,z) = -\frac{e}{\epsilon_0} (n_+ - n_e), \quad (33)$$

with the boundary conditions for absorbing walls of

$$n_e(R) \approx n_+(R) \approx 0.$$

Equations (25) and (26) repeat the continuity equations for electrons and ions. Equation (32) is the steady-state form of eq (1) for positive ions ($q = +$), while eq (33) is eq (22) with $n_- = 0$. The mobility μ and diffusion D coefficients are usually treated as independent of position. The boundary conditions require that the electron and positive ion densities are zero at the generalized boundary at R . Following Allis and Rose [28] we expressed the results in terms of an effective diffusion coefficient D_{se} for electrons defined for a steady-state discharge such that

$$k_i n n_{e0} = v_w n_{e0} \equiv \frac{n D_{se} n_{e0}}{\Lambda^2}, \quad (34)$$

where n_{e0} is the electron density at the center of the discharge. The ratio D_{se}/D_e is a measure of the change in the diffusion loss of electrons caused by the ambipolar electric fields. Note that some authors, e.g., Ingold [36] and Cohen and Kruskal [37], express the results of the theory in terms of the ionization frequency $v_i = k_i n$ required to maintain the discharge, or in terms of its equal for a steady-state discharge, the frequency of electron loss to the walls v_w . Two important limits of the solutions to eqs (25), (26), (32), and (33) have been discussed in sections 3.2 and 2 of this report. When $\lambda_{De} \ll \Lambda$ the ambipolar limit applies and $D_{se} = D_a$. When $\lambda_{De} \gg \Lambda$, free diffusion of the electrons occurs and $D_{se} = D_e$. According to the expression for the ambipolar diffusion coefficient given in eq (29), the ratio of the ambipolar diffusion coefficient to the free electron diffusion coefficient D_{se}/D_e for an active discharge ($T_e > T_+$) is equal to the ratio of the positive-ion mobility to the electron mobility. Typical experimental values of D_{se}/D_e are from 10^{-4} to a few times 10^{-2} .

A number of solutions have been obtained for the transition from free to ambipolar diffusion at high gas densities. One of the earliest was that reported by Holstein [38], who replaced the radius of the tube for electron loss by the radius minus a plasma sheath thickness very nearly equal to the screening length. A second approximation uses the idea that since electron and ion densities have the

same spatial distribution in the limits of large and small screening lengths one can assume that the ratio of the electron and ion densities is everywhere constant [28,39,40]. Since these solutions are not accurate at intermediate values of λ_{De}/Λ , one must beware of this popular approach. Numerical solutions of eqs (25), (26), (32), and (33) were obtained by Allis and Rose [28] for parallel plane geometry. More recently, numerical techniques have been used for $0 < \Lambda/\lambda_{De} < \infty$ in the $\Lambda/\lambda_+ \gg 1$ limit by Kregel [41] as part of time dependent solutions and by Ingold [36] as part of steady-state solutions for $0 < \Lambda/\lambda_+ < \infty$. Models based on the separation of the plasma into a central region matched to a sheath have been extended and refined by several authors [28,37,42,43]. The more recent results agree well with the numerical results of Allis and Rose [28]. Another approach uses power series approximations to the electron and positive ion densities in parallel-plane geometry [44,45] and cylindrical geometry [46]. For reasons which are not understood, the latter results [46] for D_{se} are lower than the numerical results [28]. An analytic solution for an isothermal plasma, i.e., $T_+ = T_e$, by Numano [47] agrees with Allis and Rose [28] for a limited range of μ_+/μ_e .

Figure 6 shows schematics of spatial distributions for the electric potential and the electron and positive-ion densities obtained by the numerical techniques [28]. The upper curve shows a schematic of the space-charge potential $V(z)$ as a function of distance for parallel-plane geometry. In the central portion of the gap near $z=0$ the potential is the same as shown in figure 4, i.e., it is approximately parabolic near its origin and increases with distance from the origin at a rate determined by the D/μ value for the electrons. At a distance from the electrodes of the order of the screening length for the electrons, the potential variation changes character and increases less rapidly, reaching a finite value at the electrodes. This finite potential allows the electrons to escape over the potential barrier and reach the wall. The transition region near the wall is known as the ion sheath, because of the dominance of positive ions. In the lower part of figure 6 we show a schematic of the calculated positive ion and electron densities. Note that the electron density curve has been multiplied by 100. The electron density decreases more rapidly than given by the cosine function characteristic of free diffusion or of ambipolar diffusion, and it approaches zero at a distance from the wall of the order of the electron screening length. The positive ion density on the other hand is much flatter and decreases

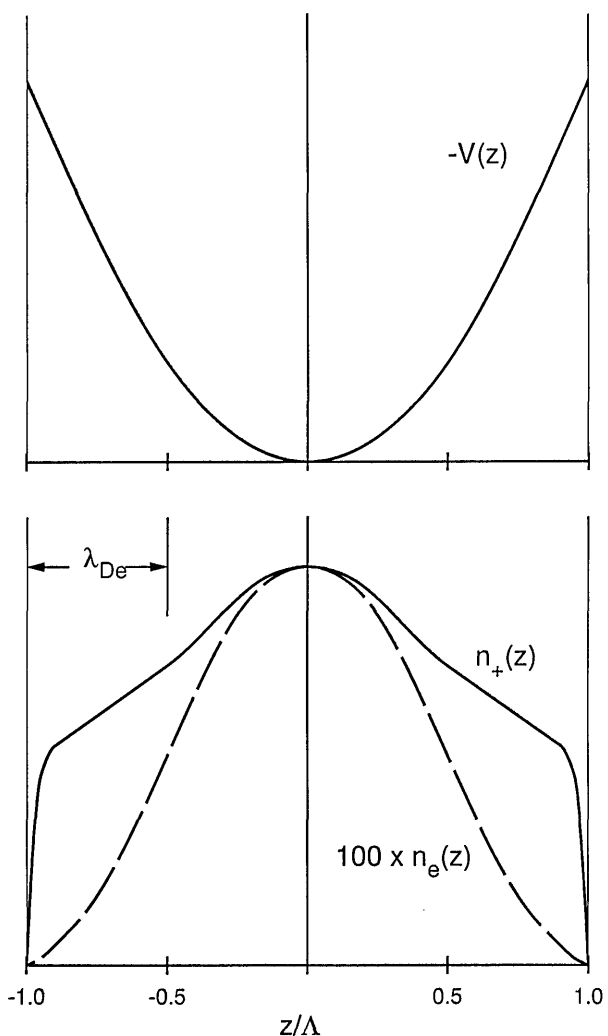


Figure 6. Schematic spatial distributions of potential and particle densities.

rapidly only at distances from the wall such that ion diffusion becomes more important than the ion drift in the space charge electric field which dominates over most of the volume.

In figure 7 we have compared some of the theoretical results for the effective diffusion coefficient as a function of the ratio of the diffusion length to the electron screening length. The simple approximation due to Holstein is indicated by '+'s. We see that it is close to the other points when the ratio of the electron mobility to the ion mobility is relatively small, as in the case of $\mu_-/\mu_+ = 32$. Holstein's approximation is much worse for larger ratios of mobility. The numerical results of Allis and Rose are indicated by the 'X's and solid circles and show the smooth transition from values D_{se}/D_e near unity at low values of the ratio Λ/λ_{De} to

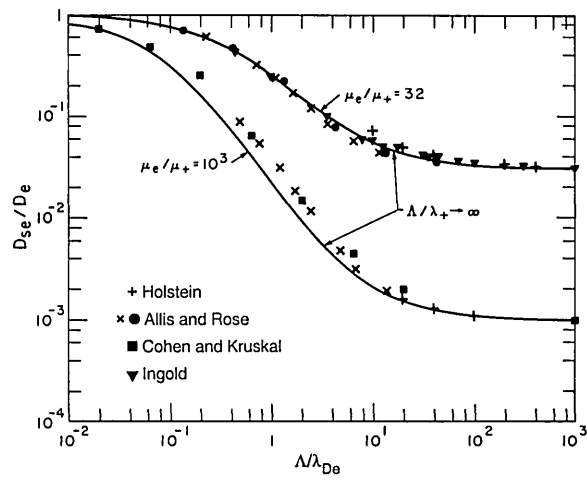


Figure 7. Normalized diffusion coefficients vs Λ/λ_{De} for $\lambda_+/\Lambda << 1$.

values equal to the ratio of mobilities of positive ions and electrons at high ratios Λ/λ_{De} . Similar ratios have been calculated numerically by Cohen and Kruskal [37], solid squares, and by Ingold [36], inverted triangles. The solid curves are empirical fits to these calculations and will be discussed later.

3.3.3 Effects of Space Charge at Low Gas Densities: $\lambda_+/\Lambda >> 1$ and $0 < \Lambda/D_e < \infty$ We now turn to the transition between free “diffusion” and ambipolar “diffusion” which occurs at low gas densities, that is when $\lambda_+/\Lambda >> 1$ and the charged particle motion approaches free-fall in the space charge electric field. The long mean free paths mean that the collisional-equilibrium model of charged particle motion eq (2) will have to be replaced by a model in which the ion velocity distribution is no longer a function of just the local electric field. The screening lengths vary from very small values to large values compared to the diffusion length. In the $\lambda_+/\Lambda >> 1$ limit, the frequency of charged particle loss or reciprocal lifetime is independent of gas density as for low Λ/λ_+ in figure 3. Nevertheless, for the sake of unity we will express the results in terms of an effective diffusion coefficient for electrons relative to the free diffusion coefficient. Here we are concerned with solutions obtained along the lower side of the square of figure 5.

We follow the treatments of Tonks and Langmuir [48] for $\lambda_{De}/\Lambda << 1$ and the treatment of Self [49] for arbitrary values of Λ/λ_{De} . Another discussion of related models is given by Dote and Shimada [50]. For simplicity we discuss only the one dimensional solution. The potential form of Poisson’s equation, eq (33), is the basic equation for this treatment. The electrons are assumed to be trapped

in the electrostatic potential and to obey the Boltzmann equation for their distribution in that potential, i.e., $n_e = n_0 \exp[-eV(z)/kT]$. The density of positive ions is

$$n_+(z) = \int_0^z \frac{dy}{v_+(y,z)} k_i n_e(y). \quad (35)$$

Here $v_+(y,z)$ is the velocity a positive ion acquires in moving of its point of production at y to the point z . The equations for the electron and ion fluxes given by eqs (25) and (26) are no longer adequate and are replaced by

$$\Gamma_e = -D_e \nabla n_e - \mu_e n_e E_s - \frac{n_e}{m_e v_{en}} \nabla (m_e v_e^2/2), \quad (36)$$

and

$$\Gamma_+ = -D_+ \nabla n_+ + \mu_+ n_+ E_s - \frac{n_+}{m_+ v_{+n}} \nabla (m_+ v_+^2/2). \quad (37)$$

Here v_{en} and v_{+n} are the collision frequencies for electrons and ions with the neutral gas and are defined for practical purposes by their relation to the corresponding mobilities, i.e., $v_j \equiv e/(m_j \mu_j)$. Equations (35)–(37) were obtained from the first two velocity moments of the Boltzmann equations for electrons and ions. The last terms on the right-hand sides of eqs (36) and (37) are called the inertia terms and become important when λ_e or λ_+ becomes comparable with the dimensions of the plasma region under consideration [36,51–55].

For the conditions of interest here the electrons are sufficiently close to equilibrium in the potential well that the inertia and flux terms of eq (36) can be neglected. On the other hand, at the low gas densities considered in this section an approximate solution to eq (37) is obtained by equating the last two terms on the right-hand side to obtain

$$\frac{m_+ v_+^2}{2e} = \int_{z_1}^{z_2} dz E_s(z) = V(z_1) - V(z_2). \quad (38)$$

Here the electron starts at rest at z_1 . Equation (38) is simply the conservation of energy in the collisionless limit. When eq (38) is solved for v_+ and used in the integral form of eq (35) for n_+ , the one dimensional form of eq (33) becomes

$$\begin{aligned} \frac{d^2 V(z)}{dz^2} = -\frac{2en_0}{\epsilon_0} \left[\left(\frac{m_+}{2e} \right)^{\frac{1}{2}} k_i n \int_0^z \frac{dy \exp[eV(y)/kT_e]}{[V(y) - V(z)]^{1/2}} \right. \end{aligned} \quad (39)$$

$$\left. - e^{-eV(z)/kT} \right].$$

In the Tonks and Langmuir treatment the left-hand side of eq (39) was neglected. From eq (33) we can see that this corresponds to the assumption of charge neutrality or that $\lambda_{De}/\Lambda \ll 1$ and results in the neglect of space charge sheaths near the walls.

Self [49] obtained numerical solutions for the complete eq (39). Once this potential has been obtained one can calculate the flux of charged particles and the effective diffusion coefficient using eqs (35) and (37). The results of this calculation for ions of one atomic mass unit are shown in figure 8. The solid triangles show the results obtained by Self for parallel-plane geometry. The inverted triangles show the results we obtained by extrapolating calculations by Ingold [36] for parallel plane geometry to small values of the Λ/λ_+ using the relations of section 3.3.5. The open circles show results obtained by Forrest and Franklin [56] for cylindrical geometry. These authors agree with the extrapolated results from Ingold when corrected for geometry at high Λ/λ_{De} . Possibly their smaller values of D_{se}/D_e at low values of Λ/λ_{De} are the result of a different numerical factor relating the density to the collisionless flow of charge to the wall. Note that the effective diffusion coefficients at large values of Λ/λ_{De} are independent of mass, while at very low Λ/λ_{De} (free fall) the values of D_{se}/D_e vary as the square root of the mass. Again the solid curve is an empirical fit to the detailed theory for parallel-plane geometry which will be discussed in section 3.3.5. The dashed curve is calculated using the empirical formula for cylindrical geometry. A simplified model for these conditions, but without explicit consideration of the sheath, has been

developed for cylindrical and rectangular geometries by Kino and Shaw [57]. Models developed for application to argon-ion lasers will be cited in section 4.1.

3.3.4 Ambipolar Motion at Various Gas Densities: $\Lambda/\lambda_{De} > > 1$ and $0 < \Lambda/\lambda_+ < \infty$ Self and Ewald [58] have combined eqs (35) through (37) with eq (33) to obtain the results shown in figure 9 by the open circles and squares for cylindrical and planar geometry, respectively. The solid circles are results obtained by Ingold [36] for planar geometry. The solid curve is calculated using the empirical formula discussed in section 3.3.5. The results shown in figure 9 correspond to the right-hand side of the square in figure 5. In figure 9 we see that the use of $\Lambda^2/\xi\lambda_+$ instead of Λ/λ_+ allows one to compress the calculations for cylindrical and parallel plane geometry into a single curve.

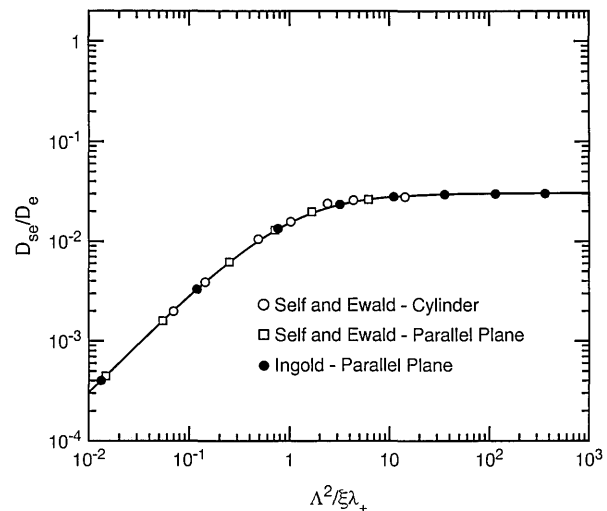


Figure 9. Normalized diffusion coefficients vs $\Lambda^2/\xi\lambda_+$ for $\lambda_{De}/\Lambda \ll 1$.

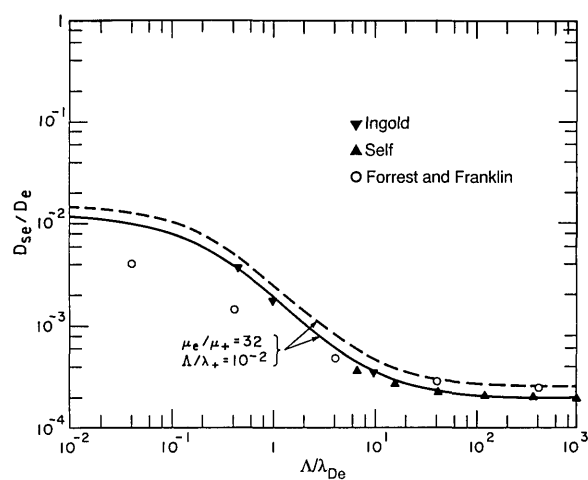


Figure 8. Normalized diffusion coefficients vs Λ/λ_{De} for $\lambda_+/\Lambda >> 1$ and ions of 1 amu.

3.3.5 General Solution: $0 < \Lambda/\lambda_{De} < \infty$ and $0 < \Lambda/\lambda_+ < \infty$ General results appropriate to essentially all of the area of figure 5 have been obtained by Forrest and Franklin [56] and by Ingold [36] for the case of $T_e >> T_+$, i.e., for the "active" discharge of Allis and Rose [28]. Some of Ingold's results are shown by the solid points in figure 10. Here again we have used $\Lambda^2/\xi\lambda_+$ instead of Λ/λ_+ in order to combine results for cylindrical and parallel plane geometry. The curve shown for $\Lambda/\lambda_{De}=0$ and the curves and points shown for $\Lambda/\lambda_{De}=\infty$ are the same as those in figures 2 and 9, respectively. The curves shown for intermediate values of Λ/λ_{De} are empirical fits obtained by

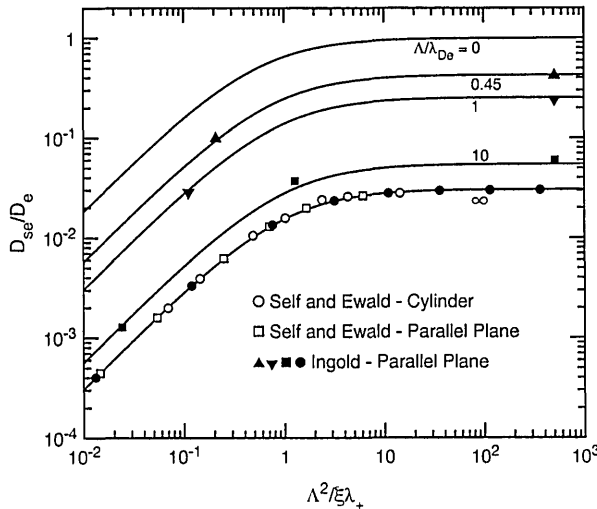


Figure 10. Normalized diffusion coefficients vs $\Lambda^2/\xi\lambda_+$ for various Λ/λ_{De} .

Muller and Phelps [59] by sliding the solid curves for $\Lambda/\lambda_{De}=0$ downward and slightly to the right, so as to pass through the calculated points from Ingold. In other words, we have assumed that the theory derived for the motion of particles in the absence of space charged fields can be scaled to fit Ingold's results for various values of the ratio of diffusion length to screening length, including the value of infinity. Extrapolations of these curves to very low values of $\Lambda^2/\xi\lambda_+$ were used to obtain the points attributed to Ingold in figure 8.

Ingold's results [36] were obtained using eq (36) and (37) for the flux of charged particles. He used boundary conditions equivalent to those of section 2.2 for a completely absorbing boundary. In figure 11 we have combined figures 7 and 8 to show the comparison of various calculations as the ratio Λ/λ_{De} is varied. Figures 10 and 11 also show a comparison of the various theoretical calculations of the effective diffusion coefficients with the smooth curves generated by the empirical formula of Muller and Phelps [59]. These formulas have been simplified by Chantry [24] with negligible changes in magnitude. The resulting relation for D_{se}/D_e is

$$\frac{D_{se}}{D_e} = \left(1 + \frac{\xi \ell_s}{\Lambda^2}\right)^{-1} \times \frac{(20 + 10(\Lambda/\lambda_{De}) + (\Lambda/\lambda_{De})^2)}{(20 + 12(\sigma+1)^{1/2}(\Lambda/\lambda_{De}) + (\sigma+1)(\Lambda/\lambda_{De})^2)}, \quad (40)$$

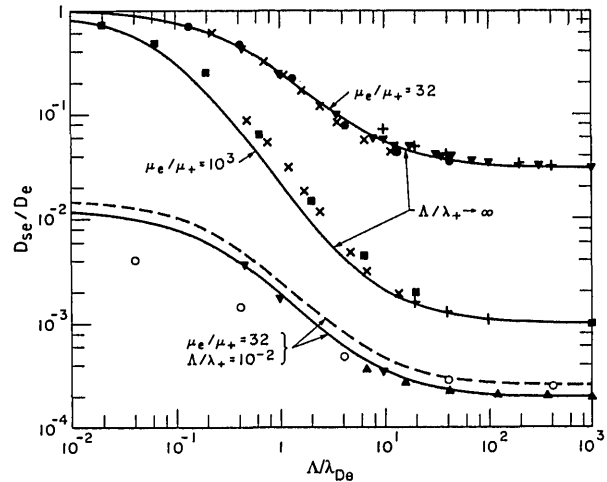


Figure 11. Normalized diffusion coefficients vs Λ/λ_{De} for various Λ/λ_+ and $\mu_e/\mu_+ = \sigma$. The symbols are the same as in figures 7 and 8.

where the effective linear extrapolation length ℓ_s defined by Chantry [24] is given by

$$\frac{\ell_s}{\lambda_+} = \sigma \left(\frac{\pi m_e}{6 m_+} \right)^{1/2} \frac{\left(1 + 3.3(\Lambda/\lambda_{De}) \right)}{\left(1 + 2.34(\sigma+1) \left[\frac{m_e}{m_+} \right]^{1/2} \left[\frac{\Lambda}{\lambda_{De}} \right] \right)}, \quad (41)$$

$\sigma = \mu_e/\mu_+$ and the boundaries are assumed to be completely absorbing. The quantity ξ was discussed in section 2.2. Note that eqs (40) and (41) correct some typographical errors in the original paper [24,60].

In the limit of large electron and ion densities or $\Lambda/\lambda_{De} > 1$, eqs (40) and (41) reduce to

$$\frac{D_{se}}{D_e} = \left(1 + \frac{(\pi/3)^{1/2} \xi \lambda_+ \sigma}{\Lambda^2 (1+\sigma)} \right)^{-1} \frac{1}{(1+\sigma)}. \quad (42)$$

Alternate empirical expressions derived from the results of Self and Ewald [58] discussed in section 3.3.4 have been given by Ferreira and Ricard [61].

Chantry [60] has suggested that eqs (40) and (41) can be used when T_e is comparable with T_+ , e.g., in thermal equilibrium where $T_e = T_+$, by replacing the $(1+\sigma)$ factor in these equations by D_e/D_a , where D_a is given by eq (29).

3.3.6 The Diffusion of Positive Ions Thus far we have discussed the results in terms of the effective diffusion coefficient for electrons. Since the production rates for electrons and ions by electron impact ionization are equal and the steady-state densities of electrons and ions are unequal, the

effective diffusion coefficients for positive ions and electrons must differ. Relatively little effort has been devoted to evaluation of the effective diffusion coefficient for positive ions in a steady-state discharge.

The results of Allis and Rose [28] can be used to calculate the effective diffusion coefficient for positive ions at high gas densities. These results are shown by the solid circles in figure 12 where D_{s+}/D_+ is plotted as a function of Λ/λ_{D+} for $\Lambda^2/\xi\ell_+ \gg 1$, where Λ_{D+} is the screening length for positive ions defined by eq (24) with $q=+$. Values of D_{se}/D_+ versus Λ/λ_{D+} are shown by the dashed curve for comparison. This plot is for $\sigma=32$ and $(D_e/\mu_e)/(D_+/\mu_+) = 100$, as one might expect in an active discharge in H₂. For values of Λ/λ_{D+} less than about 100 there are significant differences in the effective diffusion coefficients for positive ions and for electrons, but at higher Λ/λ_{D+} the positive ions and electrons diffuse together as in the ambipolar limit. The author has extended the results of Allis and Rose to low Λ/λ_{D+} by assuming that the electron density is small enough so that the electric field is determined only by the ions and that the ion production varies as the electron density, i.e., as $\cos(z/\Lambda)$. Thus, self-repulsion dominates the ion motion for $1 < \Lambda/\lambda_{D+} < 10$. The solid diamonds show numerical results. Numerical and analytical results show that for $2 < \Lambda/\lambda_{D+} < 10$, D_{s+}/D_+ varies as $(\Lambda/\lambda_{D+})^2$. For $\Lambda/\lambda_{D+} < 1$, D_{s+}/D_+ approaches 1 as expected for no space charge effects. The solid curve shows an empirical fit to the data for all Λ/λ_+ . Dote and Shimada [62] have

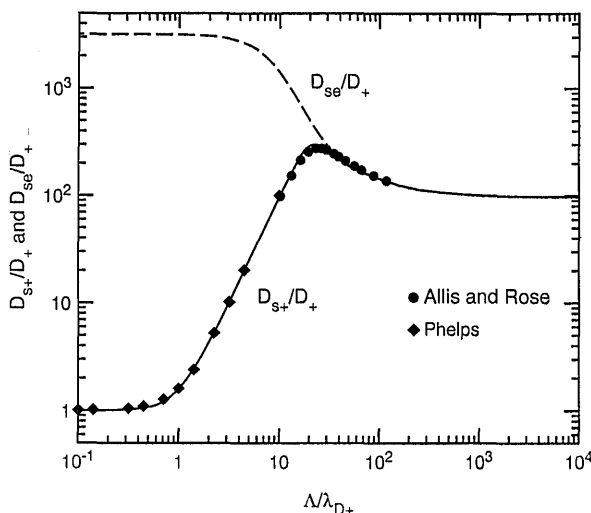


Figure 12. Normalized positive ion diffusion coefficients D_{s+}/D_+ vs Λ/λ_{D+} for $\Lambda/\lambda_+ \rightarrow \infty$.

investigated theoretically the diffusion of positive ions in an active discharge, but do not find the maximum in the D_{s+}/D_+ values found by Allis and Rose [28]. In the afterglow, where $T_e = T_+$, Gerber, Gusanow, and Gerardo [63] find a maximum in D_{s+}/D_+ similar to that of figure 12. See section 3.5.2.

3.3.7 Summary of Transitional Ambipolar Diffusion In sections 3.3.1–3.3.6 we have reviewed the available theoretical models describing the loss of charged particles to the wall of the discharge vessel when only electrons and one type of positive ion are present in the gas. The theory for the loss of electrons covers the complete range of ratios of the diffusion length to the screening length and of the diffusion length to the positive ion mean-free path. A relatively simple empirical expression enables one to relate all of the various theoretical results for the diffusion of electrons. The theoretical effective diffusion coefficient for the loss of positive ions to the walls has been extended from that for the ambipolar limit to include all values of Λ/λ_{D+} for $\Lambda/\lambda_+ > > 1$, but theory is not available for $\Lambda/\lambda_{D+} \approx 1$ and $\lambda_+/\Lambda \approx 1$.

3.4 Electrons and Several Types of Ions

In this section we review work on the simultaneous diffusion of electrons and several types of positive ions and/or negative ions.

3.4.1 Electrons, Positive Ions, and Negative Ions: $\Lambda/\lambda_{De} > > 1$ and $\Lambda/\lambda_+ (\Lambda/\lambda_-) > > 1$ This review of the simultaneous diffusion of electrons, positive ions, and negative ions is largely based on the early treatment of the subject by Oskam [1]. For recent general discussions see Rogoff [64] and Tsendin [65]. The equations appropriate to the simultaneous diffusion of electrons and one type each of positive and negative ions in the limit of $\Lambda/\lambda_{De} > > 1$ and $\Lambda/\lambda_+ > > 1$ are eqs (25) and (26) for electrons and positive ions and

$$\Gamma_-(z) = -D_- \nabla n_- - \mu_- n_- E_s \quad (43)$$

for negative ions. Here Γ_- and n_- are the flux and density of negative ions, while D_- and μ_- are the diffusion and mobility coefficients for the negative ions. As expected, eq (43) for the negative ion current is very similar to eq (25) for the electrons. In the steady state one requires that $\Gamma_e + \Gamma_- = \Gamma_+$, so that there will be no accumulation of charge within the discharge. This condition allows one to calculate the space-charge electric field from eqs (25), (26), and (43) as

$$E_s = - \frac{\left(D_e \nabla n_e + D_- \nabla n_- - D_+ \nabla n_+ \right)}{\left(\mu_e n_e + \mu_- n_- + \mu_+ n_+ \right)}. \quad (44)$$

This rather complicated expression simplifies when we take into account the condition that $\Lambda/\lambda_{De} >> 1$ so that there is charge neutrality, i.e., the sum of the electron and negative ion densities equals the positive ion density. Further simplifications result if we follow Seeliger [66] and Oskam [1] and assume that the spatial distributions of electrons and all ions are the same, i.e., that

$$\frac{\nabla n_e}{n_e} = \frac{\nabla n_-}{n_-} = \frac{\nabla n_+}{n_+} = \frac{\nabla n}{n}, \quad (45)$$

and that $n_-/n_e = \alpha$. When the congruence assumption represented by eq (45) is valid, the electric field is then given by

$$E_s = - \frac{\left(D_e + \alpha D_- - (1+\alpha) D_+ \right)}{\left(\mu_e + \alpha \mu_- + (1+\alpha) \mu_+ \right)} \frac{\nabla n}{n}. \quad (46)$$

Since the diffusion coefficient and mobility coefficient for electrons are much larger than the corresponding coefficients for negative ions and positive ions, this expression becomes rather simple when $\alpha \mu_-$ and $\alpha \mu_+ << \mu_e$, i.e., when the value of α is less than about 10. In this case the space charge electric field is determined by the electrons just as in the absence of negative ions, i.e., as in the second form of eq (27). The ambipolar diffusion coefficients for this situation are given by

$$D_{ae} = (1+\alpha) D_+ \left(1 + \frac{T_e}{T} \right) + \alpha D_- \left(\frac{T_e}{T} - 1 \right), \\ \rightarrow \left((1+\alpha) \mu_+ + \alpha \mu_- \right) \frac{D_e}{\mu_e}, \quad (47)$$

$$D_{a-} = \left[2(1+\alpha) \frac{D_+}{D_e} - \frac{T_e}{T_-} + 1 \right] D_- \\ \rightarrow - \frac{D_e}{\mu_e} \mu_-, \quad (48)$$

and

$$D_{a+} = \left(1 + \frac{T_e}{T_+} \right) D_+ \rightarrow \frac{D_e}{\mu_e} \mu_+. \quad (49)$$

Here we have used the relationship $kT/e = D/\mu_i$ to simplify the equations. The second forms of the equations are the limiting forms for $T_e >> T_-$ and T_+ . Of particular interest is the negative value for D_{a-} , which means that the negative ions flow toward the center of the discharge. This phenomenon leads to a breakdown of the assumption of congruent spatial distributions of the ions and electrons and eventually to a contraction of the discharge [66–72]. The consequences of this flow are discussed below. When $T_e = T_- = T_+$, then $D_{ae} = (1+\alpha) 2D_+$, $D_{a-} = (1+\alpha) 2D_+ D_- / D_e$, and $D_{a+} = 2D_+$. These results would be appropriate to an afterglow where the electrons have cooled to the gas temperature. See section 3.5.1.

The equations of continuity for the electrons, negative ions, and positive ions are

$$\frac{\partial n_e}{\partial t} = -\nabla \cdot \Gamma_e + k_i n n_e - k_a n n_e + k_d n n_-, \quad (50)$$

$$\frac{\partial n_-}{\partial t} = -\nabla \cdot \Gamma_- + k_a n n_e - k_d n n_-, \quad (51)$$

and

$$\frac{\partial n_+}{\partial t} = -\nabla \cdot \Gamma_+ + k_i n n_e. \quad (52)$$

Here k_a is the electron attachment rate coefficient, k_d is the collisional detachment rate coefficient for the negative ions, and k_i is the ionization rate coefficient. In eq (50) we have indicated that the electrons may be lost by flow and by electron attachment, while they are produced by electron impact ionization and by collisional detachment from the negative ion. We have neglected potentially important processes such as electron-positive ion and positive ion-negative ion recombination. In eq (51) we see that in this model the negative ions are lost by flow and by collisional detachment, and are produced by electron attachment to the neutrals. Finally, eq (52) gives the positive ion loss by flow and production by electron impact ionization. We are particularly interested in the steady state equation for the negative ions.

If we solve eqs (50)–(52) for the steady-state ratio of the negative ion density to the electron density α , we obtain

$$\alpha = \frac{n_-}{n_e} \\ = \frac{k_a n}{\left(k_d n + D_{a-}/\Lambda^2 \right)} \rightarrow \frac{k_a n}{\left(k_d n - (D_e/\mu_e)(\mu_-/\Lambda^2) \right)}. \quad (53)$$

The second form of eq (53) applies when $T_e/T_i \gg 1$ and shows that when the diffusion contribution is less than collisional detachment, the value of α is positive as required for a meaningful solution [65]. In this case one pictures the negative ions as diffusing toward the center of the discharge tube where they undergo collisional detachment. The negative charge then diffuses toward the wall of the discharge tube in the form of electrons. In a real plasma one has to be concerned that the assumption of the same spatial distribution for all ions may not be valid [65,73].

The consequences of various limiting values of α are discussed further by Oskam [1] and Rogoff [64]. The case of very large α leads to almost free diffusion of the electrons in the presence of large densities of positive and negative ions. This case will be discussed further in connection with afterglow models and experiment in section 3.5.1.

The effects of the change in steady-state, space charge fields produced by negative ions have been considered for flowing afterglows [74] and high pressure mass spectrometers [75].

3.4.2 Electrons and Several Types of Positive Ions We now consider the situation with several types of positive ions and no negative ions [1,64,76-78]. The particle flux equations for electrons and two types of positive ions, labeled 1 and 2, are

$$\Gamma_e(z) = -D_e \nabla n_e - \mu_e n_e E_s, \quad (25)$$

$$\Gamma_1(z) = -D_1 \nabla n_1 + \mu_1 n_1 E_s, \quad (54a)$$

and

$$\Gamma_2(z) = -D_2 \nabla n_2 + \mu_2 n_2 E_s. \quad (54b)$$

Here the Γ_j and n_j are the fluxes and densities of ions 1 and 2 and the D_j and μ_j are the diffusion coefficients and mobilities for these ions. In the steady-state $\Gamma_e = \Gamma_1 + \Gamma_2$ so that

$$E_s = -\frac{(D_e \nabla n_e - D_1 \nabla n_1 - D_2 \nabla n_2)}{(\mu_e n_e + \mu_- n_- + \mu_+ n_+)} \rightarrow -\frac{D_e \nabla n}{\mu_e n}. \quad (55)$$

This equation is very similar to eq (44). If one makes the assumptions that the ratio of $\nabla n/n$ is the same for each ion and for the electrons, as in eq (45), and that the plasma is quasineutral, $n_1 + n_2 - n_e \ll n_e$, one obtains the familiar expression for the electric field given in the second form

of eq (55). Substitution of this expression into eqs (25), (54a), and (54b) yields expressions for the ambipolar diffusion coefficients for each of the ions and for the electrons. These relationships were used by Phelps [77] to analyze the observed decay of helium ions and of electrons in the afterglow of a helium discharge. Note that the assumption of congruence, i.e., the equality of the $\nabla n/n$ values for the electrons and both types of ions, is not generally applicable [1,78]. It should apply when nonlinear loss and production processes, such as electron-positive ion and positive ion-negative ion recombination, are negligible and the ions are distributed in the fundamental diffusion mode [1,77]. In the case of positive ions only, we do not have the tendency for diffusion to destroy congruency as we did in the negative ion case of section 3.4.1.

3.5 Ambipolar Diffusion in Afterglow

Many experimental measurements and theoretical analyses have been applied to the diffusion of charged particles in the afterglow of a discharge. See Oskam [1] for an extensive review of the subject. Here we will be concerned with the afterglows which are dominated by diffusion. Reactions which are nonlinear in the charged particle densities, such as recombination, are neglected. The diffusion models discussed previously for steady-state electrical discharges are applicable to many afterglow experiments. We will also be concerned with departures from the description which have been given in previous sections, i.e., with phenomena such as diffusion cooling.

3.5.1 Isothermal Plasmas In this section we assume that the electron temperature is equal to the positive ion temperature and that both of these temperatures are equal to the gas temperature, i.e., $T_e = T_+ = T_g$. We also assume that $\lambda_{De}/\Lambda \ll 1$ and $\lambda_+/ \Lambda \ll 1$. For these conditions we obtain the by now familiar expression for electron particle flux in terms of the ambipolar diffusion coefficient given by eq (29). When this equation is substituted into the time-dependent electron continuity equation, we obtain

$$\frac{\partial n_e}{\partial t} = D_a \nabla^2 n_e, \quad (56)$$

where D_a is given by eq (29). We consider the solution to eq (56) for sufficiently long times such that higher order diffusion modes have disappeared. The conditions necessary for the neglect of higher order diffusion modes are discussed in detail by

McDaniel [5]. The result for the lowest diffusion mode is

$$n_e(t) = n_e(0) e^{-t/\gamma}, \quad (57)$$

where

$$\frac{1}{\gamma} = \frac{D_a}{\Lambda^2} = \frac{2D_+}{\Lambda^2} = \frac{2kT_+}{e\Lambda^2} \mu_+. \quad (58)$$

The final form of eq (58) is often used to obtain the ion mobility from measurements of the decay constant for the electron and ion densities [1,5,79]. Because of various ion conversion processes [1,77], not included in eqs (56)–(58), it is generally necessary to plot the experimental values of n/γ as a function of n and extrapolate to $n=0$. Many authors have used this technique to determine ion mobility and under proper circumstances it can yield reliable information. However, under many circumstances it has not yielded ion mobilities that agree with those measured with drift tube techniques [6,79]. We therefore need to consider sources of error in the interpretation of afterglow experiments [80]. First, we will consider the departures from ambipolar diffusion and the solutions given by eqs (57) and (58) which occur when λ_{De} becomes comparable with Λ . Second, we will discuss the phenomenon of diffusion cooling.

3.5.2 Departures from the Ambipolar Limit
 Measurements and models of the decay of electron density and ion wall current in the afterglow of pulsed discharges in helium give very direct evidence of the transition from ambipolar to free diffusion [41,63,81–84]. Figure 13 shows schematically the results of numerical solutions by Gusanow and Gerber [82] of eqs (25), (26), (32), and (33) and of eqs (1) with $k_i=0$ for the time-dependence of electron and ion densities in a helium afterglow. At early times the electron and ion densities are equal and decay with a reciprocal time constant of $D_a/\Lambda^2=2D_+/\Lambda^2$. When the charge density decreases such that when $\Lambda/\lambda_{De}\approx 10$ there is a more rapid decay of the electron and ion densities. At still lower values of Λ/λ_{De} the electron and ion densities no longer decay together. The electron decay continues to become more rapid until it approaches the free diffusion rate. The positive ions, on the other hand, soon reach a maximum decay rate corresponding to the peak in figure 12. Their decay rate then decreases to a value characteristic of the free diffusion of the positive ions, i.e., $1/\tau=D_+/\Lambda^2$. During this transition the ambipolar field decreases to zero. This transition has also been analyzed [85]

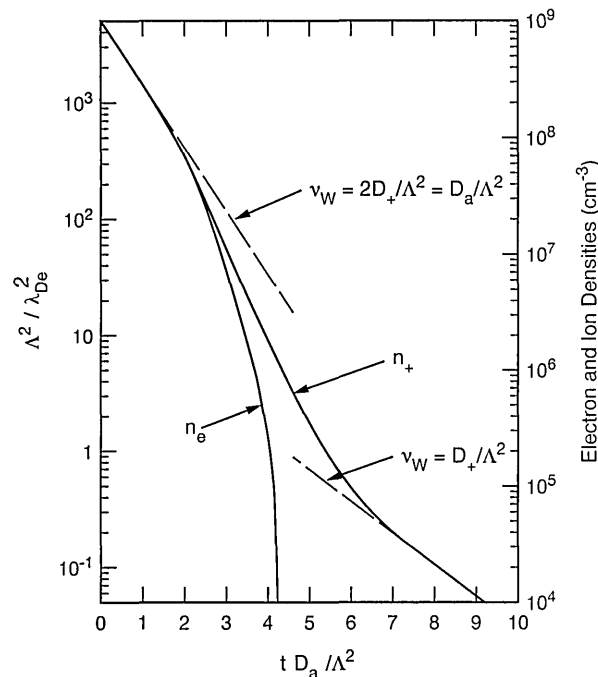


Figure 13. Schematic of afterglow transients showing transitional ambipolar diffusion.

for infinite spherical geometry using the constant ion density ratio approximation discussed in section 3.3.5.

In the case of afterglows in which negative ions are present the electrons disappear rapidly when $\Lambda/\lambda_{De}\approx 1$ and one is left with a plasma composed of negative and positive ions. According to eq (46) there is very little space charge electric field. A number of investigators have shown experimentally [86–88] and theoretically [41] that since the electric field is no longer sufficient to stop the negative ion flow, the negative ion wall current suddenly increases at this time. Qualitatively similar results have been obtained [89] using the constant ratio ion density approximation.

An interesting feature of these theories and experiment is the apparent applicability of the steady-state results to experimental afterglows [81]. This effect is presumably the result of the ability of the highly mobile electrons to readjust their density rapidly on the time scale of interest.

3.5.3 Diffusion Cooling A second phenomenon, which can cause significant errors in the simple model of the diffusion of ions in an afterglow, is that of diffusion cooling. This effect was discovered by Biondi [90] in neon afterglows where he observed that the apparent diffusion coefficient for the electrons and ions dropped by almost a factor of two at low gas densities. This effect is

particularly pronounced in neon because the relatively small ratio of electron to atom mass and low momentum transfer cross section for electrons in neon result in poor energy exchange between electrons and gas atoms. Biondi showed that the addition of small amounts of helium restored the thermal contact between electrons and the gas and led to higher values for the effective diffusion coefficient.

Figure 14(a) shows in a schematic fashion the potential well and electron distribution functions appropriate to the diffusion cooling problem. The potential well has the typical parabolic shape at the center and reaches the finite value at the walls of the container. Electrons with energies larger than that indicated by the horizontal dashed line can escape from the well to the walls. If the frequency of energy relaxation collisions is sufficiently rapid, only those electrons that are very close to the wall will be able to cross the potential barrier and the space charge field in most of the plasma will be unperturbed from the ambipolar value. As the energy relaxation frequency is reduced by decreasing the elastic collision frequency or by increasing the mass of the atom, electrons from near the center of the container can reach the wall without undergoing energy relaxation. The effect of this process is to deplete the high energy tail of the distribution as indicated by the unperturbed energy distribution $F_0(\epsilon)$ shown by the solid curve and the cooled distribution $F_C(\epsilon)$ shown by the dashed curve. The loss of high energy electrons reduces D_e/μ_e , i.e., reduces the effective temperature of the electrons, and reduces the space charge electric field and the loss of ions by ambipolar diffusion. In the limit of $D_e/\mu_e \rightarrow 0$, the ambipolar field goes to zero and the ions diffuse freely. Detailed theoretical treatments of diffusion cooling are now available [91–94].

Figure 14(b) shows the schematic of the values of $N\Lambda^2/\tau$ as a function of gas density under conditions in which diffusion cooling is important. The points and line through them indicate qualitatively the kind of experimental diffusion coefficient results obtained [88,90]. Diffusion cooling has also been observed via measurements of the decrease in radiation temperature of the electrons [95,96]. Unfortunately, the density dependence of the apparent ambipolar diffusion coefficient caused by diffusion cooling is qualitatively similar to that which would be expected if the ions were being converted from an ionic species with a low diffusion coefficient to a species with a high diffusion coefficient [77]. This possibility illustrates the need for mass spectrometric identification of the ions in such experiments.

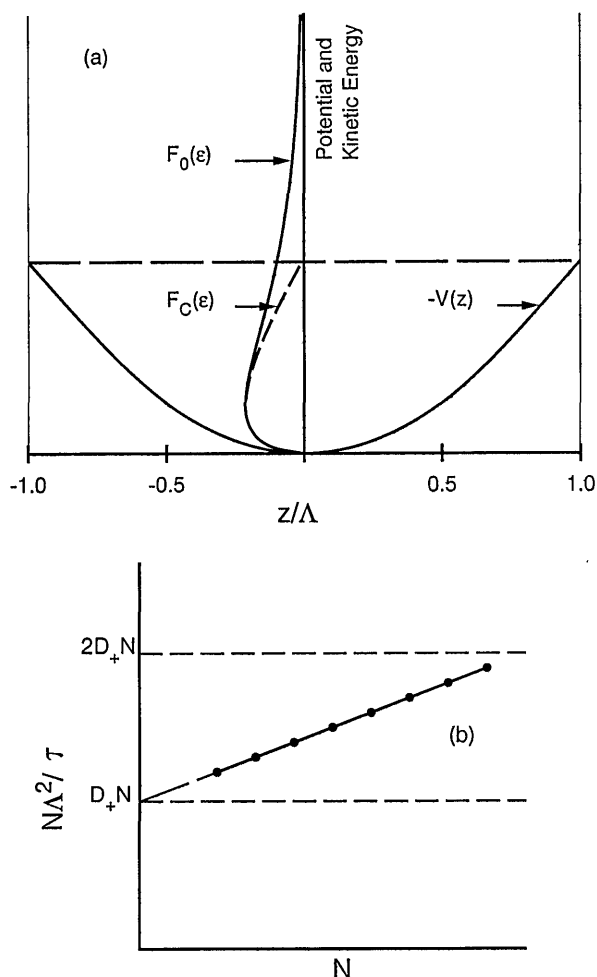


Figure 14. Schematic of electron energy distributions and data in diffusion cooling experiment.

We note that the phenomenon of electron motion from one portion of the plasma to another in times which are fast compared to energy relaxation times, which is responsible for diffusion cooling, is also responsible for excess ionization in the center of the discharge in the steady-state “active” discharge to be discussed in section 4.1.2.

4. Applications of Models of Ambipolar Diffusion

We now turn to applications of the models of ambipolar diffusion discussed in sections 2 and 3 to the interpretations of several gas discharge systems. Firstly, we consider the maintenance of steady-state dc and microwave discharges at low, moderate, and high pressures. Secondly, we summarize the effects of magnetic fields on the diffusive loss of charged particles from discharges. We

then briefly discuss the role of diffusion in transient discharges at high pressures.

4.1 Steady-State Discharge Maintenance

In this section we apply the models developed in sections 2 and 3 to the prediction of the applied electric fields, gas densities, etc. required to maintain a low power, low pressure electrical discharge in which the ionization is by single-step electron impact excitation of ground state atoms or molecules. In most models of steady-state discharges the ambipolar electric fields E_s are perpendicular to the applied electric field E_a and the effects of the ambipolar fields on the electron energy distribution function, the excitation and ionization rate coefficients, and transport in the direction of the applied field are neglected. In section 4.1.2 we will, however, summarize work on the effects of ambipolar electric fields on the electron energy distribution functions and the resultant changes in applied fields necessary to maintain the discharge.

4.1.1 Discharge Maintenance at Moderate Gas Densities: ($\Lambda/\lambda_+ > 1$, $\Lambda/\lambda_u > 1$, and $0 < \Lambda/\lambda_{De} < \infty$) We now consider the application of the theory developed for the effective diffusion coefficient for electrons to the calculations of the properties of an electric discharge. Equation (34) shows the balance between the production of electrons by electron impact ionization at the axis of the discharge and the loss of electrons by diffusion. This equation can be written as

$$n^2 \Lambda^2 = \frac{D_{se}}{D_e} \frac{(D_e n)}{k_i}. \quad (59)$$

Rose and Brown [97] have applied eq (59) and the theory developed in section 3.3.5 to an analysis of steady-state microwave discharges in H_2 and find generally good agreement between theory and experiment. Poor agreement with the simple theory represented by eq (59) is found for Ar at microwave frequencies and at dc, presumably because cumulative or multistep ionization processes are important for the rare gases [98]. Muller and Phelps [59] have applied the results discussed in section 3.3.5 for D_{se}/D_e to an analysis of low current discharges in H_2 -He mixtures and find good agreement with experiment at their higher gas densities. Hydrogen and H_2 -He gas mixtures are suitable for these comparisons because of the short lifetime of metastable H_2 states [99] and rapid

quenching of the He metastables through Penning ionization of the H_2 [4].

In the analysis of the H_2 -He positive column discharge, eq (59) has been used to calculate the product $n\Lambda$ using theoretical values of the ratio D_{se}/D_e and of nD_e/k_i . The D_{se}/D_e values are given by the empirical expressions in eqs (40) and (41) involving the ratios λ_{De}/Λ , λ_+/Λ , and ξ/Λ . The ratios λ_{De}/Λ and λ_+/Λ are calculated using the equations

$$\frac{\lambda_{De}^2}{\Lambda^2} = \frac{eD_e/\mu_e}{8\pi Ry a_0} \frac{ecA W_e}{I \Lambda^2}, \quad (60)$$

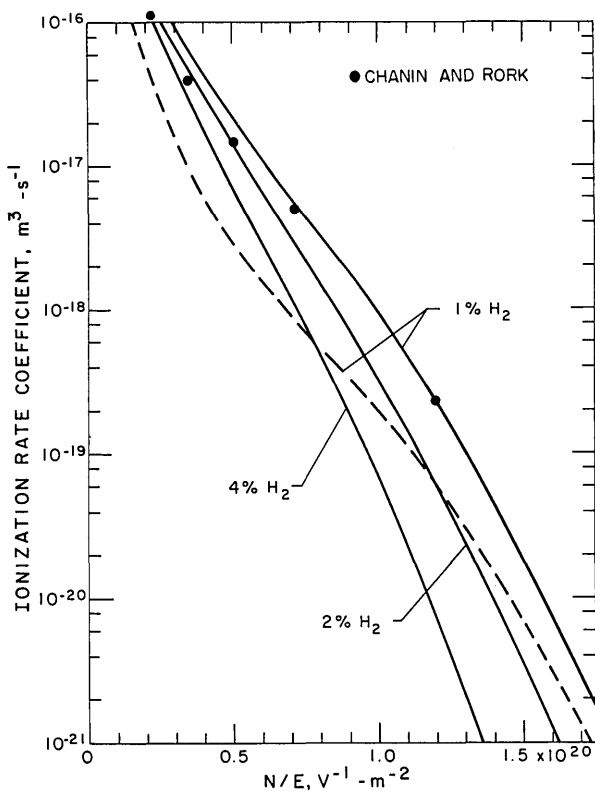
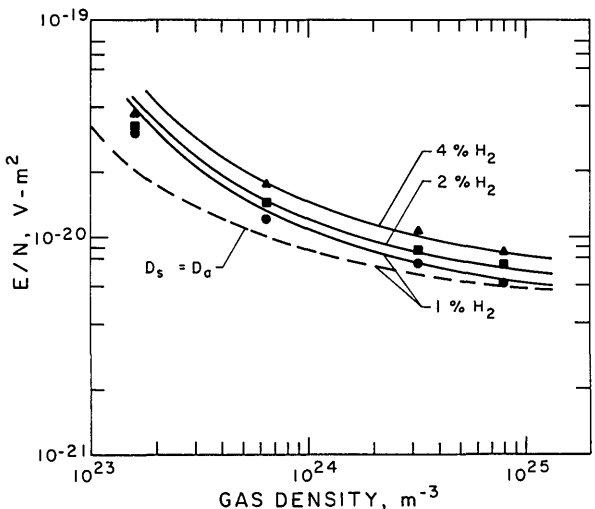
and

$$\frac{\lambda_+^2}{\Lambda^2} = \left(\frac{m_+ \mu_+ n}{e} \right)^2 \frac{3 e D_e}{m_+ \mu_e n^2 \Lambda^2}, \quad (61)$$

where c is the ratio of the mean electron density to its peak value and A is the area of the discharge. Equation (60) is a reformulation of eq (24). Note that the second factor in eq (60) is the electron density on the axis of the discharge. For a long cylindrical discharge the radius cancels out of eq (60) and the ratio Λ^2/λ_{De}^2 is proportional to I . Keeping in mind that nD_e , D_e/μ_e , and k_i are functions of E_a/n , one sees that eqs (59)–(61) also show the applicability of the experimental scaling parameters [4] $n\Lambda$, J/n^2 , and E_a/n , where $J=I/A$ is the current density at the axis of the discharge. The definition of the mean-free path of the positive ions in eq (61) is that given by Ingold [36] and involves the ion mass M_+ , the ion mobility μ_+ , and the D_e/μ_e value for electrons. The first factor on the right hand side of eq (61) is the square of the mean-free-time for ion-neutral collisions per atom evaluated from the ion mobility. The ion speed is evaluated at the effective temperature D_e/μ_e for the electrons and is determined from theory or experiment by the E_a/n value for the given gas or gas mixture.

Figure 15 shows the results of calculations of the ionization rate coefficient k_i as a function of E_a/n for the mixture of helium and hydrogen that was used in the experiments. These curves were calculated using electron collision cross section sets for helium and hydrogen and taking into account the Penning ionization of the hydrogen. The characteristic electron energy D_e/μ_e is a relatively slowly varying function of E_a/n and is not shown.

Figure 16 shows the results of this analysis. In this figure the E_a/n values are plotted as a function of n for several different fractional concentrations of hydrogen in helium. The points are the experi-

Figure 15. Ionization coefficients for H₂-He mixtures.Figure 16. Maintenance E/n for H₂-He mixtures showing comparison of experiment with predictions of transitional ambipolar diffusion theory.

mental data and the smooth curves are the results of calculations. The dashed curve shows values of E_a/n predicted when the diffusion loss is assumed to be given by the ambipolar limit. The solid curves show the results when departures from ambipolar diffusion are taken into account. The solid

curves show good agreement with experiment at the higher values of $n\Lambda$. At the lower values of $n\Lambda$ there is small but systematic disagreement between theory and experiment. The sign of this disagreement suggests that the theory has omitted a source of ionization. Muller and Phelps [59] propose that the source of ionization is the motion of the electrons from the outer portion of the discharge toward the axis in the space charge potential as discussed in section 4.1.2.

Many other comparisons have been made between positive column models and experiment. In most of them the model is very complicated because of the important ionization resulting from electron-metastable and metastable-metastable collisions [62,100-102]. Here we have cited only some of the more recent papers.

4.1.2 Radial Nonequilibrium at Low Gas Densities: ($\Lambda/\Lambda_+ > > 1$, $\Lambda/\Lambda_u \ll 1$, and $0 < \Lambda/\lambda_{De} < \infty$) In this section we are concerned with the changes in the ionization rate coefficient k_i resulting from the motion of the electrons in the potential well created by the space charge electric field as compared to the ionization coefficient in the absence of such a field. This problem has been addressed for microwave discharges by Bernstein and Holstein [103] and for dc discharges by Blank [104], Herrmann, Rutscher, and Pfau [105], and by Tsendar [106,107]. Radial energy nonequilibrium effects are very important in the low-pressure discharges used for rare gas, ion lasers [108-111].

The origin of the excess ionization is illustrated by considering electrons at large radii of the discharge which are accelerated in the axial direction to kinetic energies just below the ionization potential and then move radially inward at constant total energy to reach kinetic energies above the ionization potential. These electrons are less likely to suffer inelastic collisions than those accelerated to the same final kinetic energy in a spatially uniform electric field. After producing ionization these electrons may move radially outward at low kinetic energies where, at least in the rare gases, energy losses in inelastic collisions are small. In some models [112] the spatial change in the electron energy distribution function is approximated by a radially varying electron temperature. This process is one of "diffusion heating" and, in a sense, is the inverse of the diffusion cooling discussed in section 3.5.3.

Thus far, there appear to be no simple expressions that allow estimates of the magnitude of the increase in ionization resulting from this nonequilibrium effect.

The nonequilibrium effects caused by radial ambipolar fields discussed in this section and in section 3.5.3 do not require the introduction of a third dimension for the map of figure 5. The importance of nonequilibrium is determined by the ratio Λ/λ_u , where λ_u is an energy relaxation distance for electrons. We define λ_u in terms of the energy exchange collision frequency ν_u/n used in some analyses of electron transport data [113]. Thus, for $D_e/\mu_e > kT_g$,

$$\lambda_u = \frac{1}{\nu_u} \left(\frac{2eD_e}{m_e \mu_e} \right)^{\frac{1}{2}} = \frac{n}{W_e E} \left(\frac{2 \mu_e}{e m D_e} \right)^{\frac{1}{2}}, \quad (62)$$

where W_e is the electron drift velocity at the discharge E_a/n . Note that this relaxation distance is a property of the whole of the electron energy distribution and so may be only a rough measure of energy relaxation for the high energy tail of the electron energy distribution which is of importance in the nonequilibrium ionization. Since the ratio λ_u/λ_+ is a constant for a given gas and E_a/n , the overall scaling discussed in section 3.3.1 should be preserved.

Measurements of radial ambipolar electric fields E_s in active discharges have been made by Baghuis et al. [114] and by Ganguly and Garscadden [115]. In the first case the data were obtained at rather high pressures and currents, i.e., $\Lambda/\lambda_+ > 1$, $\Lambda/\lambda_u > 1$, and $\Lambda/\lambda_{De} > 1$, and the agreement with predictions [101] is good. In the latter case no comparison with discharge models was made.

Note that ion energy relaxation effects have already been included in the models of section 3.

4.1.3 Diffusive Nonequilibrium in High Pressure Arcs The phenomenon of diffusive nonequilibrium in high pressure arcs leads to effects such as diffusive separation or demixing of components of the gas [116,117]. Ambipolar diffusion also plays an important role in departures from local thermodynamic equilibrium by depleting the ions through transport to the wall where they recombine with electrons to produce neutrals which flow toward the center of the discharge [118–122]. Because the analysis of such effects involves the competition between diffusion, ionization, and the nonlinear loss process of electron-ion recombination, we will not consider the models used to describe these effects. Note that we have cited only some of the more recent references.

4.2 Magnetic Field Effects

The research on the effects of magnetic fields on space charge dominated plasmas is much too exten-

sive to summarize in this paper. Therefore, we limit the discussion to applied electric fields parallel to the magnetic field, as in the case of magnetic field lines parallel to the axis of the positive column of a glow discharge; to quiescent ranges of plasma parameters; to weakly ionized plasmas; to no relative motion of the magnetic field and the neutral gas; and to the ambipolar limit of $\lambda_{De}/\Lambda < 1$ [123–127]. The basic relations governing the transport of a single type of charged particles in the presence of a magnetic field are given by a number of authors [7,127] and are often expressed as modifications of the diffusion and mobility coefficients. For energy independent collision frequencies for electrons ν_{em} and ions ν_{im} with the gas, the coefficients describing electron transport parallel to the electric field and transverse to the magnetic field are:

$$\mu_{eT} = \frac{\mu_e}{1 + \omega_{Be}^2 \nu_{em}^{-2}}, \quad D_{eT} = \frac{D_e}{1 + \omega_{Be}^2 \nu_{em}^{-2}}. \quad (63)$$

In addition, the electron transport transverse to the magnetic field but perpendicular to the electric field is characterized by

$$\mu_{eP} = \frac{\mu_e \omega_{eB} \nu_{em}}{1 + \omega_{Be}^2 \nu_{em}^{-2}}, \quad (64)$$

while transport along the magnetic field is independent of B . Here $\omega_{Be} = eB/m_e$, where B is the magnetic field. Alternate derivations [124,128] of eqs (63) and (64) show that one can replace the $\omega\nu$ products by the corresponding values of $\beta_e = \mu_e B = \omega_{Be}/\nu_{em}$. The proper averaging of these expressions for gases in which the collision frequency varies with electron energy has been discussed by various authors [7,127]. In the limit of low B/n the ν 's are much larger than the ω 's and one recovers the D_e and μ_e values in the absence of a magnetic field. The corresponding equations for ions are obtained by replacing ω_{Be}/ν_{em} by $\omega_{Bi}/\nu_{im} = \mu_i B = \beta_i$, where $\omega_{Bi} = eB/M$ and M is the ion mass. The details of averaging of the mobility equations for ions have been discussed by Shunk and Walker [129].

Because of the ease with which a magnetic field prevents the transport of electrons across field lines relative to their transport along the field lines, the predictions of the models of ambipolar diffusion in the presence of a magnetic field are very dependent on the geometry [123–132]. The models usually assume spatially uniform electron and ion temperatures, a single type of positive ion, and negligible electron-ion collisions. We first consider a steady-

state plasma in which the net flow of charge to any surface element is zero, as for a container with non-conducting surfaces, and for which $\beta_e^2 >> 1$ and β_i is of the order of unity. In this case the effective ambipolar diffusion coefficient D_{ab} is given by [124,125,131,132]:

$$D_{ab} \rightarrow \frac{D_a}{1 + \mu_e \mu_i B^2}. \quad (65)$$

On the other hand, when the surfaces (or a second plasma) at the "end" of the plasma or the use of a metallic container allow efficient transport of charge across magnetic field lines, the effective diffusion coefficient is given by [123,126,130,133]

$$D_{ab} \rightarrow \frac{D_a}{1 + \mu_i^2 B^2} \text{ for } \beta_e >> 1. \quad (66)$$

Here the electrons move along the magnetic field lines until they reach the conducting end plates where they move radially. The length of the plasma in the direction of the magnetic field is assumed large enough so that ion loss in the direction of B is still small compared to that in the radial direction. The effects of sheaths at the conducting surfaces are generally neglected.

The quantitative experimental verification of eqs (65) and (66) in active discharges appears to be lacking. Not only is it difficult to satisfy the conditions of either an insulating or a highly conducting "end plate," but other assumptions of the model are often not met. For conducting end walls, Simon [123,130] found agreement with the magnetic field dependence of eq (66), but found only rough agreement of the magnitudes of the diffusion rates with his experiments and the early results of Bohm et al. [134]. Experimental results with varying degrees of insulating walls have shown significant discrepancies with theory. For example, in several experiments with positive column discharges the apparent transverse diffusion coefficient initially increases with increasing magnetic field and then begins to decrease approximately as predicted by eq (65) [112,135,136]. One reason for this effect is that at zero magnetic field and at low enough gas densities λ_{de}/Λ is large enough such that the electron energy distribution and "temperature" vary significantly with radius as discussed in section 4.1.2. When an axial magnetic field is raised such that $\beta_e \geq 1$ the effective energy relaxation length and the radial transport of electron energy are significantly decreased, the average ionization rate coefficient is reduced, and the axial E_a/n required to maintain

the discharge increases. Models of the first maximum in E_a/n have also included the effects of metastables [136]. The role of ionization waves has been debated [112,137]. A second and more dramatic increase in the apparent transverse diffusion coefficient above the values predicted by eqs (65) and (66) at β_i values greater than about unity is attributed to the onset of plasma instabilities [12,135,138,139]. The discussion of this effect is beyond the scope of this paper.

An interesting and apparently unanswered experimental question is whether the radial electric field E_s reverses sign as predicted [124] when eqs (63) and the corresponding equations for ions are substituted into eq (27) and when the magnetic field is such that $D_{er}=D_{ir}$. Similar predictions have been made for the $\lambda_+/\Lambda >> 1$ case [140]. There does not appear to be agreement as to whether conducting end walls are sufficient to short circuit the plasma [123,130] or whether a conducting outer cylinder is needed to avoid electron emission problems at the walls [141]. When electron emission is required to return electrons to the plasma, a significant "cathode fall" voltage could occur at the end plate.

The theory of section 3.3.4 has been extended to treat the diffusion of electrons and ions in a partially ionized gas subject to a magnetic field for $\lambda_{de}/\Lambda << 1$ and variable λ_+/Λ [140-143]. There appear to be no quantitative comparisons of these models with experiment [144].

Afterglow plasmas have also been used in attempts to verify the effects of a magnetic field on ambipolar diffusion [125]. Here the comparison should be simpler because of the direct measurement of the deionization rate and the possibility of thermalizing the electrons through collisions with the gas so as to achieve equal electron and ion temperatures. However, there is considerable difference among authors. Some experiments [145] show quantitative agreement with theory for magnetic fields below the onset of instabilities, while others [146-148] find varying degrees of agreement for containers with end walls of unknown effective conductivity. Theory [149] and experiments [150] show that the decay rate is highly sensitive to the alignment of the discharge tube with the magnetic field.

4.3 Transient Discharges

The onset of ambipolar diffusion plays an important role in the development of many pulsed discharges by limiting the diffusive loss of electrons

and leading to the development of a constricted, highly ionized region or channel. Here we will cite only a limited number of examples.

Ambipolar diffusion is usually included or assumed in models of the development of highly conducting channels or sparks at moderate overvoltages [16,151,152]. The reduced loss of electrons due to space charge fields allows the build up of ionization to values that result in the onset of processes such as multistep ionization, electron detachment, and thermal gas expansion.

The effects of radial electric fields caused by diffusive separation of charge appear to be small for the fast time scale and high voltages associated with the growth of the "streamer" which occurs in the later stages of electrical breakdown at high overvoltages in initially uniform and nonuniform electric fields [153].

Ambipolar diffusion has been suggested by Van Brunt and Kulkarni [154] to be important in determining the minimum time between negative corona pulses. However, details of the calculations [155] have not been reported.

One of the mechanisms leading to an increased growth of ionization in the later stages of laser breakdown is the reduction of electron loss by diffusion when the charged particle densities become large enough so that the screening length is comparable with the dimension of the region illuminated by the laser [156].

5. Discussion and Summary

We have reviewed the models that have been developed to describe measurements of the loss of electrons and ions by diffusion from weakly ionized gas discharges or plasmas to the walls of a discharge vessel. Scaling parameters for the models discussed and for a given gas are λ_+/Λ , λ_{De}/Λ , $E_a \lambda_e$, and ω_B/v_{in} when the plasma is subject to a dc applied electric field. Of course, any combination of these parameters leading to the same total number of these parameters is also acceptable. When the discharge is excited by an ac electric field the parameter ω/v_i must also be included. These model parameters translate into the experimental parameters of $n\Lambda$, J/n^2 , E_a/n , and B/n for the dc case in infinite cylindrical or parallel plane geometry, with ω/n added for the ac case. In the absence of a magnetic field and at sufficiently high rf fields the models are rather complete and have been tested against experiment. The predictions of these models have been expressed as relatively simple empiri-

cal relations covering the full range of λ_+/Λ and λ_{De}/Λ (or $n\Lambda$ and J/n^2). When a magnetic field is present models of experiment are available for all λ_+/Λ and ω_B/v_{in} ($n\Lambda$ and B/n), but only for $\lambda_{De}/\Lambda < < 1$ (or small J/n^2). With a magnetic field the experimental tests show a high sensitivity to boundary conditions and a propensity of the plasma to become unstable. Empirical relations connecting the magnetic field and other diffusion parameters have not been developed.

In many practical applications it is necessary to include nonlinear processes such as electron-excited state or electron-ion collisions in a complete plasma model. In such cases one expects degradation of the accuracy of the empirical formulas used to represent the diffusion contribution. The error in such an approximation is usually small when calculating the average rate of charge particle loss because the contribution of diffusion is decreasing as the other processes become more important. However, large errors can occur when these relations are used in the calculation of the flux of charged particles to the boundaries and when competing loss processes, such as electron-ion recombination, significantly alter the spatial distribution of the charged particles.

6. Acknowledgments

The author wishes to thank A. Gallagher, P. J. Chantry, A. Garscadden, J. Ingold, and R. J. Van Brunt for helpful discussions and references. This work was supported in part by the National Institute of Standards and Technology.

About the author: A.V. Phelps retired from the Quantum Physics Division of the NIST Center for Basic Standards in 1988. He is at the Joint Institute for Laboratory Astrophysics of the National Institute of Standards and Technology and the University of Colorado, where he has been since 1970.

7. References

- [1] Oskam, H. J., Philips Res. Repts. **13**, 335 (1958).
- [2] Cherrington, B. E., Gaseous Electronics and Gas Lasers, Pergamon, New York, (1979).
- [3] Brown, S. C., in Handbuch der Physik, Flügge, S. ed., Springer-Verlag, Berlin, (1956), Vol. 21, pp. 531-575.
- [4] Druyvesteyn, M. J., and Penning, F. M., Rev. Mod. Phys. **12**, 87 (1940); Ebert, W., *Beit. Plasmaphysik* **19**, 281 (1979).

- [5] McDaniel, E. W., *Collision Phenomena in Ionized Gases*, John Wiley and Sons, New York (1964).
- [6] Holstein, T., *Phys. Rev.* **70**, 367 (1946).
- [7] Allis, W. P., in *Handbuch der Physik*, Flügge, S., ed., Springer-Verlag, Berlin (1956), Vol. 22, pp. 383–444.
- [8] Kumar, K., Skullerud, H. R., and Robson, R. E., *Aust. J. Phys.* **33**, 343 (1980).
- [9] McDonald, A. D., *Microwave Breakdown in Gases*, John Wiley and Sons, New York (1966).
- [10] McDaniel, E. W., and Mason, E. A., *The Mobility and Diffusion of Ions in Gases*, John Wiley and Sons, New York (1973).
- [11] Huxley, L. G. H., and Crompton, R. W., *The Diffusion and Drift of Electrons in Gases*, John Wiley and Sons, New York (1974).
- [12] Hunter, S. R., and Christophorou, L. G., in *Electron-Molecule Interactions and Their Applications*, Christophorou, L. G., ed., Academic, Orlando (1984).
- [13] Raether, H., *Electron Avalanches and Breakdown in Gases*, Butterworth, Washington, DC (1964).
- [14] Dutton, J., in *Electrical Breakdown in Gases*, Meek, J. M., and Craggs, J. W., eds., John Wiley and Sons, London (1978), Chap. 3.
- [15] Francis, G., in *Handbuch der Physik*, Flügge, S., ed., Springer-Verlag, Berlin (1956), Vol. 22, pp. 53–208.
- [16] Craggs, J. D., in *Electrical Breakdown in Gases*, Meek, J. M., and Craggs, J. W., eds., John Wiley and Sons, London (1978), Chap. 3.
- [17] Gallimberti, I., *J. Phys. (Paris) Colloq. C7*, 193 (1979).
- [18] Tagashira, H., Sakai, Y., and Sakamoto, S., *J. Phys. D* **10**, 1051 (1977).
- [19] Blevin, H. A., and Fletcher, J., *Aust. J. Phys.* **37**, 593 (1984).
- [20] Penetrante, B. M., Bardsley, J. N., and Pitchford, L. C., *J. Phys. D* **18**, 1087 (1985).
- [21] Chantry, P. J., Phelps, A. V., and Schulz, G. J., *Phys. Rev.* **152**, 81 (1966).
- [22] Chandrasekhar, S., *Radiative Transfer*, Dover Publications, Inc., New York (1960), Chap. 1.
- [23] Davison, B., *Neutron Transport Theory*, Clarendon Press, Oxford (1957), Chap. 6.
- [24] Chantry, P. J., *J. Appl. Phys.* **62**, 1141 (1987).
- [25] McCoubrey, A. O., *Phys. Rev.* **93**, 1249 (1954).
- [26] Howard, C. J., *J. Phys. Chem.* **83**, 3 (1979).
- [27] Simon, A., *An Introduction to Thermonuclear Research*, Pergamon, New York (1959), Chap. 9.
- [28] Allis, W. P., and Rose, D. J., *Phys. Rev.* **93**, 84 (1954).
- [29] Schottky, W., *Phys. Z.* **25**, 635 (1924).
- [30] Frost, L. S., *Phys. Rev.* **105**, 354 (1957).
- [31] Zakharova, V. M., Kagan, Yu.M., and Perel', V. I., *Bull. Acad. Sci. USSR* **23**, 986 (1959).
- [32] Rogoff, G. L., *J. Appl. Phys.* **50**, 6806 (1979).
- [33] Chang, J.-S., Kamitsuma, M., and Chen, S.-L., *J. Phys. D* **12**, 409 (1979).
- [34] Voigt, H.-D., Winkler, R., and Wilhelm, J., *Contrib. Plasma Phys.* **28**, 557 (1988).
- [35] Jeager, E. F., Oster, L., and Phelps, A. V., *Phys. Fluids* **19**, 819 (1976).
- [36] Ingold, J. H., *Phys. Fluids* **15**, 75 (1972).
- [37] Cohen, I. M., and Kruskal, M. D., *Phys. Fluids* **8**, 920 (1965).
- [38] Holstein, T., *Phys. Rev.* **75**, A1323 (1949).
- [39] Ecker, G., *Proc. Phys. Soc. B* **67**, 485 (1954).
- [40] Eckert, H. U., *Proceedings Fifth International Conference on Ionization Phenomena in Gases*, Munich 1961, p. 537.
- [41] Kregel, M. D., *J. Appl. Phys.* **41**, 1978 (1970).
- [42] Emeleus, K. G., and Burns, J. A., *Brit. J. Appl. Phys.* **5**, 277 (1954).
- [43] Shaw, D. T.-K., *Phys. Fluids* **10**, 1110 (1967).
- [44] Belousova, L. E., *Zhur. Tech. Fiz.* **35**, 475 (1965) [Sov. Phys.-Tech. Phys. **10**, 369 (1965)].
- [45] Belousova, L. E., *Zhur. Tech. Fiz.* **41**, 669 (1971) [Sov. Phys.-Tech. Phys. **16**, 524 (1971)].
- [46] Wilhelm, J., and Winkler, R., *Beit. Plasmaphysik* **7**, 111 (1967).
- [47] Numano, M., *Phys. Fluids* **16**, 2176 (1973).
- [48] Tonks, L., and Langmuir, I., *Phys. Rev.* **34**, 876 (1929).
- [49] Self, S. A., *Phys. Fluids* **6**, 1762 (1963).
- [50] Dote, T., and Shimada, M., *J. Phys. Soc. Japan* **52**, 536 (1983).
- [51] Persson, K.-B., *Phys. Fluids* **5**, 1625 (1962).
- [52] Bienkowski, G. K., *Phys. Fluids* **10**, 381 (1967).
- [53] Friedman, H. W., *Phys. Fluids* **10**, 2053 (1967).
- [54] Friedman, H. W., and Levi, E., *Phys. Fluids* **10**, 1499 (1967).
- [55] Friedman, H. W., and Levi, E., *Phys. Fluids* **13**, 1049 (1970).
- [56] Forrest, J. R., and Franklin, R. N., *J. Phys. D* **1**, 1357 (1968).
- [57] Kino, G. S., and Shaw, E. K., *Phys. Fluids* **9**, 587 (1966).
- [58] Self, S. A., and Ewald, H. N., *Phys. Fluids* **9**, 2486 (1966).
- [59] Muller, C. H., III, and Phelps, A. V., *J. Appl. Phys.* **51**, 6141 (1980).
- [60] Chantry, P. J. (private communication, 1989).
- [61] Ferreira, C. M., and Ricard, A., *J. Appl. Phys.* **54**, 2261 (1983).
- [62] Dote, T., and Shimada, M., *J. Phys. Soc. Jap.* **51**, 3285 (1982); Dote, T., and Shimada, M., *J. Phys. D* **21**, 210 (1988).
- [63] Gerber, R. A., Gusinow, M. A., and Gerardo, J. B., *Phys. Rev. A* **3**, 1703 (1971).
- [64] Rogoff, G. L., *J. Phys. D* **18**, 1533 (1985).
- [65] Tsendin, L. D., *Zh. Tekh. Fiz.* **55**, 2318 (1985) [Sov. Phys.-Tech. Phys. **30**, 1377 (1985)].
- [66] Seeliger, Von R., *Ann. Phys.* **6**, 93 (1949).
- [67] Koniukov, M. V., *J. Exptl. Theoret. Phys. (USSR)* **34**, 908 (1958) [Sov. Phys. JETP **12**, 629 (1958)].
- [68] Koniukov, M. V., *J. Exptl. Theoret. Phys.* **34**, 1634 (1958), [Sov. Phys. JETP **12**, 1122 (1958)].
- [69] Wilhelm, J., *Die Naturwiss.* **45**, 459 (1958).
- [70] Albrecht, G., and Ecker, G., *Z. Naturforsch.* **17a**, 848 (1962).
- [71] Mikhalev, L. A., and Selin, L. N., *Zh. Tekh. Fiz.* **44**, 1095 (1974) [Sov. Phys.-Tech. Phys. **19**, 689 (1974)].
- [72] Ferreira, C. M., Gousset, G., and Touzeau, M., *J. Phys. D* **21**, 1403 (1988).
- [73] Hill, R. J., *J. Geophys. Res.* **83**, 989 (1978).
- [74] Matsuoka, S., and Tamura, T., *Int. J. Mass Spect. Ion Phys.* **40**, 331 (1981).
- [75] Hiraoka, K., Morise, K., and Shoda, T., *Int. J. Mass Spect. and Ion Processes* **67**, 11 (1985).
- [76] Dorgelo, H. B., Alting, H., and Boers, C. J., *Physica, Haag* **2**, 959 (1935).
- [77] Phelps, A. V., *Phys. Rev.* **86**, 102 (1952).
- [78] Wunderer, B. M., *IEEE Trans Plasma Sci.* **PS-6**, 406 (1978).

- [79] Biondi, M. A. and Brown, S. C., *Phys. Rev.* **75**, 1700 (1949).
- [80] Biondi, M. A., in *Methods of Experimental Physics*, ed. by Bederson, B., and Fite, W., Academic Press, New York (1968) Vol. 7-B.
- [81] Freiberg, R. J., and Weaver, L. A., *Phys. Rev.* **170**, 336 (1968).
- [82] Gusinow, M. A., and Gerber, R. A., *Phys. Rev. A* **5**, 1802 (1972).
- [83] Gerber, R. A., and Gerardo, J. B., *Phys. Rev. A* **7**, 781 (1973).
- [84] Gerber, R. A., and Gerardo, J. B., *Phys. Rev. A* **8**, 1638 (1973).
- [85] Maldonado, C. D., *J. Plasma Phys.* **2**, 167 (1968).
- [86] Fite, W. L., and Rutherford, J. A., *Discuss. Faraday Soc.* **37**, 192 (1964).
- [87] Puckett, L. J., Kregel, M. D., and Teague, M. W., *Phys. Rev. A* **4**, 1659 (1971).
- [88] Smith, D., Dean, A. G., and Adams, N. G., *J. Phys. D* **7**, 1944 (1974).
- [89] MacCallum, C. J., *Plasma Phys.* **12**, 143 (1970).
- [90] Biondi, M. A., *Phys. Rev.* **93**, 1136 (1954).
- [91] Bhattacharya, A. K., and Ingold, J. H., *J. Appl. Phys.* **43**, 1535 (1972).
- [92] Robson, R. E., *Phys. Rev. A* **13**, 1536 (1976).
- [93] Zhilinskii, A. P., and Rozhanskii, V. A., and Tsendin, L. D., *Fiz. Plasmy* **4**, 570 (1978) [Sov. J. Plasma Phys. **4**, 317 (1978)].
- [94] Kolokolov, N. B., Kudryavtsev, A. A., and Toronov, O. G., *Zh. Tekh. Phys.* **55**, 1920 (1985), [Sov. Phys.-Tech. Phys. **30**, 1128 (1985)].
- [95] Boulmer, J., Sol, C., and Gouthier, J. C., *Phys. Lett.* **41A**, 83 (1972).
- [96] Gregory, B. C., and Bergevin, B., *Phys. Rev. A* **7**, 1642 (1973).
- [97] Rose, D. J., and Brown, S. C., *Phys. Rev.* **98**, 310 (1955).
- [98] Krasik, S., Alpert, D., and McCoubrey, A. O., *Phys. Rev.* **76**, 722 (1949).
- [99] Wedding, A. B., and Phelps, A. V., *J. Chem. Phys.* **89**, 2965 (1988).
- [100] Pfau, S., and Rutscher, A., *Beit. Plasmaphysik* **8**, 85 (1968).
- [101] Smits, R. M. N., Lammres, P. H. M., Baghuis, L. C. J., Hagedorn, H. L., and Heide, J. A. v. d., *Beit. Plasmaphysik* **14**, 157 (1974).
- [102] Ferreira, C. M., Loureiro, J., and Ricard, A., *J. Appl. Phys.* **57**, 82 (1985).
- [103] Bernstein, I. B., and Holstein, T., *Phys. Rev.* **94**, 1475 (1954).
- [104] Blank, J. L., *Phys. Fluids* **11**, 1686 (1968).
- [105] Herrmann, D., Rutscher, A., and Pfau, S., *Beit. Plasmaphys.* **11**, 75 (1971).
- [106] Tsendin, L. D., *Zh. Eksp. Teor. Fiz.* **66**, 1638 (1974) [Sov. Phys.-JETP **39**, 805 (1974)].
- [107] Tsendin, L. D., *Zh. Tekh. Fiz.* **48**, 1569 (1978) [Sov. Phys.-Tech. Phys. **23**, 890 (1978)].
- [108] Valentini, H.-B., *Beit. Plasmaphysik* **19**, 151 (1979).
- [109] Valentini, H.-B., *Beit. Plasmaphysik* **19**, 221 (1979).
- [110] Valentini, H.-B., *Beit. Plasmaphysik* **20**, 25 (1980).
- [111] Valentini, H.-B., *Beit. Plasmaphysik* **24**, 83 (1984).
- [112] Deutsch, H., and Pfau, S., *Beit. Plasmaphysik* **16**, 23 (1976).
- [113] Frost, L. S., and Phelps, A. V., *Phys. Rev.* **127**, 1621 (1962).
- [114] Baghuis, L. C. J., Prins, M., Hagedoorn, H. L., and Heide, J. A. v. d., *Beit. Plasmaphysik* **15**, 235 (1975).
- [115] Ganguly, B. N., and Garscadden, A., *Phys. Rev. A* **32**, 2544 (1985).
- [116] Schulz-Gulde, E., *J. Phys. D* **13**, 1829 (1980).
- [117] Vorypaeva, N. S., Nikolaevskii, L. S., and Podmoshenskii, I. V., *Opt. Spektrosk.* **42**, 264 (1977) [Opt. Spectrosc. **42**, 149 (1977)].
- [118] Uhlenbusch, J., in *Gaseous Electronics*, edited by McGowan, J. Wm., and John, P. K., North-Holland, Amsterdam (1974) Chap. 7.
- [119] Shindo, H., Inaba, T., and Imazu, S., *J. Phys. D* **13**, 805 (1980).
- [120] Gliezes, A., Kafrouni, H., Dang Duc, H., and Maury, C., *J. Phys. D* **15**, 1031 (1982).
- [121] Kovitya, P., and Simpson, S. W., *J. Phys. D* **17**, 1829 (1984).
- [122] Farmer, A. J. D., and Haddad, G. N., *Appl. Phys. Lett.* **45**, 24 (1984).
- [123] Simon, A., *Phys. Fluids* **6**, 382 (1963).
- [124] Allis, W. P., and Buchsbaum, S. J., in *Electrons, Ions and Waves, Selected Works of William Phelps Allis*, Brown, S. C., ed., MIT Press, Cambridge (1967), pp. 212–215.
- [125] Hoh, F. C., *Rev. Mod. Phys.* **34**, 267 (1972).
- [126] Monroe, R. L., *Can. J. Phys.* **51**, 564 (1973).
- [127] Golant, V. E., Zhilinsky, A. P., Sakharov, I. E., and Brown, S. C., *Fundamentals of Plasma Physics*, John Wiley and Sons, New York (1977), pp. 301–308.
- [128] Mitchner, M., and Kruger, C. H., Jr., *Partially Ionized Gases*, John Wiley and Sons, New York (1973), p. 173.
- [129] Shunk, R. W., and Walker, J. C. G., *Planet. Space Sci.* **21**, 526 (1973).
- [130] Simon, A., *J. Geophys. Res.* **75**, 6287 (1970).
- [131] Holway, L. H., Jr., *Phys. Fluids* **8**, 1207 (1965).
- [132] Holway, L. H., Jr., *J. Geophys. Res.* **70**, 3635 (1965).
- [133] Tonks, L., *Phys. Fluids* **3**, 758 (1960).
- [134] Bohm, D., Burhop, E. H. S., Massey, H. S. W., and Williams, R. M., in *Characteristics of Electrical Discharges in Magnetic Fields*, Guthrie, A. and Walker, R. K., eds., McGraw-Hill, New York (1949) p. 65.
- [135] Zekrzewski, Z., T. Kopiczyński, and Lubański, M., *Czech. J. Phys.* **B30**, 1170 (1980).
- [136] Deutsch, H., and Klagge, S., *Beit. Plasmaphysik* **23**, 341 (1983).
- [137] Sato, M., *J. Phys. D* **11**, L101 (1978).
- [138] Hoh, F. C., and Lehnert, B., *Phys. Fluids* **3**, 600 (1960).
- [139] Kadomtsev, B. B., and Nedospasov, A. V., *J. Nucl. Energy C1*, 230 (1960).
- [140] Forrest, J. R., and Franklin, R. N., *Brit. J. Appl. Phys.* **17**, 1569 (1966).
- [141] Whitehouse, D. R., and Wollman, H. R., *Phys. Fluids* **6**, 1470 (1963).
- [142] Ewald, H. N., Crawford, F. W., and Self, S. A., *J. Appl. Phys.* **38**, 2753 (1967).
- [143] Self, S. A., *Phys. Fluids* **10**, 1569 (1967).
- [144] Bickerton, R. J., and von Engle, A., *Proc. Phys. Soc. (London)* **69B**, 468 (1956).
- [145] Ventrice, C. A., and Brown, C. E., *J. Appl. Phys.* **43**, 368 (1972).
- [146] Geissler, K. H., *Phys. Fluids* **13**, 935 (1970).
- [147] Geissler, K. H., *Phys. Rev.* **171**, 179 (1968).
- [148] Bulanin, V. V., Zhilinski, A. P., and Smirnov, V. I., *Zh. Tech. Fiz.* **39**, 617 (1969), [Sov. Phys.-Tech Phys. **14**, 464 (1969)].

- [149] Gurevich, A. V., *J. Exptl. Theoret. Phys. (USSR)* **44**, 1302 (1963) [*Sov. Phys. JETP* **17**, 878 (1963)].
- [150] Dutt, T. L., *J. Phys. B* **6**, L152 (1973).
- [151] Jaeger, E. F., Oster, L., and Phelps, A. V., *Phys. Fluids* **19**, 819 (1976).
- [152] Marode, E., Bastien, F., and Bakker, M., *J. Appl. Phys.* **50**, 140 (1979).
- [153] Yoshida, K., and Tagashira, H., *J. Phys. D* **9**, 485 (1976).
- [154] Van Brunt, R. J., and Kulkarni, S. V., *Phys. Rev. A* (submitted, 1990).
- [155] Morrow, R., *Phys. Rev. A* **32**, 1799 (1985).
- [156] Young, M., and Hercher, M., *J. Appl. Phys.* **38**, 4393 (1967).

Tables of the Inverse Laplace Transform of the Function e^{-s^β}

Volume 95

Number 4

July-August 1990

Menachem Dishon

National Institute of Standards
and Technology,
Gaithersburg, MD 20899

John T. Bendler

General Electric Corporate
Research and Development,
Schenectady, NY 12301

and

George H. Weiss

National Institutes of Health,
Bethesda, MD 20892

The inverse transform, $g(t) = \mathcal{L}^{-1}(e^{-s^\beta})$, $0 < \beta < 1$, is a stable law that arises in a number of different applications in chemical physics, polymer physics, solid-state physics, and applied mathematics. Because of its important applications, a number of investigators have suggested approximations to $g(t)$. However, there have so far been no accurately calculated values available for checking or other purposes. We present here tables, accurate to six figures, of $g(t)$ for a number of values of β between 0.25 and 0.999. In addition, since $g(t)$, regarded as a function of β , is unimodal with a peak occurring at $t = t_{\max}$

we both tabulate and graph t_{\max} and $1/g(t_{\max})$ as a function of β , as well as giving polynomial approximations to $1/g(t_{\max})$.

Key words: numerical inversion of Laplace transforms; relaxation processes; stable laws; stretched exponentials.

Accepted: November 22, 1989

1. Introduction

It has been known for at least 150 years that mechanical relaxation in solids is non-exponential, the decay often being characterized by a fractional power-law or logarithmic function [1,2]. It is also now generally recognized that all glassy materials exhibit non-exponential relaxation behavior both above and below the glass transition temperature, T_g . This is especially clear from measurements obtained from mechanical [3-6], dielectric [7-9], and photon correlation spectroscopy [10,11]. It is also seen in measurements of volumetric [12], and thermal response [13,14].

In recent years theorists have become interested in the possibility that complex disordered systems

exhibit universal features in their relaxation and transport properties, possibly arising from self-similar arrangements of obstacles to motion. This has been particularly encouraged by the observation that nearly all glassy relaxation phenomena can be described by the Kohlrausch-Williams-Watts (KWW) function

$$\phi(t;\tau) = \exp\left[-\left(\frac{t}{\tau}\right)^\beta\right], \quad 0 < \beta < 1. \quad (1)$$

In many physical applications it is convenient to represent $\phi(t;\tau)$ in the form of a Laplace transform, which we write as

$$\phi(t;\tau) = \int_0^\infty \rho_\tau(u) e^{-\frac{t}{u}} du = \int_0^\infty e^{-\nu u} h_\tau(\nu) d\nu \quad (2)$$

where

$$h_\tau(\nu) = \frac{\rho_\tau\left(\frac{1}{\nu}\right)}{\nu^2}. \quad (3)$$

Thus, the function $h_\tau(\nu)$ can be found as an inverse Laplace transform of the function $\phi(t;\tau)$. The function $h_\tau(\nu)$ has found application in the context of the theory of trap-controlled hopping in solid state physics [15,16], chromatography [17], and in the study of models for transport in disordered media [18], as well as in the deconvolution of noisy data [19].

A number of approximate algorithms have been proposed in the literature of chemical physics for the numerical evaluation of $h_\tau(\nu)$ [20-25], in addition to a representation of $h_\tau(\nu)$ in terms of a convergent series given by Pollard [26]. Without loss of generality we can set $\tau=1$ since $h_\tau(\nu)$ can be represented in terms of the inverse transform

$$h_\tau(\nu) = \frac{\tau}{2\pi i} \int_{\Gamma} e^{\nu s - s^\beta} ds \quad (4)$$

where Γ is a line to the right of the origin and parallel to the imaginary axis. The convergent series given by Pollard is

$$h_1(\nu) = \frac{1}{\pi} \sum_{k=1}^{\infty} (-1)^{k+1} \frac{\Gamma(\beta k + 1) \sin(\pi \beta k)}{k! \nu^{\beta k + 1}}. \quad (5)$$

In an earlier paper we have presented an accurate tabulation of the sine and cosine transforms of the function $\exp(-t^\beta)$, needed for the analysis of measurements of dielectric properties taken as a function of frequency [27]. In the present paper we tabulate the inverse Laplace transform $h_1(\nu)$. These tables may be used directly for the analysis of experimental data, but are also intended for use as a check on more easily programmed approximations, such as those suggested by earlier investigators [28-30].

2. Numerical Analysis

Two techniques were used to generate the tables that follow which provide an internal check on the accuracy of the computation. The first is that of

numerical inversion of the Laplace transform, using a method first suggested by Dubner and Abate [31], and later given in an improved version by Crump [32]. The second is that of direct evaluation of the series given in eq (5). The approximate inverse of a Laplace transform $\hat{g}(s) = \mathcal{L}\{g(t)\}$ can be expressed in the form of a Fourier series:

$$g_a(t) \sim \frac{e^{at}}{T} \left(\frac{\hat{g}(a)}{2} + \sum_{k=1}^{\infty} \left[R e\{\hat{g}(a + i \frac{k\pi}{T})\} \cos\left(\frac{k\pi t}{T}\right) - I m\{\hat{g}(a + i \frac{k\pi}{T})\} \sin\left(\frac{k\pi t}{T}\right) \right] \right) \quad (6)$$

with an error, $E(t) = g_a(t) - g(t)$, given by

$$E(t) = \sum_{n=1}^{\infty} e^{-2naT} g(2nT+t). \quad (7)$$

The function $\hat{g}(a + i \frac{k\pi}{T})$ can be written in terms of the parameters

$$b_k = k\pi/T, \quad r_k = \sqrt{a^2 + b_k^2}, \quad \theta_k = \tan^{-1}(b_k/a)$$

as

$$\begin{aligned} \hat{g}\left(a + i \frac{k\pi}{T}\right) &= \exp[-r_k^\beta \cos(\beta\theta_k)] \left[\cos(r_k^\beta \sin(\beta\theta_k)) \right. \\ &\quad \left. - i \sin(r_k^\beta \sin(\beta\theta_k)) \right]. \end{aligned} \quad (8)$$

In eqs (6) and (7) the constants a and T are arbitrary and can be chosen to maximize accuracy in any particular application. In the present instance, in which $\hat{g}(s) = \exp(-s^\beta)$, the choice of these parameters is quite straightforward as will be shown below.

Equation (6) was used to evaluate the inverse transform of $\hat{g}(s)$ for values of β in the range $0.20 < \beta < 0.999$ and values of t ranging from 10^{-8} (for selected values of β) to 5, to an accuracy of at least nine significant digits. In these ranges of β and t the choice of parametric ranges $a \in (2.5, 5)$ and $T \in (4, 8)$ sufficed to produce the stated accuracy. The accuracy of the numerical inversion can be checked in detail for three cases in which the inverse transforms are known exactly,

$$\beta = 1/3: \quad g(t) = \frac{1}{(3t^4)^{\frac{1}{3}}} Ai\left[\frac{1}{(3t)^{\frac{1}{3}}}\right]$$

$$\beta=1/2: \quad g(t)=\frac{\exp(-\frac{1}{4t})}{2\pi^{1/2}t^{3/2}} \quad (9)$$

$$\beta=2/3: \quad g(t)=\frac{2^{\frac{4}{3}}\exp(-\frac{4}{27t^2})}{3^{3/2}\pi^{1/2}t^{7/3}} U(\frac{1}{6}, \frac{4}{3}, \frac{4}{27t^2})$$

where $\text{Ai}(x)$ is an Airy function and $U(x, y, z)$ is a confluent hypergeometric function [29]. Typical results for the relative error are given in table 1.

Table 1. Relative errors in the numerical inversion of $\hat{g}(s)$ for $\beta=1/3$, $1/2$, and $2/3$ for different values of a and T

β		1/3	1/2	2/3
a	T	t		
2.5	4	0.1	2(-11)	3(-11)
2.5	4	1.0	2(-10)	1(-10)
2.5	4	5.0	6(-10)	5(-10)
2.5	8	0.1	2(-20)	2(-20)
5.0	4	0.01	3(-20)	1(-11)
5.0	4	0.1	4(-20)	7(-20)
5.0	4	1.0	3(-19)	2(-19)
5.0	4	5.0	1(-18)	1(-18)
				8(-19)

An alternative approach to the evaluation of $g(t)$ is through the direct series shown in eq (5). The form of the series renders it useful for finding $g(t)$ for large t , but the utility of the series form has occasionally been dismissed because of numerical problems associated with convergence at smaller t . We encountered no difficulties in finding $g(t)$ from eq (5), provided that we used a double precision routine for the gamma functions for $k \leq 22$ as well as a Padé correction to Stirling's approximation at larger k [33]. Thus, we write

$$\frac{\Gamma(1+\beta k)}{k!t^{\beta k+1}} \sim e^g \frac{P(\beta k)}{P(k)} \quad (10)$$

where

$$g = k(1-\beta) + (\beta k - \frac{1}{2})\ln(\beta k) - (k - \frac{1}{2})\ln(k) - (\beta k + 1)\ln(t) \quad (11)$$

$$P(k) = \sum_{i=0}^5 \frac{F_i}{k^i}$$

The F_i are constants with the values

$$F_0 = 1, F_1 = \frac{1}{12}, F_2 = \frac{1}{288}, F_3 = -\frac{139}{51,840},$$

$$F_4 = -\frac{571}{2,488,320}, \text{ and } F_5 = \frac{163,879}{209,018,880}.$$

3. Tables, Graphs, and Numerical Approximations

The inverse transform of the function $\hat{g}(s)$ is tabulated in table 2 for the following values of β : 0.25(0.01)0.30(0.02)0.98, 0.99, 0.995, 0.997, 0.998, and 0.999. The finer intervals in β at low values of β are required because of the considerable changes in the function in that neighborhood. Spacings in t vary with β and t in such a way that the peaks of $g(t)$ are most densely covered. There is little need to tabulate $g(t)$ for $t > 5$ because for these values, the sum of no more than 10 terms of the series in eq (5) suffice to produce $g(t)$ to six-digit accuracy for values of β in the interval (0.05, 0.999). For example, if $\beta=0.6$ the sum of seven terms of the series gives $g(10)$ to six places, and the sum of four terms gives $g(100)$ to the same accuracy. Figures 1a–c contain graphs of $g(t)$ as a function of t over the entire range of tabulated values of β . Note that for $\beta=1$ $g(t)=\delta(t-1)$, a Dirac delta function which is represented as a vertical line in figure 1c.

It is evident, from the curves shown in figure 1, that the $g(t)$ are unimodal. The position of the peak will be denoted by t_{\max} . Table 3 contains some values of t_{\max} and $g(t_{\max})$ for the values of β for which we performed our tabulations. It is interesting to observe that among the values of $g(t_{\max})$ there is a minimum value within the interval (0,1). Figure 2a shows graphs of t_{\max} and $1/g(t_{\max})$ as functions of β for values of β between 0.15 and 1. The minimum of $g(t_{\max})$ occurs at $t_{\max}=0.252+$ and is equal to 0.888+. These values correspond to $\beta=0.567+$. Figure 2b contains a plot of $1/g(t_{\max})$ as a function of t_{\max} . Finally, we have derived polynomial least-square approximations to $1/g(t_{\max})$ as a function of β . The coefficients of the approximating polynomials as well as a graphical indication of the degree of agreement with our more accurately calculated values of this function are shown in figure 3. A good approximation to $1/g(t_{\max})$ probably requires fitting some function other than a polynomial.

Table 2. Inverse Laplace transform $g(t)$ of $\hat{g}(s) = e^{-\beta s}$

t	β				
	0.25	0.26	0.27	0.28	0.29
0.00001	0.370151D-04	0.515902D-06	0.248661D-08		
0.00002	0.151806D-02	0.675577D-04	0.144824D-05	0.123255D-07	
0.00003	0.853094D-02	0.649138D-03	0.275324D-04	0.560637D-06	0.451901D-08
0.00004	0.244726D-01	0.258459D-02	0.165894D-03	0.571718D-05	0.902078D-07
0.00005	0.507423D-01	0.672926D-02	0.575158D-03	0.284658D-04	0.711259D-06
0.00006	0.873213D-01	0.137312D-01	0.145291D-02	0.940782D-04	0.330246D-05
0.00007	0.133437D+00	0.239884D-01	0.300022D-02	0.239622D-03	0.109589D-04
0.00008	0.187991D+00	0.376838D-01	0.539788D-02	0.510882D-03	0.289237D-04
0.00009	0.249798D+00	0.548385D-01	0.879472D-02	0.958456D-03	0.647631D-04
0.00010	0.317705D+00	0.753611D-01	0.133042D-01	0.163414D-02	0.128251D-03
0.00011	0.390651D+00	0.990866D-01	0.190057D-01	0.258809D-02	0.231044D-03
0.00012	0.467687D+00	0.125806D+00	0.259484D-01	0.386679D-02	0.386250D-03
0.00013	0.547978D+00	0.155287D+00	0.341556D-01	0.551183D-02	0.607956D-03
0.00014	0.630804D+00	0.187288D+00	0.436295D-01	0.755922D-02	0.910770D-03
0.00015	0.715540D+00	0.221568D+00	0.543553D-01	0.100391D-01	0.130942D-02
0.00016	0.801653D+00	0.257891D+00	0.663051D-01	0.129761D-01	0.181839D-02
0.00017	0.888689D+00	0.296036D+00	0.794409D-01	0.163891D-01	0.245168D-02
0.00018	0.976259D+00	0.335790D+00	0.937176D-01	0.202922D-01	0.322255D-02
0.00019	0.106404D+01	0.376957D+00	0.109085D+00	0.246947D-01	0.414334D-02
0.00020	0.115175D+01	0.419354D+00	0.125488D+00	0.296019D-01	0.522547D-02
0.00021	0.123915D+01	0.462814D+00	0.142873D+00	0.350156D-01	0.647923D-02
0.00022	0.132605D+01	0.507183D+00	0.161181D+00	0.409343D-01	0.791385D-02
0.00023	0.141229D+01	0.552318D+00	0.180357D+00	0.473537D-01	0.953745D-02
0.00024	0.149772D+01	0.598093D+00	0.200343D+00	0.542673D-01	0.113571D-01
0.00025	0.158223D+01	0.644389D+00	0.221084D+00	0.616668D-01	0.133787D-01
0.00030	0.198831D+01	0.880304D+00	0.334310D+00	0.105556D+00	0.266587D-01
0.00035	0.236313D+01	0.111698D+01	0.459197D+00	0.159675D+00	0.453716D-01
0.00040	0.270528D+01	0.134838D+01	0.591057D+00	0.222165D+00	0.694073D-01
0.00045	0.301586D+01	0.157109D+01	0.726376D+00	0.291223D+00	0.984011D-01
0.00050	0.329700D+01	0.178326D+01	0.862582D+00	0.365234D+00	0.131854D+00
0.00060	0.378101D+01	0.217324D+01	0.113082D+01	0.522815D+00	0.209913D+00
0.00070	0.417683D+01	0.251762D+01	0.138668D+01	0.686433D+00	0.299254D+00
0.00080	0.450132D+01	0.281968D+01	0.162607D+01	0.850458D+00	0.396103D+00
0.00090	0.476810D+01	0.308392D+01	0.184753D+01	0.101129D+01	0.497430D+00
0.00100	0.498794D+01	0.331492D+01	0.205105D+01	0.116672D+01	0.600902D+00
0.00110	0.516936D+01	0.351690D+01	0.223731D+01	0.131544D+01	0.704769D+00
0.00120	0.531912D+01	0.369363D+01	0.240740D+01	0.145678D+01	0.807740D+00
0.00130	0.544260D+01	0.384838D+01	0.256249D+01	0.159047D+01	0.908884D+00
0.00140	0.554414D+01	0.398397D+01	0.270380D+01	0.171648D+01	0.100755D+01
0.00150	0.562724D+01	0.410281D+01	0.283253D+01	0.183497D+01	0.110327D+01
0.00160	0.569476D+01	0.420700D+01	0.294978D+01	0.194618D+01	0.119577D+01
0.00170	0.574907D+01	0.429831D+01	0.305657D+01	0.205044D+01	0.128485D+01
0.00180	0.579212D+01	0.437828D+01	0.315385D+01	0.214809D+01	0.137044D+01
0.00190	0.582551D+01	0.444824D+01	0.324247D+01	0.223950D+01	0.145249D+01
0.00200	0.585062D+01	0.450934D+01	0.332320D+01	0.232501D+01	0.153104D+01

Table 2. Inverse Laplace transform $g(t)$ of $\hat{g}(s)=e^{-s\beta}$ —Continued

t	β				
	0.25	0.26	0.27	0.28	0.29
0.00210	0.586859D+01	0.456258D+01	0.339676D+01	0.240499D+01	0.160613D+01
0.00220	0.588040D+01	0.460881D+01	0.346376D+01	0.247978D+01	0.167784D+01
0.00230	0.588685D+01	0.464881D+01	0.352477D+01	0.254971D+01	0.174627D+01
0.00240	0.588868D+01	0.468323D+01	0.358032D+01	0.261507D+01	0.181152D+01
0.00250	0.588646D+01	0.471266D+01	0.363086D+01	0.267617D+01	0.187372D+01
0.00300	0.583090D+01	0.480102D+01	0.382187D+01	0.292665D+01	0.214289D+01
0.00350	0.572936D+01	0.482136D+01	0.393647D+01	0.310461D+01	0.235284D+01
0.00400	0.560506D+01	0.480024D+01	0.399971D+01	0.322986D+01	0.251601D+01
0.00450	0.547051D+01	0.475348D+01	0.402773D+01	0.331631D+01	0.264234D+01
0.00500	0.533269D+01	0.469083D+01	0.403120D+01	0.337384D+01	0.273959D+01
0.00600	0.506134D+01	0.454054D+01	0.399133D+01	0.342877D+01	0.286945D+01
0.00700	0.480602D+01	0.437755D+01	0.391576D+01	0.343198D+01	0.293927D+01
0.00800	0.457076D+01	0.421433D+01	0.382270D+01	0.340442D+01	0.296975D+01
0.00900	0.435561D+01	0.405650D+01	0.372195D+01	0.335844D+01	0.297401D+01
0.01000	0.415919D+01	0.390643D+01	0.361892D+01	0.330154D+01	0.296059D+01
0.01100	0.397972D+01	0.376497D+01	0.351666D+01	0.323842D+01	0.293520D+01
0.01200	0.381537D+01	0.363219D+01	0.341686D+01	0.317209D+01	0.290172D+01
0.01300	0.366447D+01	0.350777D+01	0.332044D+01	0.310448D+01	0.286285D+01
0.01400	0.352550D+01	0.339122D+01	0.322787D+01	0.303685D+01	0.282046D+01
0.01500	0.339714D+01	0.328200D+01	0.313931D+01	0.297004D+01	0.277590D+01
0.01600	0.327824D+01	0.317955D+01	0.305479D+01	0.290456D+01	0.273013D+01
0.01700	0.316778D+01	0.308333D+01	0.297421D+01	0.284075D+01	0.268383D+01
0.01800	0.306491D+01	0.299284D+01	0.289744D+01	0.277880D+01	0.263752D+01
0.01900	0.296885D+01	0.290761D+01	0.282430D+01	0.271882D+01	0.259154D+01
0.02000	0.287894D+01	0.282722D+01	0.275460D+01	0.266086D+01	0.254614D+01
0.02100	0.279460D+01	0.275127D+01	0.268816D+01	0.260491D+01	0.250152D+01
0.02200	0.271531D+01	0.267942D+01	0.262478D+01	0.255095D+01	0.245779D+01
0.02300	0.264063D+01	0.261135D+01	0.256428D+01	0.249893D+01	0.241504D+01
0.02400	0.257015D+01	0.254676D+01	0.250649D+01	0.244880D+01	0.237332D+01
0.02500	0.250353D+01	0.248540D+01	0.245125D+01	0.240048D+01	0.233267D+01
0.03000	0.221824D+01	0.221946D+01	0.220816D+01	0.218367D+01	0.214538D+01
0.03500	0.199355D+01	0.200649D+01	0.200950D+01	0.200190D+01	0.198306D+01
0.04000	0.181164D+01	0.183191D+01	0.184418D+01	0.184784D+01	0.184226D+01
0.04500	0.166111D+01	0.168604D+01	0.170445D+01	0.171578D+01	0.171946D+01
0.05000	0.153434D+01	0.156223D+01	0.158475D+01	0.160139D+01	0.161165D+01
0.06000	0.133230D+01	0.136312D+01	0.139020D+01	0.141316D+01	0.143158D+01
0.07000	0.117811D+01	0.120973D+01	0.123868D+01	0.126467D+01	0.128738D+01
0.08000	0.105636D+01	0.108774D+01	0.111719D+01	0.114448D+01	0.116936D+01
0.09000	0.957662D+00	0.988292D+00	0.101751D+01	0.104515D+01	0.107100D+01
0.10000	0.875953D+00	0.905594D+00	0.934205D+00	0.961646D+00	0.987760D+00
0.11000	0.807149D+00	0.835699D+00	0.863499D+00	0.890438D+00	0.916393D+00
0.12000	0.748385D+00	0.775818D+00	0.802711D+00	0.828978D+00	0.854519D+00
0.13000	0.697593D+00	0.723924D+00	0.749875D+00	0.775379D+00	0.800357D+00
0.14000	0.653241D+00	0.678505D+00	0.703514D+00	0.728214D+00	0.752545D+00
0.15000	0.614166D+00	0.638412D+00	0.662499D+00	0.686386D+00	0.710024D+00
0.16000	0.579473D+00	0.602753D+00	0.625950D+00	0.649031D+00	0.671960D+00
0.17000	0.548460D+00	0.570828D+00	0.593171D+00	0.615466D+00	0.637686D+00
0.18000	0.520567D+00	0.542074D+00	0.563604D+00	0.585140D+00	0.606661D+00
0.19000	0.495343D+00	0.516040D+00	0.536798D+00	0.557605D+00	0.578444D+00
0.20000	0.472421D+00	0.492356D+00	0.512382D+00	0.532490D+00	0.552669D+00

Table 2. Inverse Laplace transform $g(t)$ of $\hat{g}(s) = e^{-s\beta}$ —Continued

t	β				
	0.25	0.26	0.27	0.28	0.29
0.21000	0.451498D+00	0.470716D+00	0.490048D+00	0.509490D+00	0.529034D+00
0.22000	0.432322D+00	0.450866D+00	0.469541D+00	0.488347D+00	0.507281D+00
0.23000	0.414684D+00	0.432591D+00	0.450645D+00	0.468847D+00	0.487195D+00
0.24000	0.398403D+00	0.415711D+00	0.433176D+00	0.450803D+00	0.468592D+00
0.25000	0.383330D+00	0.400072D+00	0.416980D+00	0.434059D+00	0.451313D+00
0.30000	0.322103D+00	0.336439D+00	0.350960D+00	0.365674D+00	0.380590D+00
0.35000	0.277427D+00	0.289905D+00	0.302564D+00	0.315413D+00	0.328462D+00
0.40000	0.243395D+00	0.254402D+00	0.265577D+00	0.276930D+00	0.288471D+00
0.45000	0.216613D+00	0.226431D+00	0.236401D+00	0.246533D+00	0.256837D+00
0.50000	0.194994D+00	0.203832D+00	0.212807D+00	0.221929D+00	0.231205D+00
0.55000	0.177181D+00	0.185199D+00	0.193341D+00	0.201614D+00	0.210025D+00
0.60000	0.162254D+00	0.169579D+00	0.177013D+00	0.184565D+00	0.192240D+00
0.65000	0.149568D+00	0.156298D+00	0.163126D+00	0.170058D+00	0.177100D+00
0.70000	0.138657D+00	0.144872D+00	0.151174D+00	0.157569D+00	0.164062D+00
0.75000	0.129174D+00	0.134940D+00	0.140783D+00	0.146708D+00	0.152721D+00
0.80000	0.120859D+00	0.126229D+00	0.131668D+00	0.137180D+00	0.142769D+00
0.85000	0.113510D+00	0.118529D+00	0.123610D+00	0.128756D+00	0.133970D+00
0.90000	0.106968D+00	0.111675D+00	0.116437D+00	0.121256D+00	0.126136D+00
0.95000	0.101110D+00	0.105537D+00	0.110012D+00	0.114538D+00	0.119118D+00
1.00000	0.958339D-01	0.100008D+00	0.104226D+00	0.108488D+00	0.112798D+00
1.10000	0.867153D-01	0.904539D-01	0.942257D-01	0.980323D-01	0.101875D+00
1.20000	0.791153D-01	0.824909D-01	0.858919D-01	0.893196D-01	0.927749D-01
1.30000	0.726869D-01	0.757563D-01	0.788447D-01	0.819528D-01	0.850815D-01
1.40000	0.671813D-01	0.699893D-01	0.728108D-01	0.756465D-01	0.784968D-01
1.50000	0.624152D-01	0.649976D-01	0.675892D-01	0.701902D-01	0.728008D-01
1.60000	0.582505D-01	0.606366D-01	0.630282D-01	0.654252D-01	0.678277D-01
1.70000	0.545814D-01	0.567953D-01	0.590116D-01	0.612299D-01	0.634503D-01
1.80000	0.513255D-01	0.533874D-01	0.554483D-01	0.575096D-01	0.595694D-01
1.90000	0.484176D-01	0.503443D-01	0.522683D-01	0.541892D-01	0.561066D-01
2.00000	0.458055D-01	0.476113D-01	0.494124D-01	0.512084D-01	0.529989D-01
2.10000	0.434467D-01	0.451439D-01	0.468347D-01	0.485187D-01	0.501953D-01
2.20000	0.413066D-01	0.429058D-01	0.444971D-01	0.460801D-01	0.476542D-01
2.30000	0.393567D-01	0.408669D-01	0.423681D-01	0.438597D-01	0.453410D-01
2.40000	0.375729D-01	0.390022D-01	0.404214D-01	0.418299D-01	0.432270D-01
2.50000	0.359352D-01	0.372906D-01	0.386350D-01	0.399677D-01	0.412880D-01
2.60000	0.344267D-01	0.357144D-01	0.369902D-01	0.382535D-01	0.395036D-01
2.70000	0.330329D-01	0.342582D-01	0.354710D-01	0.366707D-01	0.378563D-01
2.80000	0.317409D-01	0.329092D-01	0.340640D-01	0.352050D-01	0.363314D-01
2.90000	0.305414D-01	0.316562D-01	0.327573D-01	0.338442D-01	0.349159D-01
3.00000	0.294237D-01	0.304893D-01	0.315408D-01	0.325775D-01	0.335988D-01
3.20000	0.274043D-01	0.283816D-01	0.293441D-01	0.302911D-01	0.312219D-01
3.40000	0.256298D-01	0.265302D-01	0.274154D-01	0.282845D-01	0.291370D-01
3.60000	0.240589D-01	0.248919D-01	0.257093D-01	0.265103D-01	0.272943D-01
3.80000	0.226589D-01	0.234324D-01	0.241901D-01	0.249311D-01	0.256550D-01
4.00000	0.214039D-01	0.221246D-01	0.228292D-01	0.235171D-01	0.241877D-01
4.20000	0.202728D-01	0.209463D-01	0.216036D-01	0.222442D-01	0.228674D-01
4.40000	0.192485D-01	0.198796D-01	0.204945D-01	0.210927D-01	0.216735D-01
4.60000	0.183167D-01	0.189096D-01	0.194863D-01	0.200463D-01	0.205890D-01
4.80000	0.174657D-01	0.180240D-01	0.185661D-01	0.190916D-01	0.196000D-01
5.00000	0.166856D-01	0.172124D-01	0.177231D-01	0.182174D-01	0.186946D-01

Table 2. Inverse Laplace transform $g(t)$ of $\hat{g}(s)=e^{-s\beta}$ —Continued

t	β				
	0.30	0.32	0.34	0.36	0.38
0.0001	0.577115D-05	0.121648D-08			
0.0002	0.646619D-03	0.239900D-05			
0.0003	0.513202D-02	0.651487D-04	0.107344D-06		
0.0004	0.173393D-01	0.450932D-03	0.224946D-05		
0.0005	0.392873D-01	0.165274D-02	0.171861D-04	0.212894D-07	
0.0006	0.711617D-01	0.424768D-02	0.750118D-04	0.210542D-06	
0.0007	0.112072D+00	0.875023D-02	0.231320D-03	0.120478D-05	
0.0008	0.160657D+00	0.155375D-01	0.565412D-03	0.478961D-05	0.438912D-08
0.0009	0.215447D+00	0.248343D-01	0.117278D-02	0.147371D-04	0.248393D-07
0.0010	0.275045D+00	0.367290D-01	0.215567D-02	0.375741D-04	0.104716D-06
0.0011	0.338203D+00	0.512025D-01	0.361447D-02	0.830781D-04	0.353443D-06
0.0012	0.403853D+00	0.681562D-01	0.564119D-02	0.164407D-03	0.100396D-05
0.0013	0.471095D+00	0.874382D-01	0.831519D-02	0.297882D-03	0.248718D-05
0.0014	0.539192D+00	0.108863D+00	0.117010D-01	0.502496D-03	0.551702D-05
0.0015	0.607539D+00	0.132228D+00	0.158477D-01	0.799254D-03	0.111767D-04
0.0016	0.675651D+00	0.157324D+00	0.207892D-01	0.121045D-02	0.209968D-04
0.0017	0.743142D+00	0.183942D+00	0.265457D-01	0.175892D-02	0.370175D-04
0.0018	0.809706D+00	0.211881D+00	0.331246D-01	0.246740D-02	0.618297D-04
0.0019	0.875106D+00	0.240950D+00	0.405229D-01	0.335793D-02	0.985926D-04
0.0020	0.939159D+00	0.270970D+00	0.487283D-01	0.445136D-02	0.151029D-03
0.0021	0.100173D+01	0.301776D+00	0.577210D-01	0.576702D-02	0.223396D-03
0.0022	0.106272D+01	0.333216D+00	0.674750D-01	0.732241D-02	0.320443D-03
0.0023	0.112206D+01	0.365153D+00	0.779600D-01	0.913304D-02	0.447353D-03
0.0024	0.117970D+01	0.397460D+00	0.891418D-01	0.112123D-01	0.609668D-03
0.0025	0.123562D+01	0.430026D+00	0.100984D+00	0.135716D-01	0.813220D-03
0.0030	0.148946D+01	0.593555D+00	0.168732D+00	0.298190D-01	0.266390D-02
0.0035	0.170271D+01	0.752371D+00	0.247165D+00	0.536557D-01	0.645439D-02
0.0040	0.188023D+01	0.901685D+00	0.331963D+00	0.846472D-01	0.128304D-01
0.0045	0.202727D+01	0.103934D+01	0.419697D+00	0.121852D+00	0.222298D-01
0.0050	0.214868D+01	0.116469D+01	0.507819D+00	0.164122D+00	0.348631D-01
0.0060	0.233062D+01	0.137960D+01	0.678587D+00	0.259259D+00	0.697247D-01
0.0070	0.245192D+01	0.155178D+01	0.835891D+00	0.361944D+00	0.115960D+00
0.0080	0.253036D+01	0.168824D+01	0.976603D+00	0.466212D+00	0.171035D+00
0.0090	0.257814D+01	0.179553D+01	0.110029D+01	0.568107D+00	0.232237D+00
0.0100	0.260376D+01	0.187922D+01	0.120782D+01	0.665204D+00	0.297120D+00
0.0110	0.261321D+01	0.194384D+01	0.130058D+01	0.756146D+00	0.363668D+00
0.0120	0.261078D+01	0.199304D+01	0.138014D+01	0.840293D+00	0.430308D+00
0.0130	0.259958D+01	0.202974D+01	0.144806D+01	0.917463D+00	0.495866D+00
0.0140	0.258189D+01	0.205627D+01	0.150576D+01	0.987763D+00	0.559498D+00
0.0150	0.255944D+01	0.207450D+01	0.155455D+01	0.105147D+01	0.620622D+00
0.0160	0.253349D+01	0.208594D+01	0.159556D+01	0.110897D+01	0.678861D+00
0.0170	0.250502D+01	0.209182D+01	0.162981D+01	0.116067D+01	0.733992D+00
0.0180	0.247477D+01	0.209311D+01	0.165817D+01	0.120701D+01	0.785906D+00
0.0190	0.244331D+01	0.209064D+01	0.168140D+01	0.124843D+01	0.834581D+00
0.0200	0.241107D+01	0.208507D+01	0.170017D+01	0.128534D+01	0.880053D+00

Table 2. Inverse Laplace transform $g(t)$ of $\hat{g}(s)=e^{-\beta s}$ —Continued

t	β				
	0.30	0.32	0.34	0.36	0.38
0.0210	0.237838D+01	0.207695D+01	0.171503D+01	0.131813D+01	0.922401D+00
0.0220	0.234552D+01	0.206673D+01	0.172649D+01	0.134716D+01	0.961733D+00
0.0230	0.231268D+01	0.205478D+01	0.173499D+01	0.137279D+01	0.998177D+00
0.0240	0.228001D+01	0.204143D+01	0.174088D+01	0.139531D+01	0.103187D+01
0.0250	0.224765D+01	0.202693D+01	0.174450D+01	0.141501D+01	0.106296D+01
0.0260	0.221567D+01	0.201150D+01	0.174613D+01	0.143214D+01	0.109158D+01
0.0270	0.218416D+01	0.199533D+01	0.174602D+01	0.144695D+01	0.111789D+01
0.0280	0.215315D+01	0.197858D+01	0.174439D+01	0.145965D+01	0.114203D+01
0.0290	0.212269D+01	0.196137D+01	0.174142D+01	0.147043D+01	0.116412D+01
0.0300	0.209281D+01	0.194381D+01	0.173728D+01	0.147947D+01	0.118430D+01
0.0310	0.206352D+01	0.192601D+01	0.173212D+01	0.148692D+01	0.120269D+01
0.0320	0.203482D+01	0.190803D+01	0.172607D+01	0.149294D+01	0.121942D+01
0.0330	0.200674D+01	0.188995D+01	0.171924D+01	0.149765D+01	0.123458D+01
0.0340	0.197927D+01	0.187183D+01	0.171172D+01	0.150117D+01	0.124830D+01
0.0350	0.195239D+01	0.185370D+01	0.170362D+01	0.150361D+01	0.126065D+01
0.0360	0.192612D+01	0.183561D+01	0.169501D+01	0.150508D+01	0.127175D+01
0.0370	0.190044D+01	0.181760D+01	0.168595D+01	0.150565D+01	0.128166D+01
0.0380	0.187534D+01	0.179970D+01	0.167651D+01	0.150541D+01	0.129048D+01
0.0390	0.185081D+01	0.178192D+01	0.166675D+01	0.150444D+01	0.129828D+01
0.0400	0.182684D+01	0.176430D+01	0.165670D+01	0.150279D+01	0.130512D+01
0.0410	0.180341D+01	0.174684D+01	0.164643D+01	0.150054D+01	0.131108D+01
0.0420	0.178052D+01	0.172956D+01	0.163595D+01	0.149774D+01	0.131621D+01
0.0430	0.175815D+01	0.171247D+01	0.162532D+01	0.149444D+01	0.132058D+01
0.0440	0.173628D+01	0.169558D+01	0.161455D+01	0.149068D+01	0.132422D+01
0.0450	0.171491D+01	0.167890D+01	0.160368D+01	0.148651D+01	0.132720D+01
0.0460	0.169402D+01	0.166243D+01	0.159273D+01	0.148197D+01	0.132956D+01
0.0470	0.167359D+01	0.164618D+01	0.158172D+01	0.147710D+01	0.133134D+01
0.0480	0.165362D+01	0.163015D+01	0.157067D+01	0.147191D+01	0.133258D+01
0.0490	0.163410D+01	0.161435D+01	0.155960D+01	0.146646D+01	0.133332D+01
0.0500	0.161500D+01	0.159877D+01	0.154852D+01	0.146075D+01	0.133359D+01
0.0600	0.144504D+01	0.145517D+01	0.143969D+01	0.139471D+01	0.131684D+01
0.0700	0.130645D+01	0.133216D+01	0.133847D+01	0.132177D+01	0.127837D+01
0.0800	0.119155D+01	0.122661D+01	0.124690D+01	0.124924D+01	0.123015D+01
0.0900	0.109484D+01	0.113550D+01	0.116485D+01	0.118018D+01	0.117840D+01
0.1000	0.101237D+01	0.105627D+01	0.109149D+01	0.111576D+01	0.112640D+01
0.1100	0.941223D+00	0.986854D+00	0.102582D+01	0.105624D+01	0.107582D+01
0.1200	0.879225D+00	0.925600D+00	0.966874D+00	0.100149D+01	0.102752D+01
0.1300	0.824722D+00	0.871187D+00	0.913776D+00	0.951209D+00	0.981859D+00
0.1400	0.776435D+00	0.822554D+00	0.865765D+00	0.905016D+00	0.938950D+00
0.1500	0.733358D+00	0.778843D+00	0.822190D+00	0.862536D+00	0.898755D+00
0.1600	0.694693D+00	0.739355D+00	0.782493D+00	0.823407D+00	0.861163D+00
0.1700	0.659795D+00	0.703513D+00	0.746203D+00	0.787296D+00	0.826024D+00
0.1800	0.628140D+00	0.670841D+00	0.712914D+00	0.753901D+00	0.793174D+00
0.1900	0.599296D+00	0.640941D+00	0.682282D+00	0.722953D+00	0.762444D+00
0.2000	0.572906D+00	0.613478D+00	0.654009D+00	0.694212D+00	0.733674D+00
0.2100	0.548670D+00	0.588169D+00	0.627842D+00	0.667464D+00	0.706710D+00
0.2200	0.526336D+00	0.564774D+00	0.603558D+00	0.642522D+00	0.681408D+00
0.2300	0.505687D+00	0.543084D+00	0.580968D+00	0.619217D+00	0.657637D+00
0.2400	0.486542D+00	0.522922D+00	0.559902D+00	0.597401D+00	0.635274D+00
0.2500	0.468742D+00	0.504133D+00	0.540216D+00	0.576943D+00	0.614211D+00

Table 2. Inverse Laplace transform $g(t)$ of $\hat{g}(s) = e^{-\beta s}$ —Continued

t	β				
	0.30	0.32	0.34	0.36	0.38
0.3000	0.395716D+00	0.426630D+00	0.458474D+00	0.491299D+00	0.525137D+00
0.3500	0.341722D+00	0.368917D+00	0.397083D+00	0.426309D+00	0.456686D+00
0.4000	0.300210D+00	0.324328D+00	0.349379D+00	0.375462D+00	0.402687D+00
0.4500	0.267323D+00	0.288884D+00	0.311305D+00	0.334687D+00	0.359140D+00
0.5000	0.240646D+00	0.260059D+00	0.280252D+00	0.301319D+00	0.323364D+00
0.5500	0.218584D+00	0.236178D+00	0.254471D+00	0.273549D+00	0.293507D+00
0.6000	0.200046D+00	0.216084D+00	0.232746D+00	0.250107D+00	0.268253D+00
0.6500	0.184259D+00	0.198954D+00	0.214204D+00	0.230075D+00	0.246642D+00
0.7000	0.170658D+00	0.184187D+00	0.198206D+00	0.212776D+00	0.227960D+00
0.7500	0.158825D+00	0.171331D+00	0.184272D+00	0.197699D+00	0.211668D+00
0.8000	0.148440D+00	0.160045D+00	0.172034D+00	0.184451D+00	0.197345D+00
0.8500	0.139256D+00	0.150062D+00	0.161206D+00	0.172727D+00	0.184667D+00
0.9000	0.131079D+00	0.141172D+00	0.151563D+00	0.162285D+00	0.173373D+00
0.9500	0.123754D+00	0.133208D+00	0.142923D+00	0.152929D+00	0.163256D+00
1.0000	0.117157D+00	0.126035D+00	0.135143D+00	0.144504D+00	0.154145D+00
1.1000	0.105757D+00	0.113641D+00	0.121701D+00	0.129953D+00	0.138414D+00
1.2000	0.962591D-01	0.103319D+00	0.110511D+00	0.117844D+00	0.125330D+00
1.3000	0.882314D-01	0.945984D-01	0.101060D+00	0.107624D+00	0.114296D+00
1.4000	0.813620D-01	0.871394D-01	0.929821D-01	0.988936D-01	0.104877D+00
1.5000	0.754212D-01	0.806920D-01	0.860039D-01	0.913578D-01	0.967540D-01
1.6000	0.702356D-01	0.750676D-01	0.799205D-01	0.847932D-01	0.896840D-01
1.7000	0.656724D-01	0.701212D-01	0.745741D-01	0.790284D-01	0.834810D-01
1.8000	0.616280D-01	0.657397D-01	0.698416D-01	0.739298D-01	0.779998D-01
1.9000	0.580202D-01	0.618337D-01	0.656257D-01	0.693913D-01	0.731251D-01
2.0000	0.547832D-01	0.583314D-01	0.618482D-01	0.653281D-01	0.687650D-01
2.1000	0.518640D-01	0.551748D-01	0.584460D-01	0.616714D-01	0.648445D-01
2.2000	0.492187D-01	0.523163D-01	0.553672D-01	0.583650D-01	0.613027D-01
2.3000	0.468114D-01	0.497165D-01	0.525690D-01	0.553622D-01	0.580890D-01
2.4000	0.446119D-01	0.473426D-01	0.500157D-01	0.526245D-01	0.551615D-01
2.5000	0.425952D-01	0.451673D-01	0.476776D-01	0.501192D-01	0.524848D-01
2.6000	0.407397D-01	0.431671D-01	0.455291D-01	0.478190D-01	0.500291D-01
2.7000	0.390273D-01	0.413222D-01	0.435489D-01	0.457003D-01	0.477692D-01
2.8000	0.374425D-01	0.396158D-01	0.417184D-01	0.437433D-01	0.456833D-01
2.9000	0.359719D-01	0.380332D-01	0.400218D-01	0.419307D-01	0.437529D-01
3.0000	0.346037D-01	0.365617D-01	0.384453D-01	0.402476D-01	0.419617D-01
3.1000	0.333279D-01	0.351904D-01	0.369770D-01	0.386811D-01	0.402959D-01
3.2000	0.321358D-01	0.339096D-01	0.356065D-01	0.372199D-01	0.387431D-01
3.3000	0.310194D-01	0.327109D-01	0.343246D-01	0.358540D-01	0.372927D-01
3.4000	0.299720D-01	0.315869D-01	0.331232D-01	0.345748D-01	0.359353D-01
3.5000	0.289875D-01	0.305309D-01	0.319952D-01	0.333745D-01	0.346625D-01
3.6000	0.280606D-01	0.295372D-01	0.309344D-01	0.322463D-01	0.334670D-01
3.7000	0.271865D-01	0.286006D-01	0.299350D-01	0.311841D-01	0.323421D-01
3.8000	0.263609D-01	0.277164D-01	0.289921D-01	0.301825D-01	0.312821D-01
3.9000	0.255800D-01	0.268804D-01	0.281011D-01	0.292366D-01	0.302817D-01
4.0000	0.248403D-01	0.260890D-01	0.272580D-01	0.283421D-01	0.293363D-01
4.2000	0.234726D-01	0.246266D-01	0.257013D-01	0.266919D-01	0.275936D-01
4.4000	0.222363D-01	0.233060D-01	0.242970D-01	0.252048D-01	0.260250D-01
4.6000	0.211139D-01	0.221080D-01	0.230243D-01	0.238585D-01	0.246066D-01
4.8000	0.200907D-01	0.210169D-01	0.218662D-01	0.226346D-01	0.233185D-01
5.0000	0.191544D-01	0.200192D-01	0.208083D-01	0.215177D-01	0.221443D-01

Table 2. Inverse Laplace transform $g(t)$ of $\hat{g}(s) = e^{-\beta s}$ —Continued

<i>t</i>	β				
	0.40	0.42	0.44	0.46	0.48
0.002	0.116562D-05				
0.003	0.875664D-04	0.642966D-06			
0.004	0.917142D-03	0.216038D-04	0.949439D-07		
0.005	0.406492D-02	0.197437D-03	0.259248D-05	0.458884D-08	
0.006	0.114034D-01	0.908478D-03	0.249859D-04	0.137126D-06	
0.007	0.243242D-01	0.277903D-02	0.130277D-03	0.160298D-05	0.250858D-08
0.008	0.434357D-01	0.653168D-02	0.458125D-03	0.103165D-04	0.409163D-07
0.009	0.686419D-01	0.128176D-01	0.123210D-02	0.443480D-04	0.359676D-06
0.010	0.993632D-01	0.221063D-01	0.273747D-02	0.143247D-03	0.204689D-05
0.011	0.134755D+00	0.346471D-01	0.528212D-02	0.375074D-03	0.848024D-05
0.012	0.173873D+00	0.504823D-01	0.915677D-02	0.837893D-03	0.276694D-04
0.013	0.215782D+00	0.694867D-01	0.146046D-01	0.165512D-02	0.750945D-04
0.014	0.259618D+00	0.914136D-01	0.218037D-01	0.296638D-02	0.176300D-03
0.015	0.304618D+00	0.115939D+00	0.308610D-01	0.491645D-02	0.368510D-03
0.016	0.350132D+00	0.142698D+00	0.418152D-01	0.764441D-02	0.700833D-03
0.017	0.395618D+00	0.171312D+00	0.546444D-01	0.112748D-01	0.123301D-02
0.018	0.440637D+00	0.201408D+00	0.692772D-01	0.159112D-01	0.203294D-02
0.019	0.484838D+00	0.232634D+00	0.856035D-01	0.216325D-01	0.317351D-02
0.020	0.527948D+00	0.264664D+00	0.103486D+00	0.284915D-01	0.472905D-02
0.021	0.569763D+00	0.297204D+00	0.122768D+00	0.365153D-01	0.677197D-02
0.022	0.610129D+00	0.329992D+00	0.143285D+00	0.457071D-01	0.936977D-02
0.023	0.648942D+00	0.362802D+00	0.164867D+00	0.560491D-01	0.125826D-01
0.024	0.686132D+00	0.395437D+00	0.187346D+00	0.675050D-01	0.164616D-01
0.025	0.721660D+00	0.427728D+00	0.210559D+00	0.800237D-01	0.210476D-01
0.026	0.755512D+00	0.459537D+00	0.234352D+00	0.935423D-01	0.263709D-01
0.027	0.787691D+00	0.490746D+00	0.258579D+00	0.107989D+00	0.324507D-01
0.028	0.818217D+00	0.521260D+00	0.283106D+00	0.123286D+00	0.392962D-01
0.029	0.847120D+00	0.551004D+00	0.307810D+00	0.139352D+00	0.469066D-01
0.030	0.874438D+00	0.579917D+00	0.332580D+00	0.156103D+00	0.552723D-01
0.031	0.900219D+00	0.607954D+00	0.357315D+00	0.173454D+00	0.643757D-01
0.032	0.924511D+00	0.635082D+00	0.381927D+00	0.191325D+00	0.741927D-01
0.033	0.947368D+00	0.661279D+00	0.406335D+00	0.209633D+00	0.846930D-01
0.034	0.968846D+00	0.686532D+00	0.430472D+00	0.228302D+00	0.958419D-01
0.035	0.989000D+00	0.710833D+00	0.454277D+00	0.247258D+00	0.107601D+00
0.036	0.100789D+01	0.734185D+00	0.477698D+00	0.266430D+00	0.119928D+00
0.037	0.102556D+01	0.756592D+00	0.500691D+00	0.285755D+00	0.132781D+00
0.038	0.104208D+01	0.778065D+00	0.523220D+00	0.305170D+00	0.146115D+00
0.039	0.105750D+01	0.798618D+00	0.545253D+00	0.324619D+00	0.159883D+00
0.040	0.107186D+01	0.818267D+00	0.566765D+00	0.344050D+00	0.174042D+00
0.041	0.108523D+01	0.837032D+00	0.587736D+00	0.363416D+00	0.188546D+00
0.042	0.109765D+01	0.854934D+00	0.608151D+00	0.382673D+00	0.203351D+00
0.043	0.110916D+01	0.871994D+00	0.627997D+00	0.401783D+00	0.218414D+00
0.044	0.111982D+01	0.888237D+00	0.647268D+00	0.420710D+00	0.233694D+00
0.045	0.112967D+01	0.903687D+00	0.665957D+00	0.439423D+00	0.249150D+00

Table 2. Inverse Laplace transform $g(t)$ of $\hat{g}(s) = e^{-s\beta}$ —Continued

t	β				
	0.40	0.42	0.44	0.46	0.48
0.046	0.113875D+01	0.918367D+00	0.684064D+00	0.457894D+00	0.264745D+00
0.047	0.114709D+01	0.932303D+00	0.701587D+00	0.476097D+00	0.280442D+00
0.048	0.115474D+01	0.945520D+00	0.718531D+00	0.494012D+00	0.296207D+00
0.049	0.116173D+01	0.958043D+00	0.734898D+00	0.511619D+00	0.312007D+00
0.050	0.116810D+01	0.969895D+00	0.750694D+00	0.528903D+00	0.327812D+00
0.060	0.120401D+01	0.105666D+01	0.879260D+00	0.681859D+00	0.480848D+00
0.070	0.120500D+01	0.109958D+01	0.962365D+00	0.797412D+00	0.614166D+00
0.080	0.118608D+01	0.111388D+01	0.101155D+01	0.879415D+00	0.721629D+00
0.090	0.115610D+01	0.110979D+01	0.103644D+01	0.934203D+00	0.803710D+00
0.100	0.112030D+01	0.109406D+01	0.104425D+01	0.967935D+00	0.863552D+00
0.110	0.108183D+01	0.107110D+01	0.104023D+01	0.985781D+00	0.904981D+00
0.120	0.104258D+01	0.104386D+01	0.102810D+01	0.991828D+00	0.931641D+00
0.130	0.100370D+01	0.101424D+01	0.101054D+01	0.989212D+00	0.946687D+00
0.140	0.965844D+00	0.983542D+00	0.989407D+00	0.980311D+00	0.952723D+00
0.150	0.929393D+00	0.952596D+00	0.966045D+00	0.966908D+00	0.951843D+00
0.160	0.894540D+00	0.921958D+00	0.941400D+00	0.950341D+00	0.945708D+00
0.170	0.861368D+00	0.891987D+00	0.916142D+00	0.931613D+00	0.935623D+00
0.180	0.829885D+00	0.862904D+00	0.890744D+00	0.911470D+00	0.922610D+00
0.190	0.800057D+00	0.834843D+00	0.865538D+00	0.890471D+00	0.907465D+00
0.200	0.771825D+00	0.807874D+00	0.840754D+00	0.869031D+00	0.890808D+00
0.210	0.745114D+00	0.782026D+00	0.816548D+00	0.847460D+00	0.873120D+00
0.220	0.719845D+00	0.757298D+00	0.793022D+00	0.825984D+00	0.854775D+00
0.230	0.695932D+00	0.733672D+00	0.770239D+00	0.804769D+00	0.836061D+00
0.240	0.673294D+00	0.711115D+00	0.748236D+00	0.783936D+00	0.817201D+00
0.250	0.651849D+00	0.689590D+00	0.727027D+00	0.763569D+00	0.798366D+00
0.260	0.631522D+00	0.669052D+00	0.706614D+00	0.743726D+00	0.779685D+00
0.270	0.612240D+00	0.649456D+00	0.686986D+00	0.724445D+00	0.761256D+00
0.280	0.593933D+00	0.630755D+00	0.668127D+00	0.705748D+00	0.743153D+00
0.290	0.576540D+00	0.612903D+00	0.650014D+00	0.687645D+00	0.725428D+00
0.300	0.559999D+00	0.595856D+00	0.632624D+00	0.670140D+00	0.708119D+00
0.310	0.544257D+00	0.579569D+00	0.615929D+00	0.653227D+00	0.691253D+00
0.320	0.529261D+00	0.564002D+00	0.599901D+00	0.636897D+00	0.674844D+00
0.330	0.514965D+00	0.549114D+00	0.584513D+00	0.621139D+00	0.658903D+00
0.340	0.501325D+00	0.534868D+00	0.569735D+00	0.605937D+00	0.643431D+00
0.350	0.488299D+00	0.521229D+00	0.555540D+00	0.591274D+00	0.628428D+00
0.360	0.475851D+00	0.508163D+00	0.541902D+00	0.577132D+00	0.613889D+00
0.370	0.463945D+00	0.495639D+00	0.528793D+00	0.563494D+00	0.599805D+00
0.380	0.452549D+00	0.483627D+00	0.516190D+00	0.550341D+00	0.586169D+00
0.390	0.441633D+00	0.472100D+00	0.504067D+00	0.537653D+00	0.572969D+00
0.400	0.431169D+00	0.461031D+00	0.492402D+00	0.525413D+00	0.560193D+00
0.410	0.421131D+00	0.450396D+00	0.481173D+00	0.513603D+00	0.547829D+00
0.420	0.411496D+00	0.440173D+00	0.470359D+00	0.502205D+00	0.535864D+00
0.430	0.402240D+00	0.430339D+00	0.459941D+00	0.491201D+00	0.524285D+00
0.440	0.393343D+00	0.420875D+00	0.449899D+00	0.480575D+00	0.513078D+00
0.450	0.384786D+00	0.411762D+00	0.440216D+00	0.470312D+00	0.502232D+00
0.460	0.376551D+00	0.402982D+00	0.430874D+00	0.460396D+00	0.491732D+00
0.470	0.368621D+00	0.394518D+00	0.421859D+00	0.450812D+00	0.481566D+00
0.480	0.360979D+00	0.386355D+00	0.413154D+00	0.441546D+00	0.471721D+00
0.490	0.353612D+00	0.378479D+00	0.404747D+00	0.432585D+00	0.462187D+00
0.500	0.346505D+00	0.370874D+00	0.396622D+00	0.423916D+00	0.452950D+00

Table 2. Inverse Laplace transform $g(t)$ of $\hat{g}(s) = e^{-\beta s}$ —Continued

t	β				
	0.40	0.42	0.44	0.46	0.48
0.550	0.314454D+00	0.336511D+00	0.359819D+00	0.384538D+00	0.410854D+00
0.600	0.287281D+00	0.307300D+00	0.328438D+00	0.350840D+00	0.374675D+00
0.650	0.263990D+00	0.282217D+00	0.301435D+00	0.321772D+00	0.343378D+00
0.700	0.243835D+00	0.260483D+00	0.278004D+00	0.296508D+00	0.316126D+00
0.750	0.226243D+00	0.241498D+00	0.257517D+00	0.274396D+00	0.292247D+00
0.800	0.210772D+00	0.224794D+00	0.239482D+00	0.254918D+00	0.271198D+00
0.850	0.197073D+00	0.209999D+00	0.223504D+00	0.237658D+00	0.252541D+00
0.900	0.184869D+00	0.196817D+00	0.209268D+00	0.222279D+00	0.235919D+00
0.950	0.173937D+00	0.185010D+00	0.196517D+00	0.208508D+00	0.221036D+00
1.000	0.164093D+00	0.174381D+00	0.185042D+00	0.196118D+00	0.207652D+00
1.100	0.147104D+00	0.156044D+00	0.165256D+00	0.174768D+00	0.184607D+00
1.200	0.132983D+00	0.140815D+00	0.148840D+00	0.157075D+00	0.165535D+00
1.300	0.121084D+00	0.127994D+00	0.135036D+00	0.142215D+00	0.149542D+00
1.400	0.110936D+00	0.117073D+00	0.123290D+00	0.129591D+00	0.135976D+00
1.500	0.102193D+00	0.107673D+00	0.113195D+00	0.118755D+00	0.124352D+00
1.600	0.945906D-01	0.995101D-01	0.104439D+00	0.109371D+00	0.114302D+00
1.700	0.879277D-01	0.923638D-01	0.967832D-01	0.101179D+00	0.105542D+00
1.800	0.820461D-01	0.860627D-01	0.900420D-01	0.939757D-01	0.978536D-01
1.900	0.768208D-01	0.804712D-01	0.840678D-01	0.876011D-01	0.910602D-01
2.000	0.721517D-01	0.754805D-01	0.787423D-01	0.819268D-01	0.850226D-01
2.100	0.679577D-01	0.710027D-01	0.739700D-01	0.768490D-01	0.796279D-01
2.200	0.641725D-01	0.669658D-01	0.696728D-01	0.722829D-01	0.747841D-01
2.300	0.607413D-01	0.633104D-01	0.657863D-01	0.681586D-01	0.704153D-01
2.400	0.576186D-01	0.599870D-01	0.622571D-01	0.644182D-01	0.664587D-01
2.500	0.547661D-01	0.569544D-01	0.590402D-01	0.610130D-01	0.628616D-01
2.600	0.521515D-01	0.541776D-01	0.560979D-01	0.579023D-01	0.595799D-01
2.700	0.497475D-01	0.516269D-01	0.533980D-01	0.550513D-01	0.565761D-01
2.800	0.475306D-01	0.492769D-01	0.509133D-01	0.524304D-01	0.538181D-01
2.900	0.454806D-01	0.471059D-01	0.486201D-01	0.500143D-01	0.512787D-01
3.000	0.435802D-01	0.450951D-01	0.464983D-01	0.477811D-01	0.489343D-01
3.100	0.418141D-01	0.432281D-01	0.445301D-01	0.457118D-01	0.467645D-01
3.200	0.401692D-01	0.414908D-01	0.427004D-01	0.437900D-01	0.447516D-01
3.300	0.386340D-01	0.398707D-01	0.409956D-01	0.420013D-01	0.428800D-01
3.400	0.371982D-01	0.383568D-01	0.394041D-01	0.403330D-01	0.411363D-01
3.500	0.358530D-01	0.369395D-01	0.379154D-01	0.387740D-01	0.395084D-01
3.600	0.345904D-01	0.356103D-01	0.365204D-01	0.373145D-01	0.379860D-01
3.700	0.334032D-01	0.343615D-01	0.352110D-01	0.359457D-01	0.365595D-01
3.800	0.322853D-01	0.331864D-01	0.339798D-01	0.346598D-01	0.352208D-01
3.900	0.312310D-01	0.320790D-01	0.328205D-01	0.334500D-01	0.339624D-01
4.000	0.302352D-01	0.310339D-01	0.317272D-01	0.323101D-01	0.327778D-01
4.100	0.292935D-01	0.300461D-01	0.306947D-01	0.312345D-01	0.316609D-01
4.200	0.284016D-01	0.291114D-01	0.297184D-01	0.302182D-01	0.306065D-01
4.300	0.275560D-01	0.282257D-01	0.287939D-01	0.292566D-01	0.296098D-01
4.400	0.267533D-01	0.273855D-01	0.279176D-01	0.283458D-01	0.286664D-01
4.500	0.259904D-01	0.265875D-01	0.270859D-01	0.274820D-01	0.277725D-01
4.600	0.252646D-01	0.258288D-01	0.262956D-01	0.266618D-01	0.269243D-01
4.700	0.245733D-01	0.251066D-01	0.255440D-01	0.258823D-01	0.261188D-01
4.800	0.239143D-01	0.244186D-01	0.248283D-01	0.251406D-01	0.253530D-01
4.900	0.232854D-01	0.237624D-01	0.241462D-01	0.244342D-01	0.246241D-01
5.000	0.226847D-01	0.231360D-01	0.234955D-01	0.237608D-01	0.239298D-01

Table 2. Inverse Laplace transform $g(t)$ of $\hat{g}(s) = e^{-\beta s}$ —Continued

t	β				
	0.50	0.52	0.54	0.56	0.58
0.01	0.391772D-08				
0.02	0.371680D-03	0.939964D-05	0.404234D-07		
0.03	0.130495D-01	0.169605D-02	0.893449D-04	0.115097D-05	0.152735D-08
0.04	0.680714D-01	0.183678D-01	0.286174D-02	0.193321D-03	0.351487D-05
0.05	0.170007D+00	0.684450D-01	0.190661D-01	0.306418D-02	0.211287D-03
0.06	0.297583D+00	0.153336D+00	0.607468D-01	0.163477D-01	0.245053D-02
0.07	0.428249D+00	0.260102D+00	0.129875D+00	0.487872D-01	0.119843D-01
0.08	0.547759D+00	0.373510D+00	0.219075D+00	0.103472D+00	0.355059D-01
0.09	0.649618D+00	0.482197D+00	0.317871D+00	0.176950D+00	0.769517D-01
0.10	0.732249D+00	0.579576D+00	0.417048D+00	0.262290D+00	0.135746D+00
0.11	0.796660D+00	0.662765D+00	0.510177D+00	0.352173D+00	0.207879D+00
0.12	0.844973D+00	0.731240D+00	0.593536D+00	0.440582D+00	0.287906D+00
0.13	0.879627D+00	0.785795D+00	0.665456D+00	0.523313D+00	0.370513D+00
0.14	0.902978D+00	0.827855D+00	0.725645D+00	0.597843D+00	0.451359D+00
0.15	0.917137D+00	0.859059D+00	0.774628D+00	0.662958D+00	0.527319D+00
0.16	0.923911D+00	0.881041D+00	0.813371D+00	0.718366D+00	0.596414D+00
0.17	0.924812D+00	0.895307D+00	0.843025D+00	0.764370D+00	0.657596D+00
0.18	0.921085D+00	0.903197D+00	0.864775D+00	0.801619D+00	0.710505D+00
0.19	0.913744D+00	0.905866D+00	0.879753D+00	0.830941D+00	0.755259D+00
0.20	0.903612D+00	0.904299D+00	0.889000D+00	0.853224D+00	0.792275D+00
0.21	0.891351D+00	0.899321D+00	0.893441D+00	0.869353D+00	0.822150D+00
0.22	0.877495D+00	0.891623D+00	0.893884D+00	0.880163D+00	0.845564D+00
0.23	0.862470D+00	0.881775D+00	0.891029D+00	0.886419D+00	0.863221D+00
0.24	0.846619D+00	0.870251D+00	0.885473D+00	0.888811D+00	0.875812D+00
0.25	0.830215D+00	0.857438D+00	0.877724D+00	0.887948D+00	0.883987D+00
0.26	0.813475D+00	0.843656D+00	0.868212D+00	0.884361D+00	0.888347D+00
0.27	0.796572D+00	0.829167D+00	0.857297D+00	0.878513D+00	0.889435D+00
0.28	0.779642D+00	0.814183D+00	0.845282D+00	0.870802D+00	0.887738D+00
0.29	0.762792D+00	0.798880D+00	0.832421D+00	0.861571D+00	0.883684D+00
0.30	0.746107D+00	0.783398D+00	0.818926D+00	0.851113D+00	0.877653D+00
0.31	0.729651D+00	0.767851D+00	0.804972D+00	0.839675D+00	0.869973D+00
0.32	0.713473D+00	0.752334D+00	0.790705D+00	0.827470D+00	0.860931D+00
0.33	0.697611D+00	0.736918D+00	0.776247D+00	0.814677D+00	0.850774D+00
0.34	0.682091D+00	0.721663D+00	0.761697D+00	0.801446D+00	0.839717D+00
0.35	0.666934D+00	0.706617D+00	0.747138D+00	0.787906D+00	0.827944D+00
0.36	0.652151D+00	0.691813D+00	0.732636D+00	0.774163D+00	0.815611D+00
0.37	0.637750D+00	0.677282D+00	0.718246D+00	0.760308D+00	0.802854D+00
0.38	0.623734D+00	0.663043D+00	0.704012D+00	0.746414D+00	0.789787D+00
0.39	0.610105D+00	0.649111D+00	0.689970D+00	0.732546D+00	0.776508D+00
0.40	0.596858D+00	0.635497D+00	0.676147D+00	0.718753D+00	0.763100D+00
0.41	0.583990D+00	0.622208D+00	0.662566D+00	0.705078D+00	0.749633D+00
0.42	0.571495D+00	0.609246D+00	0.649243D+00	0.691557D+00	0.736166D+00
0.43	0.559365D+00	0.596614D+00	0.636190D+00	0.678217D+00	0.722748D+00
0.44	0.547593D+00	0.584310D+00	0.623416D+00	0.665081D+00	0.709421D+00
0.45	0.536169D+00	0.572330D+00	0.610928D+00	0.652166D+00	0.696218D+00

Table 2. Inverse Laplace transform $g(t)$ of $\hat{g}(s) = e^{-s\beta}$ —Continued

t	β				
	0.50	0.52	0.54	0.56	0.58
0.46	0.525084D+00	0.560672D+00	0.598728D+00	0.639487D+00	0.683169D+00
0.47	0.514328D+00	0.549330D+00	0.586818D+00	0.627053D+00	0.670296D+00
0.48	0.503893D+00	0.538298D+00	0.575198D+00	0.614873D+00	0.657618D+00
0.49	0.493767D+00	0.527569D+00	0.563865D+00	0.602951D+00	0.645149D+00
0.50	0.483941D+00	0.517138D+00	0.552817D+00	0.591291D+00	0.632902D+00
0.51	0.474406D+00	0.506995D+00	0.542050D+00	0.579894D+00	0.620885D+00
0.52	0.465152D+00	0.497134D+00	0.531560D+00	0.568760D+00	0.609105D+00
0.53	0.456169D+00	0.487547D+00	0.521342D+00	0.557887D+00	0.597566D+00
0.54	0.447448D+00	0.478227D+00	0.511390D+00	0.547275D+00	0.586270D+00
0.55	0.438980D+00	0.469165D+00	0.501699D+00	0.536919D+00	0.575220D+00
0.56	0.430756D+00	0.460354D+00	0.492261D+00	0.526816D+00	0.564416D+00
0.57	0.422769D+00	0.451786D+00	0.483072D+00	0.516963D+00	0.553855D+00
0.58	0.415009D+00	0.443454D+00	0.474125D+00	0.507354D+00	0.543538D+00
0.59	0.407468D+00	0.435350D+00	0.465413D+00	0.497985D+00	0.533461D+00
0.60	0.400140D+00	0.427467D+00	0.456929D+00	0.488851D+00	0.523621D+00
0.61	0.393016D+00	0.419799D+00	0.448669D+00	0.479947D+00	0.514015D+00
0.62	0.386090D+00	0.412337D+00	0.440625D+00	0.471267D+00	0.504639D+00
0.63	0.379354D+00	0.405076D+00	0.432791D+00	0.462805D+00	0.495489D+00
0.64	0.372803D+00	0.398009D+00	0.425160D+00	0.454556D+00	0.486560D+00
0.65	0.366428D+00	0.391130D+00	0.417728D+00	0.446516D+00	0.477847D+00
0.66	0.360225D+00	0.384432D+00	0.410487D+00	0.438677D+00	0.469347D+00
0.67	0.354187D+00	0.377910D+00	0.403433D+00	0.431035D+00	0.461053D+00
0.68	0.348309D+00	0.371557D+00	0.396559D+00	0.423585D+00	0.452962D+00
0.69	0.342585D+00	0.365369D+00	0.389860D+00	0.416320D+00	0.445068D+00
0.70	0.337010D+00	0.359341D+00	0.383331D+00	0.409237D+00	0.437367D+00
0.71	0.331579D+00	0.353466D+00	0.376966D+00	0.402328D+00	0.429852D+00
0.72	0.326287D+00	0.347740D+00	0.370761D+00	0.395591D+00	0.422521D+00
0.73	0.321129D+00	0.342157D+00	0.364710D+00	0.389019D+00	0.415367D+00
0.74	0.316101D+00	0.336715D+00	0.358809D+00	0.382609D+00	0.408386D+00
0.75	0.311199D+00	0.331407D+00	0.353053D+00	0.376354D+00	0.401573D+00
0.76	0.306418D+00	0.326230D+00	0.347438D+00	0.370252D+00	0.394924D+00
0.77	0.301755D+00	0.321180D+00	0.341959D+00	0.364296D+00	0.388435D+00
0.78	0.297205D+00	0.316252D+00	0.336613D+00	0.358484D+00	0.382100D+00
0.79	0.292765D+00	0.311443D+00	0.331395D+00	0.352810D+00	0.375916D+00
0.80	0.288432D+00	0.306748D+00	0.326301D+00	0.347271D+00	0.369878D+00
0.81	0.284201D+00	0.302165D+00	0.321327D+00	0.341863D+00	0.363982D+00
0.82	0.280071D+00	0.297690D+00	0.316471D+00	0.336581D+00	0.358224D+00
0.83	0.276036D+00	0.293319D+00	0.311728D+00	0.331423D+00	0.352601D+00
0.84	0.272096D+00	0.289050D+00	0.307094D+00	0.326385D+00	0.347108D+00
0.85	0.268246D+00	0.284879D+00	0.302568D+00	0.321462D+00	0.341742D+00
0.86	0.264484D+00	0.280803D+00	0.298145D+00	0.316653D+00	0.336500D+00
0.87	0.260807D+00	0.276820D+00	0.293823D+00	0.311953D+00	0.331377D+00
0.88	0.257212D+00	0.272926D+00	0.289598D+00	0.307359D+00	0.326370D+00
0.89	0.253698D+00	0.269119D+00	0.285467D+00	0.302869D+00	0.321477D+00
0.90	0.250261D+00	0.265397D+00	0.281429D+00	0.298479D+00	0.316693D+00
0.91	0.246900D+00	0.261756D+00	0.277480D+00	0.294187D+00	0.312017D+00
0.92	0.243612D+00	0.258195D+00	0.273617D+00	0.289989D+00	0.307444D+00
0.93	0.240395D+00	0.254711D+00	0.269838D+00	0.285883D+00	0.302972D+00
0.94	0.237246D+00	0.251302D+00	0.266142D+00	0.281867D+00	0.298598D+00
0.95	0.234165D+00	0.247966D+00	0.262524D+00	0.277937D+00	0.294320D+00

Table 2. Inverse Laplace transform $g(t)$ of $\hat{g}(s) = e^{-s\beta}$ —Continued

t	β				
	0.50	0.52	0.54	0.56	0.58
0.96	0.231148D+00	0.244701D+00	0.258984D+00	0.274092D+00	0.290135D+00
0.97	0.228195D+00	0.241504D+00	0.255519D+00	0.270329D+00	0.286040D+00
0.98	0.225303D+00	0.238374D+00	0.252127D+00	0.266646D+00	0.282032D+00
0.99	0.222470D+00	0.235309D+00	0.248805D+00	0.263040D+00	0.278110D+00
1.00	0.219696D+00	0.232307D+00	0.245553D+00	0.259510D+00	0.274271D+00
1.05	0.206637D+00	0.218184D+00	0.230259D+00	0.242923D+00	0.256245D+00
1.10	0.194806D+00	0.205400D+00	0.216430D+00	0.227940D+00	0.239984D+00
1.15	0.184050D+00	0.193788D+00	0.203881D+00	0.214362D+00	0.225269D+00
1.20	0.174239D+00	0.183206D+00	0.192458D+00	0.202019D+00	0.211912D+00
1.25	0.165261D+00	0.173533D+00	0.182029D+00	0.190764D+00	0.199752D+00
1.30	0.157022D+00	0.164666D+00	0.172480D+00	0.180473D+00	0.188651D+00
1.35	0.149441D+00	0.156514D+00	0.163712D+00	0.171037D+00	0.178488D+00
1.40	0.142446D+00	0.149002D+00	0.155642D+00	0.162363D+00	0.169161D+00
1.45	0.135977D+00	0.142061D+00	0.148195D+00	0.154371D+00	0.160580D+00
1.50	0.129980D+00	0.135634D+00	0.141307D+00	0.146989D+00	0.152667D+00
1.60	0.119222D+00	0.124123D+00	0.128993D+00	0.133818D+00	0.138579D+00
1.70	0.109864D+00	0.114131D+00	0.118329D+00	0.122442D+00	0.126447D+00
1.80	0.101664D+00	0.105393D+00	0.109026D+00	0.112542D+00	0.115921D+00
1.90	0.944323D-01	0.977029D-01	0.100855D+00	0.103869D+00	0.106724D+00
2.00	0.880163D-01	0.908931D-01	0.936357D-01	0.962246D-01	0.986376D-01
2.10	0.822933D-01	0.848301D-01	0.872213D-01	0.894477D-01	0.914877D-01
2.20	0.771631D-01	0.794049D-01	0.814931D-01	0.834090D-01	0.851319D-01
2.30	0.725433D-01	0.745282D-01	0.763538D-01	0.780025D-01	0.794545D-01
2.40	0.683658D-01	0.701257D-01	0.717229D-01	0.731406D-01	0.743602D-01
2.50	0.645737D-01	0.661358D-01	0.675334D-01	0.687506D-01	0.697701D-01
2.60	0.611190D-01	0.625067D-01	0.637292D-01	0.647718D-01	0.656182D-01
2.70	0.579611D-01	0.591944D-01	0.602630D-01	0.611529D-01	0.618492D-01
2.80	0.550658D-01	0.561619D-01	0.570945D-01	0.578505D-01	0.584163D-01
2.90	0.524033D-01	0.533774D-01	0.541895D-01	0.548278D-01	0.552798D-01
3.00	0.499484D-01	0.508134D-01	0.515186D-01	0.520532D-01	0.524055D-01
3.10	0.476792D-01	0.484464D-01	0.490565D-01	0.494993D-01	0.497643D-01
3.20	0.455765D-01	0.462561D-01	0.467812D-01	0.471427D-01	0.473309D-01
3.30	0.436238D-01	0.442244D-01	0.446736D-01	0.449629D-01	0.450837D-01
3.40	0.418064D-01	0.423360D-01	0.427171D-01	0.429422D-01	0.430035D-01
3.50	0.401118D-01	0.405770D-01	0.408971D-01	0.410650D-01	0.410737D-01
3.60	0.385285D-01	0.389355D-01	0.392007D-01	0.393175D-01	0.392799D-01
3.70	0.370466D-01	0.374009D-01	0.376165D-01	0.376877D-01	0.376090D-01
3.80	0.356572D-01	0.359636D-01	0.361345D-01	0.361650D-01	0.360499D-01
3.90	0.343525D-01	0.346153D-01	0.347459D-01	0.347397D-01	0.345925D-01
4.00	0.331254D-01	0.333485D-01	0.334426D-01	0.334037D-01	0.332279D-01
4.10	0.319697D-01	0.321565D-01	0.322175D-01	0.321492D-01	0.319482D-01
4.20	0.308795D-01	0.310333D-01	0.310643D-01	0.309695D-01	0.307462D-01
4.30	0.298499D-01	0.299734D-01	0.299773D-01	0.298587D-01	0.296155D-01
4.40	0.288762D-01	0.289720D-01	0.289512D-01	0.288114D-01	0.285506D-01
4.50	0.279543D-01	0.280248D-01	0.279815D-01	0.278225D-01	0.275462D-01
4.60	0.270804D-01	0.271276D-01	0.270639D-01	0.268876D-01	0.265977D-01
4.70	0.262511D-01	0.262770D-01	0.261947D-01	0.260029D-01	0.257009D-01
4.80	0.254632D-01	0.254695D-01	0.253703D-01	0.251646D-01	0.248519D-01
4.90	0.247140D-01	0.247022D-01	0.245876D-01	0.243694D-01	0.240474D-01
5.00	0.240008D-01	0.239724D-01	0.238438D-01	0.236144D-01	0.232842D-01

Table 2. Inverse Laplace transform $g(t)$ of $\hat{g}(s) = e^{-s\beta}$ —Continued

t	β				
	0.60	0.62	0.64	0.66	0.68
0.04	0.753752D-08				
0.05	0.378924D-05	0.731813D-08			
0.06	0.147234D-03	0.200982D-05	0.223739D-08		
0.07	0.153136D-02	0.690699D-04	0.553632D-06		
0.08	0.749966D-02	0.739405D-03	0.210256D-04	0.716141D-07	
0.09	0.230965D-01	0.390108D-02	0.261311D-03	0.370366D-05	0.337870D-08
0.10	0.525756D-01	0.130560D-01	0.160026D-02	0.609465D-04	0.304556D-06
0.11	0.974210D-01	0.321607D-01	0.612268D-02	0.474054D-03	0.786366D-05
0.12	0.156134D+00	0.639525D-01	0.169288D-01	0.221323D-02	0.878290D-04
0.13	0.225217D+00	0.109008D+00	0.371360D-01	0.721405D-02	0.548432D-03
0.14	0.300398D+00	0.165831D+00	0.687774D-01	0.181315D-01	0.226080D-02
0.15	0.377571D+00	0.231546D+00	0.112233D+00	0.375915D-01	0.687742D-02
0.16	0.453305D+00	0.302712D+00	0.166304D+00	0.673907D-01	0.166711D-01
0.17	0.525031D+00	0.375960D+00	0.228682D+00	0.108041D+00	0.339983D-01
0.18	0.591020D+00	0.448380D+00	0.296526D+00	0.158755D+00	0.606643D-01
0.19	0.650257D+00	0.517691D+00	0.366947D+00	0.217746D+00	0.974831D-01
0.20	0.702287D+00	0.582258D+00	0.437343D+00	0.282650D+00	0.144155D+00
0.21	0.747063D+00	0.641029D+00	0.505567D+00	0.350926D+00	0.199419D+00
0.22	0.784823D+00	0.693432D+00	0.569988D+00	0.420159D+00	0.261354D+00
0.23	0.815983D+00	0.739269D+00	0.629467D+00	0.488254D+00	0.327720D+00
0.24	0.841061D+00	0.778617D+00	0.683296D+00	0.553518D+00	0.396241D+00
0.25	0.860627D+00	0.811740D+00	0.731122D+00	0.614686D+00	0.464822D+00
0.26	0.875259D+00	0.839022D+00	0.772863D+00	0.670886D+00	0.531670D+00
0.27	0.885522D+00	0.860919D+00	0.808641D+00	0.721591D+00	0.595351D+00
0.28	0.891949D+00	0.877921D+00	0.838719D+00	0.766554D+00	0.654798D+00
0.29	0.895035D+00	0.890521D+00	0.863450D+00	0.805748D+00	0.709280D+00
0.30	0.895233D+00	0.899201D+00	0.883243D+00	0.839311D+00	0.758360D+00
0.31	0.892950D+00	0.904420D+00	0.898532D+00	0.867494D+00	0.801842D+00
0.32	0.888549D+00	0.906603D+00	0.909753D+00	0.890626D+00	0.839719D+00
0.33	0.882355D+00	0.906144D+00	0.917336D+00	0.909082D+00	0.872131D+00
0.34	0.874651D+00	0.903399D+00	0.921689D+00	0.923258D+00	0.899317D+00
0.35	0.865688D+00	0.898690D+00	0.923194D+00	0.933558D+00	0.921589D+00
0.36	0.855684D+00	0.892304D+00	0.922207D+00	0.940375D+00	0.939301D+00
0.37	0.844830D+00	0.884496D+00	0.919051D+00	0.944087D+00	0.952826D+00
0.38	0.833291D+00	0.875493D+00	0.914022D+00	0.945052D+00	0.962548D+00
0.39	0.821211D+00	0.865495D+00	0.907384D+00	0.943600D+00	0.968840D+00
0.40	0.808712D+00	0.854677D+00	0.899374D+00	0.940037D+00	0.972067D+00
0.41	0.795902D+00	0.843192D+00	0.890205D+00	0.934642D+00	0.972571D+00
0.42	0.782871D+00	0.831174D+00	0.880064D+00	0.927667D+00	0.970673D+00
0.43	0.769698D+00	0.818739D+00	0.869116D+00	0.919340D+00	0.966670D+00
0.44	0.756450D+00	0.805989D+00	0.857510D+00	0.909865D+00	0.960834D+00
0.45	0.743183D+00	0.793011D+00	0.845372D+00	0.899424D+00	0.953415D+00

Table 2. Inverse Laplace transform $g(t)$ of $\hat{g}(s)=e^{-s\beta}$ —Continued

t	β				
	0.60	0.62	0.64	0.66	0.68
0.46	0.729946D+00	0.779880D+00	0.832815D+00	0.888178D+00	0.944635D+00
0.47	0.716780D+00	0.766662D+00	0.819938D+00	0.876270D+00	0.934698D+00
0.48	0.703717D+00	0.753412D+00	0.806826D+00	0.863827D+00	0.923784D+00
0.49	0.690788D+00	0.740178D+00	0.793553D+00	0.850960D+00	0.912054D+00
0.50	0.678016D+00	0.727000D+00	0.780183D+00	0.837766D+00	0.899653D+00
0.51	0.665419D+00	0.713913D+00	0.766773D+00	0.824331D+00	0.886707D+00
0.52	0.653015D+00	0.700945D+00	0.753369D+00	0.810729D+00	0.873328D+00
0.53	0.640814D+00	0.688120D+00	0.740012D+00	0.797024D+00	0.859616D+00
0.54	0.628828D+00	0.675460D+00	0.726738D+00	0.783273D+00	0.845656D+00
0.55	0.617063D+00	0.662979D+00	0.713575D+00	0.769524D+00	0.831526D+00
0.56	0.605526D+00	0.650692D+00	0.700549D+00	0.755819D+00	0.817290D+00
0.57	0.594219D+00	0.638610D+00	0.687681D+00	0.742193D+00	0.803007D+00
0.58	0.583146D+00	0.626740D+00	0.674987D+00	0.728676D+00	0.788727D+00
0.59	0.572308D+00	0.615090D+00	0.662482D+00	0.715295D+00	0.774491D+00
0.60	0.561704D+00	0.603663D+00	0.650177D+00	0.702071D+00	0.760337D+00
0.61	0.551334D+00	0.592463D+00	0.638082D+00	0.689022D+00	0.746296D+00
0.62	0.541197D+00	0.581493D+00	0.626204D+00	0.676163D+00	0.732396D+00
0.63	0.531289D+00	0.570751D+00	0.614547D+00	0.663506D+00	0.718658D+00
0.64	0.521608D+00	0.560240D+00	0.603116D+00	0.651060D+00	0.705101D+00
0.65	0.512152D+00	0.549957D+00	0.591913D+00	0.638834D+00	0.691742D+00
0.66	0.502916D+00	0.539901D+00	0.580940D+00	0.626834D+00	0.678592D+00
0.67	0.493897D+00	0.530069D+00	0.570196D+00	0.615063D+00	0.665663D+00
0.68	0.485090D+00	0.520460D+00	0.559682D+00	0.603524D+00	0.652962D+00
0.69	0.476492D+00	0.511069D+00	0.549396D+00	0.592220D+00	0.640495D+00
0.70	0.468098D+00	0.501895D+00	0.539336D+00	0.581150D+00	0.628268D+00
0.71	0.459903D+00	0.492932D+00	0.529499D+00	0.570314D+00	0.616282D+00
0.72	0.451904D+00	0.484177D+00	0.519884D+00	0.559713D+00	0.604541D+00
0.73	0.444095D+00	0.475626D+00	0.510487D+00	0.549343D+00	0.593044D+00
0.74	0.436472D+00	0.467275D+00	0.501304D+00	0.539202D+00	0.581792D+00
0.75	0.429030D+00	0.459120D+00	0.492333D+00	0.529289D+00	0.570783D+00
0.76	0.421766D+00	0.451156D+00	0.483568D+00	0.519600D+00	0.560017D+00
0.77	0.414674D+00	0.443379D+00	0.475006D+00	0.510131D+00	0.549490D+00
0.78	0.407749D+00	0.435784D+00	0.466643D+00	0.500880D+00	0.539200D+00
0.79	0.400989D+00	0.428368D+00	0.458475D+00	0.491841D+00	0.529145D+00
0.80	0.394387D+00	0.421125D+00	0.450497D+00	0.483012D+00	0.519319D+00
0.81	0.387941D+00	0.414052D+00	0.442705D+00	0.474387D+00	0.509721D+00
0.82	0.381645D+00	0.407145D+00	0.435095D+00	0.465964D+00	0.500345D+00
0.83	0.375497D+00	0.400398D+00	0.427663D+00	0.457737D+00	0.491189D+00
0.84	0.369491D+00	0.393809D+00	0.420403D+00	0.449702D+00	0.482246D+00
0.85	0.363624D+00	0.387372D+00	0.413313D+00	0.441854D+00	0.473513D+00
0.86	0.357892D+00	0.381084D+00	0.406387D+00	0.434191D+00	0.464986D+00
0.87	0.352292D+00	0.374941D+00	0.399623D+00	0.426706D+00	0.456660D+00
0.88	0.346820D+00	0.368940D+00	0.393014D+00	0.419396D+00	0.448530D+00
0.89	0.341472D+00	0.363076D+00	0.386558D+00	0.412256D+00	0.440592D+00
0.90	0.336245D+00	0.357345D+00	0.380251D+00	0.405283D+00	0.432842D+00
0.91	0.331136D+00	0.351744D+00	0.374089D+00	0.398472D+00	0.425274D+00
0.92	0.326141D+00	0.346271D+00	0.368067D+00	0.391818D+00	0.417884D+00
0.93	0.321257D+00	0.340920D+00	0.362183D+00	0.385319D+00	0.410668D+00
0.94	0.316481D+00	0.335689D+00	0.356432D+00	0.378969D+00	0.403621D+00
0.95	0.311811D+00	0.330575D+00	0.350811D+00	0.372765D+00	0.396740D+00

Table 2. Inverse Laplace transform $g(t)$ of $\hat{g}(s) = e^{-s\beta}$ —Continued

t	β				
	0.60	0.62	0.64	0.66	0.68
0.96	0.307243D+00	0.325574D+00	0.345317D+00	0.366703D+00	0.390020D+00
0.97	0.302775D+00	0.320684D+00	0.339946D+00	0.360780D+00	0.383456D+00
0.98	0.298404D+00	0.315902D+00	0.334695D+00	0.354992D+00	0.377044D+00
0.99	0.294127D+00	0.311224D+00	0.329561D+00	0.349334D+00	0.370782D+00
1.00	0.289941D+00	0.306647D+00	0.324541D+00	0.343805D+00	0.364664D+00
1.05	0.270305D+00	0.285199D+00	0.301039D+00	0.317957D+00	0.336112D+00
1.10	0.252620D+00	0.265918D+00	0.279956D+00	0.294828D+00	0.310641D+00
1.15	0.236643D+00	0.248533D+00	0.260990D+00	0.274075D+00	0.287857D+00
1.20	0.222166D+00	0.232811D+00	0.243879D+00	0.255404D+00	0.267422D+00
1.25	0.209010D+00	0.218553D+00	0.228397D+00	0.238556D+00	0.249042D+00
1.30	0.197020D+00	0.205586D+00	0.214351D+00	0.223312D+00	0.232463D+00
1.35	0.186065D+00	0.193762D+00	0.201572D+00	0.209481D+00	0.217468D+00
1.40	0.176028D+00	0.182951D+00	0.189916D+00	0.196898D+00	0.203867D+00
1.45	0.166810D+00	0.173043D+00	0.179257D+00	0.185422D+00	0.191499D+00
1.50	0.158324D+00	0.163939D+00	0.169486D+00	0.174928D+00	0.180222D+00
1.60	0.143256D+00	0.147820D+00	0.152240D+00	0.156473D+00	0.160471D+00
1.70	0.130322D+00	0.134036D+00	0.137553D+00	0.140831D+00	0.143817D+00
1.80	0.119135D+00	0.122155D+00	0.124945D+00	0.127461D+00	0.129653D+00
1.90	0.109391D+00	0.111842D+00	0.114041D+00	0.115946D+00	0.117510D+00
2.00	0.100849D+00	0.102830D+00	0.104546D+00	0.105958D+00	0.107023D+00
2.10	0.933166D-01	0.949066D-01	0.962261D-01	0.972392D-01	0.979051D-01
2.20	0.866384D-01	0.879024D-01	0.888946D-01	0.895821D-01	0.899282D-01
2.30	0.806879D-01	0.816785D-01	0.823994D-01	0.828207D-01	0.829094D-01
2.40	0.753614D-01	0.761218D-01	0.766169D-01	0.768197D-01	0.767010D-01
2.50	0.705730D-01	0.711388D-01	0.714454D-01	0.714686D-01	0.711823D-01
2.60	0.662512D-01	0.666521D-01	0.668009D-01	0.666760D-01	0.662545D-01
2.70	0.623362D-01	0.625969D-01	0.626132D-01	0.623662D-01	0.618356D-01
2.80	0.587775D-01	0.589186D-01	0.588236D-01	0.584758D-01	0.578575D-01
2.90	0.555321D-01	0.555711D-01	0.553825D-01	0.549515D-01	0.542629D-01
3.00	0.525636D-01	0.525153D-01	0.522479D-01	0.517484D-01	0.510037D-01
3.10	0.498407D-01	0.497176D-01	0.493837D-01	0.488280D-01	0.480391D-01
3.20	0.473363D-01	0.471491D-01	0.467594D-01	0.461576D-01	0.453343D-01
3.30	0.450273D-01	0.447850D-01	0.443484D-01	0.437092D-01	0.428594D-01
3.40	0.428932D-01	0.426038D-01	0.421279D-01	0.414584D-01	0.405889D-01
3.50	0.409165D-01	0.405867D-01	0.400779D-01	0.393843D-01	0.385005D-01
3.60	0.390817D-01	0.387172D-01	0.381811D-01	0.374685D-01	0.365752D-01
3.70	0.373751D-01	0.369311D-01	0.364224D-01	0.356951D-01	0.347961D-01
3.80	0.357849D-01	0.353656D-01	0.347884D-01	0.340502D-01	0.331486D-01
3.90	0.343003D-01	0.338596D-01	0.332673D-01	0.325213D-01	0.316199D-01
4.00	0.329120D-01	0.324531D-01	0.318489D-01	0.310977D-01	0.301986D-01
4.10	0.316117D-01	0.311375D-01	0.305239D-01	0.297697D-01	0.288748D-01
4.20	0.303919D-01	0.299049D-01	0.292841D-01	0.285289D-01	0.276397D-01
4.30	0.292458D-01	0.287482D-01	0.281222D-01	0.273676D-01	0.264854D-01
4.40	0.281675D-01	0.276613D-01	0.270316D-01	0.262791D-01	0.254048D-01
4.50	0.271517D-01	0.266384D-01	0.260066D-01	0.252572D-01	0.243918D-01
4.60	0.261933D-01	0.256746D-01	0.250419D-01	0.242966D-01	0.234407D-01
4.70	0.252882D-01	0.247652D-01	0.241327D-01	0.233924D-01	0.225465D-01
4.80	0.244323D-01	0.239062D-01	0.232748D-01	0.225401D-01	0.217046D-01
4.90	0.236219D-01	0.230937D-01	0.224643D-01	0.217359D-01	0.209111D-01
5.00	0.228539D-01	0.223245D-01	0.216977D-01	0.209759D-01	0.201622D-01

Table 2. Inverse Laplace transform $g(t)$ of $\hat{g}(s) = e^{-s\beta}$ —Continued

t	β				
	0.70	0.72	0.74	0.76	0.78
0.11	0.802539D-08				
0.12	0.416131D-06				
0.13	0.801084D-05	0.535037D-08			
0.14	0.768242D-04	0.237760D-06			
0.15	0.445589D-03	0.437149D-05	0.107936D-08		
0.16	0.178343D-02	0.423297D-04	0.555972D-07		
0.17	0.540032D-02	0.254785D-03	0.120269D-05		
0.18	0.132108D-01	0.107115D-02	0.136544D-04	0.410099D-08	
0.19	0.273863D-01	0.342000D-02	0.952427D-04	0.132391D-06	
0.20	0.498423D-01	0.881655D-02	0.457233D-03	0.211103D-05	
0.21	0.817871D-01	0.192061D-01	0.164189D-02	0.196205D-04	0.353918D-08
0.22	0.123485D+00	0.365905D-01	0.469218D-02	0.120010D-03	0.103722D-06
0.23	0.174261D+00	0.625878D-01	0.111829D-01	0.528740D-03	0.158778D-05
0.24	0.232686D+00	0.980918D-01	0.230376D-01	0.179620D-02	0.146465D-04
0.25	0.296847D+00	0.143121D+00	0.421740D-01	0.495599D-02	0.906410D-04
0.26	0.364621D+00	0.196860D+00	0.701107D-01	0.115610D-01	0.408322D-03
0.27	0.433905D+00	0.257841D+00	0.107666D+00	0.235257D-01	0.142562D-02
0.28	0.502783D+00	0.324180D+00	0.154827D+00	0.428024D-01	0.405009D-02
0.29	0.569621D+00	0.393822D+00	0.210783D+00	0.710024D-01	0.972639D-02
0.30	0.633115D+00	0.464738D+00	0.274087D+00	0.109084D+00	0.203496D-01
0.31	0.692288D+00	0.535079D+00	0.342878D+00	0.157188D+00	0.379935D-01
0.32	0.746468D+00	0.603260D+00	0.415108D+00	0.214639D+00	0.645330D-01
0.33	0.795254D+00	0.668005D+00	0.488734D+00	0.280076D+00	0.101284D+00
0.34	0.838463D+00	0.728348D+00	0.561872D+00	0.351658D+00	0.148762D+00
0.35	0.876092D+00	0.783619D+00	0.632888D+00	0.427292D+00	0.206607D+00
0.36	0.908274D+00	0.833406D+00	0.700445D+00	0.504840D+00	0.273657D+00
0.37	0.935238D+00	0.877515D+00	0.763518D+00	0.582284D+00	0.348137D+00
0.38	0.957285D+00	0.915930D+00	0.821377D+00	0.657835D+00	0.427889D+00
0.39	0.974756D+00	0.948772D+00	0.873563D+00	0.730005D+00	0.510608D+00
0.40	0.988018D+00	0.976262D+00	0.919839D+00	0.797622D+00	0.594035D+00
0.41	0.997443D+00	0.998694D+00	0.960161D+00	0.859834D+00	0.676112D+00
0.42	0.100340D+01	0.101641D+01	0.994629D+00	0.916075D+00	0.755071D+00
0.43	0.100625D+01	0.102977D+01	0.102346D+01	0.966034D+00	0.829487D+00
0.44	0.100634D+01	0.103916D+01	0.104694D+01	0.100961D+01	0.898284D+00
0.45	0.100398D+01	0.104496D+01	0.106542D+01	0.104688D+01	0.960716D+00
0.46	0.999474D+00	0.104752D+01	0.107928D+01	0.107803D+01	0.101634D+01
0.47	0.993096D+00	0.104720D+01	0.108891D+01	0.110337D+01	0.106495D+01
0.48	0.985095D+00	0.104434D+01	0.109471D+01	0.112326D+01	0.110657D+01
0.49	0.975701D+00	0.103923D+01	0.109706D+01	0.113809D+01	0.114138D+01
0.50	0.965119D+00	0.103218D+01	0.109634D+01	0.114829D+01	0.116967D+01
0.51	0.953534D+00	0.102342D+01	0.109290D+01	0.115430D+01	0.119182D+01
0.52	0.941112D+00	0.101322D+01	0.108707D+01	0.115653D+01	0.120828D+01
0.53	0.927999D+00	0.100177D+01	0.107915D+01	0.115539D+01	0.121951D+01
0.54	0.914327D+00	0.989279D+00	0.106943D+01	0.115127D+01	0.122600D+01
0.55	0.900212D+00	0.975915D+00	0.105816D+01	0.114454D+01	0.122823D+01

Table 2. Inverse Laplace transform $g(t)$ of $\hat{g}(s) = e^{-\beta s}$ —Continued

t	β				
	0.70	0.72	0.74	0.76	0.78
0.56	0.885755D+00	0.961835D+00	0.104558D+01	0.113554D+01	0.122666D+01
0.57	0.871047D+00	0.947176D+00	0.103189D+01	0.112457D+01	0.122174D+01
0.58	0.856167D+00	0.932061D+00	0.101728D+01	0.111192D+01	0.121388D+01
0.59	0.841183D+00	0.916597D+00	0.100192D+01	0.109785D+01	0.120348D+01
0.60	0.826154D+00	0.900879D+00	0.985952D+00	0.108258D+01	0.119089D+01
0.61	0.811133D+00	0.884991D+00	0.969517D+00	0.106634D+01	0.117643D+01
0.62	0.796165D+00	0.869005D+00	0.952726D+00	0.104930D+01	0.116041D+01
0.63	0.781287D+00	0.852983D+00	0.935682D+00	0.103163D+01	0.114309D+01
0.64	0.766533D+00	0.836982D+00	0.918475D+00	0.101347D+01	0.112470D+01
0.65	0.751931D+00	0.821048D+00	0.901183D+00	0.994947D+00	0.110545D+01
0.66	0.737504D+00	0.805221D+00	0.883872D+00	0.976182D+00	0.108554D+01
0.67	0.723272D+00	0.789536D+00	0.866603D+00	0.957269D+00	0.106513D+01
0.68	0.709251D+00	0.774023D+00	0.849425D+00	0.938292D+00	0.104436D+01
0.69	0.695454D+00	0.758706D+00	0.832381D+00	0.919326D+00	0.102337D+01
0.70	0.681893D+00	0.743606D+00	0.815508D+00	0.900434D+00	0.100225D+01
0.71	0.668576D+00	0.728739D+00	0.798836D+00	0.881670D+00	0.981101D+00
0.72	0.655509D+00	0.714120D+00	0.782393D+00	0.863080D+00	0.960011D+00
0.73	0.642696D+00	0.699759D+00	0.766198D+00	0.844704D+00	0.939045D+00
0.74	0.630141D+00	0.685666D+00	0.750270D+00	0.826575D+00	0.918264D+00
0.75	0.617847D+00	0.671846D+00	0.734623D+00	0.808718D+00	0.897716D+00
0.76	0.605812D+00	0.658304D+00	0.719268D+00	0.791158D+00	0.877445D+00
0.77	0.594038D+00	0.645043D+00	0.704213D+00	0.773910D+00	0.857483D+00
0.78	0.582524D+00	0.632065D+00	0.689465D+00	0.756991D+00	0.837860D+00
0.79	0.571266D+00	0.619370D+00	0.675027D+00	0.740409D+00	0.818599D+00
0.80	0.560263D+00	0.606957D+00	0.660903D+00	0.724174D+00	0.799716D+00
0.81	0.549513D+00	0.594826D+00	0.647093D+00	0.708292D+00	0.781226D+00
0.82	0.539010D+00	0.582973D+00	0.633597D+00	0.692764D+00	0.763138D+00
0.83	0.528753D+00	0.571395D+00	0.620414D+00	0.677594D+00	0.745461D+00
0.84	0.518736D+00	0.560090D+00	0.607541D+00	0.662780D+00	0.728197D+00
0.85	0.508956D+00	0.549054D+00	0.594976D+00	0.648322D+00	0.711349D+00
0.86	0.499407D+00	0.538281D+00	0.582714D+00	0.634217D+00	0.694917D+00
0.87	0.490086D+00	0.527768D+00	0.570751D+00	0.620462D+00	0.678898D+00
0.88	0.480987D+00	0.517509D+00	0.559083D+00	0.607051D+00	0.663290D+00
0.89	0.472106D+00	0.507500D+00	0.547704D+00	0.593981D+00	0.648089D+00
0.90	0.463438D+00	0.497735D+00	0.536609D+00	0.581245D+00	0.633288D+00
0.91	0.454978D+00	0.488210D+00	0.525793D+00	0.568838D+00	0.618882D+00
0.92	0.446721D+00	0.478918D+00	0.515248D+00	0.556752D+00	0.604863D+00
0.93	0.438662D+00	0.469854D+00	0.504970D+00	0.544982D+00	0.591224D+00
0.94	0.430796D+00	0.461013D+00	0.494952D+00	0.533521D+00	0.577958D+00
0.95	0.423119D+00	0.452390D+00	0.485189D+00	0.522361D+00	0.565056D+00
0.96	0.415625D+00	0.443978D+00	0.475673D+00	0.511495D+00	0.552509D+00
0.97	0.408311D+00	0.435774D+00	0.466399D+00	0.500916D+00	0.540308D+00
0.98	0.401170D+00	0.427770D+00	0.457360D+00	0.490617D+00	0.528446D+00
0.99	0.394200D+00	0.419963D+00	0.448551D+00	0.480590D+00	0.516914D+00
1.00	0.387395D+00	0.412347D+00	0.439966D+00	0.470828D+00	0.505701D+00
1.05	0.355701D+00	0.376959D+00	0.400185D+00	0.425753D+00	0.454141D+00
1.10	0.327524D+00	0.345630D+00	0.365142D+00	0.386282D+00	0.409320D+00
1.15	0.302412D+00	0.317828D+00	0.334203D+00	0.351647D+00	0.370279D+00
1.20	0.279972D+00	0.293092D+00	0.306816D+00	0.321173D+00	0.336177D+00
1.25	0.259863D+00	0.271019D+00	0.282501D+00	0.294279D+00	0.306293D+00

Table 2. Inverse Laplace transform $g(t)$ of $\hat{g}(s) = e^{-s\beta}$ —Continued

t	β				
	0.70	0.72	0.74	0.76	0.78
1.30	0.241790D+00	0.251266D+00	0.260848D+00	0.270466D+00	0.280013D+00
1.35	0.225501D+00	0.233536D+00	0.241504D+00	0.249312D+00	0.256820D+00
1.40	0.210779D+00	0.217574D+00	0.224170D+00	0.230456D+00	0.236276D+00
1.45	0.197435D+00	0.203163D+00	0.208590D+00	0.213595D+00	0.218014D+00
1.50	0.185309D+00	0.190115D+00	0.194544D+00	0.198469D+00	0.201723D+00
1.60	0.164168D+00	0.167488D+00	0.170330D+00	0.172569D+00	0.174046D+00
1.70	0.146448D+00	0.148647D+00	0.150320D+00	0.151348D+00	0.151590D+00
1.80	0.131460D+00	0.132810D+00	0.133615D+00	0.133771D+00	0.133151D+00
1.90	0.118676D+00	0.119378D+00	0.119538D+00	0.119063D+00	0.117846D+00
2.00	0.107688D+00	0.107895D+00	0.107573D+00	0.106644D+00	0.105016D+00
2.10	0.981775D-01	0.980035D-01	0.973231D-01	0.960682D-01	0.941615D-01
2.20	0.898914D-01	0.894253D-01	0.884781D-01	0.869920D-01	0.849027D-01
2.30	0.826289D-01	0.819389D-01	0.807947D-01	0.791477D-01	0.769447D-01
2.40	0.762284D-01	0.753671D-01	0.740791D-01	0.723236D-01	0.700569D-01
2.50	0.705586D-01	0.695672D-01	0.681760D-01	0.663512D-01	0.640573D-01
2.60	0.655121D-01	0.644229D-01	0.629600D-01	0.610953D-01	0.588004D-01
2.70	0.610005D-01	0.598390D-01	0.583285D-01	0.564461D-01	0.541690D-01
2.80	0.569507D-01	0.557369D-01	0.541974D-01	0.523138D-01	0.500683D-01
2.90	0.533013D-01	0.520511D-01	0.504972D-01	0.486248D-01	0.464202D-01
3.00	0.500009D-01	0.487271D-01	0.471699D-01	0.453179D-01	0.431608D-01
3.10	0.470062D-01	0.457187D-01	0.441669D-01	0.423421D-01	0.402368D-01
3.20	0.442803D-01	0.429871D-01	0.414474D-01	0.396545D-01	0.376038D-01
3.30	0.417916D-01	0.404992D-01	0.389765D-01	0.372191D-01	0.352243D-01
3.40	0.395133D-01	0.382266D-01	0.367248D-01	0.350052D-01	0.330669D-01
3.50	0.374220D-01	0.361450D-01	0.346670D-01	0.329867D-01	0.311046D-01
3.60	0.354977D-01	0.342335D-01	0.327812D-01	0.311411D-01	0.293147D-01
3.70	0.337228D-01	0.324738D-01	0.310489D-01	0.294492D-01	0.276774D-01
3.80	0.320821D-01	0.308502D-01	0.294536D-01	0.278943D-01	0.261758D-01
3.90	0.305623D-01	0.293489D-01	0.279812D-01	0.264619D-01	0.247953D-01
4.00	0.291516D-01	0.279578D-01	0.266192D-01	0.251394D-01	0.235232D-01
4.10	0.278398D-01	0.266662D-01	0.253569D-01	0.239158D-01	0.223483D-01
4.20	0.266176D-01	0.254649D-01	0.241847D-01	0.227815D-01	0.212610D-01
4.30	0.254771D-01	0.243454D-01	0.230940D-01	0.217278D-01	0.202527D-01
4.40	0.244109D-01	0.233005D-01	0.220776D-01	0.207473D-01	0.193159D-01
4.50	0.234128D-01	0.223236D-01	0.211286D-01	0.198332D-01	0.184439D-01
4.60	0.224768D-01	0.214088D-01	0.202413D-01	0.189798D-01	0.176310D-01
4.70	0.215980D-01	0.205510D-01	0.194103D-01	0.181816D-01	0.168717D-01
4.80	0.207717D-01	0.197454D-01	0.186309D-01	0.174340D-01	0.161616D-01
4.90	0.199937D-01	0.189879D-01	0.178990D-01	0.167328D-01	0.154963D-01
5.00	0.192603D-01	0.182746D-01	0.172106D-01	0.160741D-01	0.148722D-01

Table 2. Inverse Laplace transform $g(t)$ of $\hat{g}(s)=e^{-s\beta}$ —Continued

t	β				
	0.80	0.82	0.84	0.86	0.88
0.25	0.255413D-07				
0.26	0.477184D-06				
0.27	0.525457D-05				
0.28	0.379878D-04	0.126195D-08			
0.29	0.195935D-03	0.393014D-07			
0.30	0.769172D-03	0.661087D-06			
0.31	0.241777D-02	0.679523D-05			
0.32	0.633452D-02	0.469762D-04			
0.33	0.142827D-01	0.235440D-03	0.134598D-07		
0.34	0.284347D-01	0.907667D-03	0.277183D-06		
0.35	0.510312D-01	0.282134D-02	0.338285D-05		
0.36	0.839632D-01	0.734202D-02	0.270323D-04		
0.37	0.128408D+00	0.164880D-01	0.153019D-03		
0.38	0.184615D+00	0.327469D-01	0.653185D-03	0.211304D-07	
0.39	0.251870D+00	0.586822D-01	0.221037D-02	0.429655D-06	
0.40	0.328623D+00	0.964459D-01	0.617305D-02	0.519765D-05	
0.41	0.412712D+00	0.147350D+00	0.146982D-01	0.412273D-04	
0.42	0.501631D+00	0.211615D+00	0.306364D-01	0.231645D-03	
0.43	0.592782D+00	0.288329D+00	0.571221D-01	0.980769D-03	0.391931D-08
0.44	0.683687D+00	0.375601D+00	0.969762D-01	0.328848D-02	0.123064D-06
0.45	0.772133D+00	0.470836D+00	0.152115D+00	0.908959D-02	0.209758D-05
0.46	0.856271D+00	0.571057D+00	0.223145D+00	0.213979D-01	0.217958D-04
0.47	0.934646D+00	0.673206D+00	0.309230D+00	0.440573D-01	0.151403D-03
0.48	0.100620D+01	0.774397D+00	0.408235D+00	0.810860D-01	0.756786D-03
0.49	0.107025D+01	0.872089D+00	0.517052D+00	0.135811D+00	0.288761D-02
0.50	0.112644D+01	0.964190D+00	0.632014D+00	0.210091D+00	0.882059D-02
0.51	0.117466D+01	0.104910D+01	0.749308D+00	0.303876D+00	0.224174D-01
0.52	0.121504D+01	0.112569D+01	0.865316D+00	0.415177D+00	0.489103D-01
0.53	0.124788D+01	0.119327D+01	0.976859D+00	0.540408D+00	0.939817D-01
0.54	0.127358D+01	0.125155D+01	0.108134D+01	0.674938D+00	0.162409D+00
0.55	0.129264D+01	0.130052D+01	0.117680D+01	0.813706D+00	0.256789D+00
0.56	0.130560D+01	0.134044D+01	0.126191D+01	0.951773D+00	0.376807D+00
0.57	0.131301D+01	0.137174D+01	0.133590D+01	0.108473D+01	0.519216D+00
0.58	0.131544D+01	0.139498D+01	0.139849D+01	0.120895D+01	0.678437D+00
0.59	0.131345D+01	0.141080D+01	0.144980D+01	0.132171D+01	0.847512D+00
0.60	0.130757D+01	0.141988D+01	0.149023D+01	0.142118D+01	0.101910D+01
0.61	0.129829D+01	0.142291D+01	0.152043D+01	0.150636D+01	0.118632D+01
0.62	0.128607D+01	0.142059D+01	0.154116D+01	0.157692D+01	0.134336D+01
0.63	0.127135D+01	0.141356D+01	0.155330D+01	0.163310D+01	0.148574D+01
0.64	0.125450D+01	0.140245D+01	0.155772D+01	0.167555D+01	0.161045D+01
0.65	0.123589D+01	0.138785D+01	0.155534D+01	0.170523D+01	0.171579D+01

Table 2. Inverse Laplace transform $g(t)$ of $\hat{g}(s) = e^{-\beta s}$ —Continued

t	β				
	0.80	0.82	0.84	0.86	0.88
0.66	0.121583D+01	0.137028D+01	0.154702D+01	0.172324D+01	0.180120D+01
0.67	0.119460D+01	0.135023D+01	0.153357D+01	0.173081D+01	0.186705D+01
0.68	0.117244D+01	0.132813D+01	0.151577D+01	0.172918D+01	0.191436D+01
0.69	0.114958D+01	0.130438D+01	0.149432D+01	0.171957D+01	0.194460D+01
0.70	0.112621D+01	0.127931D+01	0.146985D+01	0.170315D+01	0.195951D+01
0.71	0.110249D+01	0.125324D+01	0.144294D+01	0.168100D+01	0.196094D+01
0.72	0.107858D+01	0.122643D+01	0.141408D+01	0.165410D+01	0.195076D+01
0.73	0.105459D+01	0.119910D+01	0.138373D+01	0.162336D+01	0.193074D+01
0.74	0.103064D+01	0.117146D+01	0.135226D+01	0.158956D+01	0.190258D+01
0.75	0.100681D+01	0.114369D+01	0.132002D+01	0.155340D+01	0.186780D+01
0.76	0.983178D+00	0.111592D+01	0.128730D+01	0.151549D+01	0.182776D+01
0.77	0.959818D+00	0.108828D+01	0.125433D+01	0.147635D+01	0.178366D+01
0.78	0.936781D+00	0.106087D+01	0.122133D+01	0.143642D+01	0.173656D+01
0.79	0.914109D+00	0.103379D+01	0.118848D+01	0.139608D+01	0.168733D+01
0.80	0.891840D+00	0.100711D+01	0.115592D+01	0.135565D+01	0.163673D+01
0.81	0.870002D+00	0.980871D+00	0.112377D+01	0.131539D+01	0.158540D+01
0.82	0.848618D+00	0.955136D+00	0.109214D+01	0.127552D+01	0.153386D+01
0.83	0.827706D+00	0.929938D+00	0.106109D+01	0.123622D+01	0.148254D+01
0.84	0.807276D+00	0.905305D+00	0.103069D+01	0.119762D+01	0.143177D+01
0.85	0.787338D+00	0.881259D+00	0.100100D+01	0.115984D+01	0.138185D+01
0.86	0.767897D+00	0.857814D+00	0.972040D+00	0.112296D+01	0.133297D+01
0.87	0.748953D+00	0.834979D+00	0.943843D+00	0.108704D+01	0.128531D+01
0.88	0.730507D+00	0.812759D+00	0.916425D+00	0.105213D+01	0.123899D+01
0.89	0.712555D+00	0.791156D+00	0.889796D+00	0.101827D+01	0.119408D+01
0.90	0.695094D+00	0.770166D+00	0.863958D+00	0.985464D+00	0.115066D+01
0.91	0.678116D+00	0.749785D+00	0.838910D+00	0.953725D+00	0.110874D+01
0.92	0.661615D+00	0.730004D+00	0.814646D+00	0.923050D+00	0.106835D+01
0.93	0.645582D+00	0.710816D+00	0.791156D+00	0.893431D+00	0.102948D+01
0.94	0.630007D+00	0.692210D+00	0.768428D+00	0.864854D+00	0.992123D+00
0.95	0.614883D+00	0.674173D+00	0.746446D+00	0.837299D+00	0.956246D+00
0.96	0.600197D+00	0.656693D+00	0.725195D+00	0.810745D+00	0.921820D+00
0.97	0.585939D+00	0.639756D+00	0.704657D+00	0.785167D+00	0.888808D+00
0.98	0.572099D+00	0.623348D+00	0.684812D+00	0.760537D+00	0.857168D+00
0.99	0.558665D+00	0.607456D+00	0.665641D+00	0.736827D+00	0.826855D+00
1.00	0.545627D+00	0.592064D+00	0.647125D+00	0.714008D+00	0.797822D+00
1.05	0.485978D+00	0.522098D+00	0.563645D+00	0.612226D+00	0.670177D+00
1.10	0.434586D+00	0.462487D+00	0.493521D+00	0.528288D+00	0.567472D+00
1.15	0.390223D+00	0.411597D+00	0.434485D+00	0.458877D+00	0.484524D+00
1.20	0.351812D+00	0.368008D+00	0.384593D+00	0.401205D+00	0.417110D+00
1.25	0.318437D+00	0.330522D+00	0.342228D+00	0.353007D+00	0.361904D+00
1.30	0.289325D+00	0.298143D+00	0.306070D+00	0.312473D+00	0.316332D+00
1.35	0.263830D+00	0.270049D+00	0.275044D+00	0.278165D+00	0.278410D+00
1.40	0.241413D+00	0.245560D+00	0.248281D+00	0.248941D+00	0.246604D+00
1.45	0.221623D+00	0.224118D+00	0.225074D+00	0.223894D+00	0.219726D+00
1.50	0.204086D+00	0.205261D+00	0.204848D+00	0.202298D+00	0.196849D+00
1.60	0.174558D+00	0.173841D+00	0.171553D+00	0.167250D+00	0.160341D+00
1.70	0.150864D+00	0.148949D+00	0.145564D+00	0.140356D+00	0.132883D+00
1.80	0.131604D+00	0.128942D+00	0.124942D+00	0.119331D+00	0.111778D+00
1.90	0.115758D+00	0.112648D+00	0.108338D+00	0.102618D+00	0.952449D-01
2.00	0.102582D+00	0.992200D-01	0.947904D-01	0.891342D-01	0.820738D-01

Table 2. Inverse Laplace transform $g(t)$ of $\hat{g}(s) = e^{-s\beta}$ —Continued

t	β				
	0.80	0.82	0.84	0.86	0.88
2.10	0.915160D-01	0.880336D-01	0.836055D-01	0.781120D-01	0.714248D-01
2.20	0.821391D-01	0.786235D-01	0.742718D-01	0.689949D-01	0.627009D-01
2.30	0.741283D-01	0.706373D-01	0.664074D-01	0.613730D-01	0.554699D-01
2.40	0.672332D-01	0.638046D-01	0.597227D-01	0.549400D-01	0.494130D-01
2.50	0.612577D-01	0.579156D-01	0.539953D-01	0.494633D-01	0.442915D-01
2.60	0.560464D-01	0.528057D-01	0.490523D-01	0.447638D-01	0.399238D-01
2.70	0.514752D-01	0.483441D-01	0.447578D-01	0.407023D-01	0.361699D-01
2.80	0.474440D-01	0.444264D-01	0.410039D-01	0.371691D-01	0.329207D-01
2.90	0.438712D-01	0.409680D-01	0.377040D-01	0.340768D-01	0.300901D-01
3.00	0.406902D-01	0.379002D-01	0.347881D-01	0.313555D-01	0.276096D-01
3.10	0.378459D-01	0.351665D-01	0.321990D-01	0.289483D-01	0.254239D-01
3.20	0.352924D-01	0.327201D-01	0.298900D-01	0.268088D-01	0.234883D-01
3.30	0.329915D-01	0.305224D-01	0.278220D-01	0.248990D-01	0.217661D-01
3.40	0.309109D-01	0.285407D-01	0.259628D-01	0.231870D-01	0.202273D-01
3.50	0.290233D-01	0.267477D-01	0.242852D-01	0.216467D-01	0.188466D-01
3.60	0.273057D-01	0.251201D-01	0.227663D-01	0.202558D-01	0.176032D-01
3.70	0.257382D-01	0.236383D-01	0.213868D-01	0.189956D-01	0.164795D-01
3.80	0.243037D-01	0.222852D-01	0.201301D-01	0.178503D-01	0.154607D-01
3.90	0.229876D-01	0.210465D-01	0.189820D-01	0.168063D-01	0.145340D-01
4.00	0.217771D-01	0.199095D-01	0.179303D-01	0.158520D-01	0.136888D-01
4.10	0.206613D-01	0.188633D-01	0.169647D-01	0.149774D-01	0.129157D-01
4.20	0.196305D-01	0.178987D-01	0.160758D-01	0.141739D-01	0.122067D-01
4.30	0.186762D-01	0.170071D-01	0.152558D-01	0.134340D-01	0.115550D-01
4.40	0.177910D-01	0.161816D-01	0.144977D-01	0.127510D-01	0.109545D-01
4.50	0.169684D-01	0.154156D-01	0.137954D-01	0.121194D-01	0.104000D-01
4.60	0.162026D-01	0.147035D-01	0.131436D-01	0.115341D-01	0.988695D-02
4.70	0.154884D-01	0.140404D-01	0.125376D-01	0.109906D-01	0.941126D-02
4.80	0.148213D-01	0.134219D-01	0.119730D-01	0.104851D-01	0.896941D-02
4.90	0.141972D-01	0.128441D-01	0.114463D-01	0.100140D-01	0.855824D-02
5.00	0.136125D-01	0.123034D-01	0.109540D-01	0.957441D-02	0.817499D-02

Table 2. Inverse Laplace transform $g(t)$ of $\hat{g}(s) = e^{-s\beta}$ —Continued

t	β				
	0.90	0.92	0.94	0.96	0.98
0.49	0.175529D-08				
0.50	0.820397D-07				
0.51	0.187578D-05				
0.52	0.241437D-04				
0.53	0.195463D-03				
0.54	0.108692D-02				
0.55	0.445324D-02				
0.56	0.142197D-01	0.139846D-08			
0.57	0.370207D-01	0.105583D-06			
0.58	0.814990D-01	0.332932D-05			
0.59	0.156250D+00	0.526634D-04			
0.60	0.267214D+00	0.481944D-03			
0.61	0.415676D+00	0.285267D-02			
0.62	0.597664D+00	0.119205D-01			
0.63	0.804762D+00	0.376784D-01			
0.64	0.102585D+01	0.951387D-01			
0.65	0.124906D+01	0.200409D+00	0.161725D-06		
0.66	0.146347D+01	0.364567D+00	0.879749D-05		
0.67	0.166018D+01	0.588766D+00	0.190728D-03		
0.68	0.183281D+01	0.863064D+00	0.204369D-02		
0.69	0.197757D+01	0.116905D+01	0.127375D-01		
0.70	0.209293D+01	0.148449D+01	0.522574D-01		
0.71	0.217915D+01	0.178792D+01	0.155091D+00		
0.72	0.223785D+01	0.206190D+01	0.357914D+00		
0.73	0.227150D+01	0.229453D+01	0.678961D+00		
0.74	0.228302D+01	0.247956D+01	0.110508D+01	0.644329D-07	
0.75	0.227556D+01	0.261551D+01	0.159526D+01	0.159988D-04	
0.76	0.225220D+01	0.270449D+01	0.209580D+01	0.793681D-03	
0.77	0.221587D+01	0.275095D+01	0.255668D+01	0.125896D-01	
0.78	0.216924D+01	0.276060D+01	0.294194D+01	0.887758D-01	
0.79	0.211465D+01	0.273958D+01	0.323279D+01	0.350948D+00	
0.80	0.205417D+01	0.269392D+01	0.342548D+01	0.916457D+00	
0.81	0.198953D+01	0.262917D+01	0.352689D+01	0.177633D+01	
0.82	0.192220D+01	0.255023D+01	0.354994D+01	0.277714D+01	
0.83	0.185338D+01	0.246128D+01	0.350992D+01	0.371726D+01	
0.84	0.178405D+01	0.236580D+01	0.342203D+01	0.444662D+01	
0.85	0.171500D+01	0.226658D+01	0.329993D+01	0.490323D+01	0.569651D-07
0.86	0.164683D+01	0.216587D+01	0.315514D+01	0.509740D+01	0.471182D-03
0.87	0.158002D+01	0.206538D+01	0.299689D+01	0.507860D+01	0.642527D-01
0.88	0.151493D+01	0.196642D+01	0.283231D+01	0.490757D+01	0.902888D+00
0.89	0.145181D+01	0.186995D+01	0.266669D+01	0.464012D+01	0.358054D+01
0.90	0.139086D+01	0.177666D+01	0.250383D+01	0.432050D+01	0.700029D+01

Table 2. Inverse Laplace transform $g(t)$ of $\hat{g}(s)=e^{-s\theta}$ —Continued

t	β				
	0.90	0.92	0.94	0.96	0.98
0.91	0.133218D+01	0.168701D+01	0.234632D+01	0.398056D+01	0.921090D+01
0.92	0.127584D+01	0.160128D+01	0.219584D+01	0.364151D+01	0.971591D+01
0.93	0.122186D+01	0.151963D+01	0.205339D+01	0.331644D+01	0.907158D+01
0.94	0.117025D+01	0.144210D+01	0.191947D+01	0.301261D+01	0.793277D+01
0.95	0.112096D+01	0.136868D+01	0.179422D+01	0.273340D+01	0.671051D+01
0.96	0.107396D+01	0.129928D+01	0.167752D+01	0.247970D+01	0.559410D+01
0.97	0.102917D+01	0.123378D+01	0.156910D+01	0.225091D+01	0.464461D+01
0.98	0.986518D+00	0.117203D+01	0.146856D+01	0.204556D+01	0.386369D+01
0.99	0.945935D+00	0.111387D+01	0.137548D+01	0.186177D+01	0.323073D+01
1.00	0.907332D+00	0.105912D+01	0.128936D+01	0.169753D+01	0.271997D+01
1.05	0.741019D+00	0.830273D+00	0.946793D+00	0.110334D+01	0.128811D+01
1.10	0.611719D+00	0.661154D+00	0.713482D+00	0.755736D+00	0.716959D+00
1.15	0.510612D+00	0.534903D+00	0.551345D+00	0.542306D+00	0.447586D+00
1.20	0.430831D+00	0.439309D+00	0.435858D+00	0.404585D+00	0.302938D+00
1.25	0.367219D+00	0.365809D+00	0.351547D+00	0.311677D+00	0.217435D+00
1.30	0.315955D+00	0.308434D+00	0.288562D+00	0.246554D+00	0.163107D+00
1.35	0.274204D+00	0.262995D+00	0.240516D+00	0.199394D+00	0.126609D+00
1.40	0.239857D+00	0.226524D+00	0.203171D+00	0.164281D+00	0.100986D+00
1.45	0.211332D+00	0.196886D+00	0.173652D+00	0.137506D+00	0.823451D-01
1.50	0.187431D+00	0.172528D+00	0.149968D+00	0.116666D+00	0.683815D-01
1.60	0.150048D+00	0.135340D+00	0.114859D+00	0.868623D-01	0.492615D-01
1.70	0.122586D+00	0.108773D+00	0.905940D-01	0.670597D-01	0.371293D-01
1.80	0.101890D+00	0.892001D-01	0.731814D-01	0.532722D-01	0.289650D-01
1.90	0.859419D-01	0.743997D-01	0.602917D-01	0.433063D-01	0.232152D-01
2.00	0.734156D-01	0.629564D-01	0.504986D-01	0.358786D-01	0.190167D-01
2.10	0.634102D-01	0.539376D-01	0.428925D-01	0.301997D-01	0.158591D-01
2.20	0.552997D-01	0.467104D-01	0.368724D-01	0.257635D-01	0.134256D-01
2.30	0.486391D-01	0.408340D-01	0.320290D-01	0.222338D-01	0.115110D-01
2.40	0.431054D-01	0.359941D-01	0.280763D-01	0.193803D-01	0.997794D-02
2.50	0.384601D-01	0.319622D-01	0.248098D-01	0.170415D-01	0.873155D-02
2.60	0.345241D-01	0.285691D-01	0.220801D-01	0.151009D-01	0.770466D-02
2.70	0.311609D-01	0.256874D-01	0.197761D-01	0.134733D-01	0.684867D-02
2.80	0.282652D-01	0.232197D-01	0.178142D-01	0.120950D-01	0.612771D-02
2.90	0.257547D-01	0.210907D-01	0.161300D-01	0.109177D-01	0.551483D-02
3.00	0.235642D-01	0.192415D-01	0.146736D-01	0.990411D-02	0.498948D-02
3.10	0.216417D-01	0.176251D-01	0.134059D-01	0.902539D-02	0.453577D-02
3.20	0.199455D-01	0.162043D-01	0.122956D-01	0.825862D-02	0.414124D-02
3.30	0.184415D-01	0.149487D-01	0.113178D-01	0.758561D-02	0.379605D-02
3.40	0.171017D-01	0.138338D-01	0.104523D-01	0.699167D-02	0.349229D-02
3.50	0.159032D-01	0.128394D-01	0.968251D-02	0.646491D-02	0.322361D-02
3.60	0.148268D-01	0.119487D-01	0.899487D-02	0.599557D-02	0.298479D-02
3.70	0.138565D-01	0.111478D-01	0.837809D-02	0.557560D-02	0.277158D-02
3.80	0.129788D-01	0.104250D-01	0.782277D-02	0.519832D-02	0.258044D-02
3.90	0.121823D-01	0.977054D-02	0.732102D-02	0.485814D-02	0.240842D-02
4.00	0.114572D-01	0.917606D-02	0.686616D-02	0.455034D-02	0.225307D-02
4.20	0.101896D-01	0.813959D-02	0.607530D-02	0.401658D-02	0.198432D-02
4.40	0.912234D-02	0.727000D-02	0.541399D-02	0.357168D-02	0.176098D-02
4.60	0.821535D-02	0.653328D-02	0.485541D-02	0.319696D-02	0.157337D-02
4.80	0.743806D-02	0.590366D-02	0.437933D-02	0.287840D-02	0.141425D-02
5.00	0.676682D-02	0.536134D-02	0.397025D-02	0.260530D-02	0.127813D-02

Table 2. Inverse Laplace transform $g(t)$ of $\hat{g}(s)=e^{-s\beta}$ —Continued

t	β				
	0.990	0.995	0.997	0.998	0.999
0.9250	0.304435D-01				
0.9300	0.724474D+00				
0.9350	0.413781D+01				
0.9400	0.103257D+02				
0.9450	0.159373D+02				
0.9460	0.167331D+02				
0.9470	0.173985D+02				
0.9480	0.179335D+02				
0.9490	0.183414D+02				
0.9500	0.186282D+02				
0.9510	0.188019D+02				
0.9520	0.188719D+02				
0.9530	0.188481D+02				
0.9540	0.187412D+02				
0.9550	0.185613D+02				
0.9560	0.183187D+02				
0.9570	0.180228D+02				
0.9580	0.176827D+02	0.207732D-01			
0.9590	0.173064D+02	0.109476D+00			
0.9600	0.169014D+02	0.413897D+00			
0.9610	0.164744D+02	0.119543D+01			
0.9620	0.160311D+02	0.277546D+01			
0.9630	0.155769D+02	0.539843D+01			
0.9640	0.151160D+02	0.909628D+01			
0.9650	0.146524D+02	0.136434D+02			
0.9660	0.141892D+02	0.186215D+02			
0.9670	0.137293D+02	0.235457D+02			
0.9680	0.132750D+02	0.279852D+02			
0.9690	0.128279D+02	0.316365D+02			
0.9700	0.123898D+02	0.343449D+02			
0.9710	0.119618D+02	0.360858D+02			
0.9720	0.115447D+02	0.369291D+02			
0.9730	0.111393D+02	0.370001D+02	0.224193D-01		
0.9740	0.107461D+02	0.364475D+02	0.327681D+00		
0.9750	0.103653D+02	0.354200D+02	0.209692D+01		
0.9760	0.999722D+01	0.340534D+02	0.747066D+01		
0.9770	0.964186D+01	0.324632D+02	0.175707D+02		
0.9780	0.929917D+01	0.307431D+02	0.307895D+02		
0.9790	0.896903D+01	0.289656D+02	0.438034D+02		
0.9800	0.865126D+01	0.271853D+02	0.537808D+02		
0.9805	0.849694D+01	0.263068D+02	0.571903D+02		
0.9810	0.834562D+01	0.254412D+02	0.595157D+02		
0.9815	0.819727D+01	0.245914D+02	0.608249D+02	0.160180D+00	
0.9820	0.805183D+01	0.237599D+02	0.612297D+02	0.889475D+00	
0.9825	0.790929D+01	0.229486D+02	0.608644D+02	0.326711D+01	

Table 2. Inverse Laplace transform $g(t)$ of $\hat{g}(s)=e^{-s\beta}$ —Continued

t	β				
	0.990	0.995	0.997	0.998	0.999
0.9830	0.776958D+01	0.221588D+02	0.598693D+02	0.871315D+01	
0.9835	0.763267D+01	0.213917D+02	0.583798D+02	0.181354D+02	
0.9840	0.749853D+01	0.206479D+02	0.565191D+02	0.311551D+02	
0.9845	0.736709D+01	0.199279D+02	0.543950D+02	0.461344D+02	
0.9850	0.723832D+01	0.192318D+02	0.520981D+02	0.609020D+02	
0.9855	0.711217D+01	0.185598D+02	0.497029D+02	0.735681D+02	
0.9860	0.698860D+01	0.179116D+02	0.472686D+02	0.829855D+02	
0.9865	0.686755D+01	0.172869D+02	0.448414D+02	0.887989D+02	
0.9870	0.674899D+01	0.166854D+02	0.424560D+02	0.912470D+02	
0.9875	0.663286D+01	0.161067D+02	0.401379D+02	0.909006D+02	
0.9880	0.651912D+01	0.155500D+02	0.379049D+02	0.884433D+02	
0.9885	0.640773D+01	0.150149D+02	0.357690D+02	0.845305D+02	
0.9890	0.629863D+01	0.145007D+02	0.337370D+02	0.797185D+02	
0.9895	0.619178D+01	0.140068D+02	0.318125D+02	0.744417D+02	0.128057D-02
0.9900	0.608714D+01	0.135325D+02	0.299960D+02	0.690183D+02	0.253893D+00
0.9901	0.606647D+01	0.134399D+02	0.296456D+02	0.679369D+02	0.542909D+00
0.9902	0.604589D+01	0.133480D+02	0.292994D+02	0.668599D+02	0.107406D+01
0.9903	0.602539D+01	0.132570D+02	0.289575D+02	0.657887D+02	0.198062D+01
0.9904	0.600498D+01	0.131666D+02	0.286198D+02	0.647244D+02	0.342758D+01
0.9905	0.598466D+01	0.130770D+02	0.282862D+02	0.636679D+02	0.560072D+01
0.9906	0.596442D+01	0.129881D+02	0.279569D+02	0.626202D+02	0.868902D+01
0.9907	0.594426D+01	0.128999D+02	0.276316D+02	0.615821D+02	0.128629D+02
0.9908	0.592419D+01	0.128125D+02	0.273105D+02	0.605543D+02	0.182520D+02
0.9909	0.590420D+01	0.127258D+02	0.269934D+02	0.595376D+02	0.249263D+02
0.9910	0.588429D+01	0.126397D+02	0.266804D+02	0.585324D+02	0.328840D+02
0.9911	0.586447D+01	0.125544D+02	0.263713D+02	0.575394D+02	0.420476D+02
0.9912	0.584473D+01	0.124698D+02	0.260663D+02	0.565589D+02	0.522680D+02
0.9913	0.582507D+01	0.123858D+02	0.257652D+02	0.555914D+02	0.633368D+02
0.9914	0.580549D+01	0.123026D+02	0.254679D+02	0.546371D+02	0.750017D+02
0.9915	0.578600D+01	0.122200D+02	0.251746D+02	0.536965D+02	0.869862D+02
0.9916	0.576658D+01	0.121381D+02	0.248850D+02	0.527696D+02	0.990079D+02
0.9917	0.574725D+01	0.120569D+02	0.245993D+02	0.518567D+02	0.110795D+03
0.9918	0.572799D+01	0.119763D+02	0.243173D+02	0.509580D+02	0.122101D+03
0.9919	0.570882D+01	0.118964D+02	0.240390D+02	0.500735D+02	0.132714D+03
0.9920	0.568973D+01	0.118171D+02	0.237644D+02	0.492033D+02	0.142460D+03
0.9921	0.567071D+01	0.117385D+02	0.234934D+02	0.483476D+02	0.151211D+03
0.9922	0.565178D+01	0.116605D+02	0.232260D+02	0.475062D+02	0.158879D+03
0.9923	0.563292D+01	0.115832D+02	0.229621D+02	0.466793D+02	0.165415D+03
0.9924	0.561415D+01	0.115065D+02	0.227018D+02	0.458667D+02	0.170805D+03
0.9925	0.559545D+01	0.114304D+02	0.224449D+02	0.450684D+02	0.175065D+03
0.9926	0.557682D+01	0.113549D+02	0.221914D+02	0.442844D+02	0.178235D+03
0.9927	0.555828D+01	0.112801D+02	0.219413D+02	0.435146D+02	0.180374D+03
0.9928	0.553981D+01	0.112058D+02	0.216946D+02	0.427588D+02	0.181552D+03
0.9929	0.552142D+01	0.111322D+02	0.214512D+02	0.420169D+02	0.181851D+03
0.9930	0.550311D+01	0.110592D+02	0.212110D+02	0.412888D+02	0.181356D+03
0.9931	0.548487D+01	0.109867D+02	0.209741D+02	0.405744D+02	0.180155D+03
0.9932	0.546671D+01	0.109149D+02	0.207403D+02	0.398734D+02	0.178335D+03
0.9933	0.544862D+01	0.108436D+02	0.205097D+02	0.391858D+02	0.175979D+03
0.9934	0.543061D+01	0.107729D+02	0.202821D+02	0.385114D+02	0.173166D+03
0.9935	0.541267D+01	0.107028D+02	0.200577D+02	0.378500D+02	0.169971D+03

Table 2. Inverse Laplace transform $g(t)$ of $\hat{g}(s) = e^{-\beta}$ —Continued

t	β				
	0.990	0.995	0.997	0.998	0.999
0.9936	0.539481D+01	0.106333D+02	0.198362D+02	0.372013D+02	0.166463D+03
0.9937	0.537702D+01	0.105643D+02	0.196177D+02	0.365653D+02	0.162703D+03
0.9938	0.535930D+01	0.104959D+02	0.194022D+02	0.359417D+02	0.158747D+03
0.9939	0.534166D+01	0.104281D+02	0.191895D+02	0.353303D+02	0.154646D+03
0.9940	0.532409D+01	0.103608D+02	0.189798D+02	0.347310D+02	0.150444D+03
0.9942	0.528917D+01	0.102278D+02	0.185686D+02	0.335676D+02	0.141883D+03
0.9944	0.525454D+01	0.100970D+02	0.181685D+02	0.324499D+02	0.133313D+03
0.9946	0.522019D+01	0.996825D+01	0.177790D+02	0.313762D+02	0.124914D+03
0.9948	0.518613D+01	0.984161D+01	0.173999D+02	0.303450D+02	0.116809D+03
0.9950	0.515235D+01	0.971701D+01	0.170309D+02	0.293546D+02	0.109080D+03
0.9960	0.498757D+01	0.912334D+01	0.153274D+02	0.249607D+02	0.770202D+02
0.9970	0.482945D+01	0.857550D+01	0.138362D+02	0.213653D+02	0.550465D+02
0.9980	0.467770D+01	0.806958D+01	0.125283D+02	0.184123D+02	0.403125D+02
0.9990	0.453203D+01	0.760198D+01	0.113782D+02	0.159741D+02	0.303186D+02
1.0000	0.439217D+01	0.716940D+01	0.103644D+02	0.139490D+02	0.233847D+02
1.0010	0.425787D+01	0.676883D+01	0.946812D+01	0.122560D+02	0.184504D+02
1.0020	0.412887D+01	0.639755D+01	0.867348D+01	0.108317D+02	0.148511D+02
1.0030	0.400493D+01	0.605304D+01	0.796691D+01	0.962565D+01	0.121648D+02
1.0040	0.388584D+01	0.573305D+01	0.733683D+01	0.859805D+01	0.101177D+02
1.0050	0.377138D+01	0.543552D+01	0.677335D+01	0.771724D+01	0.852845D+01
1.0100	0.326150D+01	0.422493D+01	0.469747D+01	0.478245D+01	0.422422D+01
1.0200	0.248913D+01	0.271963D+01	0.258091D+01	0.229363D+01	0.162193D+01
1.0300	0.194690D+01	0.187297D+01	0.160578D+01	0.132261D+01	0.841468D+00
1.0400	0.155592D+01	0.135820D+01	0.108674D+01	0.853819D+00	0.511577D+00
1.0500	0.126694D+01	0.102519D+01	0.780848D+00	0.594368D+00	0.342832D+00
1.1000	0.557631D+00	0.365425D+00	0.247198D+00	0.175463D+00	0.935803D-01
1.2000	0.192128D+00	0.109266D+00	0.691426D-01	0.473530D-01	0.243272D-01
1.3000	0.949409D-01	0.513358D-01	0.317892D-01	0.215305D-01	0.109368D-01
1.4000	0.561814D-01	0.296348D-01	0.181638D-01	0.122385D-01	0.618439D-02
1.5000	0.370172D-01	0.192470D-01	0.117281D-01	0.787899D-02	0.396971D-02
1.6000	0.261897D-01	0.134914D-01	0.819031D-02	0.549201D-02	0.276190D-02
1.7000	0.194902D-01	0.997588D-02	0.604054D-02	0.404529D-02	0.203175D-02
1.8000	0.150625D-01	0.767343D-02	0.463770D-02	0.310293D-02	0.155700D-02
1.9000	0.119859D-01	0.608435D-02	0.367208D-02	0.245513D-02	0.123108D-02
2.0000	0.976264D-02	0.494191D-02	0.297928D-02	0.199084D-02	0.997720D-03
2.2000	0.683487D-02	0.344570D-02	0.207391D-02	0.138473D-02	0.693413D-03
2.4000	0.504998D-02	0.253861D-02	0.152623D-02	0.101848D-02	0.509728D-03
2.6000	0.388252D-02	0.194762D-02	0.116996D-02	0.780411D-03	0.390419D-03
2.8000	0.307752D-02	0.154129D-02	0.925282D-03	0.617008D-03	0.308575D-03
3.0000	0.249916D-02	0.125002D-02	0.750041D-03	0.500026D-03	0.250008D-03
3.2000	0.206974D-02	0.103414D-02	0.620249D-03	0.413413D-03	0.206660D-03
3.4000	0.174220D-02	0.869712D-03	0.521449D-03	0.347500D-03	0.173682D-03
3.6000	0.148669D-02	0.741601D-03	0.444507D-03	0.296181D-03	0.148011D-03
3.8000	0.128354D-02	0.639848D-03	0.383419D-03	0.255445D-03	0.127637D-03
4.0000	0.111937D-02	0.557690D-03	0.334112D-03	0.222570D-03	0.111199D-03
4.2000	0.984811D-03	0.490399D-03	0.293739D-03	0.195657D-03	0.977428D-04
4.4000	0.873143D-03	0.434595D-03	0.260267D-03	0.173346D-03	0.865894D-04
4.6000	0.779455D-03	0.387803D-03	0.232207D-03	0.154645D-03	0.772418D-04
4.8000	0.700083D-03	0.348183D-03	0.208453D-03	0.138815D-03	0.693300D-04
5.0000	0.632254D-03	0.314341D-03	0.188167D-03	0.125297D-03	0.625745D-04

Table 3. t_{\max} and $g(t_{\max})$ as a function of β , where $g(t)$ is the inverse Laplace transform of $e^{-s\beta}$

β	t_{\max}	$g(t_{\max})$
0.15	0.00000190503	450.9129
0.16	0.00000630739	209.22449
0.17	0.0000177337	108.862395
0.18	0.0000436172	62.162073
0.19	0.0000960414	38.311543
0.20	0.000192795	25.155645
0.21	0.000357987	17.416529
0.22	0.000622088	12.610041
0.23	0.00102137	9.484013
0.24	0.00159686	7.369062
0.25	0.00239285	5.888686
0.26	0.00345532	4.821523
0.27	0.00483018	4.032270
0.28	0.00656175	3.435337
0.29	0.00869134	2.974907
0.30	0.0112561	2.613581
0.31	0.0142884	2.325679
0.32	0.0178147	2.093179
0.33	0.0218560	1.903181
0.34	0.0264274	1.746284
0.35	0.0315381	1.615524
0.36	0.0371920	1.505665
0.37	0.0433880	1.412716
0.38	0.0501201	1.333598
0.39	0.0573788	1.265907
0.40	0.0651506	1.207748
0.41	0.0734193	1.157611
0.42	0.0821662	1.114283
0.43	0.0913707	1.076782
0.44	0.101011	1.044308
0.45	0.111063	1.016202
0.46	0.121503	0.991922
0.47	0.132308	0.971016
0.48	0.143453	0.953108
0.49	0.154914	0.937885
0.50	0.166667	0.925082
0.51	0.178689	0.914477
0.52	0.190959	0.905885
0.53	0.203454	0.899150
0.54	0.216155	0.894139
0.55	0.229042	0.890746
0.56	0.242097	0.888881
0.57	0.255304	0.888472

Table 3. t_{\max} and $g(t_{\max})$ as a function of β , where $g(t)$ is the inverse Laplace transform of $e^{-s\beta}$ —Continued

β	t_{\max}	$g(t_{\max})$
0.58	0.268646	0.889461
0.59	0.282109	0.891806
0.60	0.295680	0.895475
0.61	0.309346	0.900451
0.62	0.323098	0.906726
0.63	0.336924	0.914305
0.64	0.350818	0.923202
0.65	0.364772	0.933445
0.66	0.378780	0.945070
0.67	0.392837	0.958129
0.68	0.406941	0.972686
0.69	0.421088	0.988819
0.70	0.435279	1.006623
0.71	0.449512	1.026212
0.72	0.463791	1.047719
0.73	0.478118	1.071303
0.74	0.492496	1.097151
0.75	0.506933	1.125483
0.76	0.521435	1.156560
0.77	0.536011	1.190689
0.78	0.550671	1.228239
0.79	0.565430	1.269648
0.80	0.580300	1.315445
0.81	0.595300	1.366273
0.82	0.610450	1.422918
0.83	0.625773	1.486349
0.84	0.641295	1.557781
0.85	0.657048	1.638750
0.86	0.673068	1.731228
0.87	0.689397	1.837792
0.88	0.706087	1.961869
0.89	0.723197	2.108126
0.90	0.740799	2.283081
0.91	0.758982	2.496129
0.92	0.777856	2.761327
0.93	0.797561	3.100708
0.94	0.818279	3.550899
0.95	0.840258	4.177648
0.96	0.863851	5.112078
0.97	0.889596	6.659241
0.98	0.918411	9.731437
0.990	0.9522311	18.874343
0.995	0.9725934	37.055102
0.997	0.9819976	61.229747
0.998	0.9871752	91.409296
0.999	0.9928860	181.858807
1.000	1.0000000	INFINITY
1/3	0.0233204	1.847590
2/3	0.388146	0.953613
0.56787475	0.25248543	0.888440006391162 = lowest value of $g(t_{\max})$

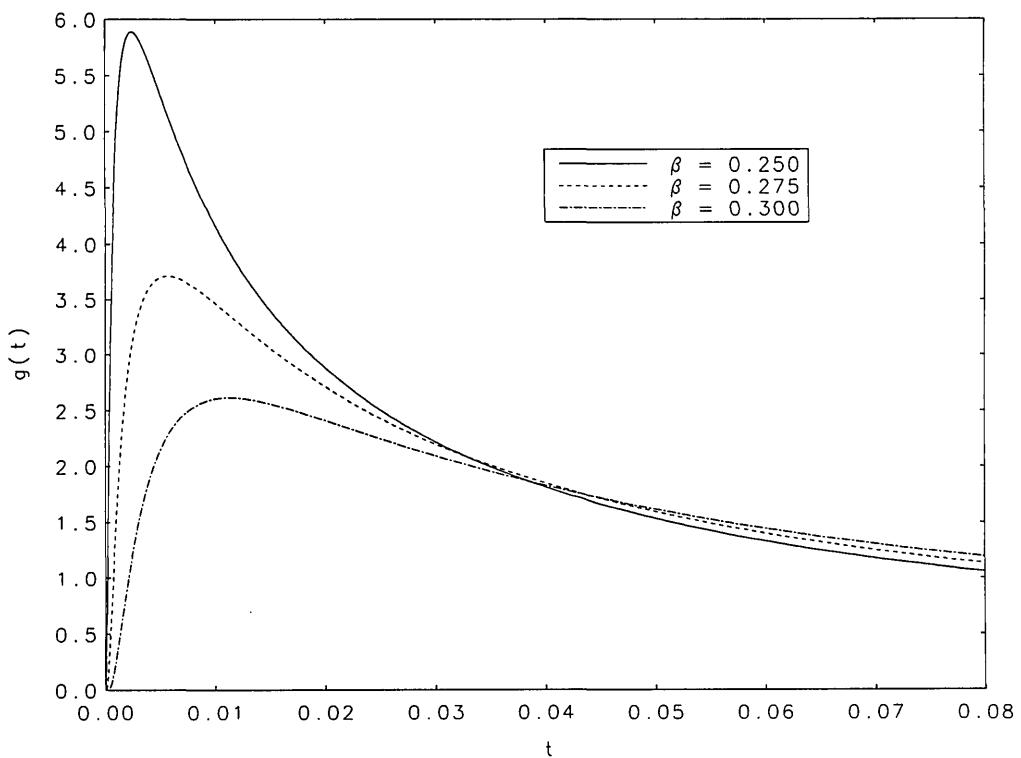


Figure 1a. Curves of $g(t)$ as a function of t in the neighborhood of the peak values for $\beta=0.25, 0.275$, and 0.30 .

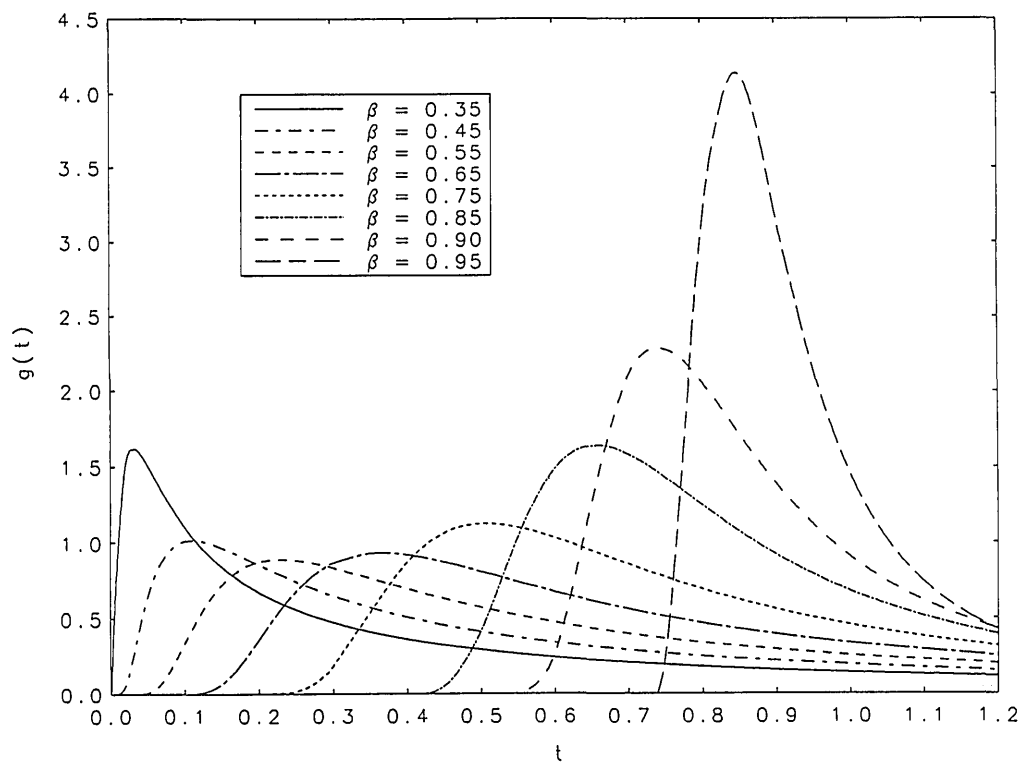


Figure 1b. Curves of $g(t)$ as a function of t in the neighborhood of the peak values for $\beta=0.35(0.1)0.95$.

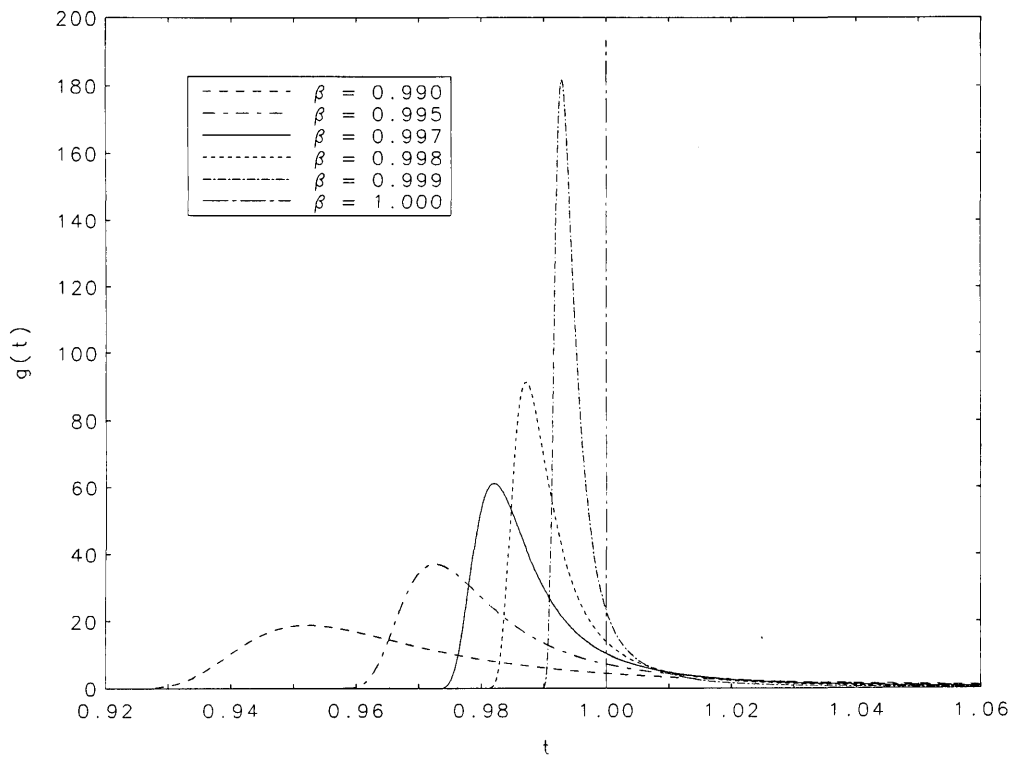


Figure 1c. Curves of $g(t)$ as a function of t in the neighborhood of the peak values for $\beta=0.99, 0.995, 0.997, 0.998$, and 0.999 . The delta function at $\beta=1$ is indicated by the vertical line.

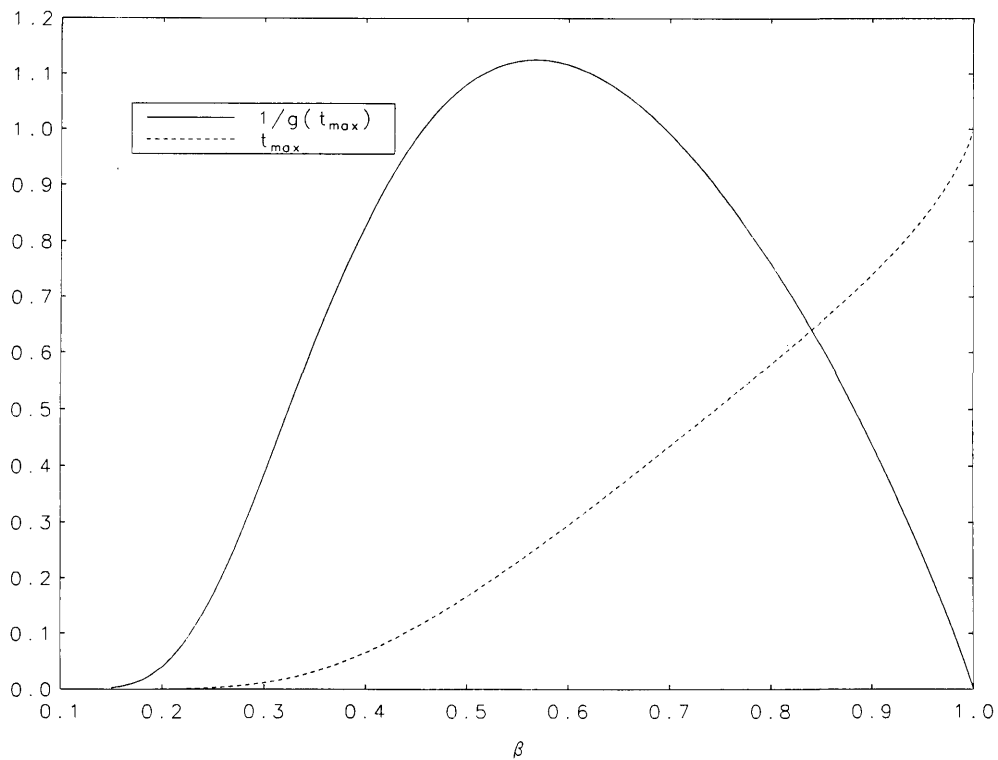


Figure 2a. Curves of t_{\max} and $1/g(t_{\max})$ plotted as a function of β .

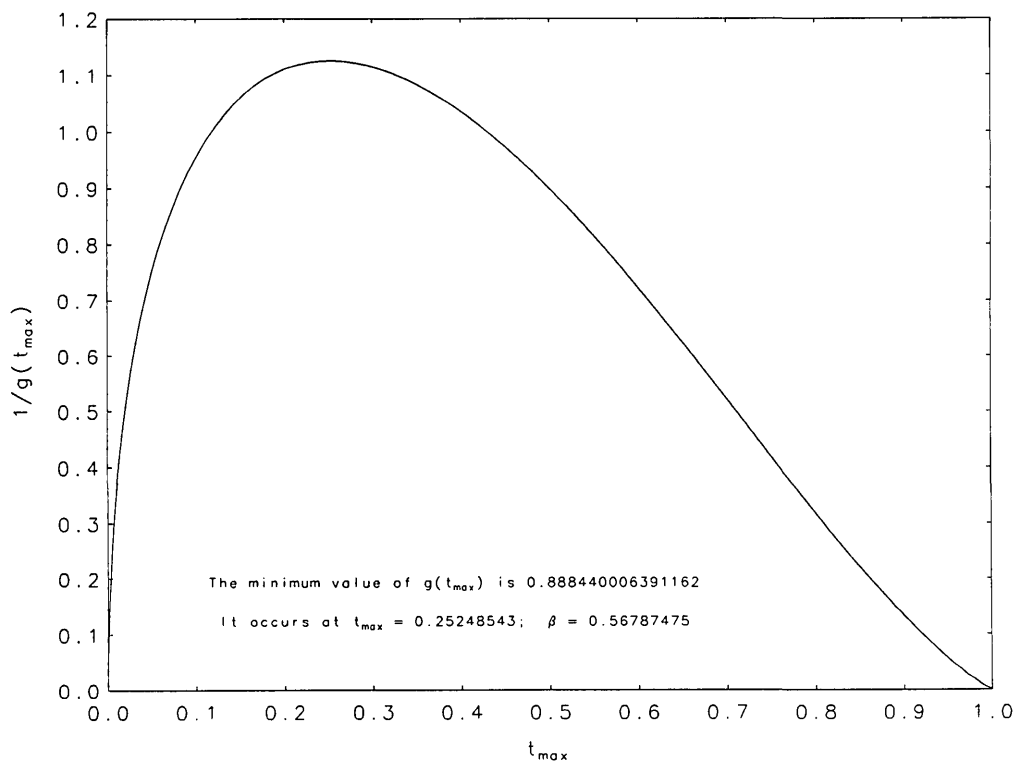


Figure 2b. Curve of $1/g(t_{\max})$ plotted as a function of t_{\max} .

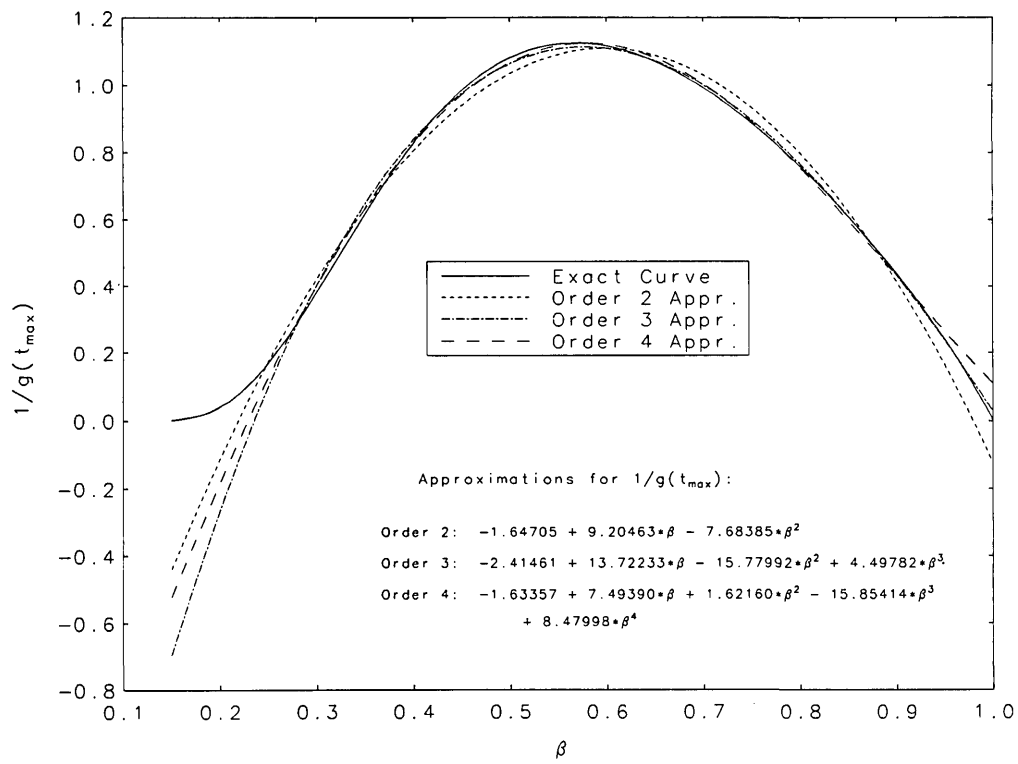


Figure 3. Second through fourth degree polynomial approximations to $1/g(t_{\max})$ as a function of β compared to the more accurately calculated value of this quantity.

4. Acknowledgment

Menachem Dishon is grateful for a position as a guest scientist at the Applied and Computational Mathematics Division of the National Institute of Standards and Technology, while on sabbatical leave from the Ministry of Defense, Tel Aviv, Israel. All computations were performed on the VAX computing facilities of the Center for Computing and Applied Mathematics at NIST.

About the authors: Menachem Dishon, an applied mathematician, served as guest scientist in NIST's Applied and Computational Mathematics Division. He has returned to his position as advisor on computerization at the Ministry of Defense, Hakirya, Tel Aviv, Israel. John T. Bendler is staff physicist at the Polymer Physics and Engineering Branch of GEC Corporate Research and Development. George H. Weiss is Chief of the Physical Sciences Laboratory, Division of Computer Research and Technology, at NIH.

5. References

- [1] For example, a historical survey is contained in Leaderman, H., Elastic and Creep Properties of Filamentous Materials and Other High Polymers, The Textile Foundation, Washington (1943).
- [2] Kohlrausch, R., Pogg. Ann. Phys. Chem. **91**, 179 (1854).
- [3] Ferry, J. D., Viscoelastic Properties of Polymers, John Wiley, New York (1970).
- [4] McCrum, N. G., Read, B. E., and Williams, G., Anelastic and Dielectric Effects in Polymeric Solids, John Wiley, New York (1967).
- [5] Struik, L. C. E., Physical Aging in Amorphous Polymers and Other Materials, Elsevier, Amsterdam (1978).
- [6] Scherer, G. W., Relaxation in Glass and Composites, John Wiley, New York (1986).
- [7] Williams, G., and Watts, D. C., Trans. Far. Soc. **66**, 80 (1970).
- [8] Davidson, D. W., and Cole, R. H., J. Chem. Phys. **19**, 1484 (1951).
- [9] Davidson, D. W., Can. J. Chem. **39**, 571 (1961).
- [10] Demoulin, C., Montrose, C. J., and Ostrowsky, N., Phys. Rev. **A9**, 1740 (1974).
- [11] Lindsey, C. P., Patterson, G. D., and Stephens, J. R., J. Polym. Sci. **17**, 1547 (1979).
- [12] Kovacs, A. J., Aklonis, J. J., Hutchinson, J. M., and Ramos, A. R., J. Polym. Sci. **17**, 1097 (1979).
- [13] Moynihan, C. T., and Lesikar, A. V., Ann. N.Y. Acad. Sci. **371**, 151 (1981).
- [14] O'Reilly, J. M., J. Appl. Phys. **50**, 6083 (1979).
- [15] Butcher, P. N., and Clark, J. D., Phil. Mag. **B42**, 191 (1980).
- [16] Clark, J. D., and Butcher, P. N., Phil. Mag. **B43**, 1017 (1981).
- [17] Weiss, G. H., Sep. Sci. Tech. **17**, 1609 (1982).
- [18] Shlesinger, M. F., Ann. Rev. Phys. Chem. **39**, 269 (1988).
- [19] Carasso, A. S., SIAM J. Appl. Math. **47**, 892 (1987).
- [20] Lindsey, C. P., and Patterson, G. D., J. Chem. Phys. **73**, 3348 (1980).
- [21] Moynihan, C. T., Boesch, L. P., and Laberge, N. L., Phys. Chem. Glasses **14**, 122 (1973).
- [22] Helfand, E., J. Chem. Phys. **78**, 1931 (1983).
- [23] Garroway, A. N., Ritchey, W. M., and Moniz, W. B., Macromolecules **15**, 1051 (1982).
- [24] Roy, A. K., Jones, A. A., and Inglefield, P. T., Macromolecules **19**, 1356 (1986).
- [25] Montroll, E. W., and Bendler, J. T., J. Stat. Phys. **34**, 129 (1984).
- [26] Pollard, H., Bull. Amer. Math. Soc. **52**, 908 (1946).
- [27] Dishon, M., Weiss, G. H., and Bendler, J. T., J. Res. Natl. Bur. Stand. (U.S.) **90**, 27 (1985).
- [28] Bergström, H., Ark. Mat. **2**, 375 (1952).
- [29] Zolotarev, V. M., Selected Trans. Math. Stat. Prob., Inst. Math. Stat. Amer. Math. Soc. **1**, 163 (1961).
- [30] Kaplan, J. I., and Garroway, A. N., J. Mag. Res. **49**, 464 (1982).
- [31] Dubner, H., and Abate, J., J. Assoc. Comp. Mach. **15**, 115 (1968).
- [32] Crump, K. S., J. Assoc. Comp. Mach. **23**, 89 (1976).
- [33] Wrench, J. W., Math. Comp. **22**, 617 (1968).

Conference Reports

INTERNATIONAL CONFERENCE ON NARROW-GAP SEMICONDUCTORS AND RELATED MATERIALS Gaithersburg, MD June 12–15, 1989

Report prepared by

D. G. Seiler

Semiconductor Electronics Division,
National Institute of Standards and Technology,
Gaithersburg, MD 20899

and

C. L. Littler

Department of Physics,
University of North Texas,
Denton, TX 76203

1. Introduction

The Semiconductor Electronics Division at the National Institute of Standards and Technology (NIST) hosted an International Conference on Narrow-Gap Semiconductors and Related Materials in Gaithersburg, MD on June 12–15, 1989. A brief background on narrow-gap semiconductors

(NGSs) is given in this paper, along with an overview of the conference itself. The major section of this report is devoted to highlights from each of the invited papers in order to put this field of semiconductor research and technology in perspective. The Conference Proceedings has been published as a special issue of *Semiconductor Science and Technology* (Institute of Physics Publishing, Bristol, March 1990, Volume 5).

1.1 Background on Narrow-Gap Semiconductors

Semiconductors are an important class of materials that not only are of scientific interest, but also have a wide variety of useful, technological applications in our modern-day world. Semiconducting phenomena have been detected in several basic forms of matter including crystals, glassy and amorphous solids, liquids, and even organic materials. A definition of a semiconductor that includes all of these materials would be somewhat too general to be useful. A narrower but more often-used definition involves the concept of a crystal which is composed of a periodic array of atoms. Here, a semiconductor is defined as a solid, crystalline material with predominantly covalent bonding and electrical conductivity that is intermediate between that of a metal and that of an insulator. The conductivity is usually strongly temperature dependent over some range of temperatures.

What are NGSs? The energy band theory of solids allows this classification of a semiconductor material in terms of the size of its fundamental energy gap, E_g , the separation between the energy of the lowest conduction band and the highest valence band. W. Zawadzki [1] has defined an NGS as a material in which the energy of an occupied electron or hole state, as measured from the corresponding band extremum, can become comparable

to the energy gap, E_g . According to this definition, any semiconductor can exhibit “narrow gap” properties under appropriate conditions (e.g., if electrons are optically excited sufficiently high above the band edge). However, a more traditional definition would identify NGSs as solids having energy gaps of less than 0.5 eV [2]. With this last definition, it is clear that NGSs are found among a broad spectrum of elements, compounds, alloys, and artificially structured materials. Table 1 gives some representative examples of NGSs. Improvements in crystal growing techniques have led to the production of many different types of alloys whose energy gaps can be adjusted by varying the composition. In particular, the emergence of molecular-beam epitaxy (MBE) technology has opened up the new field of band structure (or band gap) engineering. The MBE process refers to a technique in which several atomic (or molecular) beams impinge on a heated substrate material under ultra-high vacuum conditions. With the growth of new artificial semiconductor structures by MBE technology, the transport, optical, and other properties of the electrons and holes can be altered continuously and independently, leading to interesting new physics and new classes of semiconductor devices. Single crystalline layers are grown in registry with the substrate, permitting highly controlled epitaxial growth. Numerous specific examples of MBE-grown materials were presented at the conference.

NGSs have long been recognized for their special characteristics that give rise not only to interesting physical effects for basic studies but also to useful technological applications. In 1957, E. O. Kane [3] showed how to describe the band structure of NGSs by using the $k \cdot p$ method. This approach uses perturbation theory in conjunction with crystal symmetry requirements to investigate the wave functions and the form of the energy bands in the vicinity of high-symmetry points in k -space. The corresponding band structure can then be determined by obtaining a limited number of parameters experimentally such as energy gaps, electron and hole effective masses. This method is of considerable importance because it has a firm theoretical foundation and has been found to describe most of the semiconductor properties related to band structure. The small energy gap characteristic of an NGS usually means that the electron effective mass m^* is also small. Values of m^* less than 0.001 m_0 have been observed, where m_0 is the free electron mass. Small values of m^* lead to large carrier mobilities and many other interesting

physical properties such as high carrier saturation velocities, strong nonlinear optical effects, strong magnetic quantum effects, etc. The properties of an NGS are also more sensitive to external influences such as temperature, magnetic field, electric field, or strain, than are the larger band gap semiconductors. Some of these NGSs are used extensively as infrared detectors, particularly those that are sensitive to the regions of the electromagnetic spectrum corresponding to the atmospheric windows at 3 to 5 μm and 8 to 14 μm .

1.2 Applications of Narrow-Gap Semiconductors

Two major applications of narrow-gap materials are infrared detectors for passive imaging and diode lasers for high-resolution spectroscopy. Other applications include Hall probes for measuring magnetic fields and thermoelectric devices for power generation and cooling purposes. NGSs are also used by radio astronomers as sensitive, reliable, and comparatively fast submillimeter detectors. We briefly review the two major applications.

1.2.1 Infrared Detectors The electromagnetic radiation spectrum lying between the visible and microwave frequencies is generally defined as the infrared (IR) region. Its importance arises from the fact that every material object emits, absorbs, transmits, and reflects infrared radiation in a characteristic manner. From a study of the intensity and wavelength distribution of the radiation which has arisen from or interacted with an object, information concerning the object may be obtained. This information can be used to distinguish a body from its surroundings or to identify an unknown material. Military applications in IR technology are important for several reasons: (1) most targets of interest (vehicles, troops, etc.) differ from the surrounding terrain either in temperature or emissivity or both and thus can be seen readily by IR equipment; (2) IR systems can utilize the radiation emitted by the targets they seek (in a passive manner such that the detection system does not disclose its presence the way a radar system does); (3) IR is capable of revealing greater detail than radio or radar waves because of its shorter wavelengths. The key component of IR systems is the detector itself.

IR detectors are devices that convert electromagnetic radiation to conductive electric signals which can then be processed to obtain the information inherent in the temporal and spatial variations of the radiation. Detectors may be classified as

Table 1. Some representative narrow-gap semiconductors

Elements	Compounds					Alloys
	II-V	II-VI	III-V	IV-VI	V-VI	
Tellurium	BaAs ₃	HgS	InSb	PbS	Bi ₂ Se ₃	Hg _{1-x} Cd _x Se
Selenium	CaAs ₃	HgSe	InAs	PbSe	Bi ₂ Te ₃	Hg _{1-x} Cd _x Te
Gray Tin	Cd ₃ As ₂	HgTe		PbTe	Sb ₂ Se ₃	Hg _{1-x-y} Cd _x Mn _y Te
	Cd ₃ P ₂			SnTe	Sb ₂ Te ₃	Hg _{1-x} Fe _x Se
	α - and β -EuP ₃			GeTe		Hg _{1-x} Fe _x Te
	Zn ₃ As ₂					Hg _{1-x} Mn _x Se
	Zn ₃ P ₂					Hg _{1-x} Mn _x Te
						HgS _x Se _{1-x}
						Pb _{1-x} Mn _x Te
II-IV-V	II-IV					PbS _{1-x} Se _x
CdSnAs ₂	Mg ₂ Sn					Pb _{1-x} Sn _x Se
						Pb _{1-x} Sn _x Te
Superlattices and Quantum Wells						PbSe _x Te _{1-x}
(Many combinations from the above lists, such as HgTe/CdTe, InAs/In _{1-x} Ga _x Sb, PbTe/Pb _{1-x} Mn _x Te, etc.)						Cd _{3-x} Zn _x As ₂
						(Cd _{1-x} Mn _x) ₃ As ₂
						Pb _{1-x} Ge _x Te
						InAs _x Sb _{1-x}
						Pb _{1-x} Cd _x S
						Pb _{1-x-y} Eu _x S _y Se
						Pb _{1-x-y} Eu _x Te _y Se
						Pb _{1-x-y} Cd _x S _y Se
						Pb _{1-x} Eu _x Te
						Pb _{1-x} Eu _x Se
						Pb _{1-x} Sr _x Se

either thermal or photon detectors. The absorption of radiation in thermal detectors such as bolometers or thermopiles produces an increase in temperature which then can be measured. In photon detectors, electrons or holes, or both, are created by the absorption process, thus producing carrier concentrations and conductivities greater than the thermal equilibrium values. Important photon detectors are based upon characteristics or effects such as photoconductivity, photovoltaic effect, photoelectro-magnetic effect, and charge-transfer effects (i.e., metal-insulator-semiconductor (MIS) structures). Photon detectors are greatly superior to thermal detectors in terms of speed of response and sensitivity.

IR detectors are used extensively in military night-vision systems and remote temperature sensing. Interest also exists in heat sensing for home and industrial energy loss, medical thermography (e.g., breast cancer detection), for astronomical research, and in spectrophotometers.

1.2.2 Diode Lasers Lead-salt (i.e., PbS, PbSe, and PbTe) diode lasers have proven to be extremely valuable tools in high-resolution molecular spectroscopy with related applications to air pollution monitoring. A direct energy gap is a requirement for efficient radiative recombination and stimulated emission. The emission occurs in the infrared region at photon energies close to E_g , and the laser wavelength can be adjusted with high

precision and often over wide ranges by varying the temperature, magnetic field, or pressure in order to change E_g . Diode lasers of $\text{PbS}_{1-x}\text{Se}_x$, $\text{Pb}_{1-x}\text{Sn}_x\text{Te}$, or $\text{Pb}_{1-x}\text{Sn}_x\text{Se}$ are typically used as sources of coherent infrared radiation with wavelengths between about 4 to 30 μm . Their spectral output has an extremely narrow linewidth which is particularly attractive for high-resolution spectroscopy. Work continues today on increasing their operating temperatures, improving their output characteristics, and increasing the device operating lifetime.

2. Previous Narrow-Gap Conferences, Conference Organization, Sponsors, and Attendance

Conferences are important not only for reviewing and summarizing past research, but also for providing an overview of the current state of the art. In addition, a conference can be an important stimulus to new progress in the field. As can be seen from table 2, no conference devoted entirely to NGSs has been held since the one in Linz, Austria, in 1981. The date, place, sponsors, and published proceedings are listed there. New materials and new phenomena have subsequently arisen and, consequently, new perspectives in the field of NGSs were obtained by holding this conference. Important papers were given at the Gaithersburg Conference in 1989, covering many new materials and phenomena. The considerable progress made since the previous meeting in 1981 was reviewed, clarified, and elucidated in numerous invited talks.

The Conference Chair was David G. Seiler, Group Leader of the Materials Technology Group at the National Institute of Standards and Technology. Mike Kinch of Texas Instruments was the Program Committee Chair and Chris L. Littler the Conference Treasurer. Sponsors of the Conference were the U.S. Air Force Office of Scientific Research, American Physical Society, National Institute of Standards and Technology, National Science Foundation, U.S. Office of Naval Research, Texas Instruments, and University of North Texas. The session chairs came from well-known government, industrial, or university laboratories.

A tour through several major semiconductor laboratories of NIST's Semiconductor Electronics Division (SED) was hosted by David G. Seiler and Frank Oettinger, Division Chief. The SED conducts experimental and theoretical research on semiconductor materials, devices, and integrated circuits. The tour concentrated on visits to labs and on presentations on deep-level metrology, MBE

work, intelligent test structure metrology, and ellipsometry.

One hundred fifty-nine attendees from 14 different countries participated in the conference sessions. Seventy-two contributed and 14 invited talks were given on a wide range of bulk, film, and artificially structured materials: II-VI, III-V, IV-VI compounds and various alloy semiconductors. Topics covered ranged from IR detector device physics to the growth and characterization of artificially structured materials, as well as a review of high- T_c superconductors as IR detectors. As judged by the attendance at the conference, the quality of the talks given, the papers submitted for publication, and the oral and written comments from the attendees, the conference was a great success.

3. Highlights from Invited Papers

In this section we present some highlights selected from the invited papers given at the conference. No attempt is made to be comprehensive in these short reviews. We hope that these highlights will be interesting enough that many readers will wish to examine the complete Conference Proceedings published in *Semiconductor Science and Technology*, March 1990.

Bill Paul (Harvard University) opened the NGS Conference with some stimulating remarks and perspectives on this class of materials. He pointed out that attention to the details of the materials preparation and chemistry is essential to a determination of the correct physical properties. Furthermore, good materials preparation has been the springboard for most of the new advances in the NGS field. A review of studies on gray tin (α -Sn) was given (α -Sn was the progenitor of the whole class of zero-gap or negative-gap materials). The advent of MBE and of the production of thermodynamically metastable films may allow alloys such as Ge-Sn to be grown with direct gaps varying from about 0.5 eV to zero over a certain range of composition. Many superlattices (SLs) of the types Sn/InSb , Sn/CdTe , $\text{Sn}_x\text{Ge}_{1-x}/\text{Ge}$, $\text{Sn}_x\text{Si}_{1-x}/\text{Si}$ or $\text{Sn}/\text{Hg}_x\text{Cd}_{1-x}\text{Te}$ remain to be made and studied. He concluded that the maturing fabrication techniques for quantum wires and dots (made possible by different kinds of lithography) have already resulted in new physical phenomena and new devices and will continue to do so. One can say confidently that there are unimagined phenomena beyond the horizon, ensuring the need for meetings such as this one well into the next century.

Volume 95, Number 4, July–August 1990
Journal of Research of the National Institute of Standards and Technology

Table 2. Previous conferences on narrow-gap semiconductors

Date	Place	Sponsors and financial support	Publication
Jan. 21, 1964	Columbia Univ., New York	Topical Conference APS	Proc. of Conf. on The Physics of Semimetals published in IBM J. Res. Dev., Vol. 8, 1964. One paper on IV-VI Compounds.
April 2-4, 1968	Univ. of Durham, England		Short report of Semimetals and Narrow-Gap Semiconductors Conference given by G. A. Saunders, in J. Phys., Colloque C4, Supp. to #11-12, Vol. 29, pp. 3-8, 1968.
July 15-18, 1968	Centre National de la Recherche Scientifique, Paris, France	C.N.R.S.	International Colloquium on IV-VI Compounds, J. Phys., Colloque C4, Supp. to #11-12, Vol. 29, 1968.
Mar. 20-21, 1970	Dallas, TX, USA	Texas Instruments, ONR, LTV Research Center, Topical Conf. of APS	Physics of Semimetals and Narrow-Gap Semiconductors Conference proceedings published in J. Phys. Chem. Solid, Vol. 32, Suppl. 1, 1971, pp. 1-568.
Mar. 24-25, 1972	Univ. of Pennsylvania, Philadelphia, PA	Moore School of EE, Lab. for Res. on Struct. of Mat., Topical Conf. of APS	Physics of IV-VI Compounds and Alloys (Gordon & Breach, London, 1974).
Sept. 10-14, 1973	Nice, France Cardiff, Wales	Royal Society, Plessey Co. Limited, C.N.R.S.	Int. Conf. on The Physics of Semimetals and Narrow-Gap Semiconductors. Proceedings unpublished.
Sept. 12-15, 1977	Institute of Physics, Polish Academy of Sciences, Warsaw, Poland	Recognized by the Int. Union of Pure and Applied Physics (IUPAP)	Conf. Proc. published as Phys. of Narrow Gap Semicond. (PWN-Polish Scientific Publishing, Warsaw, 1978), pp. 1-481
Sept. 3-15, 1979	Université des Sciences et Techniques du Languedoc, Nîmes, France	Various institutions and companies includ- ing European Research Office, IBM, ONR, Thomson CSF	Int. Summer School Proc. published as Narrow-Gap Semiconductors Physics and Applications, Lecture Notes in Physics, Vol. 133 (Springer-Verlag, New York, 1980), pp. 1-572.
Sept. 14-17, 1981	Johannes Kepler Univ., Linz, Austria	IUPAP, European Phys. Soc. Austrian Phys. Soc., IBM, Siemens, European Research Office, Austrian Fed. Ministry of Science and Research	Conf. Proc. published as Physics of Narrow-Gap Semiconductors, Lecture Notes in Physics, Vol. 152 (Springer-Verlag, New York, 1982), pp. 1-485.

Gordon Osbourn (Sandia National Laboratories) reviewed the multi-quantum well (MQW) and superlattice (SL) physics which influences device performance and described the status of the leading III-V approaches for long-wavelength detection. Modern growth techniques have made possible the preparation of high-quality, single-crystal layered structures, with layer thicknesses ranging from micrometers to nanometers. These structures may provide useful alternatives to the II-VI $Hg_{1-x}Cd_xTe$ alloy system for long-wavelength detector applications. Detector technology based on III-Vs will benefit from superior bond strengths and material stability, well-behaved dopants, and high-quality III-V substrates. The MQW and SL heterostructures (HSs) have new and interesting energy band structures which depend on layer thicknesses, layer strains, and the bulk properties of the individual layers. Research has revealed a number of mechanisms for obtaining long-wavelength cutoffs in the following structures: (1) materials with "type II" band offsets (BOs) where transitions occur between hole states in one type of layer and electron states localized in the other type; (2) doping SL material with a series of back-to-back p-i-n junctions; (3) quantum-well materials with transitions occurring between the ground and first excited states in the conduction band, the energies of which are determined by the quantum size effect; and (4) strained-layer superlattice (SLS) structures with a type II BO. SLSs, such as those in the InAsSb system, are grown from lattice-mismatched alloy layers with layer thicknesses thin enough to allow complete elastic strain accommodation of the mismatch. A schematic illustration of an InAsSb SLS photovoltaic detector fabricated at Sandia is shown in figure 1. These SLS structures require minority carrier collection across the SLS layers at low temperatures for good quantum efficiencies. The carriers are collected directly from the depletion region or by diffusion from the neutral regions to the depletion region edge. Other structures reviewed were AlGaAs/GaAs, InAs/GaSb SLs, InAs/InGaSb SLSs, and InSb nipi SLs. All materials systems will require significant improvements in their detectivity values before competitive detector technologies can arise.

Horst Preier (Johannes Kepler Universität) reviewed the state of the art and the development trends of lead salt lasers. They are the key component in diode laser spectrometers. Scientific research in fields like high-resolution spectroscopy (of molecules, ions, and radicals), sub-Doppler spectroscopy in molecular beams, and heterodyne

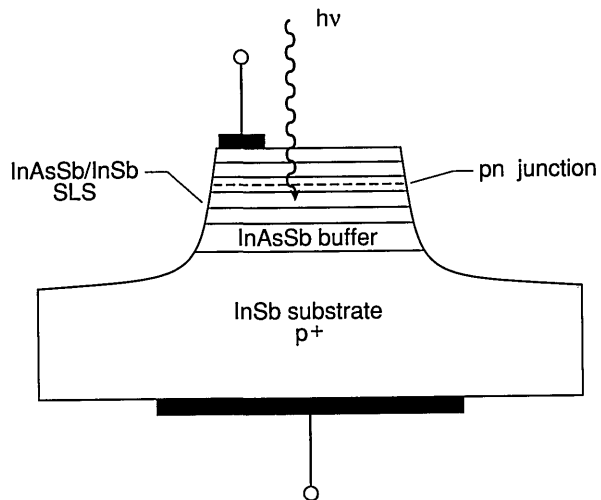


Figure 1. Schematic illustration of the InAsSb strained-layer-superlattice photodiodes fabricated at Sandia National Labs (see Conference paper of G. C. Osbourn, fig. 3). The SL is grown on a *p*-type InSb substrate with an intervening InAsSb graded buffer layer. As shown, the *pn* junction occurs within the SL structure. These SL materials can be used as direct replacements for bulk materials in standard photovoltaic or photoconductive device structures.

and acousto-optic spectroscopy relies on these diodes. Diode laser spectrometers are also used (1) in the automotive industry for time-resolved car exhaust-gas studies and for trace gas analyses, (2) for smoke stack monitoring of power plants for the detection of trace gases like NH_3 in the exhaust stream of catalytic converters, and (3) in medical diagnostics for isotope-specific analyses of exhaled breath after being treated with food or drugs labeled with stable isotopes (giving information about metabolism). The entire wavelength range from 3 to 30 μm can be covered by using ternary and quaternary compounds like PbSnTe, PbSSe, and PbEuSeTe. These lasers can be easily tuned by temperature or current and have narrow linewidths of $\approx 10^{-4} \text{ cm}^{-1}$. Only 12 institutions worldwide have been or remain involved with lead salt laser activities. The lasers have been produced by liquid phase epitaxy (LPE), hot wall epitaxy (HWE), and MBE. The advantages and disadvantages of each of these methods are summarized in figure 2. The most sophisticated and expensive technique is the MBE method. Shown in figure 3 is a typical device grown by MBE technology at Laser Analytics. The compositional control is very good, allowing exact lattice matching, and close control of the doping concentration. In-situ monitoring of the crystalline quality of the growing layers can be accomplished by RHEED analysis. Accurate thicknesses are produced by low growth rates, but

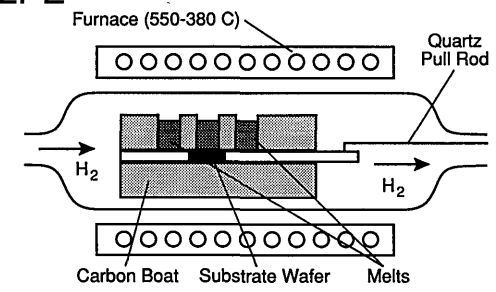
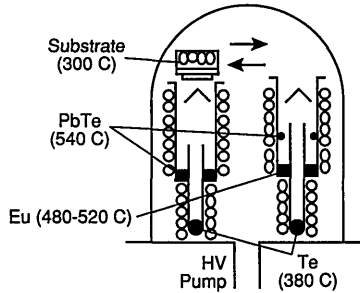
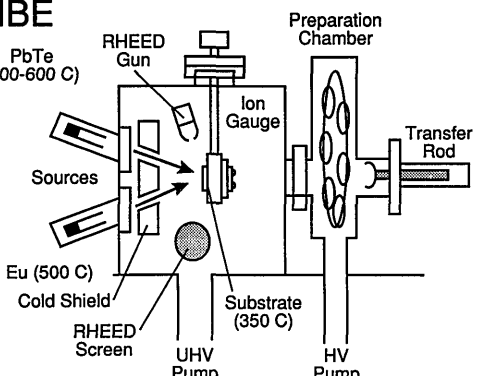
METHODS	ADVANTAGES	DISADVANTAGES
LPE 	- Simple - Cheap	- Rare earth materials difficult - Compositional change with time - Limited number of layers - No thickness control
HWE 	- Moderate price - High quality layers	- Compositional control is difficult - No in situ quality control (RHEED)
MBE 	- Highly flexible - Flux control - Lattice matched layer structures possible - Control of doping concentration	- Very expensive - Small growth rates

Figure 2. Comparison of three epitaxial growth techniques: liquid phase epitaxy (LPE), hot wall epitaxy (HWE), and molecular beam epitaxy (MBE) (see Conference paper by H. Preier, fig. 3). In the LPE method, growth occurs by controlled lowering of the melt temperature. No MQW and single QW structures can be produced by the LPE method. The HWE method is a vapor-phase epitaxy technique where substrate and source form a quasi-enclosed system. Layer structures are grown by positioning the heated substrate on top of different source furnace arrangements. As shown in the diagram, PbTe layers can be grown on the right side and PbEuTe layers on the left side. The temperature of the Eu furnace controls the Eu content, that of the Te furnace the doping concentration. Multiple-layer structures can be produced by switching the substrate back and forth. Using the MBE method, layers of various compositions can be deposited by properly combining molecular beams from different source ovens.

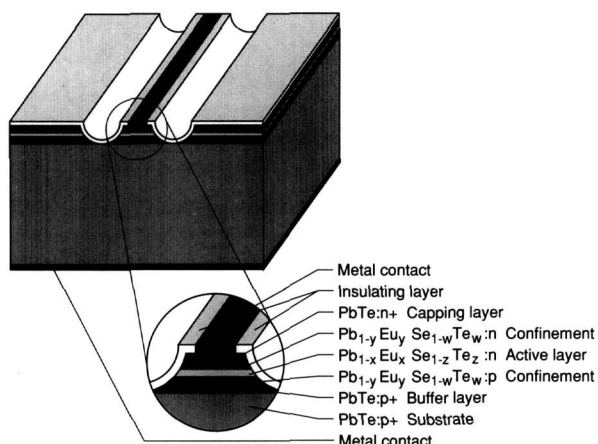


Figure 3. Schematic view of a typical device structure of an MBE grown $\text{PbEuSeTe}/\text{PbTe}$ double heterostructure laser grown at Laser Analytics (see Conference paper by H. Preier, fig. 3). Note that metal contacts have to be applied only to heavily doped PbTe and that the current is restricted to a narrow stripe region by mesa etching.

correspondingly long manufacturing times are then needed to produce the laser structure. The dominant development goal has been to increase the operating temperature to the point that only inexpensive cooling equipment is needed. Improvements in the understanding of the basic material properties of these ternary and quaternary compounds are needed to establish better theoretical models for the threshold currents.

C. Tom Elliott (Royal Signals and Radar Establishment) reviewed research work on non-equilibrium modes of operation of semiconductor devices using the phenomena of minority-carrier extraction and minority-carrier exclusion to reduce carrier densities in narrow-gap HgCdTe alloys to near "extrinsic" values at temperatures where the materials are normally intrinsic. By this means Auger noise is suppressed; it would ordinarily be a severe limiting factor for IR detectors operating at near-ambient temperatures. Experimental work on excluding-contact photoconductors (one type of non-equilibrium mode device used to study the Auger suppression) showed signal-to-noise improvements at high modulation frequencies which are consistent with the theoretically predicted Auger suppression mechanism. Bipolar transistor action, observed at temperatures where the material is near intrinsic, indicates the potential of NGSSs for devices other than IR detectors when operated in a non-equilibrium mode at ambient operating temperatures. In ordinary intrinsic semiconductor IR detectors, thermal processes compete with optical processes in the generation of free carriers and

the purpose of cooling is to reduce the thermal generation and its associated fluctuations and noise. Currently, high-sensitivity detectors for the 8- to 12- μm region are typically operated at 80 K, while those for the 3- to 5- μm region are operated around 200 K. These cooling requirements add considerably to the cost, size, and inconvenience of IR systems. The experimental and theoretical work on steady-state non-equilibrium operation described here may open up possibilities for more widespread use of NGSSs.

Peter Wolff (Massachusetts Institute of Technology) described free-carrier-induced optical nonlinearities of NGSSs. There are three electronic mechanisms that give rise to large optical nonlinearities in semiconductors: nonlinear free-carrier dynamics, band filling, and exciton resonances. There are a variety of semiconductor nonlinear optic devices, e.g., bistable phase-conjugate elements, tunable filters, and power limiters. Exciton resonances in $\text{AlGaAs}/\text{GaAs}$ SLs have large, room-temperature optical nonlinearities and are currently the most promising for optical signal-processing devices needed for all optical computers. NGSSs generally have large nonlinear optic coefficients. Comprehensive theoretical and experimental details of free-carrier optical nonlinearities were presented along with nonlinearities due to interband transitions in zero-gap materials and carrier-scattering effects.

Jerry Meyer (Naval Research Laboratory) reviewed the present understanding of band-edge and free-carrier properties in Hg-based SLs such as HgTe/CdTe . This field of study has blossomed since the first successful MBE growth of these SLs in 1982. Novel phenomena have been discovered which are distinct from anything observable in either Hg-based alloys or in wide-gap SLs. He emphasized the relation between the distinctive aspects of the SL band structures obtained theoretically and corresponding features in magneto-transport, magneto-optical, and optical data. Theoretically, there is a high sensitivity of the free carrier properties to the magnitudes of the valence band offset. For example, the identity of the dominant hole band depends on whether the valence band offset is large or small. He argued that most experimental results are qualitatively consistent with a large offset. However, there is a strong need for more detailed quantitative theories to explain the numerous unusual features of the band structure, such as mass broadening (carriers coexisting with a wide range of in-plane masses).

Günther Bauer (Montanuniversität Leoben) reviewed some of the interesting experimental investigations that have been carried out on IV-VI compound QW and SL structures. QW structures of these materials were first grown in 1980. The main application of these materials is for mid-IR lasers with relatively high operating temperatures as compared to those made from III-V materials. Many II-VI and IV-VI NGSs have large diffusion coefficients, and experiments that can give information on the diffusion constant D are important to carry out. Figure 4 shows the results of x-ray diffraction experiments on a PbTe/Pb_{1-x}Mn_xTe SL sample with $x = 0.027$ consisting of 20 periods with thicknesses $t_{\text{PbTe}} = 4.5 \text{ nm}$ and $t_{\text{PbMnTe}} = 30 \text{ nm}$. The curves for Bragg intensity versus angle exhibit satellite peaks which can be analyzed to give information on the period (34.5 nm) as well as on inter-diffusion (e.g., values for D). With increasing annealing times, more and more satellite peaks are smeared out; this directly shows the increase of D . The calculated scattered x-ray intensities are shown below each experimental curve. These kinds of experiments imply that close to the substrate, inter-diffusion will be more severe than close to the surface, since layers in the vicinity of the substrate have been at the growth temperature for a longer period of time. Thus the electronic properties will be very different for wells close to the substrate from those close to the surface. Another interesting set of experiments showing quantum confinement effects in PbMnTe/PbTe structures is seen in figure 5. A Nd-YAG laser was used to excite luminescence in PbTe and PbMnTe films and in two QW structures. Since MnTe has a greater band gap than PbTe, the $x = 2.7\%$ alloy has a greater gap than PbTe, and its photoluminescence peak appears at lower wavelengths or higher energies. For the sample with a period of 8 nm, a real SL is formed with finite dispersion along k_z , whereas for the sample with 30-nm-thick PbMnTe barriers, the carriers are confined in the PbTe wells. BOs are important parameters to understand for the artificially structured materials, and Bauer points out that electron-beam-induced current techniques showed that the valence band offsets in both PbEuSeTe and PbEuSe structures depend drastically upon temperature. Finally, PbTe *nipi* structures have been shown to have large detectivity values ($\approx 10^{11} \text{ cm Hz}^{1/2} \text{ W}^{-1}$), close to the background limit at 77 K.

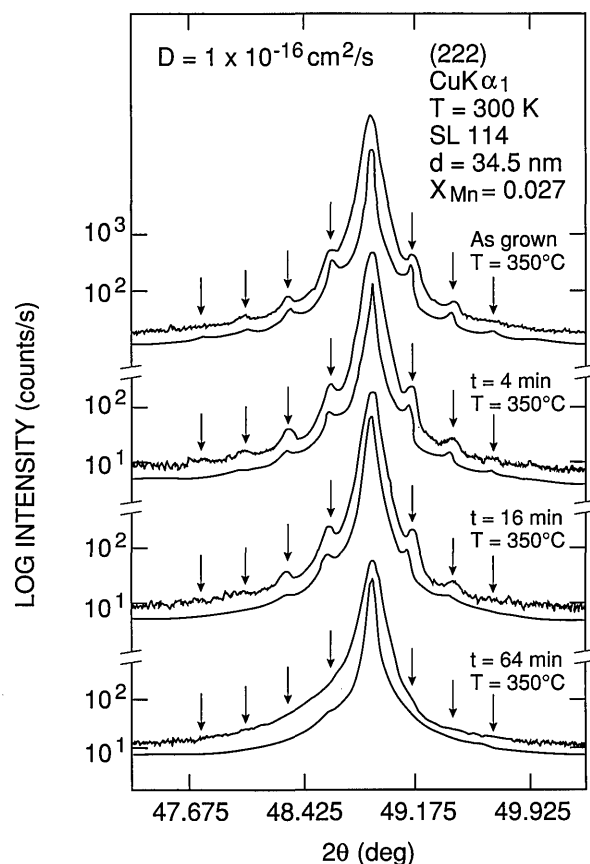


Figure 4. Example of the use of x-ray diffraction techniques to characterize MBE-grown SL structures. X-ray diffraction Bragg intensities versus angle of incidence for a Pb_{1-x}Mn_xTe structure ($x = 0.027$, 20 periods $t_{\text{PbTe}} = 4.5 \text{ nm}$, $t_{\text{PbMnTe}} = 30 \text{ nm}$) (see Conference paper by G. Bauer, fig. 4). The experimental data compare favorably with the calculated intensities shown below each data curve. The influence of the annealing time on the satellite peaks can be directly seen as discussed in the text.

H. Pascher (Universität Bayreuth) reviewed the use of optical four-wave mixing Raman techniques for observing and studying magneto-optical intraband transitions in NGSs. Coherent anti-Stokes Raman spectroscopy (CARS) is one such technique that is well suited to characterize a wide variety of samples—bulk crystals, epitaxial films, QWs, and diluted magnetic semiconductors (DMSs). The strongest Raman-like resonances in a semiconductor exposed to a magnetic field are the spin-flip resonances from which the effective g -factors of electrons and holes can be deduced. Figure 6 shows an example of the CARS technique applied to an *n*-type Hg_{1-x}Cd_xTe bulk crystal ($x = 0.231$) showing cyclotron (CR), combined spin flip (CSF), and spin resonances (SR). The effective g -factor of the sample can be extracted from the SR signals

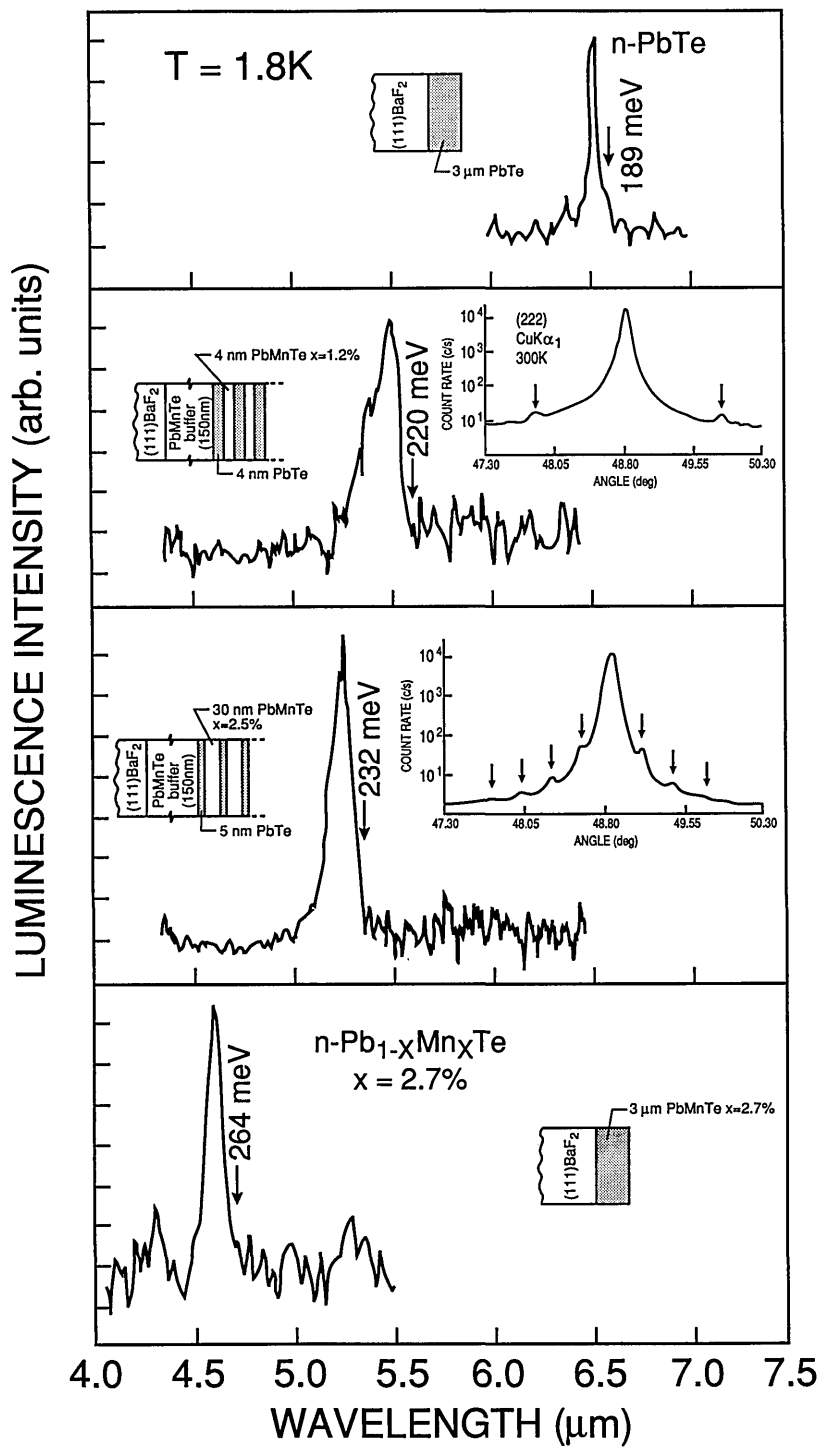


Figure 5. Characterization of various MBE-grown structures by photoluminescence techniques for PbTe and $\text{Pb}_{1-x}\text{Mn}_x\text{Te}$ films and two QW structures. The geometry of each structure is shown along with x-ray intensity versus angle data for the two QWs. As discussed in the text, these data give evidence for the quantum confinement effects that are present in certain structures.

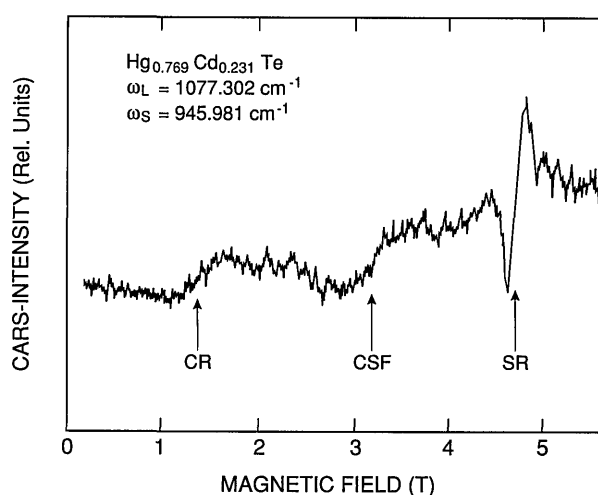


Figure 6. Example of using nonlinear optical techniques to characterize semiconductors. The CARS intensity of an *n*-type $\text{Hg}_{1-x}\text{Cd}_x\text{Te}$ sample ($x=0.231$) is shown versus magnetic field (see Conference paper by H. Pascher, fig. 9). Various Raman-like resonances appear at different magnetic fields and can be used to characterize the electronic structure of the material in a contactless manner. Cyclotron resonance (CR), combined spin flip (CSF), and spin resonance (SR) structures are shown.

and is shown plotted versus magnetic field in figure 7. Thus, very precise band-structure information can be obtained by these techniques. In MQWs and SLs of the IV-VI compounds, the nonlinear susceptibilities are enhanced with respect to the corresponding bulk materials. Strong mixing signals can be observed even in samples which were only 2- μm thick. Studies of *g*-factors of a $\text{PbTe}/\text{Pb}_{1-x}\text{Sn}_x\text{Te}$ MQW showed they were identical to those of a $\text{Pb}_{1-x}\text{Sn}_x\text{Te}$ reference sample. This proved that the electrons were confined within the $\text{Pb}_{1-x}\text{Sn}_x\text{Te}$ layers and thus the band alignment of the system is of type I.

M. Dobrowolska (University of Notre Dame) reviewed the phenomenon of spin resonance (SR) of conduction band electrons in NGSs. SR is defined as a magneto-optical transition in which the electron spin is flipped between two spin states belonging to the same Landau subband or to the same impurity state. It is important to investigate because (1) SR gives the most direct and accurate measurement of the *g*-factor, a parameter that provides detailed information about band structure and (2) SR is normally forbidden by electric-dipole selection rules, but perturbations (nonparabolicity, inversion asymmetry, and warping) relax these rules allowing insight into band-structure details. For a typical NGS at laboratory magnetic fields ($B < 10$ T), the SR transition corresponds energetically to the far-infrared (FIR) region accessible by

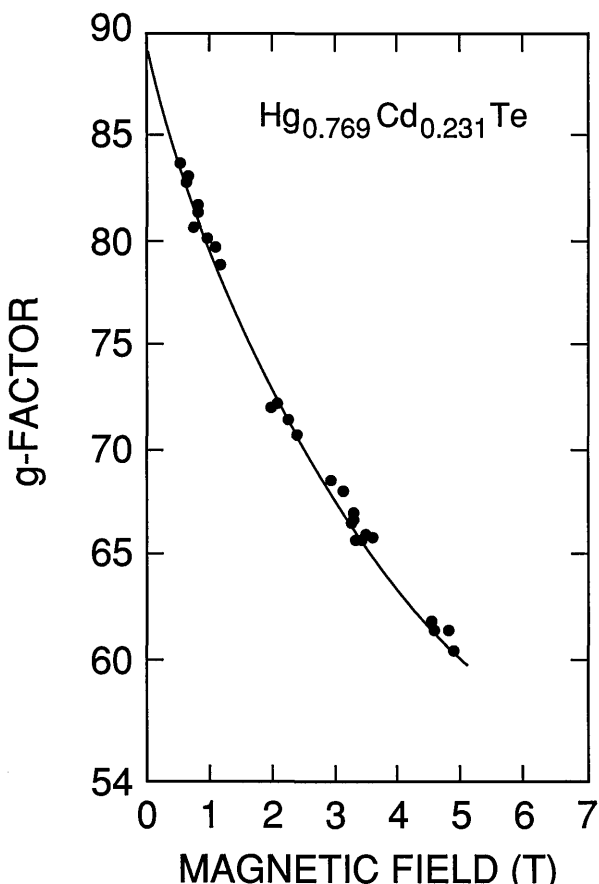


Figure 7. Effective *g*-factor of a $\text{Hg}_{1-x}\text{Cd}_x\text{Te}$ sample (shown in fig. 6) versus magnetic field (see Conference paper by H. Pascher, fig. 10). The *g*-factors can be accurately calculated from the magnetic-field positions of the SR. The magnetic-field dependence of the *g*-factor is a direct consequence of the non-parabolic nature of the conduction band.

FIR lasers. The review concentrated on InSb, but other materials such as HgSe, HgTe, $\text{Hg}_{1-x}\text{Mn}_x\text{Se}$ were also briefly discussed.

Ulrich Merkt (Universität Hamburg) reported on his investigations of quantum wires and dots near the surface of InSb that contain quasi-one-dimensional and zero-dimensional electron systems. InSb and $\text{GaAs}/\text{Ga}_{1-x}\text{Al}_x\text{As}$ heterojunctions are the first semiconductors in which electron systems can be studied in all four sets of dimensions from 3-D to 0-D. The 3-D system in InSb has been studied since 1952; the 2-D system began around 1970 with inversion layers (ILs) in metal-oxide-semiconductor (MOS) structures; and within the last 3 years 1-D and 0-D systems were created by laterally confining the ILs. Figure 8 presents the basic ideas of the quantum-wire and quantum-dot structures fabricated by Merkt. It is essentially an MOS capacitor configuration. NiCr is evaporated onto a *p*-InSb

substrate using a photoresist mask. A Schottky contact is established at the NiCr/InSb interface and the Fermi energy E_F is pinned within the band gap. Mobile electrons can be induced by a gate voltage V_g under the narrow areas where the metal has no direct contact to the InSb surface. Thus, the wires and dots can be charged without direct contacts to the inversion-layer electrons since the InSb substrate has a finite resistivity, even at liquid helium temperatures. Holographic lithography can be used to fabricate wires and dots in arrays on macroscopic areas so that sufficiently high optical absorbance signals can be attained. A simple $k \cdot p$ approach to the concept of effective mass in low-dimensional systems leads to the following: (1) In a 2-D system, the electron mass depends on subband index and on momentum parallel to the layer; (2) in a 1-D system, the mass is only defined in the direction along the wire; (3) in a 0-D system, it is no longer meaningful. For 3-D electrons in a NGS, the mass increases with momentum away from the Γ -point, giving rise to nonparabolic effects. Merkt used an optically-pumped FIR laser to perform CR experiments. The average number of electrons in a dot and the mobility could be determined. The number of electrons per dot was found to be 3 ± 1 at low V_g . The size of the dots is of the same order as the effective Bohr radius, 64 nm. Quantum dots have similarities with shallow donors in semiconductors; but unlike them, dots can have their size and electron number tuned by technological means. Quantization energies of up to 10 meV at wire widths below 100 nm were found by FIR spectroscopy.

O. A. Pankrotov (P. N. Lebedev Physical Institute) reviewed the concept of supersymmetry as applied to the electronic properties of band-inverted heterojunctions. Heterojunctions between semiconductors with mutually inverted bands contain massless spin-nondegenerate interface electron states. The universality of these states is due to the specific symmetry (the supersymmetry) of the effective Hamiltonian. Predictions of giant Landau splittings of the interface states and selection rules for optical transitions in a magnetic field were given.

Paul Kruse (Honeywell Sensors and Systems Development) gave a critical review of the physics and applications of high- T_c superconductors (HTSCs) for IR detection. With the discovery of HTSCs came the hope that they could be exploited to provide performance advantages over conventional IR detectors based upon semiconductors. Very long-wavelength photon detection at oper-

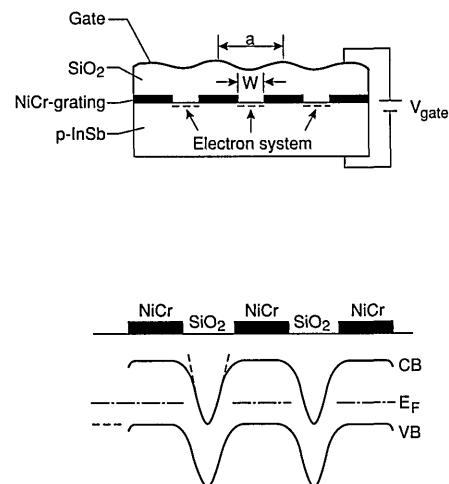


Figure 8. Schematic cross section of the microstructure field-effect device on InSb that is used for quantum wires and quantum dots (see Conference paper by U. Merkt and Ch. Sikorski, fig. 1). Basically it is an MOS capacitor. The lower half of the figure shows the corresponding band structure and Fermi level in the device.

ating temperatures near that of liquid nitrogen was thought possible because the forbidden energy gap of HTSCs was much larger than that in metallic superconductors. Kruse reviewed three ways of estimating the energy gap in YBaCuO: from the Bardeen-Cooper-Schrieffer (BCS) theory, from optical measurements, and from electrical tunneling measurements. For a transition temperature of 90 K, the BCS theory predicts a gap of 27 meV. Optical measurements gave a range of values from 15.5 to 44 meV. However, it is evidently not possible to determine the gap from optical measurements due to residual absorption in the samples. The tunneling measurements also give inconsistent results. Three types of IR detectors based upon HTSC's were presented: the transition-edge microbolometer, the non-equilibrium photo-effect, and photon-assisted tunneling detectors. Practical exploitation of these photon effects will be difficult and time consuming. However, success is likely, and the result will be a new class of very long-wavelength IR detectors and focal-plane arrays.

Jacek Kossut (Polish Academy of Sciences) reviewed the field of donor-electron correlations in DMSs with substitutional iron. Results for HgSe:Fe, Hg_{1-x}Mn_xSe:Fe, and HgSe_{1-x}Te_x:Fe were presented. Compounds involving HgSe substitutionally doped with Fe have interesting properties related to the unusual energy position of d -derived Fe states: the Fe^{+2/+3} state is superimposed on the conduction-band continuum of states

creating a resonant donor state. It is energetically possible for the Fe impurity to donate one of its six d -electrons to the conduction band provided that there are unoccupied states available in the conduction band below the Fe level, E_{Fe} . At low levels of Fe doping, the concentration n of free electrons in the conduction band is roughly proportional to the number of impurities, N_{Fe} , while n becomes nearly constant above a certain critical concentration when the Fermi level E_F becomes "pinned" to the Fe resonant level E_{Fe} . Anomalously high values of the electron mobility in this high-concentration region have been explained by the onset of spatial correlations of the donor charges, since the Coulomb repulsion between the ionized donors tends to keep them apart. Note that this correlation involves transfer of the quasi-localized electrons associated with the Fe impurities, not motion of the Fe atoms themselves. The existence of this correlation results in a dramatic reduction of the rate of scattering by ionized impurity potentials. The degree of suppression of the scattering rate is correctly reproduced by theoretical calculations that include these correlations. Other semiconducting materials (because of the resonant nature of their impurity states) may also exhibit a similar enhancement of their mobilities, e.g., DX centers associated with substitutional donors in GaAs and Cr in PbTe.

Robert S. Allgaier (formerly with the Naval Surface Warfare Center) presented an historical review covering research on a number of NGSs and semimetals during the 1945-1965 period, including IV-VI compounds (PbS, PbSe, PbTe, GeTe, and SnTe), Column-V semimetals (Sb and Bi), Bi_2Te_3 , Te, Mg_2Sn , graphite, α -Sn, InSb, and $Hg_{1-x}Cd_xTe$. The reference list is arranged chronologically and identifies the subject of each entry so that it can serve as an historical summary. The list includes many books, review articles, and conferences, plus selected individual references. Dr. Allgaier argued that the semiconductor era may have begun in 1931, when A. H. Wilson's classic papers were published. Pre-war semiconductor research focused on oxides and other large-gap materials. Only in 1944 did the semiconductor category first appear as a subject classification in Physics Abstracts. The first III-V compound semiconductor paper appeared in 1952. Other events mentioned in the review of early NGS history include (1) superconductivity in GeTe and SnTe (first observed in 1964 and 1965); (2) the mid-1950s discovery that Bi_2Te_3 was an excellent material for thermoelectric generators and coolers; (3) the use of Te in the crystal receivers of the first two decades of this

century; and (4) the early and rapid growth of InSb into the most popular member of the III-V family (it was relatively easy to grow and was quickly found to exhibit a number of very interesting properties).

Concluding remarks given by *Tony Stradling* (Imperial College) emphasized the new developments and trends occurring in the physics and technology of NGSs. He reviewed trends, selected highlights of the conference and predicted future efforts in the field. To detect trends, he analyzed the subject matter of the papers presented at this conference and at the two previous conferences in 1977 and 1981. It was quite apparent that technology subjects are now much more important. This is due to: (1) the burgeoning interest in narrow-gap detectors and sources and (2) the increasing dependence of both the physics and technology on sophisticated growth techniques such as MBE. The topic that pointed most obviously to the future was the Hamburg work on quantum dots. This work on InSb is in advance of that on GaAs/AlGaAs because of the low mass and high confinement energies involved. The remarkable and revolutionary political changes sweeping the world could reduce interest in military devices operating in the 10- μm wavelength range. However, high technology will still be important as squadrons and fleets are cut back. IR technology will be increasingly in demand in a wide variety of areas such as telecommunications, environmental and pollution monitoring, space-born astronomy, and in the field of medical diagnostics.

4. Conclusions

Narrow-gap semiconductors are important technological materials for infrared detector and laser-diode applications. The International Conference on Narrow-Gap Semiconductors and Related Materials, held in Gaithersburg, MD, June 12-15, 1989, served as an important vehicle for summarizing and disseminating up-to-date scientific research on these materials. Artificially structured materials hold great potential for new types of devices, as well as new materials for fundamental research.

5. References

- [1] W. Zawadzki, in Proc. 11th Int. Conf. Phys. of Semiconductors, Warsaw (Polish Scientific Publishers, Warsaw, 1972), p. 87.
- [2] L. Sosnowski, in Proc. Narrow Gap Semiconductors Physics and Applications, Nimes, 1979 (Springer-Verlag, New York, 1980), in Lecture Notes in Physics, Vol. 133, p. 1.
- [3] E. O. Kane, J. Phys. Chem. Solids 1, 247 (1957).

News Briefs

General Developments

ELECTRIC-FIELD METER DEVELOPED

NIST researchers have developed a new isotropic, photonic electric-field meter capable of measuring continuous-wave electric fields from 10 to 15,000 V/m over a frequency range of 10 kHz to beyond 1 GHz. For pulsed fields, the minimum detectable field is 1,000 V/m. The probe uses electro-optic modulators and optical fiber leads to cause minimum perturbation of the fields being measured and to ensure immunity of the probe to electromagnetic interference. The probe's large bandwidth and its unusual ability to measure both amplitude and phase are its salient characteristics. Potential applications include electromagnetic pulse measurement, the precise measurement of any pulsed field of suitable intensity, and the measurement of fields with multiple frequency components. For a copy of paper no. 63-69, which describes the probe, contact Jo Emery, Division 104, NIST, Boulder, CO 80303; telephone: 303/497-3237.

1990 ANNUAL DIRECTORY OF NVLAP LABS PUBLISHED

The 1990 Directory of NVLAP Accredited Laboratories (NISTIR 90-4280) lists nearly 900 domestic and foreign laboratories that are accredited by the NIST National Voluntary Laboratory Accreditation Program (NVLAP) for specific test methods as of March 1, 1990. The current fields of testing are acoustics; asbestos fiber analysis; carpet; commercial products—paint, paper, plastic, and seals and sealants; computer applications; construction testing services—concrete, cement, aggregates, soil and rock, admixtures, geotextiles, road and paving; electromagnetic compatibility and telecommunications; personnel radiation dosimetry; solid fuel

room heaters; and thermal insulation. The labs are listed alphabetically by field of testing. The asbestos labs are listed by state and city. To obtain a copy of the directory, send a self-addressed mailing label to: NVLAP, A124 Building 411, NIST, Gaithersburg, MD 20899; telephone: 301/975-4016. Information also is available by computer on the NVLAP bulletin board at 301/948-2058.

BIOPROCESSING RESEARCH IN SPACE

Since space flight began, effects of weightlessness on man, plants, and animals have been of interest. Initial studies aimed at identifying potential catastrophic consequences of space flight on humans found no serious, immediate effects. Subsequent research has focused on using the weightless environment to answer scientific questions about living matter and physical processes. The effects of gravity on single cells and biochemical purification methods have been studied by teams of scientists, including NIST scientists. In one project, a small fraction of human kidney cells that produce plasminogen activators (enzymes that help dissolve blood clots) was separated in an electric field on a space shuttle mission. The NIST group has analyzed enzymes from these and other fractions of kidney cells. The NIST group also carried out theoretical studies on gravity-related forces inside and outside living cells. The group has flown experiments on suborbital sounding rockets to study the transport of liquids and dissolved materials in biochemical purification processes. For information, contact Paul Todd at the Chemical Engineering Science Division, NIST, Boulder, CO 80303; telephone: 303/497-5563.

MEASURING THERMAL CONDUCTIVITY OF CERAMICS

NIST scientists have developed an instrument to determine thermal conductivity of materials at high temperature. The apparatus, a miniature guarded-

hot-plate, can measure thermal conductivity of ceramics and ceramic composites at temperatures between 700 and 1500 K in neutral or mildly oxidizing atmospheres. The apparatus is made of boron nitride and high-purity alumina. These materials were selected for their thermal and electrical properties as well as high-temperature compatibility with metallic components in the system. Thermocouple-grade platinum and platinum-rhodium wiring are used for both the heater and thermometry elements. Typical specimen diameter is 7 cm with a thickness between 1 and 8 mm. Specimens must be stable at high temperatures and chemically compatible with system components. For a copy of paper no. 68-89, describing the apparatus, contact Jo Emery, Division 104, NIST, Boulder, CO 80303; telephone: 303/497-3237.

COMMERCE REPORT TAGS 1990s "EMERGING TECHNOLOGIES"

Twelve of today's "emerging technologies" will represent a combined world market of about \$1 trillion by the year 2000, according to a report issued by the Commerce Department's Technology Administration. Emerging Technologies: A Survey of Technical and Economic Opportunities assesses the competitive position of the United States vis-a-vis Japan and Europe and makes 13 recommendations for actions by industry and government to improve U.S. competitiveness. The emerging technologies cited are advanced materials, superconductors, advanced semiconductor devices, digital imaging technology, high-density data storage, high-performance computing, optoelectronics, artificial intelligence, flexible computer-integrated manufacturing, sensor technology, biotechnology, and medical devices and diagnostics. NIST contributed to the technical analysis sections of the report.

ASTM APPROVES NIST CONE CALORIMETER AS STANDARD

"How big is the fire?" is a question commonly asked by furniture manufacturers regarding the burning behavior of their product. ASTM, a U.S. voluntary standards organization, has approved a test method (E1354) that will help answer that question. Based on a device developed by researchers at NIST, it provides the data critical to predicting the fire hazard of a product from a small sample of material. Traditionally, manufacturers

conduct full-scale burn tests on a new piece of furniture to determine its burning behavior. As a more efficient and less costly alternative, the NIST cone calorimeter provides more information than many full-scale tests and at a reduced cost. It measures the heat released and rate at which it is released, the time it takes for a material to ignite, the amount of smoke produced, and the amount of several known toxic gases.

NIST SEEKING PROPOSALS FOR COURSEWARE STANDARDS

Over the next several years, the federal government will invest millions of dollars on computer-based interactive training software, often called "courseware," and the hardware needed to run it. Currently, several manufacturers offer high-performance, low-cost hardware. However, because of proprietary interfaces, software written to run on one manufacturer's product often will not run on another's without expensive reprogramming. Standardizing the protocols that define how software modules communicate will help make it possible to use the courseware on any manufacturer's equipment. Researchers at NIST are considering a possible Federal Information Processing Standard for these protocols. For information, contact Systems and Software Technology Division, B266 Technology Building, NIST, Gaithersburg, MD 20899; telephone: 301/975-3345.

NEW PHASE NOISE MEASUREMENT SYSTEM DEVELOPED

NIST scientists have developed a more accurate system for measuring phase noise in oscillators, amplifiers, frequency synthesizers, and other electronic components. Of interest to military and civilian calibration laboratories and companies producing high-precision navigation and communications equipment, the new system has an accuracy 2 to 4 times that of current commercial equipment, and its frequency range is 25 times greater. It can directly measure phase noise at carrier frequencies from 5 MHz to 26 GHz and from 33 to 50 GHz. With external mixers, the measurement range can be extended beyond 100 GHz. Bandwidths vary from 0.1 Hz to 10 percent of the carrier frequency up to a maximum of 1 GHz. For a copy of paper no. 23-90 describing the system, contact Jo Emery, Division 104, NIST, Boulder, CO 80303; telephone: 303/497-3237.

NIST METHOD ALLOWS QUICKER, CHEAPER ANALYSES

Preparing samples of contaminated soils, sediments, and sludges for analysis of environmentally hazardous trace elements can be time consuming. Typically such preparations, in which the sample is immersed in acid and heated with hot plates and reflux systems, take 8 to 24 h to complete. Now a project of NIST and the Environmental Protection Agency (EPA) has produced a method that uses a heating device similar to a kitchen microwave oven to cut drastically the sample preparation time. Research at NIST has shown that by using microwave energy to heat a sample in acid within a closed vessel, the processing time can be shaved to 10 min. Because so much time is saved, the NIST/EPA method substantially lowers the cost of each analysis. Recent tests also indicate that the new technique will allow trace elements to be detected at lower levels. The method was accepted by EPA after a successful demonstration involving 15 laboratories and will be added to EPA's procedures for its Resource Conservation and Recovery Program and its "Superfund" program.

QUALITY SOFTWARE TO BE FOCUS OF UPCOMING LECTURES

The failure of software used to operate high-integrity systems—such as hospital equipment—can be more than annoying. It can result in injuries or even deaths and can cost businesses millions of dollars. In 1986, for example, several people were killed when a software-controlled radiation therapy machine exposed patients to a massive radiation overdose. To discuss software problems and potential solutions, NIST is sponsoring a lecture series to begin this fall. The first lecture is scheduled for October 23 at 2 p.m. at NIST headquarters in Gaithersburg, MD. Dr. Barry Boehm of the Defense Advanced Research Projects Agency will discuss software engineering and the major issues that must be addressed in developing and operating high-integrity systems. For information, contact Dolores Wallace at NIST, telephone: 301/975-3340.

FIRST LABS ACCREDITED FOR EMI TESTING

The first group of testing laboratories has been accredited under the National Voluntary Laboratory Accreditation Program (NVLAP) for selected test methods in a military standard (MIL STD-462) for measuring electromagnetic interference (EMI)

characteristics. The labs, eight from the private sector and one U.S. Navy facility, are accredited under the Electromagnetic Compatibility and Telecommunications Testing Program managed by NIST. MIL STD-462 is the test method companion to MIL STD-461, "Electromagnetic Emission and Susceptibility Requirements for the Control of Electromagnetic Interference." The U.S. Naval Air Systems Command (NAVAIR) has instructed the use of NVLAP accredited labs for certain NAVAIR procurement processes. The accredited labs had applied to NVLAP for accreditation in up to 25 test methods in radiated emissions, conducted emissions, radiated susceptibility, and conducted susceptibility. For information on this program, contact: Jeffrey Horlick, A124 Building 411, NIST, Gaithersburg, MD 20899; telephone: 301/975-4016; fax: 301/975-3839.

STANDARDS FOR LOW-TEMPERATURE SUPERCONDUCTORS

NIST has a highly successful program to develop standards for conventional (low-temperature) superconductors in support of Department of Energy large-scale applications such as the Superconducting Super Collider. Standardized measurement techniques developed by NIST have saved time and money and resulted in better communication among researchers, producers, and users of superconductors. The latest report on this program, covering 1988 and 1989, contains results of critical-current studies on a large conductor Reference Material, the effect of power supply current ripple, the measurements of large conductors, and an interlaboratory comparison of niobium-tin wires. It also discusses magnetic losses in multifilamentary niobium-tin and niobium-titanium wires. Development of Standards for Superconductors, Final Report, January 1988-December 1989 (NISTIR 90-3935) is available from the National Technical Information Service, Springfield, Va. 22161. Order by PB #90-196536 for \$23 prepaid.

COMPUTER CONTROL TO ASSURE QUALITY WELDS

NIST scientists have developed a computer-aided system to study the behavior of a welding arc in real time and the transfer of the metal through the arc to the weld. Using a microcomputer, the researchers analyze the fluctuations in the current and voltage values as a function of various welding parameters such as power supply voltage setting. This analysis then allows them to control, in real

time, the stability of the arc and the uniformity of metal transfer from the wire to the weld joint. "Computer control that can achieve the same weld integrity and consistency as an experienced welder permits substantial automation and the resultant benefits," they report in Welding Journal. The work is part of on-going NIST research to develop measurement technology that improves the welding process. For a copy of the article, paper no. 25-90, contact Jo Emery, Division 104, NIST, Boulder, CO 80303; telephone: 303/497-3237.

MECHANICAL PROPERTIES AND PERFORMANCE GROUP ESTABLISHED

NIST has established a new group on mechanical properties and performance to address national needs for expanded capabilities in the mechanical characterization of engineering materials and components. Chief among these needs are industrial requirements for mechanical test methods for new kinds of materials (e.g., intermetallics and composites) and for mechanical property measurements from the micro scale (e.g., electronic solder connections) to multimillion pound-force scales (e.g., fracture behavior in pressure vessel steels).

The group has a twofold mission. The first is to develop new and improved test methods and standards that will facilitate reliable measurements of mechanical behavior under various kinds of severe environmental and operating conditions that are experienced both in processing and in service. The second is to provide expert analytical and mechanical testing services for other parts of NIST, for other government agencies, and, under certain conditions, for the private sector, too. The extensive facilities available for this work include a wide range of mechanical testing equipment with associated instrumentation for tensile, compressive, and torsion tests, and also for various combined load and fracture tests. In addition, separate, well-equipped laboratories are devoted to fatigue, creep, impact, and hardness testing. The staff has experience in all of these areas as well as in the related fields of analytical fracture mechanics, failure analysis, quantitative metallography, stress analysis, and modeling of mechanical processes.

OXYGEN COMPATIBILITY OF ALUMINUM-LITHIUM ALLOYS

Aluminum-lithium alloys offer significant advantages for aerospace applications due primarily to their high strength-to-weight ratio. In considering

aluminum-lithium alloys for the advanced launch system (ALS), the Air Force was concerned about their oxygen compatibility. Initial tests indicated that aluminum-lithium was extremely reactive and not suitable for use in an oxygen environment. The Air Force asked NIST to conduct oxygen compatibility tests on aluminum-lithium alloys in accordance with NASA standards. Subsequent testing revealed that aluminum-lithium alloys and currently used alloys are about equally reactive in oxygen-compatibility, mechanical impact tests, but less flammable as indicated in promoted combustion tests. Since these new alloys are still under consideration for possible use in the ALS program, the mechanical performance of aluminum-lithium alloys is now being evaluated.

OAK RIDGE NATIONAL LABORATORY AND NIST COLLABORATE ON SUPERMIRRORS

Oak Ridge National Laboratory (ORNL), NIST, and industry are currently conducting a joint program of research and development of the neutron optical devices known as supermirrors. These thin-film, layered structures are vapor deposited in a particular sequence with appropriate materials so that the critical angle for total external reflection for neutrons is significantly enhanced. Supermirror guides transport neutron beams from reactor (or other) source to experimental station with significantly increased intensity relative to conventional guides.

NIST scientists are measuring the reflectivity of the supermirrors using a neutron reflectometer at the NIST reactor. The effect of interfacial roughness and diffusion between layers is also being studied by analyzing the diffuse scattering of neutrons and x rays by the supermirrors. To complement the diffraction data, real space images of the multilayers in cross section will be obtained by NIST's microanalysis research group using transmission electron microscopy. The interfacial roughness decreases neutron specular reflectivity and consequently the transport efficiency of the guide tube. It is, therefore, important to determine which manufacturing processes and which materials minimize this roughness. Because neutrons make many reflections in a typical guide tube, high reflectivities ($\geq 98\%$) are required. Thus far, supermirror reflectivities have been produced with critical angles about twice that obtained using an ordinary Ni film, which is two-thirds of what is sought.

NIST INSTALLS NEW HIGH-CURRENT 420 kV X-RADIOGRAPHY FACILITY

NIST has installed a new high-current, high-energy, industrial radiography source. The new facility, available to all NIST researchers as well as outside industry users, greatly expands NIST's on-site capabilities for industrial radiographic applications. The high energy (420 kV) and high current (10 mA) will permit imaging through 10 cm of steel. In a recent application for the American Dental Association Paffenbarger Research Center, zirconium alloy ingots were radiographed to select specimens free of internal casting defects prior to machining.

The x-ray tube is mounted on a movable gantry to permit various beam orientations. The source is rated for 100 percent duty cycle and provides for automatic timing of exposures from 1 to 100 min or may be operated manually for any period. The stable high-current device is also well suited for x-ray fluorescence studies in basic physics. For example, NIST scientists plan to use the source to stimulate fluorescence from actinide elements.

DECOMPOSITION OF ENERGETIC MOLECULES FROM METASTABLE VIBRATIONAL STATES

Energetic molecules important for rocket fuels or explosives are in many cases unstable at room temperature. This instability occurs because a few vibrationally excited molecules, always present in chemical systems at thermal equilibrium, have sufficient energy to decompose; under certain conditions such unimolecular fragmentation events trigger violent chain reactions. Experiments performed at NIST take advantage of the unimolecular decomposition process to obtain new insight into the nature of the forces that bind energetic molecules and determine their stability.

The experiments provide an extraordinary microscopic view of the motion of individual atoms as vibrationally excited molecules evolve into fragments. The measurements allow NIST scientists to deduce the geometry, energy, and forces acting within molecules at the instant of fragmentation. Specific vibrational motions were excited in HN₃ using ps and ns pulsed visible lasers. Subsequent evolution of these energized molecules was observed using time-delayed ultraviolet laser pulses to excite fluorescence from emerging NH fragments.

The product states and appearance rates are highly dependent upon the initial vibrational mo-

tion and energy. For example, molecules energized to $v_{NH}=5$ and 6 decompose to produce exclusively NH(X³ Σ) fragments (called the spin-forbidden channel), while at higher energies, when $v_{NH}=7$ is excited, NH(a¹ Δ) products prevail (the spin-allowed channel). Characteristic lifetimes for fragmentation of vibrationally excited HN₃ range over 4 orders of magnitude, from 200 ns for $v_{NH}=5$ to approximately 10 ps for $v_{NH}=7$. The rapid increase of dissociation rate with increasing vibrational energy was completely unexpected and has forced a rethinking of the decomposition process. The lifetime data are important for understanding the stability of many energetic molecules and have never before been experimentally obtained.

REVISED POSIX STANDARD APPROVED

The Secretary of Commerce approved a revision to Federal Information Processing Standard (FIPS) 151, POSIX: Portable Operating System Interface for Computer Environments. Effective September 28, 1990, the revised FIPS 151-1 adopts IEEE Standard 1003.1-1988, which defines a C language source interface to an operating system environment. FIPS 151-1 will permit federal agencies to exercise more effective control over the production, management, and use of information resources by promoting the portability of computer applications at the source code level.

GLOBAL POTENTIAL OF OPEN SYSTEMS INTERCONNECTION (OSI) TECHNOLOGY DEMONSTRATED

OSINET, a regional OSI research and demonstration network administered by NIST, joined forces with four other regional networks to demonstrate the worldwide interoperability achievable using OSI products. The March 1990 CeBit trade show in Hanover, West Germany, was the site of the launch event for a global collaboration effort called OSIONe, which includes regional networks from Australia (OSIcon), Europe (EurOSInet), Japan (INTAPNET), and Singapore (OSNET) in addition to OSINET.

The OSIONe demonstration featured a business transaction using OSI electronic mail services to transfer data and documents between the OSIONe platform at CeBit and satellite locations around the world served by the OSIONe networks. Participants in the demonstration included Digital Equipment Corporation, Hewlett-Packard, Xerox, and NCR Corporation. Each OSIONe network will host a similar demonstration in the next 18 months.

HYPertext STANDARDIZATION WORKSHOP PROCEEDINGS PUBLISHED

NIST Special Publication 500-178, Proceedings of the Hypertext Standardization Workshop January 16-18, 1990, presents the results of the first workshop sponsored by NIST's hypertext project. The workshop, which attracted about 65 participants, provided a forum for presentation and discussion of existing and proposed approaches to hypertext standardization. The workshop goals were to consider hypertext system definitions, to identify viable approaches for pursuing standards, to seek commonality among alternatives whenever possible, and to progress towards a coordinated plan for standard development, i.e., a hypertext reference model. Future workshops are planned.

NIST BEGINS STRUCTURED QUERY LANGUAGE (SQL) VALIDATION SERVICE

NIST opened an SQL validation service to provide an independent source of analysis of vendor conformance to FIPS 127-1, Database Language SQL. Performed on a cost-reimbursable basis, the service will review the supplier's conformance testing procedures, witness the testing, and evaluate test results. Using version 2.0 of the SQL test suite, the validation service will produce a registered SQL validation report. NIST will publish a listing of validated implementations on a quarterly basis.

HIGH-QUALITY IN-SITU YBa₂Cu₃O₇ FILMS FABRICATED USING A NEW

STATE-OF-THE-ART DEPOSITION SYSTEM

NIST has put into operation a multiworkstation deposition system for thin films and used it to produce epitaxial films of the ceramic high-critical-temperature superconductor YBa₂Cu₃O₇. These films have been measured to show zero resistance at temperatures over 88 K. The process is an in-situ sputter process on MgO substrates. The films were made in the unusually short time of within 3 weeks of acceptance of the new system, which was specified by NIST to have the capability for carrying out a number of processing steps without a requirement for breaking vacuum between steps. Other specified capabilities include the deposition of a large variety of contact layers, in-situ anneals, ion beam cleaning and edge milling, and provision for vacuum transfer of specimens to other systems, i.e., for surface analysis. The substrate temperature can be controlled over a range of 77 to 1200 K. NIST

plans to use the system to develop ultra-low-resistivity thin-film contacts for both superconducting and semiconducting cryogenic electronics, to produce thin-film weak-link structures for magnetic field detectors, and to fabricate superlattices.

U.S./CANADA RENEW SI UNIT AGREEMENTS, ADD OTHERS

NIST and the Canadian National Research Council (NRC) have renewed statements recognizing the equivalency of their national standards for five units of physical measurement as defined by the International System of Units (SI). NIST director John W. Lyons and NRC president Pierre O. Perron signed agreements on June 11, 1990, in Ottawa, renewing the recognition of equivalency of standards for electric capacitance, electric resistance, length, time, and voltage. New statements also were signed to recognize the equivalency of the national standards for the SI units of mass and luminous intensity, and for the measurement of temperature, as well as the national time scales of the United States and Canada. The statement for the measurement of temperature reflects the new International Temperature Scale adopted by the International Committee of Weights and Measures effective Jan. 1, 1990. The official equivalency of these units is important for improving trade between the two countries. For information contact: Dr. Barry N. Taylor, B160 Physics Building, NIST, Gaithersburg, MD 20899, 301/975-4220.

COOPERATIVE PROGRAM TACKLES AUTOMATED INSPECTION

Six industrial firms have joined forces with NIST in a cooperative research program to develop an automated inspection system for manufactured parts. The six firms will provide software, machines, and researchers to the NIST "Quality in Automation" program. Researchers use the contributed software and machines for three-dimensional computer-aided design of parts, graphic selection of inspection paths, and examination of the actual manufactured product. Engineers compare the manufactured parts with the original computer-aided design. NIST shares research results with the respective firms, providing suggestions for improvements, compatibility, and expansion of the products. For information on the program, contact Steven D. Phillips, A107 Metrology Building, NIST, Gaithersburg, MD 20899, 301/975-3565.

DATE SET FOR UNIFORM GAS PUMP PRICING

The nation's weights and measures officials set January 1, 1999 as the target date for establishing national uniformity in motor-fuel dispensers used in multi-tier pricing. The decision affects gasoline service station pumps and other motor-fuel dispensers that use different prices for the fuel depending on whether it is paid for in cash or by credit card. The decision was made at the 75th Anniversary Annual Meeting of the National Conference on Weights and Measures (NCWM), in Washington, DC. This concludes action for implementing a policy adopted by the conference in 1989 requiring that all dispensers used in the multi-tier pricing of motor fuels must either be able to compute the accurate total sale price for each unit price used—generally cash or credit—or must be dedicated to sell only at one unit price. For information on NCWM and the annual meeting, contact the National Conference on Weights and Measures, P.O. Box 4025, Gaithersburg, MD 20855, 301/975-4012.

DESIGN FOR A RADIOSCOPIC IMAGE QUALITY INDICATOR

A long-established way to test the quality of a weld is to x-ray it and analyze the film for flaws and imperfections. More recently, this process has been computerized and digitized so that film can be replaced by an electronic system that projects the image on a video screen. This permits real-time examination of the weld and improves productivity by allowing the object to be rotated during inspection. But the procedure has been inhibited by lack of an indicator that evaluates image quality as the specimen and its associated image quality indicator (IQI) are rotated. NIST scientists have developed a design for an indicator that has spherical symmetry and provides the same image quality information independent of rotation. "Preliminary investigations, including image analysis of film radiographs, indicate that the central portion of the IQI can be used to measure thickness sensitivity to the 1 percent and 2 percent levels," the scientists report. Future work will be aimed at developing a technique to give quantitative measurements of quality. For a copy of paper no. 24-90, which describes the design, contact Jo Emery, Division 104, NIST, Boulder, CO 80303, 303/497-3237.

NOVEL PROCESS FOR GROWING CRYSTALS

NIST scientists have developed a novel process, called osmotic dewatering, for growing single crystals of inorganic and organic materials, including proteins. Osmotic dewatering occurs when two aqueous salt solutions are separated by a semipermeable membrane through which only water can pass; the osmotic pressure difference causes slow transport of water from the dilute solution containing a protein to a concentrated salt solution. The process removes water, and only water, from the mother liquor in which crystals are grown. The method permits slow and controllable nucleation and growth needed to form large, single crystals suitable for study by x-ray crystallography. Using this method, the NIST scientists have grown crystals of lysozyme, a protein, to about 1 mm in size and of high quality for x-ray crystallography. They also have grown crystals of triglycine sulfate, a material used in electronic applications. A paper, no. 35-90, describing the process is available from Jo Emery, Division 104, NIST, Boulder, CO 80303, 303/497-3237.

SECURITY FOR "OPEN" NETWORKS

In addition to their many advantages, computer networks have opened up new opportunities for mischief and crime. Through the National Security Agency's (NSA) Secure Data Network System (SDNS) project, NIST is working with NSA and private industry to help make networks secure as well as "open." Their goal is to develop a framework of computer security standards that manufacturers can use in network products incorporating Open Systems Interconnection protocols. NIST has compiled 10 documents from phase one of the SDNS project into three publications, which include specifications for controlling access to the network, security protocols for protecting data in networks, and procedures for managing the keys needed to encrypt and decrypt information. NIST would like potential users and vendors of security products to comment on these three documents: Secure Data Network System (SDNS) Network, Transport, and Message Security Protocols (NISTIR 90-4250); Secure Data Network System (SDNS) Access Control Documents (NISTIR 90-4259); and Secure Data Network System (SDNS) Key Management Documents (NISTIR 90-4262). They are available from the National Technical Information Service, Springfield, VA. Call 703/487-4600 for ordering information.

NIST GATT STANDARDS CODE ACTIVITIES REPORTED

GATT Standards Code Activities of the National Institute of Standards and Technology (NIST) 1989 (NISTIR 4314) describes the role of the NIST Standards Code and Information Program (SCI) in support of the GATT Agreement on Technical Barriers to Trade (GATT Standards Code). The annual report also gives statistics on 10 years of the code's implementation in the United States. SCI staff operate the U.S. GATT inquiry point for information on standards and certification activities that might affect U.S. trade. SCI also coordinates comments on foreign regulations, arranges for translations of foreign texts, and maintains the GATT "hotline" (301/975-4041, not toll free) that provides the latest information on notifications of proposed foreign regulations issued by the GATT Secretariat in Geneva. To obtain a copy of the report, send a self-addressed mailing label to Standards Code and Information Program, A629 Administration Building, NIST, Gaithersburg, MD 20899, 301/975-4037.

COMPUTERIZED WELDING DATA AVAILABLE

Persons interested in the computerization of welding data will want to get a new publication from NIST that includes the proceedings of a 1988 conference on this subject. The publication presents an overview of computers and databases, papers on applications software, and various case studies. Specific topics include application of artificial intelligence to welding, on-line access to worldwide sources of materials performance data, a weld improvement program, and expert systems for diagnosing problems in welding power sources. The publication also includes the proceedings of a workshop on future computerization needs in the welding industry and an informal survey of registrants' use of computers on the job. Computerization of Welding Data—Proceedings of the Conference and Workshop (NIST Special Publication 781) is available from the Superintendent of Documents, U.S. Government Printing Office, Washington, DC 20402. Order by stock no. 003-003-03006-6 for \$5 prepaid.

IMPROVED TESTING FOR EM SUSCEPTIBILITY

Two new NIST publications discuss improved methods for testing aircraft, large operational systems, and electronic equipment for susceptibility to electromagnetic (EM) fields. Recent Improvements in Time-Domain EMC Measurement System (NISTIR 89-3927) describes techniques for determining critical resonant frequencies and the current response of internal wiring of helicopters due to external EM fields. The measurement method uses a train of low-level radiated pulses that do not disturb other spectrum users, are safe, and can be used in a noisy EM environment. Facilities for Improving Evaluations of Electromagnetic Susceptibilities of Weapon Systems and Electronic Equipment (NISTIR 89-3928) discusses the preliminary design of a facility for EM susceptibility testing that combines features of the transverse electromagnetic cell for low-frequency testing and the reverberating chamber for high-frequency operation. Both publications are available from the National Technical Information Service, Springfield, VA 22161. Order NISTIR 89-3927 by PB #90-155821 for \$15; order NISTIR 89-3928 by PB #90-155862 for \$15.

NEAR-FIELD GAIN OF PYRAMIDAL HORNS

Calibrations of electromagnetic probes, electromagnetic interference and compatibility tests, and antenna measurements are carried out in the NIST anechoic chamber. They require that a transmitting antenna in the chamber generate a known field throughout a certain volume. At NIST, a series of pyramidal transmitting horns are used above 450 MHz. NIST has published a comparison of the theoretical and measured near-field gains of these horns for frequencies from 18 to 40 GHz. Near-Field Gain of Pyramidal Horns from 18 to 40 GHz (NISTIR 89-3924) describes the theory and measurement techniques used and shows that the discrepancy between theory and measurement is typically within ± 0.3 dB for distances between 0.5 and 4 m from the horn aperture. NISTIR 89-3924 is available from the National Technical Information Service, Springfield, VA 22161. Order by PB #90-155854 for \$15.

Calibration Services

NOISE CALIBRATIONS EXTENDED

Coaxial noise sources can now be calibrated by NIST in the additional frequency range of 1 to 2 GHz, and sources with APC3.5 precision connectors can now be accommodated in the 2- to 12-GHz range. With these new services, NIST can now calibrate sources from 1 to 12 GHz with precision N, APC7, GR900, and various rectangular waveguide flange connectors. Sources with APC3.5 connectors can be calibrated at 2 to 12 GHz for all noise power spectral densities up to 18,000 K. The frequency range for APC3.5 connectors is expected to be extended down to 1 GHz by the end of September 1990. Measurement uncertainties typically range from 1 to 3 percent. Noise calibrations are needed by manufacturers and users of microwave equipment because noise is the ultimate limiting factor in electromagnetic system performance. Low-noise products are specified so that the equipment itself doesn't distort the signal being processed. Test equipment must be calibrated to determine if the products meet specifications. For information, contact George J. Counas, Division 723.02, NIST, Boulder, CO 80303; telephone: 303/497-3664.

the Standard Reference Materials Program, Room 204, Building 202, NIST, Gaithersburg, MD 20899; telephone: 301/975-OSRM (6776), FAX: 301/948-3730.

AQUEOUS SOLUTIONS VALUABLE FOR CALIBRATING INSTRUMENTS

To ensure accurate measurements, chemists frequently need single-element standard solutions that can be used to calibrate instruments for analytical techniques such as atomic absorption spectrometry, optical emission (plasma) spectrometry, or spectrophotometry. For several years, NIST has sold individual aqueous solutions of several elements for these purposes. Now the agency is making available separate spectrometric standard solutions for the metals lanthanum and scandium. These standard reference materials (SRMs) are each certified to contain an elemental concentration of 10 mg/mL in a 50-mL solution. The materials, SRM 3127 (lanthanum) and SRM 3148 (scandium), are available for \$76 and \$144, respectively, from the Office of Standard Reference Materials, Room 204, Building 202, NIST, Gaithersburg, MD 20899; telephone: 301/975-6776.

Standard Reference Materials

LOW-ALLOY STEEL STANDARDS AVAILABLE FOR PRODUCERS

Two new standard reference materials (SRMs) are available from NIST for producers to use in determining the carbon and sulfur content in metals. The SRMs should be particularly useful in calibrating automated combustion analyzer systems as well as for other quality control procedures, including specification testing to meet industry and government requirements. The low-alloy steel standards are in the form of pins that are 4 mm in diameter, 12 mm in length, and approximately 1 g each in weight. SRM 2159 is certified for 0.016 percent of carbon and 0.0023 percent sulfur by weight, and SRM 2160 is certified for 0.584 percent carbon and 0.012 percent sulfur by weight. SRMs 2159 and 2160 are available in units of 200 g for \$200 from

Standard Reference Data

PC DATABASE AVAILABLE FOR BIOCHEMISTS

A new computerized database for biochemists in industrial laboratories and universities worldwide brings together for the first time all of the published information on the successful crystallization of proteins and nucleic acids. This important research tool for the design of new drugs and chemical processes was developed by a NIST research chemist. The database is designed for personal computers and contains crystal data and the crystallization conditions for more than 1,000 crystal forms of over 600 biological macromolecules. For each crystal entry there is a complete description of crystallization conditions and related crystallographic data. Also provided are evaluated critical data on the physical characteristics of known crystals, including unit cell parameters, space group, crystal density, and diffraction limit. NIST/CARB Biological Macromolecule Crystallization Data-

base, Standard Reference Database 21 is available for \$300 from Standard Reference Data Program, A323 Physics Building, NIST, Gaithersburg, MD 20899; telephone: 301/975-2208.

PC DATABASE FOR EVALUATING REFRIGERANTS ANNOUNCED

Refrigeration engineers, chemical and equipment manufacturers, and others who use chlorofluorocarbons have a new research tool. A new personal computer (PC) software package enables users to assess several environmentally acceptable refrigerants and mixtures as possible replacements for currently used materials. The NIST Thermodynamic Properties of Refrigerant Mixtures (REFPROP) Database can produce rapidly tables of the thermodynamic properties for 15 partially and fully halogenated chlorofluorocarbon refrigerants and 20 of their mixtures. Users also have the option to calculate other mixtures of the 15 refrigerants by using their own data. The refrigerants in the REFPROP program are: R11, R12, R13, R13B1, R14, R22, R23, R113, R114, R123, R124, R134, R134a, R142b, and R152a. The database is designed to be stored on a hard disk of any AT or XT-class PC and occupies 250 kilobytes. To order NIST Standard Reference Database 23, REFPROP, available for \$225, contact: Standard Reference Data Program, A323 Physics Building, NIST, Gaithersburg, MD 20899; telephone: 301/975-2208.

NEW VEEL PC PROGRAM OFFERS RAPID ACCESS TO DATA

A new personal computer (PC) program gives chemists, environmentalists, combustion engineers, and researchers in industry rapid access to all important published information available on the vibrational and electronic energy levels of short-lived molecules important to many complex reactions. The program consists of two searchable databases that contain experimental data on the vibrational fundamentals of ground-state transient molecules with 3 to 16 atoms, excited-state transient molecules with 3 to 6 atoms, and the electronic energy levels of transient molecules with 3 to 6 atoms, along with associated index and reference files. Search paths are available by molecule (formula or Chemical Abstract Service registry number), by transition wavenumber (vibrational fundamental or electronic band origin), and by wavelength range for electronic transitions. To

order NIST Vibrational and Electronic Energy Levels of Small Polyatomic Transient Molecules Database (VEEL), Standard Reference Database 26, contact Standard Reference Data Program, A323 Physics Building, NIST, Gaithersburg, MD 20899, 301/975-2208.

MAJOR EXPANSION ANNOUNCED FOR MASS SPECTRAL DATABASE

More than 4,000 new analytical mass spectra have been added to the NIST/EPA/MSDC Mass Spectral Database, a major international resource used by analytical chemists and environmental scientists to identify unknown substances. The database now contains complete spectra for approximately 54,000 chemical compounds. A major research effort has corrected several thousand errors that had crept into the data collection over the years. Mass spectrometry is an analytical technique used widely in pharmaceutical, biological, and environmental research as well as in the chemical industry. EPA requires environmentalists to use this database for analyzing "tentatively identified compounds" at hazardous waste sites. The database is available on standard diskettes for personal computers (PCs) or on magnetic tape. To order PC Version 3.0, or to obtain a license agreement for the database in magnetic-tape form, contact the Standard Reference Data Program, A323 Physics Building, NIST, Gaithersburg, MD 20899, 301/975-2208.

NEW MASS SPECTRAL DATABASE OF COMMON COMPOUNDS

The NIST Mass Spectral Database of Common Compounds (Standard Reference Database 1B) is a new personal computer-based (PC) collection of 10,215 complete spectra and data for the most commercially available chemical compounds, widely used drugs, and environmentally important compounds. Diagrams showing the molecular structures of 97 percent of the chemicals are included. The database uses the same fast software for data searches that was developed for the larger NIST /EPA/MSDC Mass Spectral Database. The new database will be useful as a teaching aid, or for researchers with limited disk storage space. The database does not qualify under EPA regulations for reporting "tentatively identified compounds" at hazardous waste sites. Standard Reference Database 1B is available for \$350 from the Standard Reference Data Program, A323 Physics Building, NIST, Gaithersburg, MD 20899, 301/975-2208.

Calendar

September 11-12, 1990

SIXTH BIENNIAL SYMPOSIUM ON OPTICAL FIBER MEASUREMENTS

Location: National Institute of
Standards and Technology
Boulder, CO

This symposium will be devoted entirely to the topic of measurements for fiber, related components, and systems. It provides a forum for reporting the results of recent measurement research and an opportunity for discussions that can lead to further progress. Topics will include measurements on telecommunications fibers (attenuation, cut-off wavelength, mode-field diameter, polarization properties, geometry/index profile, reflectometry), fiber lasers and amplifiers, fibers for sensors, couplers, connectors, multiplexers, integrated optics, sources, detectors, modulators, switches, long-haul systems, LANs, subscriber loops, field and laboratory instrumentation, and standards.

Contact: Douglas Franzen, 724.02, NIST, 325 Broadway, Boulder, CO 80303-3328, 303/497-3346.

September 18-20, 1990

ELECTRONIC PUBLISHING '90

Location: National Institute of
Standards and Technology
Gaithersburg, MD

Electronic Publishing '90 (EP90) will be the third in a series of international conferences established to bring together researchers in all areas of electronic publishing systems. EP86, held in Nottingham, England, was sponsored by the British Computer Society. EP88, held in Nice, France, was sponsored by INRIA. The proceedings of papers presented at the earlier sessions were published by Cambridge University Press and have received wide dissemination. The proceedings of

EP90 will also be published in book form and will be available at the conference. EP90 will adopt a broad definition of "electronic publishing." Electronic publishing will be taken to encompass all aspects of computer-assisted preparation, presentation, transmittal, storage, and retrieval of documents. The scope of the conference also includes the design of the related computer systems, the design of their components, and the theory that underlies such systems. Both linear and non-linear documents are appropriate subjects for discussion. Sponsored by NIST.

Contact: Lawrence A. Welsch, B252 Technology Building, NIST, Gaithersburg, MD 20899, 301/975-3345.

October 1-4, 1990

13th NATIONAL COMPUTER SECURITY CONFERENCE Information System Security: Standards—The Key To The Future

Location: Omni Shoreham Hotel
Washington, DC

This conference provides a forum for the government and the private sector to share current information that is useful and of general interest to the conference participants on technologies, present and future, that are designed to meet the ever-growing challenge of telecommunications and automated information systems security. The conference will offer multiple tracks for the needs of users, vendors, and the research and development communities. The focus of the conference will be on: systems application guidance; awareness, training and education; ethics; evaluation and certification; innovations and new products; management and administration; and disaster prevention and recovery. Sponsored by NIST and the National Computer Security Center.

Contact: Irene Gilbert, A216 Technology Building, NIST, Gaithersburg, MD 20899, 301/975-3360.